Atomistically-Informed Finite Element Simulations of Phase Transformations and Fracture in Materials

A DISSERTATION
SUBMITTED TO THE FACULTY OF THE GRADUATE SCHOOL
OF THE UNIVERSITY OF MINNESOTA
BY

Jiadi Fan

IN PARTIAL FULFILLMENT OF THE REQUIREMENTS
FOR THE DEGREE OF
DOCTOR OF PHILOSOPHY

Ellad B. Tadmor (advisor)

January, 2020

Acknowledgements

The five and half years of life as a Ph.D. student has been a great journey to me, through which I have learned so many precious things that will always be valuable for the rest of my life. I would like to take this opportunity to give acknowledgements to all that have helped me immensely along the way, without which it would not have been possible for me to present my work here today.

I would like to first express my sincerest thanks to Professor Dr. Ellad B. Tadmor, for being a great advisor and friend to me. He has always been helpful and resourceful when I needed help for my research work; he has always encouraged me to "dig it deeper" on my research field; and moreover, he has always cared about my future career as a mentor. His valuable advice as well as the passion and devotion he has shown in his career helped me to shape my career view and discover what I want to pursue in my own career life. Special thanks to Tadmor's family for holding Thanksgiving dinner every year and inviting me to their home like a family member. Other professors I would like to thank are my committee members and our collaborators on projects. I would like to thank my committee Dr. Ryan S. Elliott, Dr. Perry H. Leo, Dr. Henryk K. Stolarski, and Dr. Andreas Stein for listening to all my presentations and giving valuable comments to my work. I would like to thank Dr. Christopher W. Macosko for the collaboration with us on the multiscale modeling for epoxy-graphene composite project.

During my research work I have explored many techniques that used to be new to me. Thanks to the help of many great scientists and researchers, these learning experiences all turned out to be fruitful. Throughout all these years, I have met and worked with many wonderful people as co-workers in the lab. It has been a pleasure to work with them. I would like to especially thank the following people: Dr. Alexandros

Anastasiou, Dr. Mingjian Wen, Dr. Kuan Zhang, Dr. Hao Xu, Dr. Fan Feng, Hanlin Gu, Kunwei Liu, Dr. Siyao He, and Dr. Yuqiang Qian. I would like to thanks the University of Minnesota for providing me studentship and such a nice research and study environment. Special thanks go to the department of Aerospace engineering and Mechanics for providing me the teaching assistant position to support me financially. I must thank my parents for their encouragement and moral support, my brothers and sisters in Christ from Life Spring Fellowship (LSF) and Providence Campus Evangelical Fellowship (PCEF) for their friendship, pastor Stephen Maa from Twin City Chinese Christian Church (T4C) and pastor Lihua Zhou from PCEF for their spiritual cares.

Finally I would like to thank the Lord my God as my savior and shepherd, the provider to everything I need. For many times, I were in a big hardship, feeling that no one can help me out, as if I were in the desert. However, my Lord gave me hope, and let me see His blessing beyond the surrounding.

> "In a desert land he found him, in a barren and howling waste. He shielded him and cared for him; he guarded him as the apple of his eye, like an eagle that stirs up its nest and hovers over its young, that spreads its wings to catch them and carries them on its pinions. The LORD alone led him; no foreign god was with him."–*Deuteronomy* 32:10-12 (NIV)

For many times, I prayed to Him to remove my pain. He did not remove the pain as I wished, but gave me patience and peace in heart. He opened my eyes and gave me wisdom to learn the lesson he wanted me to learn through out the pains.

> "But he said to me, 'My grace is sufficient for you, for my power is made perfect in weakness.' Therefore I will boast all the more gladly about my weaknesses, so that Christ's power may rest on me. " –*Corinthians 2* 12:9 (NIV)

For many times, I saw my own sins in every aspect of life and deal with them fearlessly with His power and strength, and that I can experience the fullness of His abundant love and be a blessing to others through the same love. So many times in the lab, He gave me the wisdom, courage, and endurance right where I needed them. It was His mercy and grace that have led me here thus far, and will keep leading me on.

"And we know that all things work together for good to them that love God,
to them who are called according to His purpose" – *Romans* 8:28 (KJV)

Though I tried not to miss anyone, I know there are still many people not mentioned here who have also help me directly or indirectly throughout all these years. My Lord knows that I have always held a grateful heart to them all.

Soli Deo Gloria.

Abstract

Multiscale material modeling is a powerful computational method to investigate materials at disparate length and/or time scales, and has been widely employed to study a large variety of problems in science and engineering. In this dissertation, an atomistically-informed finite element method (AFEM) is introduced, which involves two scales of calculations: the finite element method (FEM) and atomistic simulation. The FEM as a powerful tool to simulate material response in the continuum scale is widely used in solid mechanics field. However, phenomenological model is usually employed as constitutive law, which lacks the fundamental insights of material. Atomistic simulation can provide us with thermomechanical properties of material based on the interactions between atoms, but is limited to small model size due to the computational efficiency. In the AFEM presented in this dissertation, the material properties are calculated from the atomistic scale simulations, and are employed in the continuum scale FEM simulations as material parameters. Using such a modeling method, we can predict the large scale mechanical response of a system without losing atomistic insights of materials. The AFEM is implemented in an *in situ* simulation of a diamond anvil cell to predict the phase transformation of silicon under pressure, and a cohesive element simulation of epoxy–graphene composite to study the fracture mechanism at small graphene loading.

Contents

Acknowledgements **i**

Abstract **iv**

List of Tables **ix**

List of Figures **xi**

1 Introduction **1**

1.1 Introduction to multiscale modeling 1

1.2 Constitutive law in the finite element method 2

1.3 Interatomic potential in atomistic simulations 4

1.3.1 Pair potentials 4

1.3.2 EAM potentials 5

1.3.3 Three-body potentials 5

1.3.4 Force field 6

1.4 Outline of chapter contents 11

2 Enabling Atomistic Multiscale Simulation in Commercial Finite Element Software Packages: Toward the Study of Solid-solid Phase Transformations **14**

2.1 Introduction 15

2.2 Cauchy-Born kinematics 16

2.3 Numerical examples 21

2.3.1 Uniaxial compression of a fcc Cu nanoplate with a hole 21

2.3.2 PT in a nanoindentation simulation of diamond-cubic Si 24
2.4 Conclusion and future directions 25

3 Modified Blatz-Ko Model for High-pressure Diamond Anvil Cell Materials: Helium and Rhenium 29
3.1 Introduction 30
3.2 Modified Blatz-Ko model 31
3.3 Kinematics of material deformation under hydrostatic pressure 34
3.4 Voigt and Reuss bounds 38
3.5 Fitting the modified Blatz-Ko model to helium and rhenium 39
3.5.1 Helium 40
3.5.2 Rhenium 43
3.6 Numerical example 47
3.7 Conclusion 55

4 A Multiscale Simulation of Phase Transformation for Silicon in Diamond Anvil Cell 56
4.1 Introduction 56
4.2 Problem formation 58
4.3 Results and discussion 61
4.4 Conclusion 63

5 Molecular Dynamics Predictions of Thermomechanical Properties of an Epoxy Thermosetting Polymer 66
5.1 Introduction 67
5.2 MD simulation methodology 68
5.2.1 DGEBA/Jeffamine D230 system 68
5.2.2 Force field and simulation details 68
5.2.3 Crosslinking methodology 69
5.3 Results and discussion 76
5.3.1 Crosslinking and temperature induced volume change 76
5.3.2 Gel point and glass transition temperature 79
5.3.3 Mechanical response to uniaxial tension and simple shear 84

5.4 Conclusion 87

6 Molecular Dynamics Based Cohesive Zone Law for Describing an Epoxy-Graphene Interface Mechanics 91

6.1 Introduction 92
6.2 Structure and formation of epoxy-nanofiller interfaces 94
6.3 Properties of epoxy–SLG/MLG/MLGO interfaces 97
6.3.1 Mass density 97
6.3.2 Mechanical response under uniaxial tension 97
6.3.3 Mechanical response under simple shear 101
6.4 Fracture Energy 106
6.5 The cohesive law 111
6.6 Conclusion 115

7 Rescaling Cohesive Element Properties for Mesh Independent Fracture Simulations 117

7.1 Introduction 117
7.2 1D analysis of cohesive element effects on FEM model properties 120
7.2.1 Cohesive Laws 120
7.2.2 Static properties in 1D: Effective stiffness 120
7.2.3 Dynamic properties in 1D: Effective speed of sound 122
7.2.4 Rescaling cohesive element properties for mesh independence . . 123
7.3 Numerical results for the cohesive element rescaling method 124
7.3.1 Uniaxial stretching problem 125
7.3.2 Beam bending problem 128
7.3.3 Impact bar problem 130
7.3.4 Kalthoff plate impact problem 132
7.4 Conclusion 134

8 An Atomistically-informed Multiscale Simulation for Epoxy–graphene Composites: Toughening Mechanism at Small Graphene Loading 136

8.1 Introduction 137
8.2 Methods 138

8.2.1 Model setup 138
8.2.2 Material properties 140
8.3 Results and discussion 146
8.4 Conclusion 147

9 Conclusions and Future Directions **149**

Appendix A. Theoretical Solution of Curing Agent Occupation Problem **152**

Appendix B. Analytical Solution of E_{eff}/E and $c_{\text{eff}}/c_{\text{b}}$ Ratio for a Model with Triangular Elements **155**

B.1 Analytical solution of E_{eff}/E ratio for a model with triangular elements 155
B.2 Analytical solution of $c_{\text{eff}}/c_{\text{b}}$ ratio of a model with triangular elements . 157

References **159**

List of Tables

1.1 The parameters of the Stillinger-Weber potential for diamond-cubic silicon 7

1.2 A review of different classical force fields for epoxy crosslinking MD simulations. 10

3.1 Coefficients for the second Piola-Kirchhoff stress tensor for the modified Blatz-Ko model. 32

3.2 Coefficients for the material elasticity tensor of the modified Blatz-Ko model. 34

3.3 The elastic constants $\tilde{C}_{ij}$ with respect to the intermediate configuration of single-crystal hcp He at different pressures and the corresponding Jacobian J_0 obtained from experimental measurements at 300 K [1]. Pressures and elastic constants are in GPa, the Jacobian is unitless. 41

3.4 The temperature derivative of elastic constants of single-crystal hcp Re measured at atmospheric pressure. Units in GPa/K. Source: [2]. 46

3.5 The elastic constants $\tilde{C}_{ij}$ relative to the intermediate configuration of single-crystal hcp Re at different pressures and the corresponding Jacobian J_0. Results at 0 K are taken from [3] and extrapolated to 300 K using Eq. (3.39). Pressure and elastic constants are in GPa. 46

5.1 References to MD simulations of thermosetting polymers. Computed properties: shear strength (τ_y), yield strength (σ_y), shear modulus (G), Young's modulus (E), gel point, density, volume change (ΔV), and glass transition temperature (T_g). 68

5.2 The a_i and b_i parameters in Eq. (5.3) for H, C, N, and O obtained from experiment [4]. 75

5.3 Mass density of DGEBA/Jeffamine D230 epoxy predicted by DREIDING and AMBER at different conversions at 300 K compared with an experimental result for high conversion epoxy. Units in g/cm^3 79
5.4 Mechanical properties of DGEBA/Jeffamine D230 epoxy predicted by the DREIDING and AMBER FFs for samples with 80% conversion at 300 K at a strain rate of 10^8 s^{-1}, compared with experimental results obtained at strain rates in the range 5.7×10^{-4} to 8.3×10^{-3} s^{-1}. . . . 88
6.1 The average mass density of epoxy in the epoxy–SLG/MLG/MLGO interfaces compared with the density of bulk epoxy obtained from MD simulations and experiments [5] at 300 K and atmospheric pressure. Unit in g/cm^3. 99
6.2 Young's modulus for epoxy–SLG/MLG/MLGO interfaces at 300 K and atmospheric pressure compared with bulk epoxy. Units in GPa. 100
6.3 Ultimate tensile strength of epoxy–SLG/MLG/MLGO interfaces at 300 K and atmospheric pressure compared with the yield strength of bulk epoxy. Units in MPa. 100
6.4 Shear modulus for the epoxy–SLG/MLG/MLGO interfaces at 300 K and atmospheric pressure compared with bulk epoxy. Units in GPa. 104
6.5 Ultimate shear strength of epoxy–SLG/MLG/MLGO interfaces at 300 K and atmospheric pressure compared with bulk epoxy. Units in MPa. . . 105
6.6 The fibril spacing D (in Å) for different simulation cell sizes. The fibril spacing for System-I at a higher strain is not available because there is only one void in the simulation cell. 112
6.7 Parameters obtained from MD simulations for the epoxy–MLG/MLGO critical energy release rate in Eq. (6.14). 112
8.1 The critical force to break the CTS and the corresponding fracture toughness at different graphene loading. 145

List of Figures

1.1 The interaction between atom pairs. (a) Atoms are in equilibrium. (b) Distance between the red atom and other atoms are far apart, the red atom is pulling back by attract force. (c) Distance between the red atom and other atoms are close, the red atom is pushing away by repel force. 5

1.2 Schematic diagram of (a) bond stretching, (b) bond bending, (c) dihedral interaction, (d) improper interaction, (e) van de Waals interaction, and (f) electrostatic interaction. 8

2.1 A schematic diagram showing the kinematics of lattice invariant shear. The solid square is the structure of interest, the dashed line is the original lattice. (a) The original lattice before shearing. (b) The deformed structure has not reproduced the original structure, thus lattice invariant shear has not yet happened. (c) The lattice invariant shear happens, because the top surface of the sheared lattice overlaps with its right neighbor. . 19

2.2 Shear parameter vs. potential energy density diagram of fcc Cu. 20

2.3 A schematic diagram showing the shuffle relaxation during the lattice invariant shear of a multi-lattice crystal (a) Shear without shuffle relaxation. The first basis atoms reproduces the original lattice, while the shuffles have a lag. (b) Shear with shuffle relaxation, the shuffle goes to the centriod of the tetrahedron to minimized the potential energy. . . . 20

2.4 (a) Lattice invariant shear for diamond-cubic Si with the shuffle relaxation using Eq. (2.6) (blue line) and without the shuffle relaxation using Eq. (2.5) (red line). (b) is a zoom-in diagram of one fourth of the blue line in (a). The small pit is due to the nonphysical prediction of Stillinger-Weber potential for Si. 21

2.5 A diagram shows the boundary conditions and mesh for (a) the fcc Cu nanoplate with a hole problem, and (b) the nanoindentation of diamond-cubic Si problem. The red arrow shows the crystallographic orientation. 23
2.6 (a) The Cauchy stress σ_{yy} near the hole. Unit in GPa. (b) The stress concentration ratio at the hole calculated from the linear anisotropic model, the SVK model, and the CB-KIM model. 23
2.7 A schematic diagram showing the energy configurations of system and PT identification algorithm. (a) the deformed structure goes back to the initial configuration after energy minimization, PT does not happened. (b) The deformed structure conquers the energy barrier and goes to a different energy configuration. PT happens. 25
2.8 (a) The reaction force-displacement curve of the indenter. The local drop of reaction force at displacement of 0.325 μm and 0.475 μm are due to the PT of silicon. The green elements represent the original diamond-cubic silicon shown in (b). The red elements represent bct5 silicon shown in (c). The yellow elements represent β-Sn silicon shown in (d). Figures in (b), (c) and (d) are generated using OVITO [6]. 26
2.9 σ_{yy} and the maximum principal stress contour and the corresponding phase at different indentation depth (0.325 μm, 0.475 μm, and 0.5 μm). Stress unit in MPa. 27
3.1 Kinematics of an isotropic material subjected to hydrostatic compression followed by an arbitrary deformation. 35
3.2 The effective elastic constants $\tilde{C}_{11}^{\mathrm{V,R}}$ and $\tilde{C}_{12}^{\mathrm{V,R}}$ for an hcp He polycrystal obtained from Eq. (3.31) based on experimental measurements at 300 K [1]. The red circles and the blue triangles are Reuss bounds and Voigt bounds, respectively. 41
3.3 The isothermal pressure-volume EOS for hcp helium. The red circles are experimental results from [1]. The green line is the curve fitted to the Rose-Vinet EOS in Eq. (3.35). 43
3.4 The effective elastic constants as a function of J_0 (red circles are Reuss bounds, blue triangles are Voigt bounds) and the fitted modified Blatz-Ko model (green lines) for an hcp He polycrystal. 44

3.5 The modified Blatz-Ko model EOS curve (green line) compared with DAC experiments by Zha et al. [1] (red dots) and X-ray diffraction measurements by Loubeyre et al. [7] (blue triangles). 44
3.6 The effective elastic constants as a function of J_0 (red circles for the Reuss bounds, blue triangles for the Voigt bounds) and the fitted modified Blatz-Ko model results (green line) for hcp Re polycrystal. 48
3.7 The modified Blatz-Ko model EOS curve (green line) compared with results from shock wave experiment by Marsh [8] (red dots), and DAC experiments by Zha et al. [2] (blue triangles), Duffy et al. [9] (yellow squares), and Anzellini et al. [10] (purple stars). 48
3.8 The geometry and mesh of (a) model-I: rhenium spherical pressure vessel (green) subjected to internal pressure loading, and (b) model-II: rhenium spherical pressure vessel (green) filled with a solid helium core (blue). The models are cut in half to show the meshes in the cross section. . . . 50
3.9 The outward radial displacement of the inner surface of the spherical vessel as a function of time for (a) model-I, (b) model-II, and (c) model-III. 51
3.10 The maximum principal stress field in the spherical vessel for (a) model-I, (b) model-II, and (c) model-III. Only the rhenium vessel is shown in (b) and (c). The models are cut in half to show the stress distribution on the inner surface. The small irregular fluctuations in the stress are due to numerical noise from variations in the mesh and the imposed contact boundary conditions between the rhenium vessel and helium core. . . . 52
3.11 The average contact pressure between the rhenium vessel and helium in the model-III simulation. 53
3.12 The maximum principal stress of (a) rhenium pressure vessel and (b) helium core under uniaxial compression between two rigid flat plates displaced inwards by 0.02 m. The models are cut in half to show the stress distribution in the cross section. (The squiggly black lines in the figure are an artifact of the visualization method used to create a sliced cross-section of the deformed body.) 54

4.1 The geometry for (a) the anvil and the gasket. The purple region of (a) is shown in (b), which are the pressure transmission medium (bule) and the sample (red). Unit in millimeter. 59
4.2 Mesh for (a) the assembled DAC system, (b) the anvil, (c) the gasket, (d) the pressure transmission medium, and (e) the sample. 60
4.3 (a) A zoomed-in diagram of a sample in the chamber formed by gasket and anvils. The upper anvil is removed to show the interior of the chamber. The white region represents the surfaces that are subjected to the initial pressure of 11.65 GPa. (b) The stress state of material in (a). Unit of the scaling legend is MPa. 62
4.4 (a) The contact pressure and (b) the radial expansion between helium/rhenium (blue) and helium/silicon sample (red). 62
4.5 The pressure, maximum principal stress, and the phases of the silicon sample at anvil displacements of 0.02 mm, 0.022 mm, and 0.024 mm. . . 64
4.6 The pressure, maximum principal stress, and the phase of the silicon sample under hydrostatic pressure of 20 GPa. 64
5.1 Molecular structure of (a) DGEBA and (b) Jeffamine D230. 69
5.2 Reactions involved in the curing of an epoxy. 70
5.3 Molecular structures of (a) active DGEBA and (b) active Jeffamine D230 with $n = 2$. The color coding in the figures is carbon (gray), active carbon (blue), oxygen (green), hydrogen (white) and active nitrogen (purple). Covalent bonds between atoms are shown as thick lines. Figures are generated using OVITO [6]. 71
5.4 The final degrees of conversion of epoxy systems after a 200 ps crosslinking simulation as a function of the threshold distance. Results are for the DREIDING FF. Error bars represent the standard deviation of three independent simulations. 73

5.5 DGEBA/Jeffamine D230 system with an 87% degree of conversion. Active carbon atoms (blue), active nitrogen atoms (purple), and newly created C-N bonds (red) are emphasized. (a) An active nitrogen atom that forms one bond with a periodic image of an active carbon. (b) An active nitrogen atom that forms two bonds with active carbon atoms. (c) An active nitrogen atom that forms zero bonds with active carbon atoms. (d) An active nitrogen that forms one bond with an active carbon atoms. Figures are generated using OVITO [6]. 74
5.6 The RDF for epoxy with 87% conversion obtained from the crosslinking simulation. 75
5.7 Structure factor for a simulated DGEBA/Jeffamine D230 epoxy with 87% conversion computed using Eq. (5.2) (blue line with triangles) compared with experimental measurements for DGEBA/DETA epoxy (orange dots) [11] and DGEBA/TEA epoxy (green crosses) [12]. The abscissas are converted from q to 2θ using Eq. (5.4) for λ_{inc} =1.542 Å. 77
5.8 The volume (red triangles) and volume shrinkage (blue squares) of DGEBA/Jeffamine D230 system at 300 K as a function of conversion predicted by (a) DREIDING FF, and (b) AMBER FF. Error bars represent the standard deviation from three independent simulations. 78
5.9 Mass density of DGEBA/Jeffamine D230 as a function of conversion at different temperatures. Results are obtained with the DREIDING FF. Error bars represent the standard deviation of three independent simulations. 79
5.10 Molecular weight of the largest group (red triangles) and the second-largest group (blue squares) as a function of the degree of conversion. The dashed line is a theoretical prediction of the gel point at 57.5%. Results are obtained using the DREIDING FF. Error bars represent the standard deviation of three independent simulations. 80
5.11 Percentage of Jeffamine D230 molecules linked to 0 to 4 epoxide groups at different conversions. The black lines are theoretical results. The blue triangles are MD simulation results using the DREIDING FF. Error bars represent the standard deviation of three independent simulations. . . . 81

5.12 Mass density of DGEBA/Jeffamine D230 epoxy as a function of temperature at 20% (red squares) and 80% (blue triangles) conversions. Results obtained from MD simulations using the DREIDING FF. Data points and error bars represent the mean and standard deviation in 50 ps windows during the cooling process, which had a total duration of 2 ns. 82
5.13 T_g as a function of conversion obtained by the AMBER FF (red squares) and the DREIDING FF (blue triangles). The simulation results are adjusted by the WLF equation and also fit to the DiBenedetto's equation (Eq. (5.5)) with least squares. The experimental T_g is shown as a range at high conversion (80%–100%) [13, 14]. Error bars represent the standard deviation of three independent simulations. 83
5.14 Stress strain curves of for samples with 80% conversion under (a) uniaxial tension and (b) simple shear, obtained from MD simulations using the DREIDING FF at three strain rates (10^7, 10^8, and 10^9 s^{-1}). The results are smoothed by a Savitzky–Golay filter. 85
5.15 (a) Young's modulus as a function of crosslinking conversion. The black diamond represents the experimental results [13, 15–17]. (b) Shear modulus as a function of crosslinking conversion. Error bars correspond to the standard deviation of simulations in three deformation directions of three independent configurations. 86
5.16 (a) Yield strength as a function of crosslinking conversion. The black diamonds represents the experimental results [15, 17]. (b) Shear strength as a function of crosslinking conversion. Error bars correspond to the standard deviation of simulations in three deformation directions of three independent configurations. 87
6.1 (a) Single-layer graphene (b) Multilayer graphene formed by stacking four layers of single-layer graphene in an AB pattern. (c) Single-layer graphene oxide with each carbon (red) bonded to oxygen (blue). (d) Multilayer graphene oxide comprised of four stacked layers of (c). Covalent bonds between atoms are shown as thick lines. Figures generated using OVITO [6]. 95

6.2 Interfacial DGEBA/Jeffamine D230 epoxy and (a) single-layer graphene, (b) multilayer graphene, and (c) multilayer graphene oxide. Figures generated using OVITO [6]. 96
6.3 Epoxy density profiles in the direction normal to the interface in epoxy–SLG/MLG/MLGO with a conversion of (a)-(c) 0% and (d)-(f) 80% at 300 K and atmospheric pressure. 98
6.4 Tensile stress–strain curves obtained from MD simulations of uniaxial tension in the direction normal to the interface for epoxy–SLG/MLG/MLGO systems compared with bulk epoxy. 98
6.5 Comparison of (a) Young's modulus and (b) ultimate tensile strength for epoxy–SLG/MLG/MLGO interfaces and yield strength for bulk epoxy. Error bars represent the standard deviation of three independent simulations. 100
6.6 Snapshots of the epoxy–MLG interface under uniaxial tension at different strain levels. Two periodic images are displayed in the direction normal to the interface. 101
6.7 Mass density evolution during uniaxial tension at strains of 0.04, 0.08, 0.12, 0.16 and 0.2 for (a) epoxy–SLG, (b) epoxy–MLG, and (c) epoxy–MLGO interfaces. 102
6.8 Cross-section area shrinkage during uniaxial tension for (a) epoxy–SLG, (b) epoxy–MLG, and (c) epoxy–MLGO interfaces. 102
6.9 Shear stress–strain curves for MD simulations of simple shear parallel to epoxy–SLG/MLG/MLGO interfaces in the graphene zigzag direction compared with bulk epoxy. 103
6.10 Comparison of (a) the shear modulus and (b) the ultimate shear strength for epoxy–SLG/MLG/MLGO interfaces and bulk epoxy. Error bar represents the standard deviation of three independent simulations. 104
6.11 Shear response under mixed-mode conditions: (a) shear modulus, (b) shear strength, and (c) shear strain at failure for epoxy–MLG/MLGO interfaces under different normal strains. The error bars represent the standard deviations from three independent simulations. The results are fitted to the dashed lines with linear regressions. 105

6.12 Schematic diagrams of (a) a semi-infinite strip model for bulk epoxy subjected to an uniform drawing stress σ_{d}, (b) similar to (a) for an epoxy–graphene interface, and (c) process zone fibril structure. 106
6.13 Schematic stress–strain curve for (a) bulk epoxy and (b) epoxy–graphene interface. 107
6.14 Stress–strain curves for uniaxial tension of epoxy–MLG/MLGO systems upto failure due to interfacial debonding. 110
6.15 Trilinear mode I cohesive law (blue lines) and the stress–strain curve obtained from MD simulations (red dashed lines) for (a) epoxy–MLG and (b) epoxy–MLGO interfaces. 113
6.16 Mode II cohesive law for (a) epoxy–MLG and (b) epoxy–MLGO interfaces at different normal strains ranging from -0.03 to 0.03. 115
7.1 Bilinear cohesive laws in (a) tension, and (b) shear. 121
7.2 Two types of 1D periodic cells. (a) One square bulk element and one cohesive element before (left) and after (right) uniaxial stretching. (b) Two triangular bulk elements separated by a cohesive elements at 45° and 0° before (left) and after (right) uniaxial stretching. 121
7.3 Dependence of effective properties on cohesive element properties. (a) The solid curve is the relation between E_{eff}/E and K/E, the dashed curve is the relation between $c_{\mathrm{eff}}/c_{\mathrm{b}}$ and K/E. (b) The relation between E_{eff}/E and $c_{\mathrm{eff}}/c_{\mathrm{b}}$ and the normalized cohesive element thickness d/h (both curves overlap). 124
7.4 Geometries of the tested models. (a) Uniaxial stretching. (b) Beam bending. (c) Bar impact. (d) Kalthoff plate impact experiment (the model represents only half of the full structure due to symmetry). The expected crack direction is shown as a dashed line. 125
7.5 Uniaxial stretching results for a mesh size of $h = 3$ mm. The graph shows the numerical and analytical results for E_{eff}/E at different d/h ratios. The analytical results are obtained from Eq. (7.8). 126
7.6 Effective stiffness in uniaxial stretching for a uniform mesh. (a) The normalized effective stiffness as a function of mesh size. (b) The four meshes studied in (a). 127

7.7 Uniaxial stretching results for a nonuniform mesh. (a) Normalized element stiffness measured in the simulation as a function of element size. Each point is an average over the stiffness of all elements of that size. (b) The nonuniform mesh with elements ranging from $h = 1$ mm on the bottom to $h = 3$ mm on the top studied in (a). 127
7.8 (a) The relation between the deflection at the end of the beam and the d/h ratio. The horizontal dashed line is deflection for a bulk model without cohesive elements. (b) The relation between E_{eff}/E and d/h. Numerical and analytic results overlap. 129
7.9 Numerical results of beam end deflection with/without mesh rescaling method. The horizontal dashed line is -0.0147 mm, which is the beam end deflection corresponding to $E_{\text{eff}}/E = 90.66\%$ 129
7.10 (a) Velocity as a function of time at the midpoint of a 1D bar model (without cohesive elements) used to compute the speed of sound (see text). (b) The effect of cohesive elements on the speed of sound. Numerical and analytical results for $c_{\text{eff}}/c_{\text{b}}$ as a function of the d/h ratio. Analytical results are obtained from Eq. (7.12). 130
7.11 (a) Effective longitudinal speed of sound as a function of mesh size in a 1D bar impact problem. (b) The four meshes studied in (a). 131
7.12 Crack propagation for a model with two mesh sizes. (a) Mesh size $h = 3$ mm, cohesive element thickness $d = 0.15$ mm, $d/h = 0.05$. (b) $h = 1$ mm, $d = 0.15$ mm, $d/h = 0.15$. (c) $h = 1$ mm, $d = 0.05$ mm, $d/h = 0.05$. 133
7.13 Crack length as a function of time in a Kalthoff plate impact simulation. 134
8.1 Geometry of a CTS [18]. 139
8.2 The mesh and boundary conditions for the CTS model, and a zoom-in figure for *region A*. 141
8.3 Zoom in of the crack tip in *region A* with toughener loading of (a) 0.0165%, epoxy–MLG cohesive elements (red line)/epoxy–epoxy cohesive elements (black line) ratio is 250/9180, (b) 0.033% (500/9180), (c) 0.05% (750/9180), (d) 0.064% (1000/9180), (e) 0.1% (1500/9180), and (f) 0.128% (2000/9180). 141
8.4 Schematic diagram of mode I bilinear fracture cohesive zone law. 142

8.5 The cohesive zone law for epoxy–MLG interface. (a) The trapezoidal-shape law for for mode I fracture, and (b) the bilinear law for mode II fracture at normal strain from -0.03 to 0.03. 144
8.6 Schematic diagram of a mode II bilinear cohesive zone law. 144
8.7 The simulations predicted K_{Ic} (blue) compared with the experimental results (red) [13]. 145
8.8 The normal stress contour at the crack tip at the applied displacement of 0.14 mm for (a) pure epoxy with graphene loading of 0 wt%, and composite with graphene loading of (b) 0.033 wt%, (c) 0.067 wt% and (d) 0.1 wt%. The unit of the scale legend is Pa. The black lines in the model represent the micro-cracks formed in the epoxy matrix. 147
B.1 1D periodic unit cell containing two triangular elements separated by cohesive elements at 45° and 0° before (left) and after (right) uniaxial stretching. 156
B.2 Zoomed view of the inclined cohesive element (gray rectangle). 157

Chapter 1

Introduction

1.1 Introduction to multiscale modeling

Multiscale material modeling involves phenomena at disparate length and/or time scales spanning several orders of magnitude. Material responses in these scales are all important, without any of them the model can not accurately describe the physical phenomena. Multiscale method can be classified into two broad categories: *concurrent* and *sequential* methods. *Concurrent* methods employ models at different scales simultaneously, and can be further classified into two sub-categories: *partitioned-domain* and *hierarchical* methods. In the *partitioned-domain* approach, the physical problem is divided into two or more contiguous regions with different scales used in each region. It performs the full fine-scale simulation in only part of domain, while assumes that the coarse-scale model is sufficiently accurate for the rest of the problem [19]. One of the well-known partitioned-domain methods is the quasicontinuum (QC) method proposed by Tadmor *et al.* [20–26], and continues to be developed today [27–29]. In the QC method, a model is divided into the atomistic domain and the finite element method (FEM) domain. The atomistic domain is implemented in the region where material is subjected to the stress concentration or nonlinear deformation (e.g. crack tips in fracture simulations), while the FEM domain is implemented in the rest region of model. *Hierarchical* methods, on the other hand, make use of both scales everywhere in a model. Specifically, the coarse-scale model appeals to the fine-scale model to determine a constitutive law and, conversely, the fine-scale model looks to the coarse-scale model

for its boundary conditions. One example of the hierarchical multiscale methods is the Cauchy-Born (CB) rule which is employed as the constitutive law in the FEM region of a QC model. It assumes that the atoms behave as material points embedded in the continuum, and simply follow the macroscopic deformation gradient. The continuum scale material properties can then be calculated based on the atomistic potential energy. *Sequential* multiscale approaches assume the fine-scale simulations are performed as a pre-processing step to the coarse-scale models. For example, the fine-scale model generates parameters that are needed to complete the coarse-scale model description, after which it is assumed that the fine-scale model is no longer required.

Finite element method as a powerful tool to simulate material response in the continuum scale has been widely used in engineering and science. However, phenomenological model is usually employed as constitutive law, which lacks the fundamental insights of material. Atomistic simulation can provide us with thermomechancial properties of material based on the more fundamental interactions between atoms, but is limited to small model size due to the computational efficiency. In this dissertation, an atomistically-informed finite element method (AFEM) is introduced, aiming to simulate the continuum scale material response based on the material properties obtained from atomistic scale calculations. Next, I will introduce the constitutive law in a nonlinear FEM, and the interatomic potential in atomistic simulations.

1.2 Constitutive law in the finite element method

FEM subdivides a large and complex domain into smaller and simpler elements. The mechanical response of each element follows a constitutive law, which is conventionally characterized by an empirical equation fitting to experimental data. A constitutive law can be a linear equation when a linear elastic material is subjected to infinitesimal deformation. However, complex physical phenomena require FEM to have accurate predictions over highly nonlinear phenomena.

When *nonlinear FEM* is used in the literature, it means either geometrical nonlinearity, or material nonlinearity, or both of them. Geometrical nonlinearity is due to the large deformation of material. The simplest geometrically-nonlinear model is the Saint Venant-Kirchhoff (SVK) model, which is just an extension of the linear elastic material

model to the nonlinear regime. The strain energy function of the SVK model is

$$W = \frac{1}{2}(\mathbb{C} : \boldsymbol{E}) : \boldsymbol{E}, \tag{1.1}$$

where $\mathbb{C}$ is the elastic constant tensor, which keeps constant during simulation. $\boldsymbol{E} = \frac{1}{2}(\boldsymbol{F}^{\mathrm{T}}\boldsymbol{F} - \boldsymbol{I})$ is the Lagrangian strain tensor, where $\boldsymbol{F}$ is the deformation gradient, $\boldsymbol{I}$ is the identity tensor. The 2nd Piola-Kirchhoff (PK) stress $\boldsymbol{S}$ is linear to $\boldsymbol{E}$:

$$\boldsymbol{S} = \frac{\partial W}{\partial \boldsymbol{E}} = \mathbb{C} : \boldsymbol{E}. \tag{1.2}$$

The Cauchy stress $\boldsymbol{\sigma}$ is

$$\boldsymbol{\sigma} = J^{-1}\boldsymbol{F}(\mathbb{C} : \boldsymbol{E})\boldsymbol{F}^{T}, \tag{1.3}$$

where $J = \det \boldsymbol{F}$ is the Jacobian.

Material nonlinearity is due to the nonlinear relationship between stress and strain. For example, stress is a nonlinear function of strain, or the stress-strain relation is path-dependent (stress depends on strain history as well as the strain itself), etc. The neo-Hookean model includes both materially and geometrical nonlinearities. The strain energy function of a neo-Hookean material is

$$W = \frac{\mu}{2}(\bar{I}_{\mathrm{C}} - 3) + \frac{\kappa}{2}(J-1)^2, \tag{1.4}$$

where $\bar{I}_{\mathrm{C}} = \mathrm{tr}(\bar{\boldsymbol{C}})$, $\bar{\boldsymbol{C}} = \bar{\boldsymbol{F}}^{T}\bar{\boldsymbol{F}}$, and $\bar{\boldsymbol{F}} = J^{-1/3}\boldsymbol{F}$, μ and κ are the shear modulus and the bulk modulus, respectively. The 2nd PK stress $\boldsymbol{S}$ and the elastic constant tensor $\mathbb{C}$ are

$$\boldsymbol{S} = \frac{\partial W}{\partial \boldsymbol{E}} = \mu J^{-2/3}\left(\boldsymbol{I} - \frac{I_{\mathrm{C}}}{3}\boldsymbol{C}^{-1}\right) + \kappa J(J-1)\boldsymbol{C}^{-1}, \tag{1.5}$$

$$\begin{aligned}\mathbb{C} = \frac{\partial^2 W}{\partial \boldsymbol{E}^2} =& \frac{2}{3}\mu J^{-2/3}\left[-\boldsymbol{C}^{-1}\otimes\boldsymbol{I} - \boldsymbol{I}\otimes\boldsymbol{C}^{-1} + I_{\mathrm{C}}\mathbb{I} + \frac{I_{\mathrm{C}}}{3}\boldsymbol{C}^{-1}\otimes\boldsymbol{C}^{-1}\right] \\ &+ \kappa J\left[(2J-1)\boldsymbol{C}^{-1}\otimes\boldsymbol{C}^{-1} - 2(J-1)\mathbb{I}\right],\end{aligned} \tag{1.6}$$

where $I_{\mathrm{C}} = \mathrm{tr}(\boldsymbol{C})$, $\boldsymbol{C} = \boldsymbol{F}^{T}\boldsymbol{F}$, and $\mathbb{I}$ is a fourth-order tensor with components $\mathbb{I}_{ijkl} = C^{-1}_{ik}C^{-1}_{jl}$. Evaluate Eq. (1.6) at the identity, we obtain the linear elastic constant tensor

$$\mathbb{C}_{ijkl}\,|_{\boldsymbol{F}=\boldsymbol{I}} = \mu(\delta_{il}\delta_{jk} + \delta_{ik}\delta_{jl}) + \lambda\delta_{ij}\delta_{kl}, \tag{1.7}$$

where $\lambda = (\kappa - \frac{2}{3}\mu)$ and μ are the Lamé constants.

1.3 Interatomic potential in atomistic simulations

Atomistic simulation is a powerful tool to investigate thermomechanical properties of material on the microscopic scale. The interactions between atoms can be analogous to nonlinear springs shown in Fig. 1.1. If the distance between atoms are neither too close nor too far away, atoms are in equilibrium as shown in Fig. 1.1(a). If two atoms are too far apart or too close, they attract or repel each other by the long range electrical forces, shown in Fig. 1.1(b) and (c). An interatomic potential $\mathcal{V}^{\text{int}}$ is used to describe these interactions between atoms, which is a function of distances between each atom pair. For a system contains N atoms,

$$\mathcal{V}^{\text{int}} = \phi_0 + \frac{1}{2!}\sum_{\substack{\alpha,\beta \\ \alpha\neq\beta}} \phi_2(r^{\alpha\beta}) + \frac{1}{3!}\sum_{\substack{\alpha,\beta,\gamma \\ \alpha\neq\beta\neq\gamma}} \phi_3(r^{\alpha\beta}, r^{\beta\gamma}, r^{\alpha\gamma}) + ..., \tag{1.8}$$

where ϕ_0 is the reference energy, ϕ_n denotes n-body interaction, $r^{\alpha\beta}$ is the distance between atoms α and β. A cutoff radius r_{cut} is usually used to speed up the energy calculation, which means beyond r_{cut}, atoms interact so weakly that they make essentially no contribution to the total potential energy. A classic interatomic potential is a physics-driven functional form associated with parameters fit to reference data obtained from experiments or first principle calculations.

1.3.1 Pair potentials

Atoms interact with all neighbors have distance within the cutoff radius, but pair potentials only consider two-body interactions and ignore the higher order interactions. Retaining only the ϕ_2 sum in Eq. (1.8) and setting $\phi_0 = 0$, we obtain the pair potential:

$$\mathcal{V}^{\text{int}} = \frac{1}{2!}\sum_{\substack{\alpha,\beta \\ \alpha\neq\beta}} \phi_2(r^{\alpha\beta}). \tag{1.9}$$

The most common and widely used pair potential is the Lennard-Jones potential [30–32], which takes the form

$$\phi_2(r^{\alpha\beta}) = 4\epsilon\left[\left(\frac{d}{r^{\alpha\beta}}\right)^{12} - \left(\frac{d}{r^{\alpha\beta}}\right)^{6}\right], \tag{1.10}$$

where d and ϵ are material parameters.

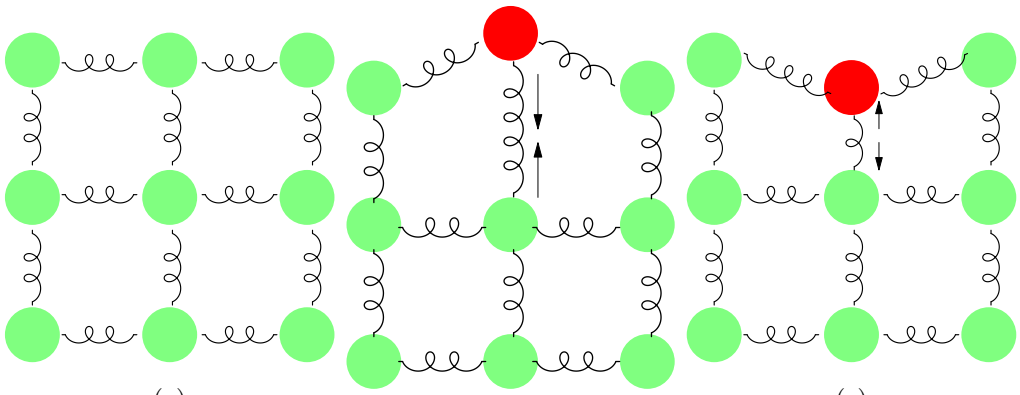

Figure 1.1: The interaction between atom pairs. (a) Atoms are in equilibrium. (b) Distance between the red atom and other atoms are far apart, the red atom is pulling back by attract force. (c) Distance between the red atom and other atoms are close, the red atom is pushing away by repel force.

1.3.2 EAM potentials

A mortified form of the pair potential is the EAM (embedded atom method) potential [33–35], which calculates the contribution of energy to embed an atom into the electron cloud generated by its neighbors. The contribution of atom α to the total energy potential E^α is

$$E^\alpha = U_\alpha(\rho^\alpha(r^{\alpha\beta})) + \frac{1}{2}\sum_{\substack{\beta \\ \beta\neq\alpha}} \phi_2(r^{\alpha\beta}), \tag{1.11}$$

where ϕ_2 is the pair potential function. U_α is the energy associated with embedding an atom α at a point whose environment is defined by an electron density function ρ^α. The interatomic potential $\mathcal{V}^{\text{int}}$ is the summation of contribution from each atom in the system

$$\mathcal{V}^{\text{int}} = \sum_\alpha E^\alpha. \tag{1.12}$$

1.3.3 Three-body potentials

Material with a strong covalent-bonding character such as silicon needs an interatomic potential with bond-angle dependence. Thus, it is necessary to at least take three-body

interactions into account. One widely used three-body potential is the Stillinger-Weber potential [36], which includes the pair contribution ϕ_2, and the triplet contribution ϕ_3 of Eq. (1.8):

$$\phi_2(\hat{r}^{\alpha\beta}) = \epsilon f_2(\hat{r}^{\alpha\beta}), \tag{1.13}$$

$$\phi_3(\hat{r}^{\alpha\beta}, \hat{r}^{\alpha\gamma}, \hat{r}^{\beta\gamma}) = \epsilon f_3(\hat{r}^{\alpha\beta}, \hat{r}^{\alpha\gamma}, \hat{r}^{\beta\gamma}). \tag{1.14}$$

In Eq. (1.13), f_2 is a cutoff function that ensures the potential energy smoothly decays to zero as $\hat{r}^{\alpha\beta}$ goes to $\hat{r}_{\text{cut}}$, where $\hat{r}^{\alpha\beta} = r^{\alpha\beta}/d$ is the distance between a pair of atoms normalized by d, $\hat{r}_{\text{cut}} = r_{\text{cut}}/d$ is cutoff radius normalized by d.

$$f_2(\hat{r}) = \begin{cases} A\,(\,B\,\hat{r}^{-p} - \hat{r}^{-q})e^{(\hat{r}-a)^{-1}}, & \hat{r} < \hat{r}_{\text{cut}}, \\ 0, & \text{otherwise.} \end{cases} \tag{1.15}$$

In Eq. (1.14), f_3 is an energy minimization function which minimizes the three-body potential energy at given angles

$$f_3(\hat{r}^{\alpha\beta}, \hat{r}^{\alpha\gamma}, \hat{r}^{\beta\gamma}) = h(\hat{r}^{\alpha\beta}, \hat{r}^{\alpha\gamma}, \theta^{\beta\alpha\gamma}) + h(\hat{r}^{\beta\gamma}, \hat{r}^{\alpha\beta}, \theta^{\gamma\beta\alpha}) + h(\hat{r}^{\alpha\gamma}, \hat{r}^{\beta\gamma}, \theta^{\alpha\gamma\beta}), \tag{1.16}$$

where $\theta^{\beta\alpha\gamma}$ denotes the angle formed by the bonds $\beta - \alpha$ and $\gamma - \alpha$ with the vertex at atom α, the function h is designed differently for different materials and crystal structures. The h function for diamond-cubic silicon is

$$h(\hat{r}_1, \hat{r}_2, \theta) = \begin{cases} \xi \exp[\omega(\hat{r}_1 - a)^{-1} + \omega(\hat{r}_2 - a)^{-1}](\cos\theta + \frac{1}{3})^2, & \hat{r}_1 < \hat{r}_{\text{cut}} \text{ and } \hat{r}_2 < \hat{r}_{\text{cut}}, \\ 0, & \text{otherwise,} \end{cases} \tag{1.17}$$

where ξ and ω are material parameters. When $\theta = 109°28'$, Eq. (1.17) equals zero which leads to a minimum of potential energy. The parameters of the Stillinger-Weber potential for diamond-cubic silicon are listed in Table 1.1.

1.3.4 Force field

The interatomic potentials introduced above are used for a cluster of atoms. However, in simulations of organic materials with explicit molecular structures such as DNA, proteins, polymers, etc. a force field (FF) is usually used to describe the interactions between atoms inside a molecule or between molecules. The general form of a FF

Table 1.1: The parameters of the Stillinger-Weber potential for diamond-cubic silicon

d	2.0951 Å	ϵ	2.1682 eV
A	7.049556277	B	0.6022245584
p	4	q	0
$\hat{r}_{\text{cut}}$	1.80	ξ	21.0
ω	1.2	θ	109°28′

includes of a number of bonded and non-bonded interactions terms:

$$\begin{aligned}\mathcal{V}^{\text{int}}(\boldsymbol{r}_1, \boldsymbol{r}_2, ...\boldsymbol{r}_{\text{N}}) = &\sum_{i_{\text{bond}}}^{N_{\text{bond}}} \mathcal{V}_{\text{bond}}(i_{\text{bond}}, \boldsymbol{r}^{\alpha}, \boldsymbol{r}^{\beta}) \\ &+ \sum_{i_{\text{angle}}}^{N_{\text{angle}}} \mathcal{V}_{\text{angle}}(i_{\text{angle}}, \boldsymbol{r}^{\alpha}, \boldsymbol{r}^{\beta}, \boldsymbol{r}^{\gamma}) \\ &+ \sum_{i_{\text{dihedral}}}^{N_{\text{dihedral}}} \mathcal{V}_{\text{dihedral}}(i_{\text{dihedral}}, \boldsymbol{r}^{\alpha}, \boldsymbol{r}^{\beta}, \boldsymbol{r}^{\gamma}, \boldsymbol{r}^{\zeta}) \\ &+ \sum_{i_{\text{improper}}}^{N_{\text{improper}}} \mathcal{V}_{\text{imporper}}(i_{\text{improper}}, \boldsymbol{r}^{\alpha}, \boldsymbol{r}^{\beta}, \boldsymbol{r}^{\gamma}, \boldsymbol{r}^{\zeta}) \\ &+ \sum_{\substack{\alpha,\beta \\ \alpha \neq \beta}} \mathcal{V}_{\text{vdw}}(r^{\alpha\beta}) \\ &+ \sum_{\substack{\alpha,\beta \\ \alpha \neq \beta}} \mathcal{V}_{\text{electrostatic}}(r^{\alpha\beta}),\end{aligned} \tag{1.18}$$

where the first four terms represent bonded interactions: the bond stretching energy $\mathcal{V}_{\text{bond}}$, the bond bending energy $\mathcal{V}_{\text{angle}}$, the dihedral angle torsion energy $\mathcal{V}_{\text{dihedral}}$, and the improper torsion energy $\mathcal{V}_{\text{improper}}$, shown in Fig. 1.2(a)-(d), while the last two terms are non-bonded interactions: the van der Waals interaction energy $\mathcal{V}_{\text{vdw}}$, and the electrostatic energy $\mathcal{V}_{\text{electrostatic}}$, shown in Fig. 1.2(e)-(f). In Eq. (1.18), $\boldsymbol{r}^{\alpha}$, $\boldsymbol{r}^{\beta}$, $\boldsymbol{r}^{\gamma}$, and $\boldsymbol{r}^{\zeta}$ are the positions of the particles specifically involved in a interaction; N_{bond}, N_{angle}, N_{dihedral}, and N_{improper} are the total number of the associated interactions; i_{bond}, i_{angle}, i_{dihedral}, and i_{improper} specify an individual interaction for each type.

We use the DREIDING FF [37] as an example to introduce the functional form of

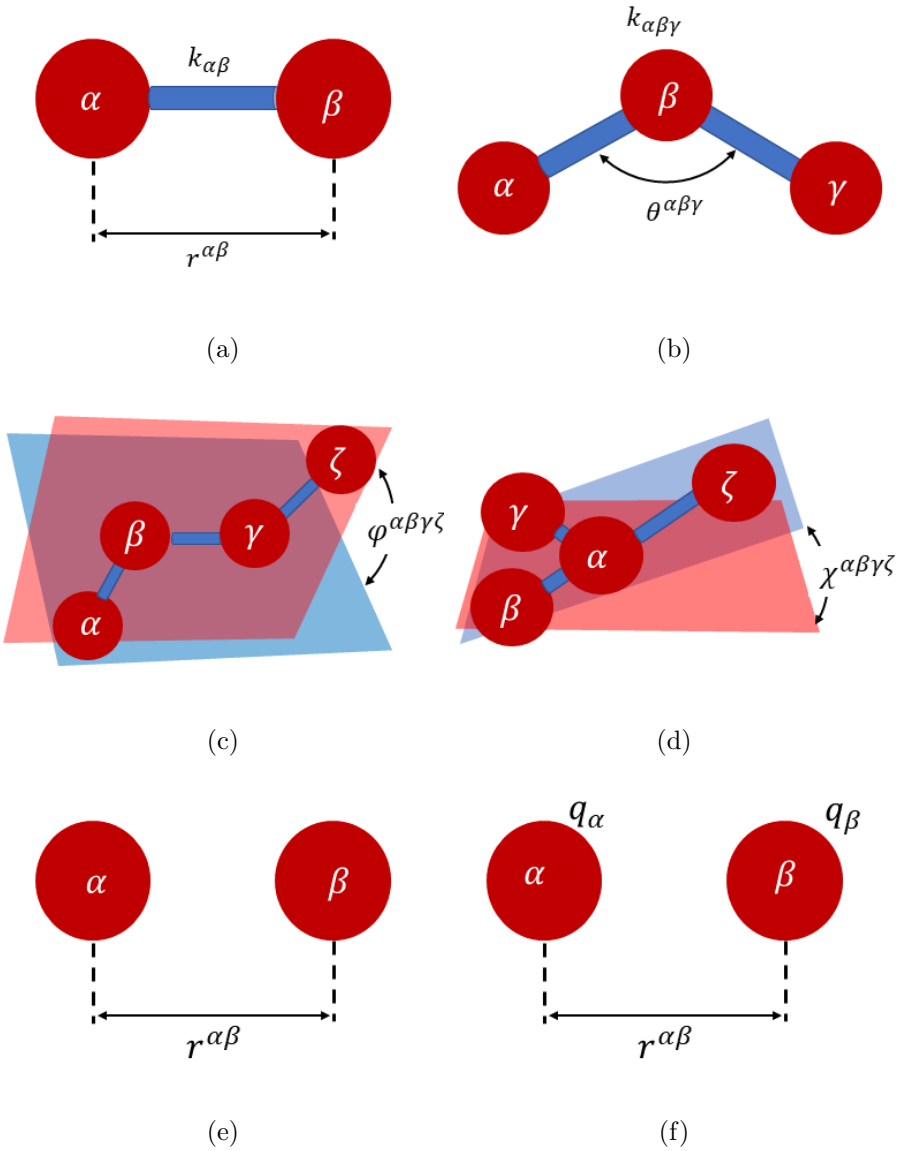

Figure 1.2: Schematic diagram of (a) bond stretching, (b) bond bending, (c) dihedral interaction, (d) improper interaction, (e) van de Waals interaction, and (f) electrostatic interaction.

each type of interactions. The bond stretching energy has a harmonic form:

$$\mathcal{V}_{\text{bond}} = \frac{k_{\alpha\beta}}{2}(r^{\alpha\beta} - r_0)^2, \tag{1.19}$$

where r_0 is the reference bond length, $k_{\alpha\beta}$ is the stiffness for bond stretching, and $r^{\alpha\beta}$ is the distance between atom α and β, hence the current length of bond. The bond bending energy has a harmonic form:

$$\mathcal{V}_{\text{angle}} = \frac{k_{\alpha\beta\gamma}}{2}(\theta^{\alpha\beta\gamma} - \theta_0)^2, \tag{1.20}$$

where θ_0 is again the reference angle, $k_{\alpha\beta\gamma}$ is the stiffness for bond bending, and $\theta^{\alpha\beta\gamma}$ is the current bond angle. The dihedral torsion energy is

$$\mathcal{V}_{\text{dihedral}} = k^{\text{dih}}_{\alpha\beta\gamma\zeta}\left[1 + \cos(n^{\alpha\beta\gamma\zeta}\phi^{\alpha\beta\gamma\zeta} - \phi_0)\right], \tag{1.21}$$

where ϕ_0 is the reference dihedral angle, $k^{\text{dih}}_{\alpha\beta\gamma\zeta}$ is a material parameter, $n^{\alpha\beta\gamma\zeta}$ is the multiplicity which indicates the number of minima as the bond is rotated through 360°, $\phi^{\alpha\beta\gamma\zeta}$ is the current dihedral angle. The improper torsion energy has a harmonic form:

$$\mathcal{V}_{\text{improper}} = \frac{k^{\text{imp}}_{\alpha\beta\gamma\zeta}}{2}(\chi^{\alpha\beta\gamma\zeta} - \chi_0)^2, \tag{1.22}$$

where χ_0 is the reference improper torsion angle, $k^{\text{imp}}_{\alpha\beta\gamma\zeta}$ is material parameter, and $\chi^{\alpha\beta\gamma\zeta}$ is the current improper torsion angle. DREIDING FF uses the 12-6 Lennard-Jones form for the van der Waals interaction, which has form:

$$\mathcal{V}_{\text{vdw}} = 4\epsilon_{\alpha\beta}\left[\left(\frac{\sigma_{\alpha\beta}}{r^{\alpha\beta}}\right)^{12} - \left(\frac{\sigma_{\alpha\beta}}{r^{\alpha\beta}}\right)^{6}\right], \tag{1.23}$$

where $\epsilon_{\alpha\beta}$ and $\sigma_{\alpha\beta}$ are material parameters, $r^{\alpha\beta}$ is the separation distance between two atoms. The electrostatic interaction (also known as Coulomb interaction) is expressed using the Coulomb's law:

$$\mathcal{V}_{\text{electrostatic}} = \frac{q_\alpha q_\beta}{4\pi\epsilon_0\epsilon_R r^{\alpha\beta}}, \tag{1.24}$$

where q_α and q_β are the charges of atoms a and b, respectively, $r^{\alpha\beta}$ is the distance between two atoms, $\epsilon_0 = 8.8542 \times 10^{-12}$ $\text{C}^2\text{N}^{-1}\text{m}^{-2}$ is the permittivity of vacuum, ϵ_R is the dielectric constant ($\epsilon_R = 0$ for a vacuum by definition).

Different FFs with more sophisticated functional form have been proposed in the literature for different purposes. Roughly speaking, three trends can be attributed to

the development of FFs. In one direction, FFs are made to be very generic, allowing for a wide range of coverage. The DREIDING FF falls into this category. In the other direction, the focus is on improving the quality of predictions in a rather concentrated application area. The AMBER [38,39] and OPLS [40,41] FFs fall into this category. In the last category, attention is focused on achieving high accuracy in predicting various molecular properties with a fairly broad coverage. To achieve this goal, complex functional forms including non-diagonal cross-coupling terms and higher order terms are used, thus resulting in less computational efficiency. In addition to the covalent interaction terms and long-range interactions, force fields in this family contain cross-terms between covalent interactions to modulate vibrational energies and are parameterized using a combination of *ab initio* data and experimental data, such as the PCFF [42,43], and COMPASS [44, 45] FFs. A brief summary of different classical FFs is listed in Table 1.2.

Table 1.2: A review of different classical force fields for epoxy crosslinking MD simulations.

Ref.	Name	Summary
[37]	DREDIING	• A generic force field for predicting structures and dynamics of organic, biological , and main-group inorganic molecules. • Use general force constants and geometry parameters based on simple hybridization considerations. New atoms can be added to the force field quite simply. • In general, computational efficiency is higher because there are fewer parameters, but efficiency also depends on the cut-off radius of long-range interactions.
[38, 39]	AMBER GAFF	• AMBER and GAFF (general AMBER force field) are designed for proteins and nucleic acids and have parameters for most organic and pharmaceutical molecules that are composed of H, C, N, O, S, P and halogens.

[40, 41]	OPLS	• Optimized potential for liquid simulations (OPLS) is directly parametrized to reproduce experimental thermodynamic and structural data on pure organic liquids. • Bond stretching, angle bend, and torsional terms of OPLS are adopted form the AMBER FF, but claims to have apparent improvements in predicting crystal structures of some organic materials (i.e. cyclic hexapeptide, cyclic pentapeptide and protein crambin).
[42, 43]	PCFF	• PCFF is developed especially for organic materials and polymers. • The force field parameters are derived by fitting to quantum mechanical data including total energies, first and second derivatives of the total energies, and electrostatic potentials.
[44, 45]	CAMPASS	• The COMPASS force field (condensed-phase optimized molecular potentials for atomistic simulation studies) uses a combined ab-initio and empirical fitting procedure. DFT calculations are used to generate fitting data that is difficult obtain experimentally. • The COMPASS FF is now marketed by Biovia Inc.[46]

1.4 Outline of chapter contents

In this dissertation, AFEM simulations are used to study the PTs of silicon in an *in situ* diamond anvil cell (DAC) simulation (chapter 2, 3, and 4), and the crack propagation in epoxy-graphene composite material (chapter 5, 6, 7, and 8). In chapter 2, the Cauchy-Born kinematics for simple crystal and multi-crystal is introduced, which is used to be the constitutive relation for silicon in a DAC simulation. The approach to implement the Cauchy-Born kinematics with a commercial finite element code Abaqus [47] is also introduced. Two examples (uniaxial compression of fcc Cu nanoplate with

a hole, and nanoindentation of diamond-cubic silicon) are used to demonstrate the effectiveness of this method in predicting material's nonlinear response and PTs. The pressure transmission medium (helium) and the gasket (rhenium) used in a DAC experiment is usually subjected to ultra-high pressure, and the elastic constants of these materials increase with pressure. A modified Blatz-Ko hyperelastic model is proposed in chapter 3 to describe the pressure-dependence of the elastic constants. In chapter 4, an *in situ* simulation of DAC experiment is performed to study the PT of silicon under pressure. The diamond-cubic to β-Sn and bct5 PTs are predicted in the DAC at pressure of 17 GPa. We also found that the inhomogeneous pressure environment after the condensation of helium is important for PTs of silicon, because if the silicon is subjected to hydrostatic pressure up to 50 GPa (this hydrostatic environment is not available in experiment because the liquid solidify at a pressure of 11.65 GPa), no PT is predicted by our model.

Graphene and graphene-based materials have been added into epoxy matrix to increase the fracture toughness (K_{Ic}) of epoxy composites. Although the appearance of K_{Ic} peak at small graphene loading provides opportunity to produce the cost-effective epoxy–graphene composites, the toughening mechanism at small graphene loading is still under study. We would like to use a cohesive element model to study the crack propagation in an epoxy–graphene composite. Cohesive elements are inserted between each bulk epoxy element near the initial notch of a compact tension specimen (CTS) to mimic the arbitrary crack propagation. Different amounts of cohesive elements are defined as effective epoxy–graphene cohesive elements which follow a constitutive law based on the interfacial properties of epoxy–graphene interface. The interfacial properties for epoxy–graphene interface are difficult to measure from experiment due to the two-dimensional material nature of graphene, thus, we alternatively use MD simulation to obtain these properties. In chapter 5, the crosslinking process of epoxy is simulated using MD. The molecular structure of epoxy obtained from the MD simulation is validated by comparing the X-ray diffraction pattern and radial distribution function with experimental results. Thermomechanical properties such as glass transition temperature, gel point, mass density, volume shrinkage ratio, Young's modulus, shear modulus, yield strength and shear strength are calculated and compared with experimental result while available. In chapter 6, the interface systems constructed by epoxy and single

layer graphene, multilayer graphene and multilayer graphene oxide is formed in MD simulations. The interfacial properties of these systems are studied via performing the uniaxial tension and simple shear simulations. Cohesive zone laws that can be used in FEM simulations are obtained from the interfacial properties obtained from MD simulations. Although the approach of inserting cohesive elements between each bulk element allow arbitrary crack propagation if the element size is fine enough, the cohesive brings artificial compliance into the which makes the simulation mesh-dependent. Thus, in chapter 7, a method is introduced to obtain mesh independent simulation by properly rescaling the cohesive element properties. In chapter 8, we perform a FEM simulation for an epoxy/graphene composite material. Crack propagation is simulated by the breakdown of cohesive elements. Two kinds of constitutive laws are implemented for the cohesive elements: the bilinear epoxy–epoxy cohesive zone law, and the epoxy–graphene cohesive zone law obtained from chapter 6. The predicted K_{Ic} are compared with the experimental results. Fracture mechanisms at different graphene loading are discussed.

Finally, this dissertation is concluded in chapter 9 with a summary and some future directions.

Chapter 2

Enabling Atomistic Multiscale Simulation in Commercial Finite Element Software Packages: Toward the Study of Solid-solid Phase Transformations

In this chapter, a concurrent multiscale modeling approach is proposed to implement the Cauchy-Born rule in commercial finite element software packages. This approach embeds an atomistic calculation within a finite element framework. The constitutive response of a macroscopic material point could be obtained by deforming the underlying crystal structure by the local deformation gradient to obtain the local state of mechanical response. The effectiveness of this multiscale approach for predicting nonlinear material response and phase transformation (PT) is demonstrated with two example problems: uniaxial compression of a fcc Cu nanoplate with a hole, and nanoindentation of diamond-cubic Si. In the first problem, the stress concentration ratio calculated from this multiscale approach is compared with those calculated from linear elastic model and SVK hyperelastic model. In the second problem, diamond-cubic to bct5 and β-Sn PTs are predicted under the indenter, which are in good agreement with the experimental

results and the previous numerical simulations.

2.1 Introduction

FEM has been widely used in solid mechanics field. However, the conventional phenomenological models used in FEM fail to accurately describe the complexity of nonlinear mechanical responses of material. Take PT of silicon as an example, at a hydrostatic pressure of 12 GPa the initial glass-like diamond-cubic Si transforms to a metallic material β-Sn Si. Further compression of β-Sn Si leads to a series of transitions to other phases with completely different material properties with the original diamond-cubic phase [48–51]. Due to the complexity of this PT process, it is difficult to accurately predict the mechanical responses of silicon under PTs with one phenomenological model. Thus, we need a model that is based on more fundamental insights of material. Several multiscale approaches were developed under this requirement. Kevrekidis, Gear and coworkers proposed an "equation-free" method [52–55], in which any small scale system can be studied with the goal of establishing large scale governing equations. E *et al.* proposed a heterogeneous multiscale method [56], in which the structure of equations at large scale is assumed to be known, and the missing parameters can be computed from a small scale model. Tadmor *et al.* proposed a quasicontinuum method [20], which is a mixed continuum and atomistic approach for simulating the mechanical response of crystalline materials. Specifically, an atomistic model is implemented in critical regions that are subjected to large deformation or stress concentration, while a continuum model is implemented for the rest regions.

The continuum region of a QC model is driven by the Cauchy-Born rule which was firstly proposed by Cauchy who was studying the elasticity of simple crystals [57], and later improved by Born [58, 59] by introducing finite temperature into the system, and expanding it to multi-lattice crystals by allowing internal degrees of freedom between the sublattices. The basic idea of the CB rule is that every point in a continuum solid corresponds to a large region in the atomic scale. Thus, the constitutive response at that point such as the stress-strain curve, strain energy density etc., may be obtained by deforming the underlying crystal structure by the local deformation gradient and calculate the local state of mechanical response. The CB rule assumes the material to

be ideal crystal. When this breaks down, for example near the dislocations and grain boundaries, the nonlocal version of the QC model must be used, where the explicit position of atoms are taken into account. Smith *et al.* used the CB rule to study the PT of silicon under nanoindentation. The simulation results are in good agreement with the experimental results in macroscopic measures such as load vs. displacement and load vs. resistance curves, but predicted the bct5 phase rather than the experimental observation of β-Sn phase under the indenter [60]. Recently, the CB rule has been further developed. For example, Elliott *et al.* proposed a cascading CB rule [61, 62], which allows the increasing of periodic size of a unit cell by performing a phonon stability analysis within each dynamical lattice representation. Arroyo and Zhang proposed an exponential CB rule [63, 64] to describe the nonlinear deformation of curved two-dimensional materials. Here, we will focus entirely on the basic CB rule with ideal crystal assumption.

Although CB rule has shown its robustness in predicting nonlinear responses of crystalline materials, it has not been implemented in commercial FEM software. In this chapter, we implement the CB rule in Abaqus [47] in order to explore nonlinear material response and PT prediction capabilities of commercial FEM software. In section 2.2, we discuss the CB kinematics for simple-lattice and multi-lattice crystals. Lattice invariant shear simulations are performed to explain the importance of the internal degrees of freedom for shuffles in a multi-lattice crystal. In section 2.3, the CB rule is implemented in Abaqus. Two boundary value problems (uniaxial compression of a fcc Cu nanoplate with a hole, and nanoindentation of diamond-cubic Si) are set up to demonstrate the effectiveness of the CB rule-based multiscale approach on predicting nonlinear material response and PTs of crystalline materials. Finally, section 2.4 summarizes this chapter and provides some future work directions.

2.2 Cauchy-Born kinematics

Crystals can be described as a combination of lattice and basis atoms. Lattice is an infinite arrangement of points with regular pattern in three dimensions. Crystals are generated by placing one atom (single-lattice crystal) or a group of atoms (multi-lattice crystal) in every lattice point. In a simple-lattice crystal, the mean position of atoms (the statistical average positions of atoms under thermal vibrations) $\bar{\boldsymbol{R}}^{[l]}$ can be described

in the Einstein notation as

$$\bar{\boldsymbol{R}}^{[\boldsymbol{l}]} = l_i \bar{\boldsymbol{A}}_i, \quad l_i \in \mathbb{Z}, \tag{2.1}$$

where $\bar{\boldsymbol{A}}_i$ are three linearly independent vectors in the reference configuration, and $\mathbb{Z}$ is a set of all integers, $i = 1, 2, 3$ for a three dimensional structure and the summation convention over pairs of repeated indices is observed. The superscript $[\boldsymbol{l}]$ indicates that the mean positions of atoms for simple-lattice crystal only depends on $\boldsymbol{l}$ for given $\bar{\boldsymbol{A}}_i$. In a multi-lattice crystal, the mean positions of atoms can be described as

$$\bar{\boldsymbol{R}}^{[\boldsymbol{l},m]} = \bar{\boldsymbol{R}}^{[\boldsymbol{l}]} + \bar{\boldsymbol{Z}}^m = l_i \bar{\boldsymbol{A}}_i + \bar{\boldsymbol{Z}}^m, \quad l_i \in \mathbb{Z} \quad \text{and} \quad m = 0, ..., N_B - 1, \tag{2.2}$$

where $\bar{\boldsymbol{Z}}^m$ is the mean position of basis atom m relative to the lattice site, N_B is the number of basis atoms. The mean position of atom $\bar{\boldsymbol{R}}^{[\boldsymbol{l},m]}$ depends on both the first basis atom represented by $\boldsymbol{l}$ and the rest basis atoms m (also called shuffles).

The early study of the CB kinematics was taken by Cauchy, who assumed that atoms behave as material point embedded in continuum body, and exactly follow the macroscopic local deformation gradient [57]

$$\boldsymbol{r}^{[\boldsymbol{l}]} = \boldsymbol{F} \boldsymbol{R}^{[\boldsymbol{l}]}, \quad \boldsymbol{l} \in \mathbb{Z}^3, \tag{2.3}$$

where $\boldsymbol{r}^{[\boldsymbol{l}]}$ and $\boldsymbol{R}^{[\boldsymbol{l}]}$ are the positions of atoms in the deformed and reference configuration, respectively. $\boldsymbol{F}$ is the macroscopic local deformation gradient. Later, Born [58, 59] introduced the idea of the mean positions of atoms and considered the case of multi-lattice crystals. The internal relative motions of shuffles inside the unit cell needs to be considered in addition to the overall deformation of lattices

$$\bar{\boldsymbol{r}}^{[\boldsymbol{l},m]} = \boldsymbol{F} \bar{\boldsymbol{R}}^{[\boldsymbol{l},m]} + \boldsymbol{s}^m = \boldsymbol{F}(\bar{\boldsymbol{R}}^{[\boldsymbol{l}]} + \bar{\boldsymbol{Z}}^m) + \boldsymbol{s}^m, \quad \boldsymbol{l} \in \mathbb{Z}^3 \quad \text{and} \quad m = 0, ..., N_B - 1, \tag{2.4}$$

where $\boldsymbol{s}^m$ is the additional motion of shuffle m relative to the deformed atom position. The potential energy density of a multi-lattice crystal is

$$W(\boldsymbol{F}, \boldsymbol{s}^m) = \frac{1}{\Omega_0} E_{\text{unit}}(\bar{\boldsymbol{r}}^{[\boldsymbol{l},m]}) = \frac{1}{\Omega_0} E_{\text{unit}}(\boldsymbol{F} \bar{\boldsymbol{R}}^{[\boldsymbol{l},m]} + \boldsymbol{s}^m), \quad m = 0, ..., N_B - 1, \tag{2.5}$$

where Ω_0 is the reference volume of the unit cell, E_{unit} is the potential energy for the atoms in the unit cell. Performing energy minimizing to Eq. (2.5) with respect to shuffle

displacement $\boldsymbol{s}^m$, we obtain an effective potential energy density W_{eff}, which is only a function of the overall deformation gradient $\boldsymbol{F}$,

$$W_{\text{eff}}(\boldsymbol{F}) = \min_{\boldsymbol{s}^m} W(\boldsymbol{F}, \boldsymbol{s}^m). \tag{2.6}$$

W_{eff} is used as the strain energy density in the FEM framework. The Cauchy stress is

$$\boldsymbol{\sigma} = J^{-1}(\frac{\partial W_{\text{eff}}}{\partial \boldsymbol{F}})\boldsymbol{F}^T. \tag{2.7}$$

The elastic constant tensor is

$$\mathbb{C} = \frac{\partial^2 W_{\text{eff}}}{\partial \boldsymbol{E}^2}. \tag{2.8}$$

Next, we will use the lattice invariant shear of fcc Cu and diamond-cubic Si to demonstrate the CB kinematics and show the influence of the additional motion of shuffle to the mechanical response of multi-lattice crystal. Lattice invariant shear happens in the ideal crystals, when the deformed crystal structure exactly reproduces the original crystal structure, shown in Fig. 2.1. The deformation gradient for simple shear is

$$\boldsymbol{F} = \boldsymbol{I} + \tau \boldsymbol{p} \otimes \boldsymbol{n}, \tag{2.9}$$

where τ is the shear parameter, $\boldsymbol{p}$ is a normal vector of the shear direction, and $\boldsymbol{n}$ is a normal vector of the normal direction of the slip plane. In this work, we choose a crystallographic orientation of [1 0 0] along x-axis, and [0 1 0] along y-axis, [$\bar{1}$ 1 0] as the shear direction, and [1 1 1] as the slip plane normal. The Knowledgebase of Interatomic Models (KIM) project [65] is used for providing the interatomic potential models we used in this work.

Fcc Cu is a simple-lattice crystal with one basis atom in the primitive unit cell. Using Eqs. (2.5) and (2.9) and employing the EAM potential for Cu [66, 67], the potential energy density vs. shear parameter curve is shown in Fig. 2.2. The potential energy density of the system return to the initial value when $\tau = \sqrt{6}/2$, which indicates the lattice invariant shear. Diamond-cubic Si is a multi-lattice crystal with two basis atoms placing at the vertex and centroid of the tetrahedral unit cell, respectively. A schematic diagram showing the lattice invariant shear of diamond-cubic Si with and without the additional shift of shuffle are shown in Fig. 2.3. The two-dimensional diagram is a projection of the three-dimensional tetrahedron in [1 1 $\bar{2}$] plane (yellow area). The

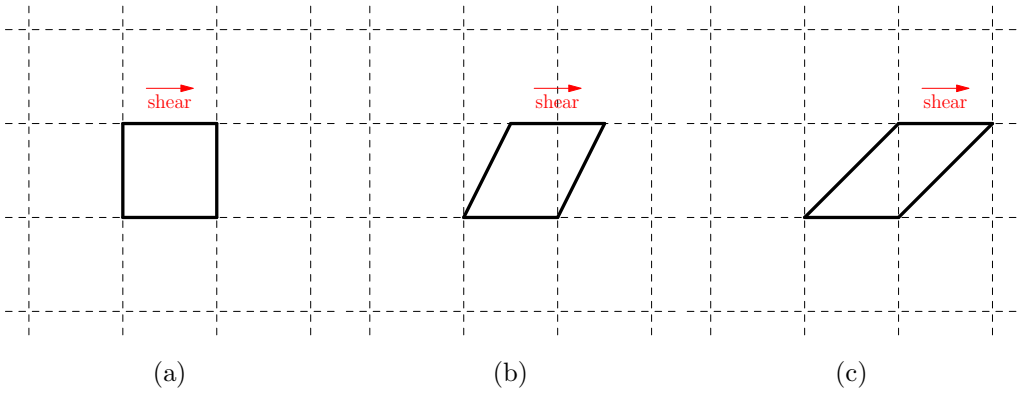

Figure 2.1: A schematic diagram showing the kinematics of lattice invariant shear. The solid square is the structure of interest, the dashed line is the original lattice. (a) The original lattice before shearing. (b) The deformed structure has not reproduced the original structure, thus lattice invariant shear has not yet happened. (c) The lattice invariant shear happens, because the top surface of the sheared lattice overlaps with its right neighbor.

base atom on the bottom surface is fixed, the atoms in plane [1 1 1] (top surface) are subjected to shear in [$\bar{1}$ 1 0] direction. In Fig. 2.3(a), we see that the shuffle atom (red) lags far behind the three atoms (green) above it and the tetrahedron get distorted during the shearing process. When the three top atoms move one period, the structure is far from the ideal diamond structure. However, if the additional internal motions of shuffle is allowed, the shuffle shifts back to the centroid of the tetrahedron to minimize the potential energy, shown in Fig. 2.3(b). The bond angles between the shuffle and the upper atoms remain the ideal angle of 109°28′. Using Eqs. (2.9), (2.5) and (2.6) and employing the Stillinger-Weber potential for Si [68], the potential energy vs. shear parameter curves with and without the shuffle relaxation are shown in Fig. 2.4(a) and (b). We can see that the shuffle relaxation significantly reduces the energy barrier of the lattice invariant shear, and reduces the lattice invariant shear period to one fourth of that without the shuffle relaxation.

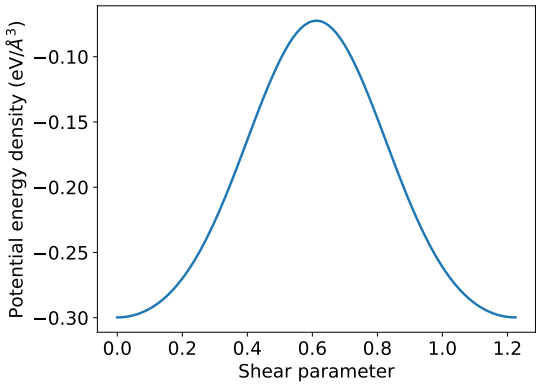

Figure 2.2: Shear parameter vs. potential energy density diagram of fcc Cu.

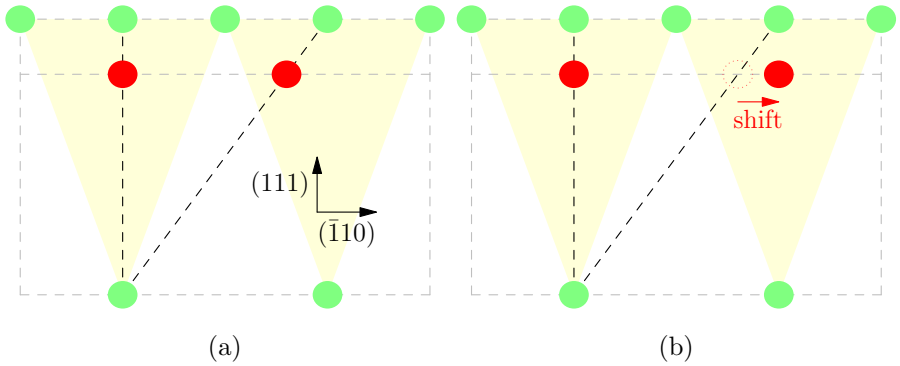

Figure 2.3: A schematic diagram showing the shuffle relaxation during the lattice invariant shear of a multi-lattice crystal (a) Shear without shuffle relaxation. The first basis atoms reproduces the original lattice, while the shuffles have a lag. (b) Shear with shuffle relaxation, the shuffle goes to the centriod of the tetrahedron to minimized the potential energy.

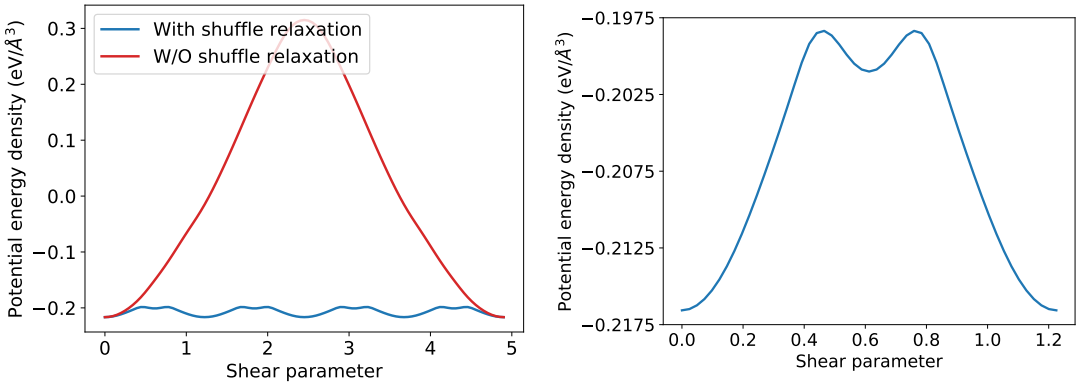

(a) (b)

Figure 2.4: (a) Lattice invariant shear for diamond-cubic Si with the shuffle relaxation using Eq. (2.6) (blue line) and without the shuffle relaxation using Eq. (2.5) (red line). (b) is a zoom-in diagram of one fourth of the blue line in (a). The small pit is due to the nonphysical prediction of Stillinger-Weber potential for Si.

2.3 Numerical examples

The motivation of this paper is to implement the CB rule in FEM framework to explore the multiscale modeling capability of commercial FEM software. In practice, the KIM compliant CB rule (CB-KIM) is implemented in Abaqus as VUMAT user material subroutine. In each step of calculation, Abaqus passes the deformation gradient of integration point $\boldsymbol{F}$ to the CB-KIM subroutine, an ideal crystal is built up and deformed with Eq. (2.3) or (2.4). By employing an interatomic potential, the potential energy density is calculated with Eq. (2.5) or (2.6). The Cauchy stress is calculated from Eq. (2.7). We use two example problems to demonstrate the effectiveness of this method for prediction of nonlinear material response and PT.

2.3.1 Uniaxial compression of a fcc Cu nanoplate with a hole

The plate with a hole problem was firstly studied by Kirsch [69] who obtained a theoretical stress concentration ratio of 3 for infinite plate made by isotropic material under small strain. In our work, a 200 μm by 200 μm fcc Cu plate with a hole with a diameter of 10 μm in the center is subject to a uniform compression of 1 GPa on the top

edge, and the bottom edge is fixed by rollers, shown in Fig. 2.5(a). Static simulation is performed with the linear anisotropic material model with three independent elastic constant for material with cubic symmetry: C_{11}=174.1 GPa, C_{12}=127.2 GPa, and C_{66}=83.9 GPa [70]. Explicit dynamic simulations are performed with the SVK model with the same material properties as the linear anisotropic model, and the CB-KIM model with crystallographic orientation of [1 0 0] along x-axis and [0 1 0] along y-axis. An EAM potential for fcc Cu [66, 67] is employed in the CB-KIM model.

The Cauchy stress σ_{yy} near the hole obtained by these three models are shown in Fig. 2.6(a). The stress concentration ratios Ω along x-axis are shown in Fig. 2.6(b). The linear anisotropic material model gives a stress concentration ratio of 2.4. The closed-form solution for stress concentration factor at the hole in an infinite anisotropic plate is given by

$$\Omega = \frac{\sigma_{yy}}{\sigma_\infty} = \frac{3 + \beta_1 + \beta_2 - \beta_1\beta_2}{(1+\beta_1)(1+\beta_2)}, \tag{2.10}$$

where σ_{yy} is the stress at the hole, σ_∞ is the remote applied stress, β_1, β_2 are parameters defined as

$$\beta_1 = \frac{\sqrt{\alpha_1} - 1}{\sqrt{\alpha_1} + 1}, \qquad \beta_2 = \frac{\sqrt{\alpha_2} - 1}{\sqrt{\alpha_2} + 1}, \tag{2.11}$$

where the parameters α_1 and α_2 represent relationship between the material compliances:

$$\alpha_1\alpha_2 = \frac{S_{11}}{S_{22}}, \qquad \alpha_1 + \alpha_2 = \frac{S_{66} + 2S_{12}}{S_{22}}, \tag{2.12}$$

where S_{ij} represent the components of material compliance $\boldsymbol{S}$ in the Voigt notation, and $\boldsymbol{S} = \boldsymbol{C}^{-1}$. For fcc Cu, $S_{11} = S_{22} = S_{33}$, $S_{12} = S_{13} = S_{23}$ and $S_{44} = S_{55} = S_{66}$. Explicit expression for α_1 and α_2 are

$$\alpha_1, \alpha_2 = \frac{S_{66} + 2S_{12}}{2S_{11}} \pm \frac{1}{2}\sqrt{\left(\frac{S_{66} + 2S_{12}}{S_{11}}\right)^2 - 4}. \tag{2.13}$$

Substitute the elastic constants for fcc Cu into Eqs. (2.13), (2.11), and (2.10), the stress concentration ratio at the hole for the fcc Cu plate is 2.4, which is in good agreement with the simulation result for linear anisotropic model. The SVK model gives a concentration ratio of 2.59 due to the nonlinear geometry effect. The CB-KIM model gives a slightly lower concentration ratio of 2.54.

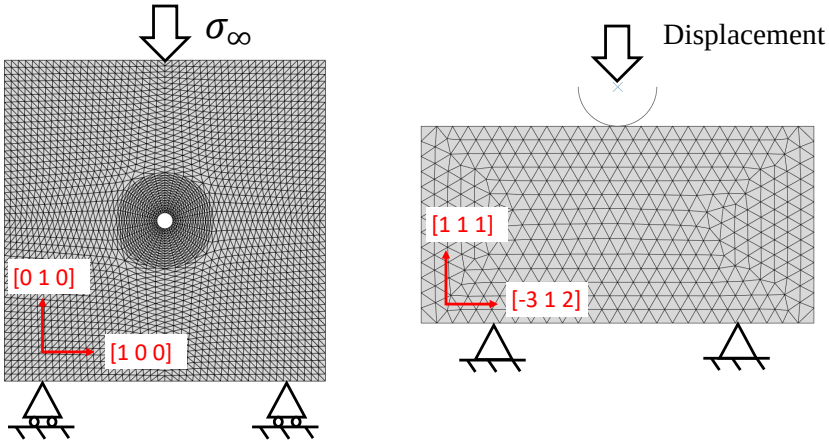

(a) (b)

Figure 2.5: A diagram shows the boundary conditions and mesh for (a) the fcc Cu nanoplate with a hole problem, and (b) the nanoindentation of diamond-cubic Si problem. The red arrow shows the crystallographic orientation.

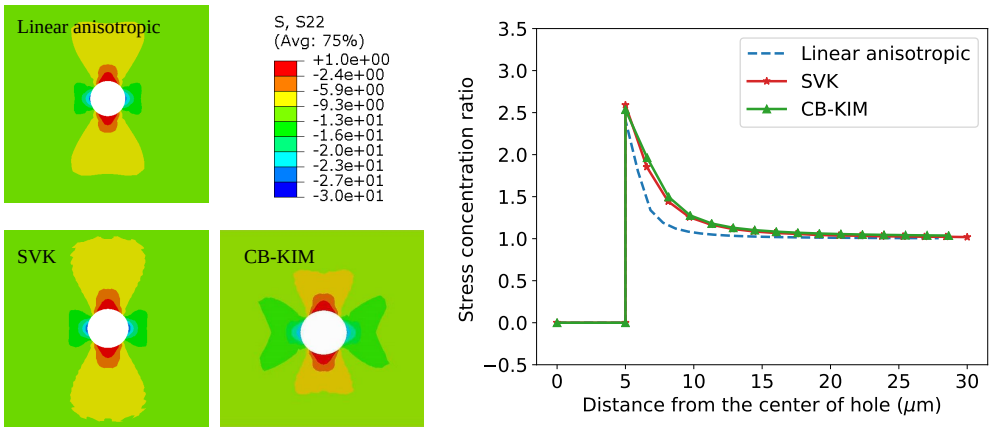

(a) (b)

Figure 2.6: (a) The Cauchy stress σ_{yy} near the hole. Unit in GPa. (b) The stress concentration ratio at the hole calculated from the linear anisotropic model, the SVK model, and the CB-KIM model.

2.3.2 PT in a nanoindentation simulation of diamond-cubic Si

The PT identification algorithm is shown in Fig. 2.7. If the energy of the system goes beyond the energy barrier between two phases under an applied load, the crystal structure releases to phase 2 when the load is removed as shown in Fig. 2.7(b), which indicates PT from phase 1 to phase 2. Otherwise, the crystal structure returns to phase 1 as shown in Fig. 2.7(a), which means no PT happens. The CB-KIM model records the positions of atoms $\bar{\boldsymbol{r}}^{[\boldsymbol{l},m]}$ for each element. The released positions of atoms $\bar{\boldsymbol{r}}^{[\boldsymbol{l},m]}_{\text{relx}}$ is calculated by minimizing the potential energy in a unit cell

$$\bar{\boldsymbol{r}}^{[\boldsymbol{l},m]}_{\text{relx}} = \min_{\bar{\boldsymbol{r}}} E_{\text{unit}}(\bar{\boldsymbol{r}}). \tag{2.14}$$

If the released crystal structure is different with the original structure, PT happens.

To estimate the effectiveness of the PT prediction for the CB-KIM model, a nanoindentation simulation is set up to study the stress-induced PT for diamond-cubic Si, shown in Fig. 2.5(b). A 5 μm by 10 μm two-dimensional block is fixed on the bottom surface. A semicircle rigid indenter with a diameter of 2 μm has a 0.5 μm downward displacement with a constant speed of 10 mm/s. The CB-KIM model with the Stillinger-Weber potential for silicon [68] is employed as the constitutive law for the block. The crystallographic orientation is defined as [$\bar{3}$ 1 2] along x-axis and [1 1 1] along y-axis, which was used in previous QC simulation [60] to study the PT of silicon under indenter. Before PT occurs, the reaction force initially increases linearly with the indentation depth but has local drop after high pressure phases (β-Sn and bct5) begin forming, as shown in Fig. 2.8(a). The Cauchy stress under the indenter σ_{yy}, the maximum principal strain, and the corresponding phases obtained using Eq. (2.14) at different indentation depths are shown in Fig. 2.9. Changes of the stress distribution and concentrations of strain are observed under the indenter where PTs happen. Our prediction of the diamond-cubic to bct5 and β-Sn PT is in a reasonable agreement with Smith and Tadmor's previous works [60, 71], in which only the bct5 phase was predicted under the indenter. In experiments [49, 72, 73], β-Sn phase is observed under the indenter but bct5 is not observed. The discrepancies between simulation and experiment perhaps are due to the shortcomings in the Stillinger-Weber potential, and to the restriction to a two-atom unit cell in the simulation. However, since an *in situ* indentation experiment is not currently available, it is also possible that bct5 does form during experiments, but

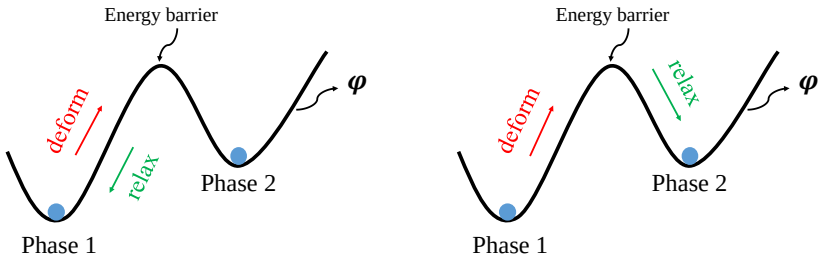

(a) (b)

Figure 2.7: A schematic diagram showing the energy configurations of system and PT identification algorithm. (a) the deformed structure goes back to the initial configuration after energy minimization, PT does not happened. (b) The deformed structure conquers the energy barrier and goes to a different energy configuration. PT happens.

has not been detected.

2.4 Conclusion and future directions

In this chapter, a Cauchy-Born rule based, KIM compliant method is implemented in Abaqus to explore the multiscale material modeling capability of commercial FEM software. This method uses an atomistic level calculation as constitutive relation, thus includes more fundamental insights of material. The effectiveness of this CB-KIM model approach is demonstrated in two example problems. In the uniaxial compression of the fcc Cu nanoplate with a hole problem, the stress concentration ratio near the hole predicted by the CB-KIM model is higher than the results predicted by the linear anisotropic model due to the nonlinear effect, but is very close to ratio predicted using the SVK model. A problem with more complex phenomena may be needed to show the difference between the CB-KIM model and the conventional hyperelastic model. In the nanoindentation of diamond-cubic Si problem, the CB-KIM model predicts the diamond-cubic to bct5 and PT underneath the indenter, which is in reasonable agreement with the previous experimental results and a QC simulation. We also notice that PT of Si changes the local stress distribution and the reaction force on indenter.

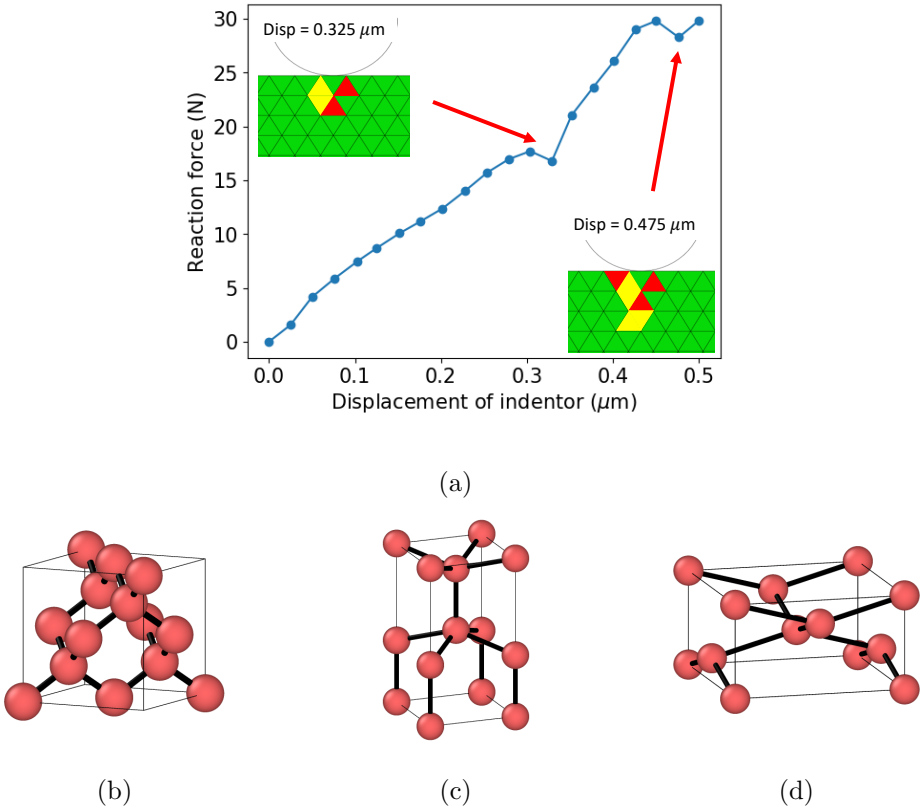

(a)

(b) (c) (d)

Figure 2.8: (a) The reaction force-displacement curve of the indenter. The local drop of reaction force at displacement of 0.325 μm and 0.475 μm are due to the PT of silicon. The green elements represent the original diamond-cubic silicon shown in (b). The red elements represent bct5 silicon shown in (c). The yellow elements represent β-Sn silicon shown in (d). Figures in (b), (c) and (d) are generated using OVITO [6].

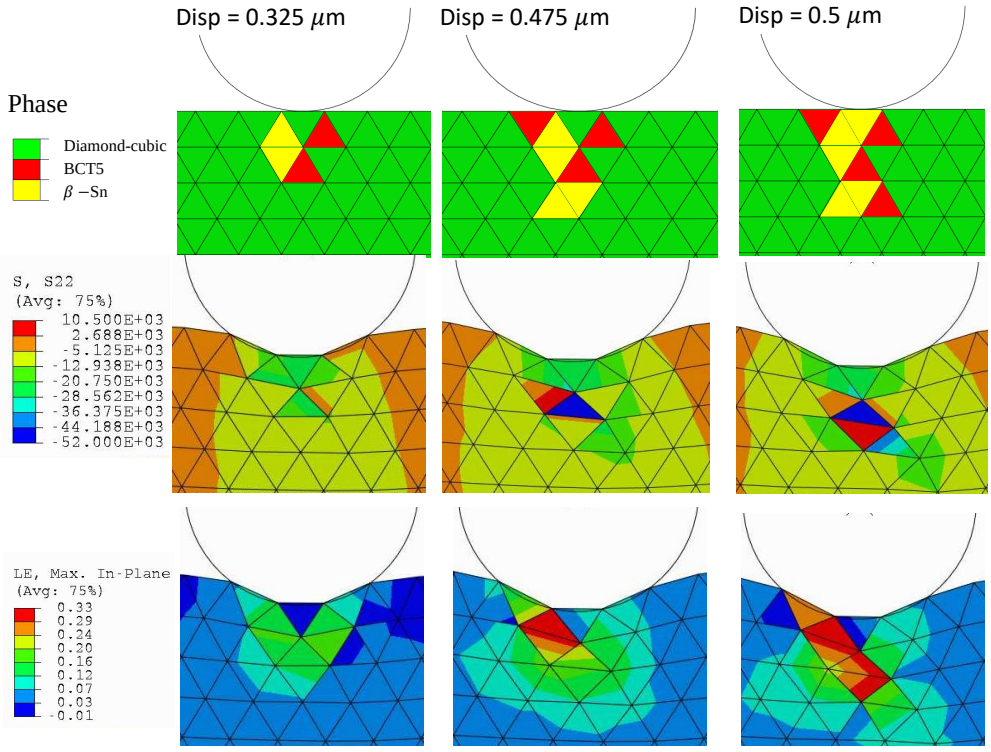

Figure 2.9: σ_{yy} and the maximum principal stress contour and the corresponding phase at different indentation depth (0.325 μm, 0.475 μm, and 0.5 μm). Stress unit in MPa.

Some future directions are remarked here:

- In the current model, we use the effective potential energy density obtained by minimizing the potential energy with respect to shuffles. However, it is important to treat the shuffle displacements as degrees of freedom, which means Eq. (2.5) shall be used to calculate the strain energy density instead of Eq. (2.6). Some deformation modes may be precluded by the current approach. Eq. (2.5) is more accurate, though has more degrees of freedom. Thus a more robust solver is required.

- The current model is suitable for bulk material a fixed size of unit cell. Thus, it can not predict the PTs that involve period extensions of unit cell, and the deformation of two-dimensional materials. Take use of the cascading Cauchy-Born rule and the exponential Cauchy-Born rule will expand the applicability of this model.

- The current model assumes the material to be an ideal crystal without defects, thus may overestimate the PT initiation pressure. Future directions includes introducing crystal defects like nucleation, dislocation, grain boundary into the model.

- The current model does not consider the dynamical action of atoms. However in a real material system, the atoms have thermal vibration near their mean positions. Other future directions include introduce finite temperature into this model, like the method used in the Hyper-QC model [29].

Chapter 3

Modified Blatz-Ko Model for High-pressure Diamond Anvil Cell Materials: Helium and Rhenium

A modified Blatz-Ko hyperelastic model for isotropic polycrystalline hexagonal close-packed materials under high-pressure conditions is introduced. The model describes the pressure dependence of the elastic constants and is therefore suitable for ultra-high pressure applications. The model is fit to effective isotropic elastic moduli computed as an average of the Voigt and Reuss bounds of single-crystal data obtained from first principles and experimental measurements. Parameterizations are obtained for helium and rhenium, which are used as the pressure transmission medium and gasket material in diamond anvil cell experiments. Predicted equations of state are in very good agreement with experiments. The models are demonstrated using the commercial finite element code Abaqus [47] by studying the diametrical compression of a self-equilibrated spherical rhenium pressure-vessel filled with solid helium. The new modified Blatz-Ko models can be used in numerical simulations of DAC experiments for design and analysis purposes.

3.1 Introduction

The response of hexagonal close-packed (hcp) helium and rhenium polycrystals to mechanical loading at ultra-high pressures is of great interest in diamond anvil cell (DAC) experiments reaching pressures up to 100 GPa [74]. Due to the high condensation pressure and low shear modulus of helium, it is commonly used as a pressure transmission medium in DAC experiments [75–78]. Liquid helium crystallizes into an hcp structure at a pressure of 11.65 GPa at room temperature [79, 80]. Rhenium is widely used as the gasket material in DAC experiments [81–84] due to its very high bulk modulus (360.3 GPa) [85] and absence of phase transformations at high pressures. In order to perform finite element simulations of DAC experiments, constitutive relations are required for isotropic polycrystalline helium and rhenium under ultra-high pressure. Such relations must capture the strong pressure-dependence of the elastic constants of these materials and be able to describe the finite strains experienced under ultra-high pressure loadings. To our knowledge, no such models have been reported in the literature.

In this chapter, a new modified Blatz-Ko [86] nonlinear constitutive model is proposed for isotropic polycrystalline hcp materials at high pressure. In order to fit the model to helium and rhenium, the pressure-dependence of the isotropic elastic constants of these materials is required, which is not available in literature. Instead, the isotropic elastic constants are estimated from Reuss and Voigt bounds computed from the five independent elastic constants (C_{11}, C_{33}, C_{13}, C_{12}, C_{44}) of single-crystal hcp. For helium, single-crystal pressure-dependent elastic constants have been measured using high-pressure Brillouin DAC experiments [1]. For rhenium, there are measurements using X-ray diffraction [9] and ultrasonic [85] techniques. However, the X-ray measurements are in contradiction with first principle calculations [3, 87], and the ultrasonic measurements are limited to a very narrow pressure range. Instead, we derive pressure-dependent results for single crystal rhenium by extrapolating first principles results at 0 K [3] to room temperature using a thermodynamics approach.

This chapter is organized as follows. In section 3.2, the modified Blatz-Ko strain energy density, stress tensor, and elasticity tensor are introduced. In section 3.3, the

kinematics of deformation in the presence of hydrostatic loading is described, and expressions are derived for the elastic constants under arbitrary loading conditions. Section 3.4 introduces Voigt and Reuss averages, which provide upper and lower bounds on the effective elastic constants of isotropic polycrystals. In section 3.5, a least-squares procedure is used to fit the modified Blatz-Ko model to helium and rhenium using Voigt and Reuss bounds applied to single-crystal data. The model is validated by comparing the predicted equations of state (EOS) (pressure versus volume relations) with experimental measurements up to a hydrostatic pressure of 50 GPa for helium and 270 GPa for rhenium. In Section 3.6, a simple numerical example demonstrates how to use the derived models in a finite element method simulation. This chapter concludes in section 3.7 with a brief summary.

3.2 Modified Blatz-Ko model

Various constitutive models have been developed in the past for compressible hyperelastic materials, including the neo-Hookean, Mooney–Rivlin, and the Blatz–Ko models [88]. However, these models are unable to capture the pressure dependence of the elastic constants for helium and rhenium at high pressure. We found that the minimal model that was able to capture this effect was a Blatz–Ko model modified to include a volumetric term as explained below.

The Blatz-Ko model [86] was introduced to describe the mechanical response of compressible materials, specifically rubber-foams, under large deformation. In order to improve the agreement with high-pressure properties of helium and rhenium, a modified Blatz-Ko model is proposed that includes an additional second-order volume-dependent term. The modified Blatz-Ko strain energy density (SED) function is

$$\begin{aligned}\Psi(\boldsymbol{E}) = \Psi(I_1, I_2, I_3) = A_1 \left[(I_1 - 3) + \frac{1}{\beta}(I_3^{-\beta} - 1)\right] \\ + A_2 \left[\left(\frac{I_2}{I_3} - 3\right) + \frac{1}{\beta}(I_3^{\beta} - 1)\right] + A_3(\sqrt{I_3} - 1)^2,\end{aligned} \tag{3.1}$$

where A_1, A_2, A_3, and β are material parameters, and

$$I_1 = \operatorname{tr} \boldsymbol{C}, \qquad I_2 = \operatorname{tr} \boldsymbol{C}^{-1} \det \boldsymbol{C}, \qquad I_3 = \det \boldsymbol{C}, \tag{3.2}$$

Table 3.1: Coefficients for the second Piola-Kirchhoff stress tensor for the modified Blatz-Ko model.

γ_1	$2(A_1 + A_2 I_1/I_3)$
γ_2	$-2A_2/I_3$
γ_3	$-2A_1 I_3^{-\beta} + 2A_2 I_3^{\beta} - 2A_2 I_2/I_3 + 2A_3 I_3 - 2A_3\sqrt{I_3}$

are the principal invariants of the right Cauchy-Green deformation tensor $\boldsymbol{C} = 2\boldsymbol{E} + \boldsymbol{I} = \boldsymbol{F}^T\boldsymbol{F}$, where $\boldsymbol{E}$ is the Lagrangian strain tensor, $\boldsymbol{F}$ is the deformation gradient, and $\boldsymbol{I}$ is the identity tensor. The additional term $A_3(\sqrt{I_3} - 1)^2$ is introduced to represent the volumetric response. Eq. (3.1) reduces to the original Blatz-Ko model with

$$A_1 = f\frac{\mu}{2}, \quad A_2 = (1-f)\frac{\mu}{2}, \quad A_3 = 0, \quad \beta = \frac{\nu}{1-2\nu}, \tag{3.3}$$

in which μ is the shear modulus, ν is Poisson's ratio, and $f \in [0, 1]$ is a material parameter quantifying the relative importance of the two terms in the Blatz-Ko energy. Note that if $I_3 = 1$, both the original and modified Blatz-Ko models reduce to the incompressible Mooney-Rivlin model, and if $f = 1$ the original Blatz-Ko model reduces to the compressible neo-Hookean model.

The second Piola-Kirchhoff stress $\boldsymbol{S}$ follows from Eq. (3.1) by differentiating the modified Blatz-Ko energy with respect to the Lagrangian strain tensor [89],

$$\boldsymbol{S} = \frac{\partial \Psi(\boldsymbol{E})}{\partial \boldsymbol{E}} = \gamma_1 \boldsymbol{I} + \gamma_2 \boldsymbol{C} + \gamma_3 \boldsymbol{C}^{-1}, \tag{3.4}$$

where the coefficients γ_i are given by

$$\gamma_1 = 2\left(\frac{\partial \Psi}{\partial I_1} + I_1\frac{\partial \Psi}{\partial I_2}\right), \quad \gamma_2 = -2\frac{\partial \Psi}{\partial I_2}, \quad \gamma_3 = 2I_3\frac{\partial \Psi}{\partial I_3}. \tag{3.5}$$

The expressions for these coefficients for the modified Blatz-Ko model are given in Table 3.1. The Cauchy stress $\boldsymbol{\sigma}$ follows as

$$\boldsymbol{\sigma} = J^{-1}\boldsymbol{F}\boldsymbol{S}\boldsymbol{F}^T = J^{-1}\left(\gamma_1 \boldsymbol{B} + \gamma_2 \boldsymbol{B}^2 + \gamma_3 \boldsymbol{I}\right), \tag{3.6}$$

where $J = \det \boldsymbol{F} = \sqrt{I_3}$ is the Jacobian, and $\boldsymbol{B} = \boldsymbol{F}\boldsymbol{F}^T$ is the left Cauchy-Green deformation tensor.

The material elasticity tensor is obtained as the second derivative of Eq. (3.1) [89]:

$$\begin{aligned}\mathbb{C} = \frac{\partial^2 \Psi(\boldsymbol{E})}{\partial \boldsymbol{E} \partial \boldsymbol{E}} &= \alpha_1 \boldsymbol{I} \otimes \boldsymbol{I} + \alpha_2 (\boldsymbol{I} \otimes \boldsymbol{C} + \boldsymbol{C} \otimes \boldsymbol{I}) \\ &+ \alpha_3 (\boldsymbol{I} \otimes \boldsymbol{C}^{-1} + \boldsymbol{C}^{-1} \otimes \boldsymbol{I}) + \alpha_4 \boldsymbol{C} \otimes \boldsymbol{C} \\ &+ \alpha_5 (\boldsymbol{C} \otimes \boldsymbol{C}^{-1} + \boldsymbol{C}^{-1} \otimes \boldsymbol{C}) + \alpha_6 \boldsymbol{C}^{-1} \otimes \boldsymbol{C}^{-1} \\ &+ \alpha_7 \boldsymbol{C}^{-1} \odot \boldsymbol{C}^{-1} + \alpha_8 \mathbb{I}, \end{aligned} \tag{3.7}$$

where $\boldsymbol{C}^{-1} \odot \boldsymbol{C}^{-1}$ is a fourth-order tensor with components relative to an orthonormal (Cartesian) basis $(\boldsymbol{e}_1, \boldsymbol{e}_2, \boldsymbol{e}_3)$ defined as

$$\left[\boldsymbol{C}^{-1} \odot \boldsymbol{C}^{-1}\right]_{IJKL} \equiv -\frac{\partial C^{-1}_{IJ}}{\partial C_{KL}} = \frac{1}{2}(C^{-1}_{IK} C^{-1}_{JL} + C^{-1}_{IL} C^{-1}_{JK}), \tag{3.8}$$

and $\mathbb{I}$ is the symmetric fourth-order identity tensor,

$$\mathbb{I} = \frac{1}{2}(\delta_{IK}\delta_{JL} + \delta_{IL}\delta_{JK}) \boldsymbol{e}_I \otimes \boldsymbol{e}_J \otimes \boldsymbol{e}_K \otimes \boldsymbol{e}_L. \tag{3.9}$$

Here δ is the Kronecker delta and the summation convention over pairs of repeated indices is observed. The one-half factor in Eqs. (3.8) and (3.9) is due to taking a derivative with respect to a symmetric tensor [90]. The coefficients α_i in Eq. (3.7) are

$$\begin{aligned}
\alpha_1 &= 4\left(\frac{\partial^2 \Psi}{\partial I_1 \partial I_1} + 2I_1 \frac{\partial^2 \Psi}{\partial I_1 \partial I_2} + \frac{\partial \Psi}{\partial I_2} + I_1^2 \frac{\partial^2 \Psi}{\partial I_2 \partial I_2}\right), \\
\alpha_2 &= -4\left(\frac{\partial^2 \Psi}{\partial I_1 \partial I_2} + I_1 \frac{\partial^2 \Psi}{\partial I_2 \partial I_2}\right), \\
\alpha_3 &= 4\left(I_3 \frac{\partial^2 \Psi}{\partial I_1 \partial I_3} + I_1 I_3 \frac{\partial^2 \Psi}{\partial I_2 \partial I_3}\right), \qquad \alpha_4 = 4\frac{\partial^2 \Psi}{\partial I_2 \partial I_2}, \\
\alpha_5 &= -4I_3 \frac{\partial^2 \Psi}{\partial I_2 \partial I_3}, \qquad \alpha_6 = 4\left(I_3 \frac{\partial \Psi}{\partial I_3} + I_3^2 \frac{\partial^2 \Psi}{\partial I_3 \partial I_3}\right), \\
\alpha_7 &= -4I_3 \frac{\partial \Psi}{\partial I_3}, \qquad \alpha_8 = -4\frac{\partial \Psi}{\partial I_2}.
\end{aligned} \tag{3.10}$$

The expressions for these coefficients for the modified Blatz-Ko model are given in Table 3.2. Substituting the coefficients in Table 3.2 into Eq. (3.7), an explicit expression for

Table 3.2: Coefficients for the material elasticity tensor of the modified Blatz-Ko model.

α_1	$4A_2/I_3$
α_2	0
α_3	$-4A_2I_1/I_3$
α_4	0
α_5	$4A_2/I_3$
α_6	$4A_1\beta I_3^{-\beta} + 4A_2\beta I_3^{\beta} + 4A_2I_2/I_3 + 4A_3I_3 - 2A_3\sqrt{I_3}$
α_7	$4A_1I_3^{-\beta} - 4A_2I_3^{\beta} + 4A_2I_2/I_3 - 4A_3I_3 + 4A_3\sqrt{I_3}$
α_8	$-4A_2/I_3$

the material elasticity tensor of the modified Blatz-Ko model is obtained,

$$\begin{aligned}\mathbb{C} = {} & 4A_2/I_3\boldsymbol{I}\otimes\boldsymbol{I} - 4A_2I_1/I_3\left(\boldsymbol{I}\otimes\boldsymbol{C}^{-1} + \boldsymbol{C}^{-1}\otimes\boldsymbol{I}\right) \\ & + 4A_2/I_3\left(\boldsymbol{C}\otimes\boldsymbol{C}^{-1} + \boldsymbol{C}^{-1}\otimes\boldsymbol{C}\right) \\ & + \left(4A_1\beta I_3^{-\beta} + 4A_2\beta I_3^{\beta} + 4A_2I_2/I_3 + 4A_3I_3 - 2A_3\sqrt{I_3}\right)\left(\boldsymbol{C}^{-1}\otimes\boldsymbol{C}^{-1}\right) \\ & + \left(4A_1I_3^{-\beta} - 4A_2I_3^{\beta} + 4A_2I_2/I_3 - 4A_3I_3 + 4A_3\sqrt{I_3}\right)\left(\boldsymbol{C}^{-1}\odot\boldsymbol{C}^{-1}\right) - 4A_2/I_3\mathbb{I}.\end{aligned} \tag{3.11}$$

3.3 Kinematics of material deformation under hydrostatic pressure

Consider a material body subjected to a hydrostatic loading followed by an arbitrary deformation. The kinematics of such a process can be represented in terms of three states as depicted in Fig. 3.1 [91]. The material is initially in a reference configuration with volume V_0 and coordinates $\boldsymbol{X} = X_I\boldsymbol{e}_I$. It is then hydrostatically deformed to an intermediate state by a homogeneous deformation mapping $\boldsymbol{\varphi}^{01}$,

$$\tilde{\boldsymbol{X}} = \boldsymbol{\varphi}^0(\boldsymbol{X}) = \boldsymbol{F}^0\boldsymbol{X}, \tag{3.12}$$

[1] A body under hydrostatic loading is subjected to the same hydrostatic stress state on all internal and external surface. Under these conditions the body experiences a uniform deformation.

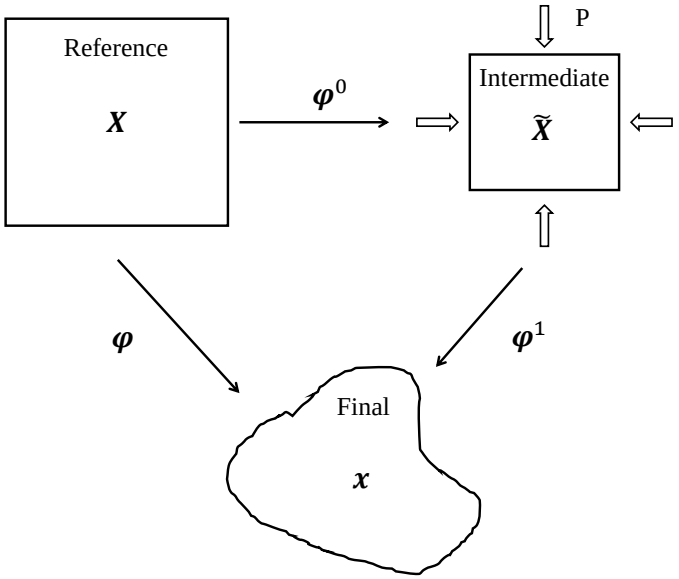

Figure 3.1: Kinematics of an isotropic material subjected to hydrostatic compression followed by an arbitrary deformation.

where $\boldsymbol{F}^0$ is a constant deformation gradient. The volume of the body in the intermediate state is $\tilde{V} = V^0 \det \boldsymbol{F}^0$. Next, the intermediate configuration is subjected to an arbitrary spatially-varying deformation mapping $\boldsymbol{\varphi}^1$,

$$\boldsymbol{x} = \boldsymbol{\varphi}^1(\tilde{\boldsymbol{X}}). \tag{3.13}$$

The local deformation at each point in the intermediate configuration is characterized by the deformation gradient $\boldsymbol{F}^1 = \nabla \boldsymbol{\varphi}^1$. The kinematics can also be represented by the deformation mapping $\boldsymbol{\varphi}$, which is a composition of the deformations $\boldsymbol{\varphi}^0$ and $\boldsymbol{\varphi}^1$:

$$\boldsymbol{\varphi}(\boldsymbol{X}) = \boldsymbol{\varphi}^1(\boldsymbol{\varphi}^0(\boldsymbol{X})). \tag{3.14}$$

The corresponding deformation gradient $\boldsymbol{F}$ is given by

$$\boldsymbol{F} = \boldsymbol{F}^1 \boldsymbol{F}^0. \tag{3.15}$$

The Lagrangian strain tensors associated with $\boldsymbol{F}$, $\boldsymbol{F}^0$ and $\boldsymbol{F}^1$ are

$$\begin{aligned}
\boldsymbol{E} &= \frac{1}{2}(\boldsymbol{F}^T\boldsymbol{F} - \boldsymbol{I}), \quad E_{IJ} = \frac{1}{2}\left(\frac{\partial\varphi_k}{\partial X_I}\frac{\partial\varphi_k}{\partial X_J} - \delta_{IJ}\right), \\
\boldsymbol{E}^0 &= \frac{1}{2}((\boldsymbol{F}^0)^T\boldsymbol{F}^0 - \boldsymbol{I}), \quad E^0_{IJ} = \frac{1}{2}\left(\frac{\partial\varphi^0_K}{\partial X_I}\frac{\partial\varphi^0_K}{\partial X_J} - \delta_{IJ}\right), \\
\boldsymbol{E}^1 &= \frac{1}{2}((\boldsymbol{F}^1)^T\boldsymbol{F}^1 - \boldsymbol{I}), \quad E^1_{IJ} = \frac{1}{2}\left(\frac{\partial\varphi^1_k}{\partial \tilde{X}_I}\frac{\partial\varphi^1_k}{\partial \tilde{X}_J} - \delta_{IJ}\right).
\end{aligned} \tag{3.16}$$

Substituting Eq. (3.14) into the expression for $\boldsymbol{E}$ in Eq. (3.16) gives

$$\boldsymbol{E} = (\boldsymbol{F}^0)^T\boldsymbol{E}^1\boldsymbol{F}^0 + \boldsymbol{E}^0. \tag{3.17}$$

The derivative of $\boldsymbol{E}$ with respect to $\boldsymbol{E}^1$ will also be required,

$$\begin{aligned}
\frac{\partial E_{IJ}}{\partial E^1_{PQ}} &= \frac{\partial(F^0_{AI}E^1_{AB}F^0_{BJ})}{\partial E^1_{PQ}} \\
&= \frac{1}{2}(F^0_{AI}\delta_{AP}\delta_{BQ}F^0_{BJ} + F^0_{AI}\delta_{AQ}\delta_{BP}F^0_{BJ}) \\
&= \frac{1}{2}(F^0_{PI}F^0_{QJ} + F^0_{QI}F^0_{PJ}).
\end{aligned} \tag{3.18}$$

Referring back to the modified Blatz-Ko function in Eq. (3.1), the SED relative to the intermediate configuration is defined as

$$\tilde{\Psi}(\boldsymbol{E}^1) = J_0^{-1}\Psi(\boldsymbol{E}), \tag{3.19}$$

where $J_0 = \det \boldsymbol{F}^0$ is the Jacobian of the mapping from the reference to the intermediate configuration. The associated elasticity tensor with respect to the intermediate state $\tilde{\mathbb{C}}$ is defined as

$$\tilde{\mathbb{C}} = \frac{\partial^2\tilde{\Psi}}{\partial\boldsymbol{E}^1\partial\boldsymbol{E}^1} = J_0^{-1}\frac{\partial^2\Psi}{\partial\boldsymbol{E}^1\partial\boldsymbol{E}^1}. \tag{3.20}$$

Applying the chain rule gives

$$\begin{aligned}
\tilde{\mathbb{C}}_{IJKL} &= J_0^{-1}\frac{\partial^2\Psi}{\partial E^1_{IJ}\partial E^1_{KL}} = J_0^{-1}\frac{\partial}{\partial E^1_{IJ}}\left(\frac{\partial\Psi}{\partial E^1_{KL}}\right) \\
&= J_0^{-1}\frac{\partial}{\partial E^1_{IJ}}\left(\frac{\partial\Psi}{\partial E_{PQ}}\frac{\partial E_{PQ}}{\partial E^1_{KL}}\right) \\
&= J_0^{-1}\left(\frac{\partial^2\Psi}{\partial E_{PQ}\partial E_{RS}}\frac{\partial E_{RS}}{\partial E^1_{IJ}}\frac{\partial E_{PQ}}{\partial E^1_{KL}} + \frac{\partial\Psi}{\partial E_{PQ}}\frac{\partial^2 E_{PQ}}{\partial E^1_{IJ}\partial E^1_{KL}}\right).
\end{aligned} \tag{3.21}$$

Substituting Eq. (3.18) into Eq. (3.21) provides the relation between $\tilde{\mathbb{C}}$ and $\mathbb{C}$:

$$\begin{aligned}\tilde{\mathbb{C}}_{IJKL} &= J_0^{-1} F^0_{IR} F^0_{JS} F^0_{KP} F^0_{LQ} \frac{\partial^2 \Psi}{\partial E_{PQ} \partial E_{RS}} \\ &= J_0^{-1} F^0_{IR} F^0_{JS} F^0_{KP} F^0_{LQ} \mathbb{C}_{RSPQ},\end{aligned} \tag{3.22}$$

where $\mathbb{C}$ is defined in Eq. (3.11) for a modified Blatz-Ko material.

Next consider the elasticity constants of a material under hydrostatic pressure. The deformation gradient $\boldsymbol{F}^0$ and the right Cauchy-Green tensor $\boldsymbol{C}^0$ are

$$\boldsymbol{F}^0 = \begin{bmatrix} \lambda & 0 & 0 \\ 0 & \lambda & 0 \\ 0 & 0 & \lambda \end{bmatrix} \quad \text{and} \quad \boldsymbol{C}^0 = \begin{bmatrix} \lambda^2 & 0 & 0 \\ 0 & \lambda^2 & 0 \\ 0 & 0 & \lambda^2 \end{bmatrix}, \tag{3.23}$$

where λ is the principal stretch. The principal invariants of $\boldsymbol{C}^0$ are

$$\begin{aligned} I_1 &= \operatorname{tr} \boldsymbol{C}^0 = 3\lambda^2, \\ I_2 &= \operatorname{tr}(\boldsymbol{C}^0)^{-1} \det \boldsymbol{C}^0 = 3\lambda^4, \\ I_3 &= \det \boldsymbol{C}^0 = \lambda^6, \end{aligned} \tag{3.24}$$

and $J_0 = \lambda^3$. Substituting Eqs. (3.23) and (3.24) into Eq. (3.11) and using $\lambda = J_0^{1/3}$, we obtain the components of the material elasticity tensor $\mathbb{C}$ under hydrostatic pressure. For an isotropic material there are two independent constants that yield three distinct components, which in Voigt notation are

$$\begin{aligned} C_{11} &= \mathbb{C}_{1111} = 4A_1(\beta+1) J_0^{-2\beta-\frac{4}{3}} + 4A_2(\beta-1) J_0^{2\beta-\frac{4}{3}} + 8A_2 J_0^{-2} + 2A_3 J_0^{-\frac{1}{3}}, \\ C_{12} &= \mathbb{C}_{1122} = 4A_1\beta J_0^{-2\beta-\frac{4}{3}} + 4A_2\beta J_0^{2\beta-\frac{4}{3}} + 4A_3 J_0^{\frac{2}{3}} - 2A_3 J_0^{-\frac{1}{3}}, \\ C_{44} &= \mathbb{C}_{2323} = 2A_1 J_0^{-2\beta-\frac{4}{3}} - 2A_2 J_0^{2\beta-\frac{4}{3}} + 4A_2 J_0^{-2} - 2A_3 J_0^{\frac{2}{3}} + 2A_3 J_0^{-\frac{1}{3}}. \end{aligned} \tag{3.25}$$

The corresponding elasticity tensor components relative to the intermediate configuration follow from Eq. (3.22),

$$\begin{aligned} \tilde{C}_{11} &= \tilde{\mathbb{C}}_{1111} = 4A_1(\beta+1) J_0^{-2\beta-1} + 4A_2(\beta-1) J_0^{2\beta-1} + 8A_2 J_0^{-\frac{5}{3}} + 2A_3, \\ \tilde{C}_{12} &= \tilde{\mathbb{C}}_{1122} = 4A_1\beta J_0^{-2\beta-1} + 4A_2\beta J_0^{2\beta-1} + 4A_3 J_0 - 2A_3, \\ \tilde{C}_{44} &= \tilde{\mathbb{C}}_{2323} = 2A_1 J_0^{-2\beta-1} - 2A_2 J_0^{2\beta-1} + 4A_2 J_0^{-\frac{5}{3}} - 2A_3 J_0 + 2A_3. \end{aligned} \tag{3.26}$$

In Eqs. (3.25) and (3.26), J_0 characterizes the initial imposed hydrostatic deformation, and A_1, A_2, A_3, and β are material parameters. Notice that $C_{44} = \frac{1}{2}(C_{11} - C_{12})$ and $\tilde{C}_{44} = \frac{1}{2}(\tilde{C}_{11} - \tilde{C}_{12})$, thus the modified Blatz-Ko model is isotropic in the reference configuration and when subjected to hydrostatic deformation. Isotropy is lost for a general deformation that breaks this symmetry.

3.4 Voigt and Reuss bounds

Our objective is to parameterize the modified Blatz-Ko model presented in the previous section using experimental results or first principles calculations. In cases where these results are only available for single crystals, it is necessary to obtain effective isotropic properties to which the Blatz-Ko model can be fit. The Voigt and Reuss averages provide upper and lower bounds on the effective isotropic elastic moduli of a randomly distributed polycrystal [92–94].

The Voigt bound is obtained by assuming that all grains in the material undergo the same uniform strain when subjected to a given average stress field [92, 95]. This leads to the following effective Young's modulus and Poisson's ratio:

$$\begin{aligned} E^{\mathrm{V}} &= \frac{(F - G + 3H)(F + 2G)}{2F + 3G + H}, \\ \upsilon^{\mathrm{V}} &= \frac{F + 4G - 2H}{4F + 6G + 2H}, \end{aligned} \tag{3.27}$$

where

$$\begin{aligned} F &= \frac{1}{3}(C^{\mathrm{sc}}_{11} + C^{\mathrm{sc}}_{22} + C^{\mathrm{sc}}_{33}), \\ G &= \frac{1}{3}(C^{\mathrm{sc}}_{12} + C^{\mathrm{sc}}_{23} + C^{\mathrm{sc}}_{13}), \\ H &= \frac{1}{3}(C^{\mathrm{sc}}_{44} + C^{\mathrm{sc}}_{55} + C^{\mathrm{sc}}_{66}), \end{aligned} \tag{3.28}$$

and C^{sc}_{ij} are the components in Voigt notation of the elastic constants matrix $\boldsymbol{C}^{\mathrm{sc}}$ for a single crystal. For an hcp crystal, $C^{\mathrm{sc}}_{11} = C^{\mathrm{sc}}_{22}$, $C^{\mathrm{sc}}_{13} = C^{\mathrm{sc}}_{23}$, $C^{\mathrm{sc}}_{44} = C^{\mathrm{sc}}_{55} = C^{\mathrm{sc}}_{66}$.

The Reuss bound is obtained by assuming that all grains in the material are in the same uniform stress state when subjected to a given average strain field. This leads to

the following effective Young's modulus and Poisson's ratio:

$$E^{\mathrm{R}} = \frac{5}{3F' + 2G' + H'},$$
$$v^{\mathrm{R}} = -\frac{2F' + 8G' - H'}{6F' + 4G' + 2H'}, \tag{3.29}$$

where

$$F' = \frac{1}{3}(S^{\mathrm{sc}}_{11} + S^{\mathrm{sc}}_{22} + S^{\mathrm{sc}}_{33}),$$
$$G' = \frac{1}{3}(S^{\mathrm{sc}}_{12} + S^{\mathrm{sc}}_{23} + S^{\mathrm{sc}}_{13}),$$
$$H' = \frac{1}{3}(S^{\mathrm{sc}}_{44} + S^{\mathrm{sc}}_{55} + S^{\mathrm{sc}}_{66}), \tag{3.30}$$

and S^{sc}_{ij} are the components in Voigt notation of the compliance matrix $\boldsymbol{S}^{\mathrm{sc}}$ for a single crystal ($\boldsymbol{S}^{\mathrm{sc}} = (\boldsymbol{C}^{\mathrm{sc}})^{-1}$). For an hcp crystal, $S^{\mathrm{sc}}_{11} = S^{\mathrm{sc}}_{22}, S^{\mathrm{sc}}_{13} = S^{\mathrm{sc}}_{23}, S^{\mathrm{sc}}_{44} = S^{\mathrm{sc}}_{55} = S^{\mathrm{sc}}_{66}$.

The elastic constants for the effective isotropic medium for the Voigt (V) and Reuss (R) averages are related to Young's modulus and Poisson's ratio obtained above through the standard relations,

$$C^{\mathrm{V,R}}_{11} = \frac{E^{\mathrm{V,R}}(1 - \nu^{\mathrm{V,R}})}{(1 + \nu^{\mathrm{V,R}})(1 - 2\nu^{\mathrm{V,R}})},$$
$$C^{\mathrm{V,R}}_{12} = \frac{E^{\mathrm{V,R}}\nu^{\mathrm{V,R}}}{(1 + \nu^{\mathrm{V,R}})(1 - 2\nu^{\mathrm{V,R}})}. \tag{3.31}$$

3.5 Fitting the modified Blatz-Ko model to helium and rhenium

To obtain the modified Blatz-Ko model for a specific material, the SED function is fit to the 1111 and 1122 components of the elasticity tensor. The reference data are the elastic constants of an hcp single crystal (C_{11}, C_{33}, C_{13}, C_{12}, C_{44}) obtained from either experimental measurements or first principle calculations. The Voigt and Reuss averages are used to obtain the elastic constants for the effective isotropic medium $C^{\mathrm{V,R}}_{11}$ and $C^{\mathrm{V,R}}_{12}$. Eqs. (3.25) or (3.26) are fitted to $C^{\mathrm{V,R}}_{11}$ and $C^{\mathrm{V,R}}_{12}$ using least squares, depending on whether the reference elastic constants are defined with respect to the reference or intermediate configurations. Using the elastic constants in Eq. (3.26), the

least-squares cost function is

$$\Pi(A_1, A_2, A_3, \beta) = \sum_{i=1}^{N} \left[\left(\tilde{C}_{11}(J_0^i, A_1, A_2, A_3, \beta) - \tilde{C}_{11}^{\text{ref}}(J_0^i) \right)^2 + \left(\tilde{C}_{12}(J_0^i, A_1, A_2, A_3, \beta) - \tilde{C}_{12}^{\text{ref}}(J_0^i) \right)^2 \right], \tag{3.32}$$

where N is the number of reference data points (corresponding to different pressures), J_0^i is the Jacobian for the ith data point, $\tilde{C}_{11}$ and $\tilde{C}_{12}$ are the elastic constants defined in Eq. (3.26), and $\tilde{C}_{11}^{\text{ref}}$ and $\tilde{C}_{12}^{\text{ref}}$ are the reference data computed from single-crystal data using either the Voigt or Reuss bounds. In the examples below, the two bounds were very close, so the reference values were taken to be their average,

$$\tilde{C}_{ij}^{\text{ref}} = \frac{1}{2} \left(\tilde{C}_{ij}^{\text{V}} + \tilde{C}_{ij}^{\text{R}} \right). \tag{3.33}$$

The accuracy of the parameterization is evaluated using an average normalized root-mean-square deviation (ANRMSD) measure, which represents the differences between elastic constants predicted by the modified Blatz-Ko model and the reference data normalized by the range of the reference data.

$$\text{ANRMSD} = \frac{1}{2} \left(\frac{\sqrt{\frac{1}{N} \sum_{i=1}^{N} \left[\tilde{C}_{11}^{\text{fit}}(J_0^i) - \tilde{C}_{11}^{\text{ref}}(J_0^i) \right]^2}}{\tilde{C}_{11\text{max}}^{\text{ref}} - \tilde{C}_{11\text{min}}^{\text{ref}}} + \frac{\sqrt{\frac{1}{N} \sum_{i=1}^{N} \left[\tilde{C}_{12}^{\text{fit}}(J_0^i) - \tilde{C}_{12}^{\text{ref}}(J_0^i) \right]^2}}{\tilde{C}_{12\text{max}}^{\text{ref}} - \tilde{C}_{12\text{min}}^{\text{ref}}} \right), \tag{3.34}$$

where $\tilde{C}_{ij}^{\text{fit}}$ are the elastic constants obtained from the fitted modified Blatz-Ko model, and $\tilde{C}_{ij\text{max}}^{\text{ref}} - \tilde{C}_{ij\text{min}}^{\text{ref}}$ is the range of the reference data over the pressure domain.

3.5.1 Helium

The modified Blatz-Ko model for an isotropic hcp helium polycrystal is obtained using experimental elastic constants for single-crystal hcp helium at temperature $T = 300$ K for different pressures given in [1] and tabulated in Table 3.3. These values were obtained from high-pressure Brillouin DAC experiments, which are in good agreement with the

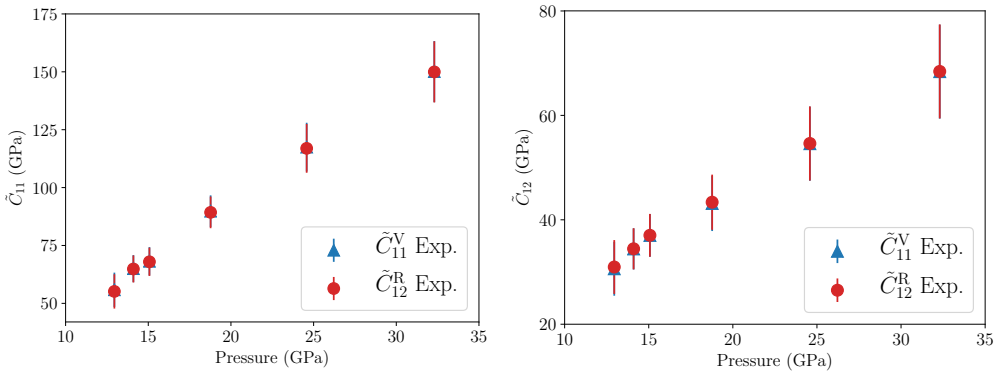

Figure 3.2: The effective elastic constants $\tilde{C}_{11}^{\mathrm{V,R}}$ and $\tilde{C}_{12}^{\mathrm{V,R}}$ for an hcp He polycrystal obtained from Eq. (3.31) based on experimental measurements at 300 K [1]. The red circles and the blue triangles are Reuss bounds and Voigt bounds, respectively.

Table 3.3: The elastic constants $\tilde{C}_{ij}$ with respect to the intermediate configuration of single-crystal hcp He at different pressures and the corresponding Jacobian J_0 obtained from experimental measurements at 300 K [1]. Pressures and elastic constants are in GPa, the Jacobian is unitless.

p	J_0	$\tilde{C}_{11}$	$\tilde{C}_{33}$	$\tilde{C}_{12}$	$\tilde{C}_{13}$	$\tilde{C}_{44}$
12.95	0.964	61.5	56.7	26.0	29.9	10.6
14.10	0.938	67.3	62.1	32.4	35.0	15.0
15.07	0.918	71.3	68.4	37.4	35.2	14.5
18.77	0.852	93.7	96.6	41.3	40.4	20.9
24.58	0.780	125.1	116.9	54.6	50.9	29.0
32.30	0.711	154.2	150.6	67.4	66.7	39.4

results obtained from MD simulation [91] using the Young-McMahan-Ross potential [96,97]. The effective Voigt and Reuss bounds for $\tilde{C}_{11}$ and $\tilde{C}_{12}$ obtained from Eq. (3.31) for the values in Table 3.3 are plotted as a function of hydrostatic pressure in Fig. 3.2. The effective elastic constants increase significantly with pressure, roughly doubling over the studied range of pressures. As mentioned above, the Voigt and Reuss bounds are close, therefore the averaging in Eq. (3.33) is reasonable. In order to compute the cost function in Eq. (3.32), the hydrostatic pressure must be related to the Jacobian relative to the reference state. To obtain this relation, the experimental isothermal pressure-volume EOS for hcp helium from [1] is used, as shown in Fig. 3.3, and fit to the Rose-Vinet EOS [98],

$$\begin{aligned} p &= 3K_0 \left(\frac{1-\eta}{\eta^2}\right) e^{\frac{3}{2}(K_0'-1)(1-\eta)}, \\ \eta &= (V/V_0)^{\frac{1}{3}}, \end{aligned} \tag{3.35}$$

where $V_0 = 25.35$ cm^3/mol is the reference volume, $K_0 = 0.0064(\pm 0.0003)$ GPa is the bulk modulus of helium, $K_0' = 9.71(\pm 0.06)$ is the derivative of bulk modulus with respect to pressure, all evaluated at zero pressure for helium [1]. Choosing as the reference volume, the volume obtained from Eq. (3.35) for $p = 11.65$ GPa (the experimental condensation pressure of helium [79]), the Jacobian at each pressure is computed as shown Table 3.3. The elastic constants versus the Jacobian are plotted in Fig. 3.4 along with the relations in Eq. (3.26) with parameters $A_1 = 4.28$ GJ/m^3, $A_2 = 2.23$ GJ/m^3, $A_3 = -1.37$ GJ/m^3, and $\beta = 1.20$ obtained by minimizing the cost function in Eq. (3.32). The agreement between the model predictions and fitting data is very good with an ANRMSD of 3.79%. Substituting the obtained parameters into Eqs. (3.1) and (3.6), the SED (in GJ/m^3) and the Cauchy stress (in GPa) for an isotropic hcp helium polycrystal are

$$\Psi(I_1, I_2, I_3) = 4.28I_1 + 2.23\frac{I_2}{I_3} + 3.57I_3^{-1.2} + 1.86I_3^{1.2} - 1.37(\sqrt{I_3} - 1)^2 - 24.96, \tag{3.36}$$

$$\begin{aligned} \boldsymbol{\sigma} = J^{-1} \Bigg[&\left(8.56 + 4.46\frac{I_1}{I_3}\right)\boldsymbol{B} - \frac{4.46}{I_3}\boldsymbol{B}^2 \\ &+ \left(4.46I_3^{1.2} - 8.56I_3^{-1.2} - 4.46\frac{I_2}{I_3} - 2.74I_3 + 2.74\sqrt{I_3}\right)\boldsymbol{I}\Bigg] - 11.65\boldsymbol{I}. \end{aligned} \tag{3.37}$$

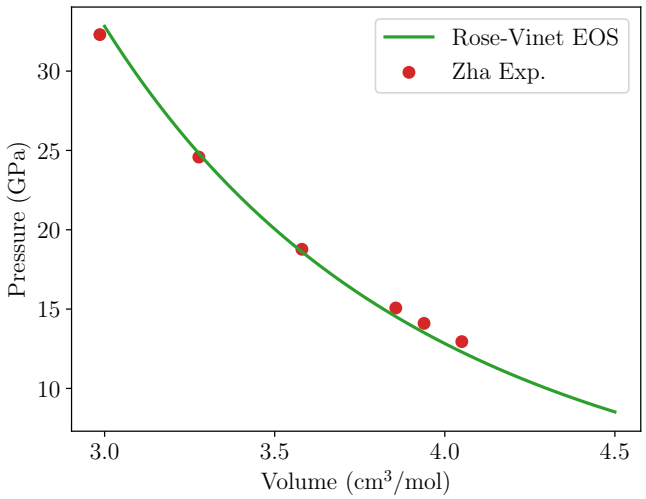

Figure 3.3: The isothermal pressure-volume EOS for hcp helium. The red circles are experimental results from [1]. The green line is the curve fitted to the Rose-Vinet EOS in Eq. (3.35).

Note that in the reference state ($I_1 = I_2 = 3$, $I_3 = 1$, $\boldsymbol{B} = \boldsymbol{I}$, $J = 1$) the Cauchy stress tensor is equal to $-11.65\boldsymbol{I}$ GPa, which is the condensation pressure of helium. The EOS corresponding to Eq. (3.37) (i.e. the pressure–volume relation) follows as

$$\begin{aligned} p = &-8.56(V/V_0)^{-\frac{1}{3}} + 4.46(V/V_0)^{-\frac{5}{3}} + 8.56(V/V_0)^{-3.4} \\ &- 4.46(V/V_0)^{1.4} + 2.74(V/V_0) + 8.91, \end{aligned} \tag{3.38}$$

where p is the hydrostatic pressure, V/V_0 is the volume change ratio. This result is in good agreement with the experimentally measured EOS for hcp helium at room temperature [1, 7] as shown in Fig. 3.5.

3.5.2 Rhenium

Parameterizing the modified Blatz-Ko model for rhenium requires the room temperature elastic constants for single-crystal hcp rhenium at different pressures. The pressure-dependent elastic constants of rhenium up to 37 GPa were obtained experimentally by Duffy et al. [9] using X-ray diffraction. However, the authors point out that their results are inconsistent with a previous ultrasonic study with pressures up to about 0.4

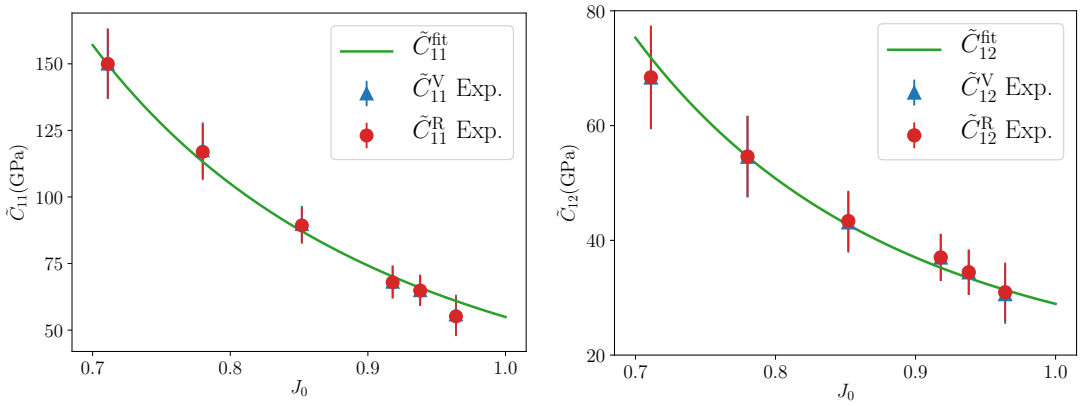

Figure 3.4: The effective elastic constants as a function of J_0 (red circles are Reuss bounds, blue triangles are Voigt bounds) and the fitted modified Blatz-Ko model (green lines) for an hcp He polycrystal.

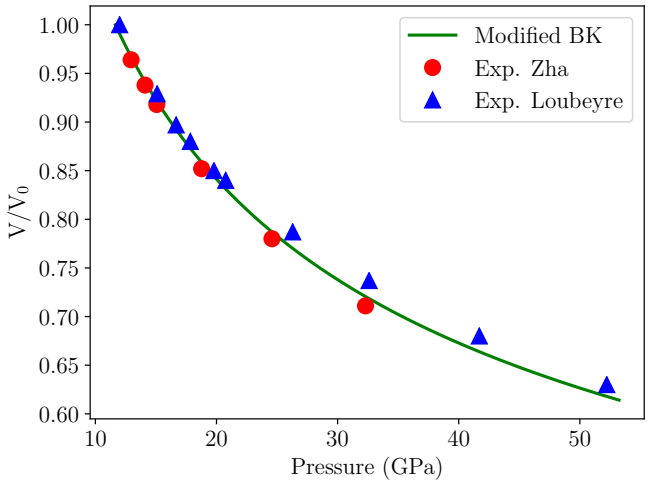

Figure 3.5: The modified Blatz-Ko model EOS curve (green line) compared with DAC experiments by Zha et al. [1] (red dots) and X-ray diffraction measurements by Loubeyre et al. [7] (blue triangles).

GPa [85]. We are not aware of other reliable experimental data for rhenium at higher pressures. Instead, the pressure-dependent elastic constants are constructed using first principles results at 0 K for a range of pressures and extrapolate to room temperature using a thermodynamics approach [99].

Lv et al. [3] and Steinle-Neumann [87] computed the elastic constants of rhenium over a range of pressures at 0 K. We use the results of Lv et al. [3] since they cover a broader pressure range. The elastic constants at a non-zero temperature T are obtained through a first-order Taylor expansion (which is valid as long as T is not too large) [100, 101]:

$$\tilde{C}_{ij}(p,T) = \tilde{C}_{ij}(p,0) + \left.\frac{\partial \tilde{C}_{ij}(p,T)}{\partial T}\right|_{T=0} T, \tag{3.39}$$

where $\tilde{C}_{ij}(p,T)$ are the elastic constants at hydrostatic pressure p and temperature T. In general, $\partial \tilde{C}_{ij}/\partial T$ is a function of the pressure p (or equivalently the volume V). However, Anderson et al. [102, 103] provided a condition for $\partial \tilde{C}_{ij}/\partial T$ to be independent of pressure (volume) in terms of the dimensionless Anderson-Grüneisen parameter δ_T,

$$\delta_T = -\frac{1}{\alpha_V K_T}\left(\frac{\partial K_T}{\partial T}\right)_p, \tag{3.40}$$

where α_V is the volume thermal expansion coefficient and K_T is the isothermal bulk modulus. The Anderson condition for $\partial \tilde{C}_{ij}/\partial T$ to be independent of pressure is

$$\left|\delta_T - K'\right| \leq 0.2, \tag{3.41}$$

where K' is the derivative of K_T with respect to pressure,

$$K' = \left(\frac{\partial K_T}{\partial p}\right)_T. \tag{3.42}$$

For rhenium at room temperature, $K' = 4.5$ [2, 9], $\alpha_V K_T = 0.00776$ GPa/K, and $\partial K_T/\partial T = -0.03654$ GPa/K [2], which gives $\delta_T = 4.7$. Thus, rhenium satisfies the Anderson condition. Assuming that $\partial \tilde{C}_{ij}/\partial T$ is also independent of temperature between 0 K and room temperature, Eq. (3.39) can be used with the values in Table 3.4 measured at atmospheric pressure [2]. The reference elastic constants at 0 K [3] and the extrapolated values at 300 K are listed in Table 3.5.

The effective Voigt and Reuss bounds for $\tilde{C}_{11}$ and $\tilde{C}_{12}$ obtained from Eq. (3.31) for the values in Table 3.5 are plotted as a function of J_0 in Fig. 3.6 along with

Table 3.4: The temperature derivative of elastic constants of single-crystal hcp Re measured at atmospheric pressure. Units in GPa/K. Source: [2].

$\partial\tilde{C}_{11}/\partial T$	-0.0935
$\partial\tilde{C}_{33}/\partial T$	-0.1055
$\partial\tilde{C}_{12}/\partial T$	0.0003
$\partial\tilde{C}_{13}/\partial T$	0.0248
$\partial\tilde{C}_{44}/\partial T$	-0.0331

Table 3.5: The elastic constants $\tilde{C}_{ij}$ relative to the intermediate configuration of single-crystal hcp Re at different pressures and the corresponding Jacobian J_0. Results at 0 K are taken from [3] and extrapolated to 300 K using Eq. (3.39). Pressure and elastic constants are in GPa.

		0 K					300 K				
p	J_0	$\tilde{C}_{11}$	$\tilde{C}_{33}$	$\tilde{C}_{12}$	$\tilde{C}_{13}$	$\tilde{C}_{44}$	$\tilde{C}_{11}$	$\tilde{C}_{33}$	$\tilde{C}_{12}$	$\tilde{C}_{13}$	$\tilde{C}_{44}$
0	1	608.30	708.30	308.30	208.30	162.50	580.25	676.65	308.39	215.74	152.57
10	0.975	685.40	789.60	337.50	233.30	179.20	657.35	757.95	337.59	240.74	169.27
20	0.954	760.40	862.50	366.70	256.20	193.80	732.35	830.85	366.79	263.64	183.87
25	0.944	797.90	900.00	381.30	268.80	200.00	769.85	868.35	381.39	276.24	190.07
30	0.935	829.20	933.30	397.90	281.30	206.30	801.15	901.65	397.99	288.74	196.37
40	0.917	897.90	997.90	422.90	308.30	222.90	869.85	966.25	422.99	315.74	212.97
50	0.902	954.20	1052.10	458.30	337.50	235.40	926.15	1020.45	458.39	344.94	225.47

the relations in Eq. (3.26) with parameters $A_1 = 29.90$ GJ/m^3, $A_2 = 46.86$ GJ/m^3, $A_3 = -179.61$ GJ/m^3, and $\beta = 1.77$ obtained by minimizing the cost function in Eq. (3.32). The agreement is very good with an ANRMSD of 2.36%. Substituting the above parameters into Eqs. (3.1) and (3.6), the SED and the Cauchy stress for an isotropic hcp rhenium polycrystal are

$$\begin{aligned}\Psi(I_1, I_2, I_3) = 29.9I_1 + 46.86\frac{I_2}{I_3} + 16.89I_3^{-1.77} \\ + 26.48I_3^{1.77} - 176.61(\sqrt{I_3} - 1)^2 - 273.65,\end{aligned} \tag{3.43}$$

$$\begin{aligned}\boldsymbol{\sigma} = J^{-1}\left[\left(59.8 + 93.72\frac{I_1}{I_3}\right)\boldsymbol{B} - \frac{93.72}{I_3}\boldsymbol{B}^2\right. \\ \left. + \left(93.72I_3^{1.77} - 59.8I_3^{-1.77} - 93.72\frac{I_2}{I_3} - 359.22I_3 + 359.22\sqrt{I_3}\right)\boldsymbol{I}\right].\end{aligned} \tag{3.44}$$

The corresponding EOS,

$$\begin{aligned}p = -59.8(V/V_0)^{-\frac{1}{3}} + 93.72(V/V_0)^{-\frac{5}{3}} + 59.8(V/V_0)^{-4.54} \\ - 93.72(V/V_0)^{2.54} + 359.2(V/V_0) - 359.2,\end{aligned} \tag{3.45}$$

is in good agreement with experimental measurements for hcp rhenium at room temperature [2,8,9] as shown in Fig. 3.7.

3.6 Numerical example

The motivation for the analysis presented in this chapter is to derive a hyperelastic model for rhenium and helium for use in finite element method (FEM) simulations of a DAC experiment, in which helium is used as the pressure medium in a chamber sealed by a rhenium gasket. In practice, helium is introduced into the chamber in liquid form and solidifies during the experiment due to pressure imposed by the diamond anvils [104]. This process cannot be directly modeled using the helium constitutive relation developed in this chapter because it does not describe the gaseous or liquid states of this material or the solidification process. Rather the constitutive relation is limited to solid helium with the condensation pressure represented as a residual hydrostatic pressure of 11.65 GPa in its undeformed state. This creates a situation where the rhenium and

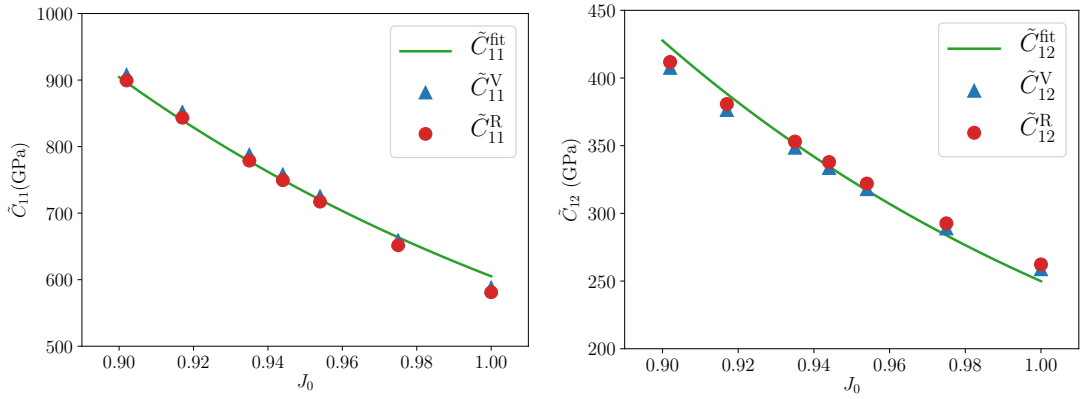

Figure 3.6: The effective elastic constants as a function of J_0 (red circles for the Reuss bounds, blue triangles for the Voigt bounds) and the fitted modified Blatz-Ko model results (green line) for hcp Re polycrystal.

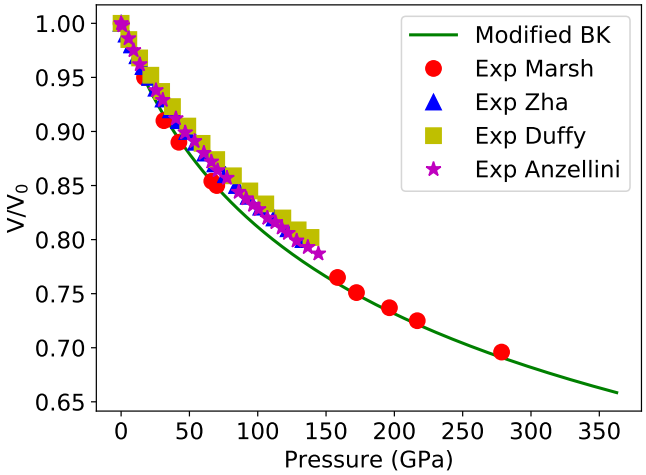

Figure 3.7: The modified Blatz-Ko model EOS curve (green line) compared with results from shock wave experiment by Marsh [8] (red dots), and DAC experiments by Zha et al. [2] (blue triangles), Duffy et al. [9] (yellow squares), and Anzellini et al. [10] (purple stars).

helium constitutive relations have different stress states in their reference configuration, which requires care when setting up an FEM simulation.

Simulations of the DAC apparatus will be described in the next chapter. In the remainder of this chapter we show through a simple didactic example how the two constitutive models developed in this paper, which have different reference states, can be used together in an FEM simulation. Consider a spherical rhenium pressure vessel with inner and outer radii of $a = 0.09$ m and $b = 0.1$ m. Assume that the process that we are modeling is one where helium is gradually introduced into the vessel, first liquefying, and then at a pressure of 11.65 GPa solidifying into an hcp polycrystalline structure. The resulting structure is one where the rhenium sphere is expanded (relative to its reference state) to be in equilibrium with an internal pressure of 11.65 GPa and the corresponding deformed cavity is filled with a solid helium core (in its reference state) at the same pressure.[2] We simulate this process using the commercial FEM code Abaqus with the rhenium and helium constitutive models implemented as VUMAT user material subroutines written in Fortran. The mass densities of rhenium and solid helium are 21.2 g/cm^3 and 0.21 g/cm^3, respectively. Simulations are performed using explicit dynamics for a duration of 1 s.

First, we simulate the response of the rhenium pressure vessel to a linearly increasing pressure loading (model-I) up to a pressure 11.65 GPa (without including the helium explicitly) as shown in Fig. 3.8(a). This is consistent with the experimental process described above where helium is gradually introduced into the vessel.[3] The outer radial displacement of the inner surface of the pressure vessel as a function of time t (with a pressure $p(t) = 11.65t$ GPa) is shown in Fig. 3.9(a). The response is initially linear but exhibits nonlinear behavior at the upper range of the pressure. The maximum principal stress (which is equal to the tangential stress) is shown in Fig 3.10(a). The stress ranges from 72.5 GPa on the inner surface to 66.6 GPa on the outer surface. It is instructive to compare these values with the elasticity theory solution for a thick-walled spherical

[2]This is not a physical problem since in practice the internal pressure would lead to rupture of the rhenium vessel, which has a tensile strength of about 1 GPa. However, modeling a realistic problem is not the intent of this example.

[3]This will not capture the nonequilibrium processes occurring when the helium liquefies and later solidifies, but the end state will be correct.

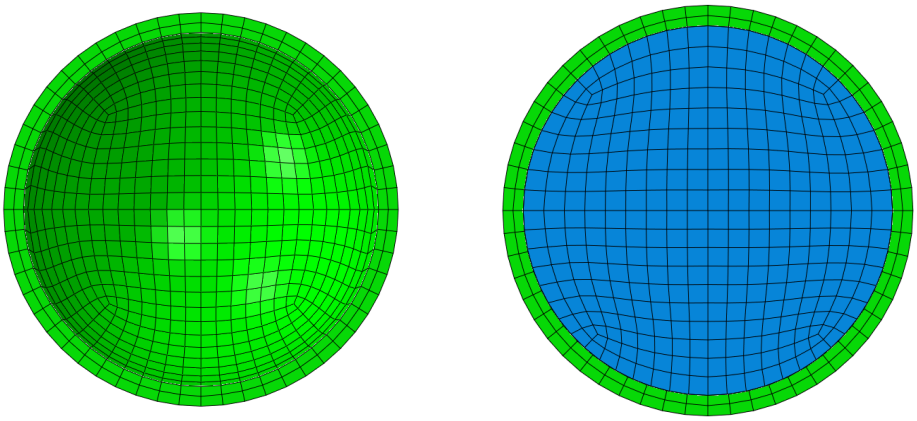

(a) (b)

Figure 3.8: The geometry and mesh of (a) model-I: rhenium spherical pressure vessel (green) subjected to internal pressure loading, and (b) model-II: rhenium spherical pressure vessel (green) filled with a solid helium core (blue). The models are cut in half to show the meshes in the cross section.

pressure vessel [105]. The tangential stress at a distance r from the origin is

$$\sigma_{\mathrm{t}}(r) = \frac{pa^3}{2r^3}\frac{2r^3 + b^3}{b^3 - a^3}. \tag{3.46}$$

For $a = 0.09$ m, $b = 0.1$ m and $p = 11.65$ GPa this gives a tangential stress of 52.8 GPa and 47.0 GPa on the inner and outer surfaces, respectively. These values are significantly different from the simulation results due to nonlinear geometric and material effects. (The elasticity solution is limited to small strains and a linear elastic constitutive model.)[4]

Next, we explore how to perform the FEM simulation with the helium explicitly included in the model as a spherical core exerting a pressure on the surrounding rhenium vessel (Fig. 3.8(b)). First, consider a "naive" approach where the helium and rhenium are placed in the reference model in their undeformed states (model-II). The helium includes a residual hydrostatic pressure of 11.65 GPa and the rhenium is stress free. The system responds by expanding the helium and reducing this pressure until the

[4]When the pressure is reduced to small values, the FEM solution is in agreement with the elasticity theory prediction.

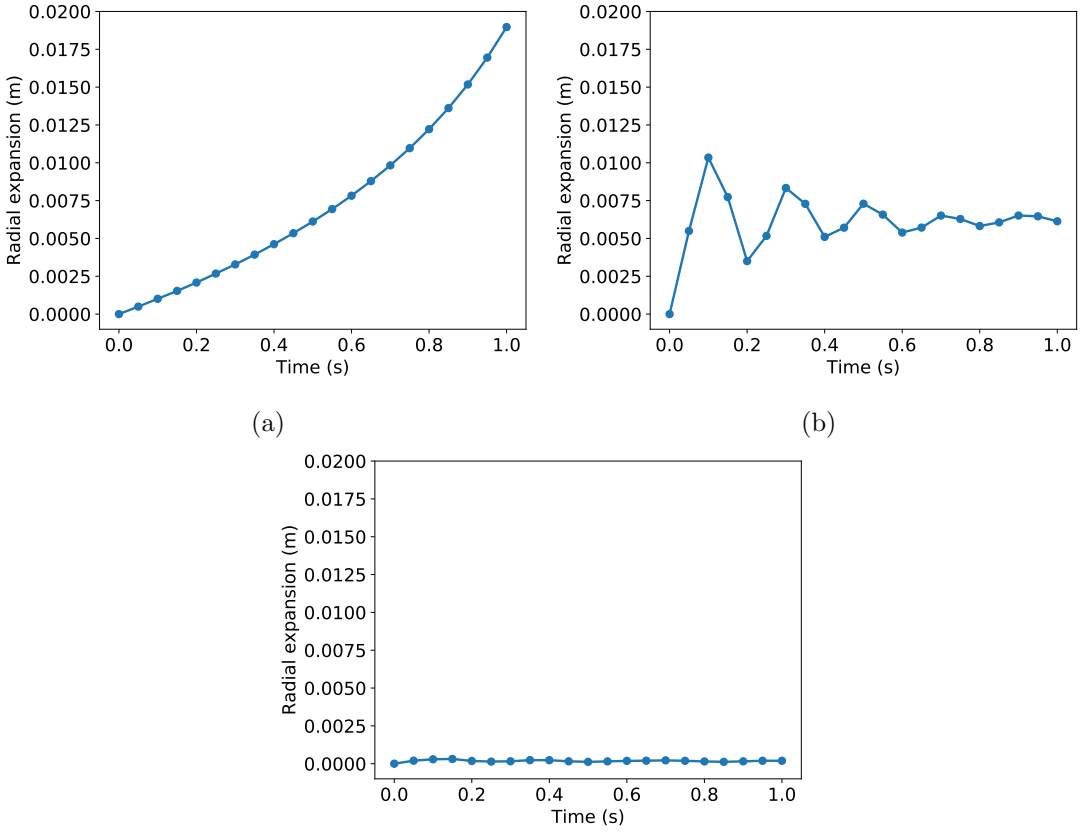

Figure 3.9: The outward radial displacement of the inner surface of the spherical vessel as a function of time for (a) model-I, (b) model-II, and (c) model-III.

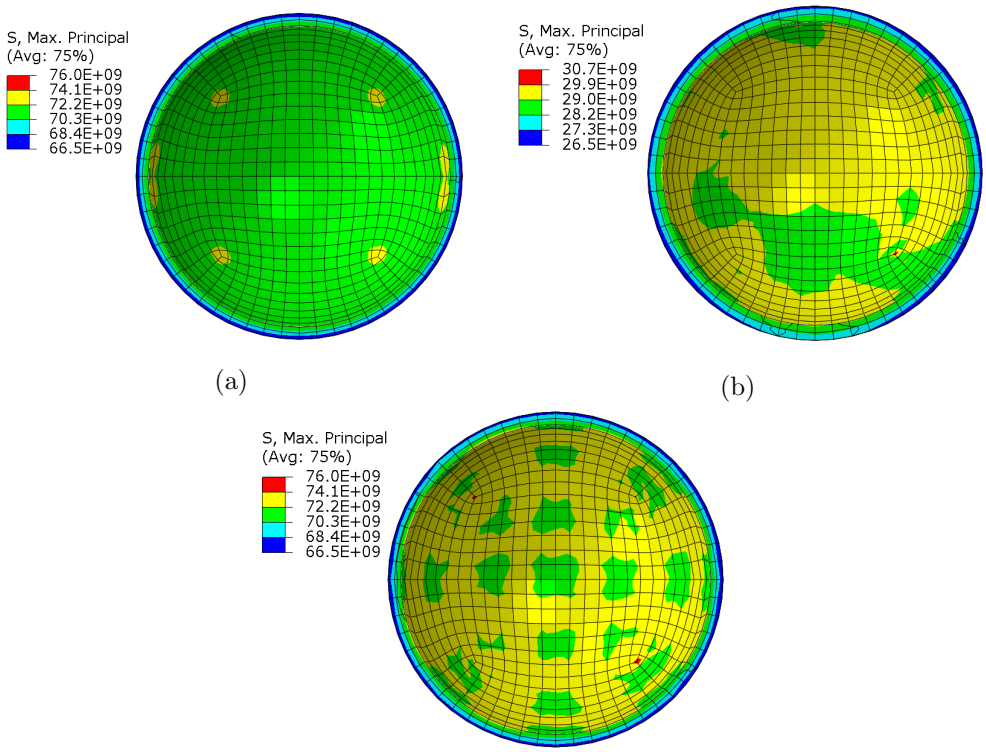

Figure 3.10: The maximum principal stress field in the spherical vessel for (a) model-I, (b) model-II, and (c) model-III. Only the rhenium vessel is shown in (b) and (c). The models are cut in half to show the stress distribution on the inner surface. The small irregular fluctuations in the stress are due to numerical noise from variations in the mesh and the imposed contact boundary conditions between the rhenium vessel and helium core.

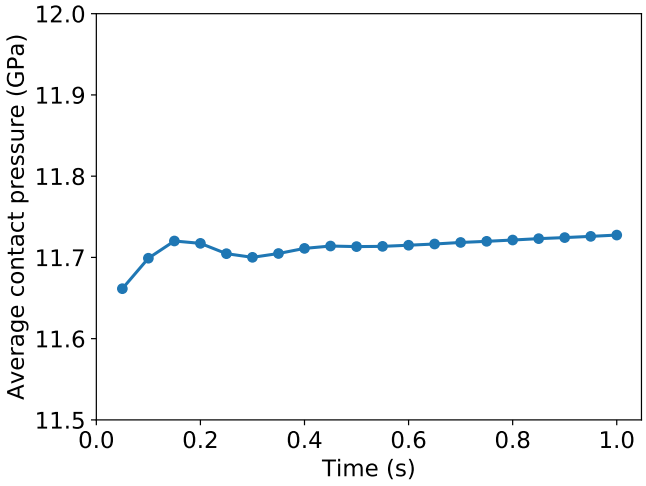

Figure 3.11: The average contact pressure between the rhenium vessel and helium in the model-III simulation.

helium and rhenium are in equilibrium with each other. The radial expansion is shown in Fig. 3.9(b). Following some dynamic oscillations (reduced by an imposed viscous damping) the response converges to an expansion of about 0.006 m. The pressure in the helium drops to 6.0 GPa. The principal stresses in the rhenium, shown in Fig. 3.10, are 30.7 GPa and 26.5 GPa on the inner and outer surfaces, respectively.

Clearly model-II is not consistent with the experimental process where the helium is pumped in to a pressure of 11.65 GPa (as described by model-I). Instead in model-III, the following procedure is followed: (1) The nodal positions of the rhenium vessel in the final step of the model-I simulation are imported as an initial deformed state; (2) the solid helium core is added with an outer radius matching the deformed inner radius of the rhenium vessel; (3) a "hard" contact with no overclosure allowed in the normal direction and zero friction[5] in the tangential direction is defined between the outer surface of helium core and the inner surface of the rhenium vessel [107]; (4) the combined system is evolved under explicit dynamics to an equilibrium steady state. The radial expansion of the vessel is close to zero as shown in Fig. 3.9(c). The maximum

[5]Sliding is negligible between helium and rhenium in this problem due to spherical symmetry. Under more general conditions, one should consider defining a friction coefficient between helium and rhenium. For example, in a rotational DAC experiment, the helium is subjected to a large shear strain [106].

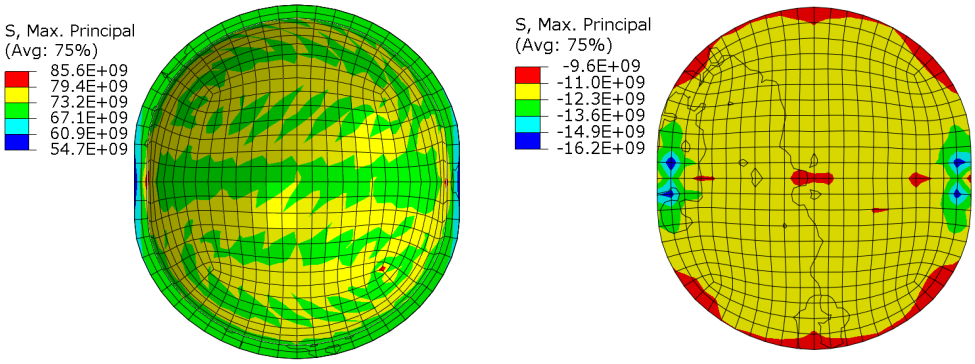

(a) (b)

Figure 3.12: The maximum principal stress of (a) rhenium pressure vessel and (b) helium core under uniaxial compression between two rigid flat plates displaced inwards by 0.02 m. The models are cut in half to show the stress distribution in the cross section. (The squiggly black lines in the figure are an artifact of the visualization method used to create a sliced cross-section of the deformed body.)

principal stress in the vessel is shown in Fig. 3.10(c), which is very close to the results in model-I. The average contact pressure between the rhenium and helium is shown in Fig. 3.11 with an average value of 11.71 GPa, which is close to the residual hydrostatic pressure of solid helium. These results indicate that the initial state created from model-I with the helium core insert is at equilibrium from the start and can be used as an initial configuration for further deformation. For example, Fig. 3.12 shows the principal stresses in the rhenium–helium system when subjected to a diametrical compression between two rigid flat plates. The applied compression decreases the stress on the outer surface of the rhenium vessel near the contact region and increases it on the outer surface (cf. Fig. 3.10). In the helium core, the stress increases in magnitude close to the contact region, and decreases in regions near the top and bottom of the core. A similar initialization procedure can be used for other geometries and loadings, such as in a DAC experiment.

3.7 Conclusion

A modified Blatz-Ko hyperelastic constitutive model is proposed for helium and rhenium, which are used respectively as the pressure transmission medium and gasket material in DAC experiments. The new model describes the response of these materials under ultra-high hydrostatic pressure and finite deformation. The models are fit to isotropic elastic constant versus pressure data obtained using Voigt and Reuss bounds applied to single-crystal data available in the literature from experiment (for helium) and first principle calculation (for rhenium) extrapolated to room temperature using a thermodynamics approach. The equations of state for helium and rhenium predicted by the models are in good agreement with experimental measurements. Due to the use of pressure-dependent elastic constants in the fitting of the models, they are expected to perform well for systems (such as DAC experiments) where the stress state corresponds to a small (to moderate) deviation from purely-hydrostatic. A procedure is proposed for FEM simulations that include both rhenium and helium to address the different stress states of these materials in their reference configuration. This is demonstrated with an example of a spherical rhenium pressure vessel containing solidified helium that is diametrically compressed between two rigid flat plates.

The new constitutive relations are suitable for performing nonlinear finite element simulations of a DAC apparatus. Future work involves combining these models with a local quasicontinuum method employing a Cauchy-Born approach for silicon [108–110] to model phase transformation *in situ* in a DAC experiment.

Chapter 4

A Multiscale Simulation of Phase Transformation for Silicon in Diamond Anvil Cell

An *in situ* multiscale simulation of a diamond anvil cell (DAC) is reported to study the phase transformations (PTs) of silicon under pressure, with emphasis on the effect of inhomogeneous pressure around the sample. The gasket (rhenium) and pressure transmission medium (helium) are simulated with a modified Blatz-Ko hyperelastic model, which can describe the pressure-dependence of the elastic constants. The silicon sample is simulated with a Cauchy-Born rule-based multiscale model, in which the macroscopic material response is obtained from the atomistic scale calculation. We find that the inhomogeneous pressure environment after condensation of helium is important for PTs. We predict the diamond-cubic to β-Sn and bct5 PTs under an average pressure of 17 GPa. However, no PT is predicted if the sample is subject to hydrostatic pressure up to 50 GPa.

4.1 Introduction

Diamond anvil cell (DAC) is considered one of the dominant devices in ultrahigh pressure research. By compressing a sample between two opposing placed diamond anvils,

hundreds of gigapascal pressures are generated in experiments [111–113]. The development of the DAC technique has enabled researchers to explore high-pressure science, like the phase transformations (PTs) of silicon under pressure. Several experiments have showen the diamond-cubic to body-centered-tetragonal (β-Sn) PT, which occurs at pressure of 11.7–12.5 GPa [48, 51, 114]. PT to simple hexagonal phase at around 16 GPa, to an intermediate primitive hexagonal phase between 35 and 40 GPa, and hexagonal close-packed (hcp) phase at around 40 GPa were also observed [51, 115].

The pressure generating device of a DAC usually includes four parts: diamond anvils, the gasket to prevent the anvils from contacting, the pressure transmission medium to generate hydrostatic pressure environment, and the sample which is placed in the chamber formed by anvils and gasket, and filled with the pressure transmission medium. Diamond is the hardest known material, and is unlikely to have PTs under high pressure. In addition, diamond is transparent to X-ray and has a simple diffraction pattern, which can be easily removed from the diffraction patterns of the sample [116]. However, even a small shock applied between two diamond anvils in contact can break at least one of them due to its nature of brittleness. Thus, a gasket is placed between two anvils to prevent the destruction of diamonds. Rhenium is widely used as the gasket material in DAC experiments [81–84] due to its high bulk modulus (360.3 GPa) [85] and absence of PTs at high pressures. The gasket and anvils form an enclosed chamber containing pressure transmission medium, which generates a homogeneous pressurization environment around the sample. Liquid helium is commonly used as pressure transmission medium [75–78] due to its high condensation pressure and low shear modulus. However, liquid helium crystallizes into an hcp structure at a pressure of 11.65 GPa at room temperature [79, 80], which may break the homogeneous pressurization environment.

The finite element method has been widely used to study the mechanical responses of material in a DAC, and to improve the geometrical and material properties of the DAC devices. Adams *et al.* [117] used a linear elastic model to obtain the optimal material and geometrical parameters for a DAC device, which can minimize tension in anvils. Kondrat'yev *et al.* [118] used a linear elastic model to obtain the optimal material properties for gasket. Moss *et al.* found by FEM that the increase in the yield strength of the gasket can help to achieve ultra-high pressure [119]. Feng, Levitas, and coworkers implemented an elastoplastic model in FEM simulations to study the pressure

distribution on the diamond contact surface [120], strain-induced PTs in the sample [121–123], and the problem on the compression and torsion of a sample in rotational DAC [121, 124–126].

Although the crystallization of pressure transmission medium may break the homogeneous pressure environment and change the stress distribution around samples, the pressure transmission medium was not considered in the previous numerical studies. In addition, the elastic constants of rhenium and the solidified helium increase with pressure [1, 9, 85], which was not addressed in the previous works. Furthermore, it is difficult to use a phenomenological model to describe the PT of silicon due to the complexity of this process. Therefore, a model based on more fundamental insights of material response in the atomistic scale is needed to precisely predict the PTs of silicon. Taking the limitations introduced above in mind, we simulate the rhenium and helium with a modified Blatz-Ko hyperelastic model, which is able to describe the pressure dependence of elastic constants. An atomistically-informed, Cauchy-Born rule based multiscale model (CB-KIM) is implemented to the silicon sample, which can obtain the mechanical response from atomistic scale calculations. These models are implemented in a commercial FEM code Abaqus [47] using VUMAT user material subroutine. In section 4.2, the simulation details including the geometry and boundary conditions of a DAC, and the approach to introducing the pressure transmission medium in a FEM simulation are introduced. In section 4.3, the *in situ* simulation results are compared with the results of the same silicon sample subjected to homogeneous pressure condition. The article concludes in section 4.4 with a brief summary.

4.2 Problem formation

A schematic of a DAC is shown in Fig. 8.1. We ignore the anisotropy of the diamond anvil in the circumferential direction to use an axisymmetric geometry. The mesh for different parts are shown in Fig. 8.2. The thickness of the sample is usually in the range of 0.02 to 0.03 mm [127]. We use the thickness of 0.023 mm in this work, other geometry dimensions are also in the range of experiments [128]. No PT is observed for diamond under a pressure up to 378 GPa [129]. Thus, we model the diamond anvil with a linear elastic isotropic material with Young's modulus $E = 1220$ GPa, the Possion's

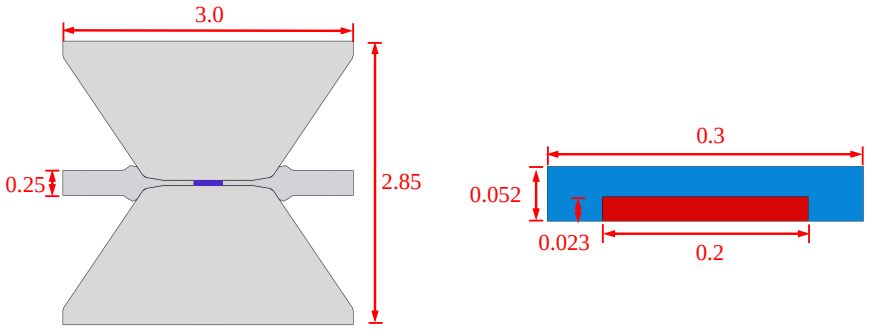

(a) (b)

Figure 4.1: The geometry for (a) the anvil and the gasket. The purple region of (a) is shown in (b), which are the pressure transmission medium (bule) and the sample (red). Unit in millimeter.

ratio $\nu = 0.2$, and mass density of 3.52 g/cm^3 [130]. The rhenium and helium are simulated with the modified Blatz-Ko model introduced in chapter 3 with mass density of 21.2 g/cm^3 and 0.21 g/cm^3, respectively. The silicon sample is simulated with the CB-KIM model introduced in chapter 2 with mass density of 2.33 g/cm^3. The [1 0 0] crystallographic direction of silicon points along the x-axis, and [0 1 0] crystallographic direction points along y-axis.

In a DAC experiment, helium is introduced into the chamber in liquid form and solidifies during the experiment due to pressure imposed by the diamond anvils [104]. This process cannot be directly simulated using the modified Blatz-Ko model because it does not describe the gaseous or liquid states of this material or the condensation process. Rather the constitutive relation is limited to solid helium with the condensation pressure represented in Eq. (3.37) as a residual hydrostatic pressure of 11.65 GPa in its undeformed state. This creates a simulation where the helium and the other materials in a DAC model have different stress states in their reference configurations, which requires care when setting up a FEM simulation. We follow the procedure proposed in chapter 3 work:

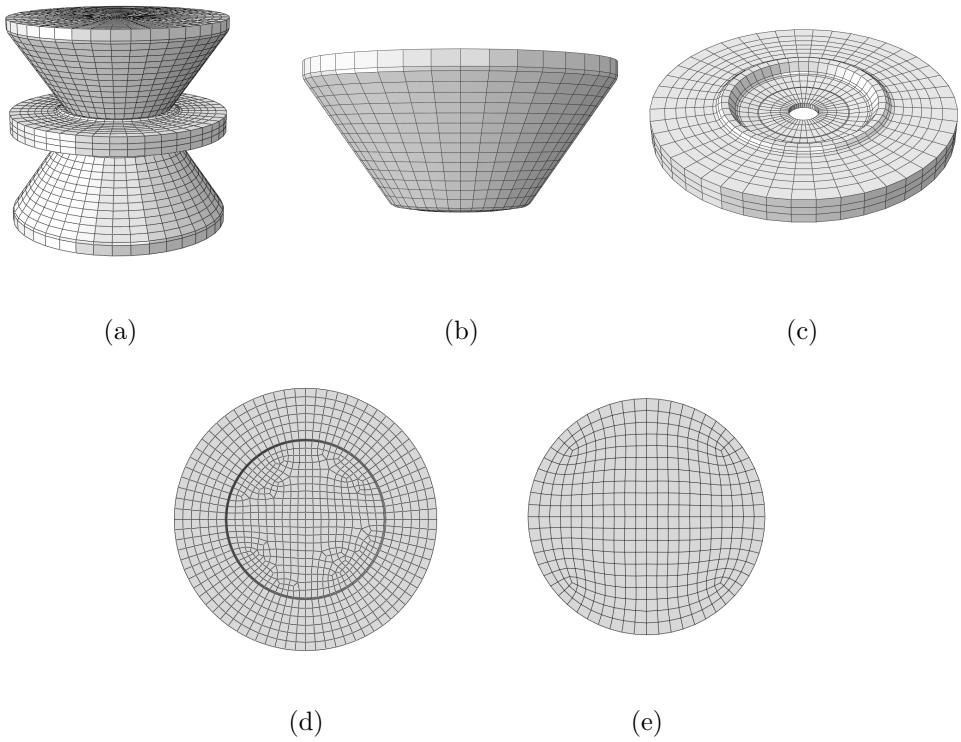

Figure 4.2: Mesh for (a) the assembled DAC system, (b) the anvil, (c) the gasket, (d) the pressure transmission medium, and (e) the sample.

- Step 1: we replace the helium in a DAC model with a hydrostatic pressure of 11.65 GPa applied on the surfaces that have contact with helium (the inner surface of gasket, the surfaces of anvils and sample), shown in write color in Fig. 4.3(a). Simulation is performed using explicit dynamics for a duration of 1 s. The stress state after Step 1 is shown in Fig. 4.3(b). We can see that the silicon sample is subjected to a uniform compressive stress of 11.65 GPa, the inner surface of the gasket is expanded due to the pressure. No PTs are observed in silicon.

- Step 2: The nodal positions of the anvil, gasket, and sample in the last step from Step 1 are imposed as an initial deformed state. The solid helium is added with an outer boundaries matching the deformed geometries of the anvil, gasket and sample. A "hard" contact with no overclosure allowed in the normal direction of contact surfaces and zero friction in the tangential direction of contact surfaces is defined between helium and the rest parts.

- Step 3: The combined system is evolved under explicit dynamics for a duration of 1 s to reach an equilibrium steady state. The contact pressure and radial expansion between helium/rhenium and helium/silicon sample are shown in Fig. 4.4. We can see that the contact pressure have very small deviations with an average of 11.65 GPa, and the radial expansions are almost zero, which indicates the effectiveness of our approach to introduce helium into the system.

- Step 4: After introducing the helium into the system, the bottom surface of the lower anvil is fixed, a downward displacement of 0.024 mm is applied on the top surface of the upper anvil with a constant rate of 0.024 mm/s. The helium and rhenium are compressed by the loading generated by anvils, and transmit the loading to the silicon sample.

4.3 Results and discussion

The β-Sn and bct5 phases are formed during the DAC simulation. It is reasonable that not just a single transformed phase would form in the DAC. The energy surface of the two-atom silicon unit cell is complicated with a large number of local minima

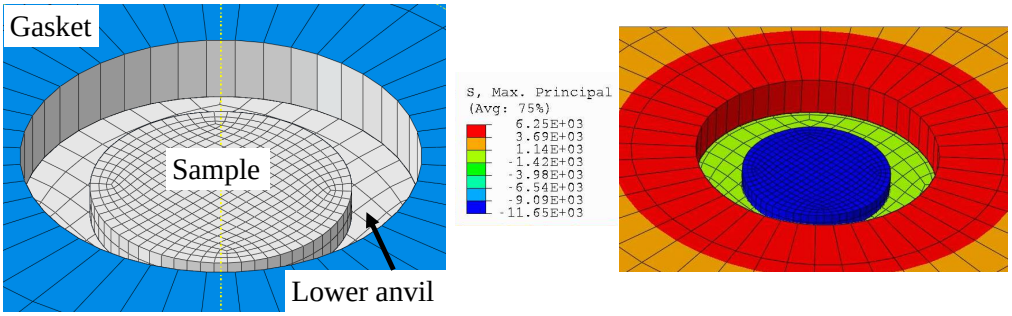

(a) (b)

Figure 4.3: (a) A zoomed-in diagram of a sample in the chamber formed by gasket and anvils. The upper anvil is removed to show the interior of the chamber. The white region represents the surfaces that are subjected to the initial pressure of 11.65 GPa. (b) The stress state of material in (a). Unit of the scaling legend is MPa.

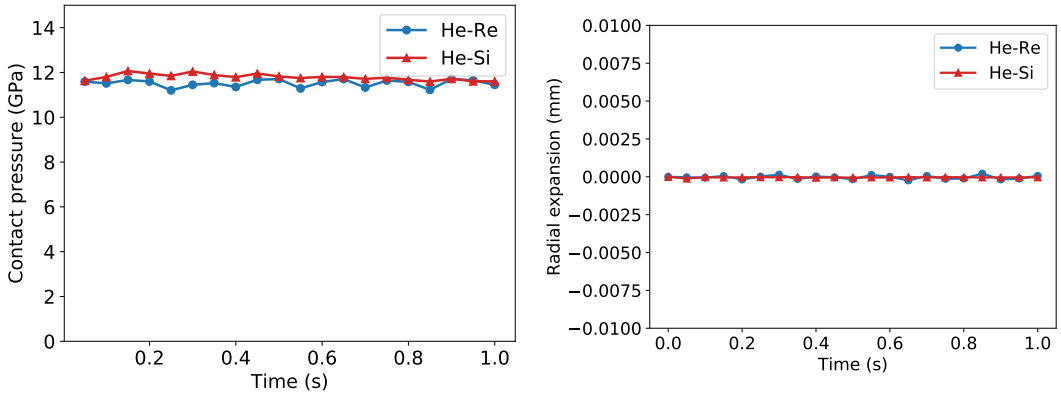

(a) (b)

Figure 4.4: (a) The contact pressure and (b) the radial expansion between helium/rhenium (blue) and helium/silicon sample (red).

corresponding to different phases. The inhomogeneous strain field formed by the solidified helium makes it possible for the silicon unit cell to have large inhomogeneous deformation and form a variety of different local minima in the configurational space.

The pressure, maximum principal stress, and the phases of the silicon sample at anvil displacements of 0.02 mm, 0.022 mm, and 0.024 mm are shown in Fig. 4.5. The distorted elements is either due to the rapidly varying strain fields generated by the solidified helium, or the change of local strain field caused by PTs. The average pressure of the sample when PT initiates (at anvil displacement of 0.02 mm) is 17 GPa. We compare the *in situ* DAC simulation with a simulation in which silicon is subjected to a hydrostatic pressure of 20 GPa. The pressure, maximum principal stress and the phases of the silicon is shown in Fig. 4.6. We can see that the sample is compressed uniformly with final maximum principal stress of -20 GPa. No PT is observed during the compressing process. We increase the hydrostatic pressure to 50 GPa, and still obtain uniform resulting stress without PT.

We compare our simulation results with available experiments. PT of silicon to β-Sn under pressure is widely observed by DAC experiments at pressure of 11.7–12.5 GPa [48, 51]. Our predicted average PT pressure is 17 GPa, which is higher than the experimental data. This is because the CB-KIM model used in this simulation assumes the material to be ideal crystal. However, the real crystal includes defects like dislocations and grain boundaries, which reduce the PT initiation pressure. Another difference between simulation and experiment is the nature of phase formed in the DAC. Bct5 phase was not reported by experiments, although it has been obtained by first principle calculation [131], MD simulations [132, 133] and quasicontinuum simulations [60, 71]. The discrepancies between simulation and experiment perhaps due to the shortcomings of the interatomistic potential. However, it is also possible that bct5 does form during experiments, but has not been detected.

4.4 Conclusion

In this paper, an *in situ* simulation of DAC is performed to study the PTs of silicon under pressure. The silicon sample is placed in a chamber formed by diamond anvils and rhenium gasket containing helium as pressure transmission medium. However,

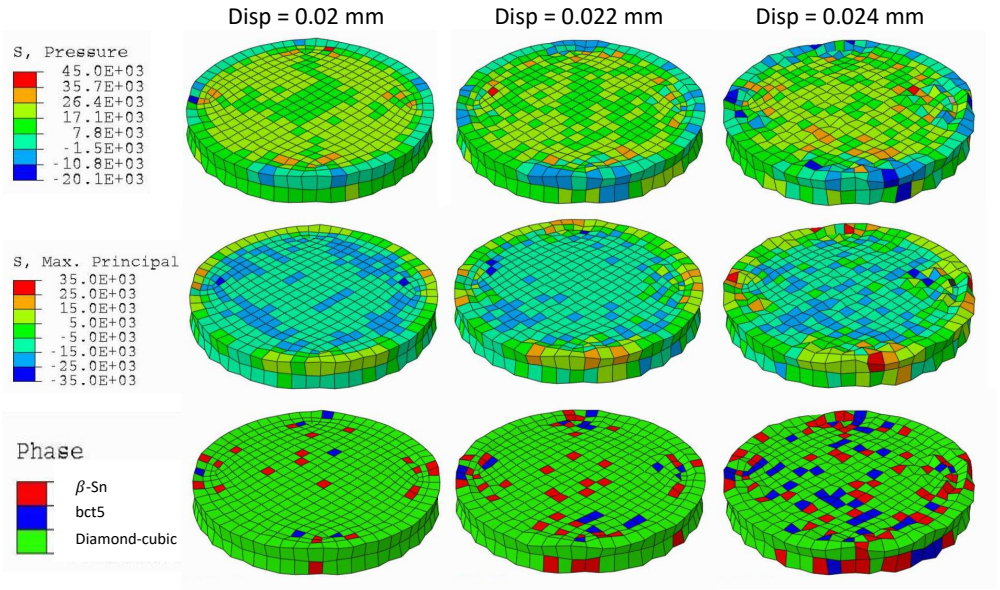

Figure 4.5: The pressure, maximum principal stress, and the phases of the silicon sample at anvil displacements of 0.02 mm, 0.022 mm, and 0.024 mm.

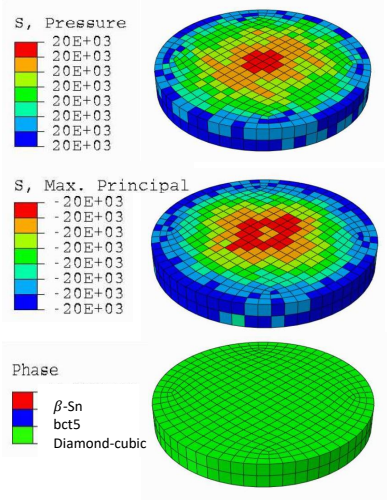

Figure 4.6: The pressure, maximum principal stress, and the phase of the silicon sample under hydrostatic pressure of 20 GPa.

the condensation of helium under pressure of 11.65 GPa may change the hydrostatic pressure environment surrounding the sample. The diamond anvil is modeled as linear elastic material. The helium and rhenium are simulated using a modified Blatz-Ko hyperelastic model which can describe the pressure-dependence of elastic constants. The sample is modeled with a Cauchy-Born rule based multiscale model, which can predict the PT from atomistic calculation. The helium is carefully introduced into the system to obtain the same initial conditions with other materials. We found that the non-hydrostatic pressure environment plays an important role in the PTs of silicon. The diamond-cubic to β-Sn and bct5 PTs are observed for the sample under an average pressure of 17 GPa in the *in situ* simulation. However, if the silicon is subjected to homogeneous pressurization (this environment is not available in the experiment because the pressure transmission medium helium solidify at a pressure of 11.65 GPa), PT is not predicted under pressure up to 50 GPa. Our simulation results are in line with the experiments results and numerical predictions from MD simulations and quasicontinuum simulations. The predicted PT initiation pressure (17 GPa) is higher than experiments (11.7–12.5 GPa) because the model we use in this simulation assume ideal crystal, but real crystal includes defects which reduced the PT pressure.

Chapter 5

Molecular Dynamics Predictions of Thermomechanical Properties of an Epoxy Thermosetting Polymer

This chapter reports the thermomechanical properties of a thermosetting polymer formed by curing a DGEBA resin with a Jeffamine D230 agent predicted by molecular dynamics (MD) simulations. A multistep crosslinking approach is used to form the crosslinked network of the thermosetting polymer. The radial distribution function and X-ray diffraction pattern of the MD predicted crosslinked structure are calculated and compared with experimental results to validate the epoxy network system. Thermomechanical properties such as mass density, gel point, glass transition temperature (T_g), elastic moduli (Young's modulus and shear modulus), yield strengths and shear strength are calculated at different temperatures and crosslinking conversions by employing the DREIDING and AMBER force fields. The MD predicted results are in good agreement with theoretical studies and existing experimental data. We find a significant increase of T_g, yield strength, and shear strength with crosslinking conversion. The elastic modulus is less sensitive to the strain rate, but the yield strength is significantly strain-rate dependent.

5.1 Introduction

Epoxy polymers form a class of thermosetting polymers that are chemically synthesized by curing resins containing epoxide groups and curing agents containing active hydrogens such as amines. Epoxy compounds have been used in a wide variety of applications, including adhesives, coatings and structural materials [134]. The thermomechanical properties of epoxies are important for evaluating their performance and reliability. Such properties can be measured experimentally, however, experiments can be time-consuming and costly to perform. Further, it can be difficult to measure properties of epoxy at different crosslinking conversions while the curing process is ongoing at high temperatures.

An alternative approach gaining popularity in recent years is to obtain polymer properties through molecular-scale computer simulations. Doherty *et al.* [135] provide a comprehensive review of the early developments in this field in which the simulations were not completely molecular due to limitations in computing resources. More recently with improvements in computer hardware and computational algorithms, fully-atomistic molecular dynamics (MD) simulations using empirical force fields (FFs) are being used to study the polymerization and thermomechanical properties of thermosetting polymers for a variety of materials (a summary of results is shown in Table 5.1). MD simulations have been used to compute properties such as the glass transition temperature, gel point, elastic constants, and polymerization-induced volume change [136]. In this chapter we employ MD to comprehensively study the structure and thermomechanical properties of the crosslinked DGEBA/Jeffamine D230 epoxy system using two popular FFs for this material: DREIDING [37] and AMBER [39]. We begin with a discussion of our MD simulation procedure including the crosslinking algorithm used to generate the epoxy structure and validation of the structure by comparison of radial distribution function (RDF) and X-ray diffraction (XRD) pattern results with experiments. We then discuss MD simulation predictions for key thermomechanical properties including mass density, gel point, glass transition temperature, elastic moduli, and yield strengths, and their dependence on temperature and crosslinking conversion. The simulation results are compared with the theoretical values and experimental data where available, as well as MD simulations of similar epoxy systems available in the literature. We conclude

Table 5.1: References to MD simulations of thermosetting polymers. Computed properties: shear strength (τ_y), yield strength (σ_y), shear modulus (G), Young's modulus (E), gel point, density, volume change (ΔV), and glass transition temperature (T_g).

Material	τ_y	σ_y	G	E	Gel point	Density	ΔV	T_g
CYMEL1172/1158[137]	-	-	-	-	-	[137]	[137]	-
PDMS[138]	-	[138]	-	[138]	-	-	-	-
DGEBA/IPD[139]	-	-	[139]	[139]	-	-	-	-
EPON862/TETA[140]	-	-	-	[140]	-	-	[140]	[140]
EPON862/DGEBA[141–143]	-	[141]	[142]	[141, 142]	[143]	-	[142, 143]	[141–143]
EPON862/POSS[144]	-	-	-	-	-	-	[144]	[144]
EPN1180/BPA[145]	-	[145]	-	[145]	[145]	-	[145]	[145]
This work	⋆	⋆	⋆	⋆	⋆	⋆	⋆	⋆

with a summary and an assessment of the limitations of MD for studying thermosetting polymers, along with suggestions for improving accuracy of predictions.

5.2 MD simulation methodology

5.2.1 DGEBA/Jeffamine D230 system

The DGEBA/Jeffamine D230 epoxy system consists of a bisphenol A diglycidyl ether (DGEBA) resin and a Jeffamine D230 curing agent. The molecular structures are shown in Fig. 5.1. DGEBA is a commonly used epoxy resin with one epoxide group at each end of the monomer. Jeffamine D230 polyetheramine is a difunctional primary amine with an average molecular weight of about 230. The primary amine group is located on a secondary carbon atom at the end of the aliphatic polyether chain. The average number of oxypropylene monomers is $n = 2.5$.

5.2.2 Force field and simulation details

The DREIDING [37] and AMBER [39] FFs are employed in all simulations using the open source MD code LAMMPS [146]. Both of these potentials include *bonded interactions* representing immutable covalent bonds, and *nonbonded interactions* representing long-range van der Waals and Coulombic interactions. The DREIDING FF employs a generic functional form that can be applied to a broad range of systems, whereas

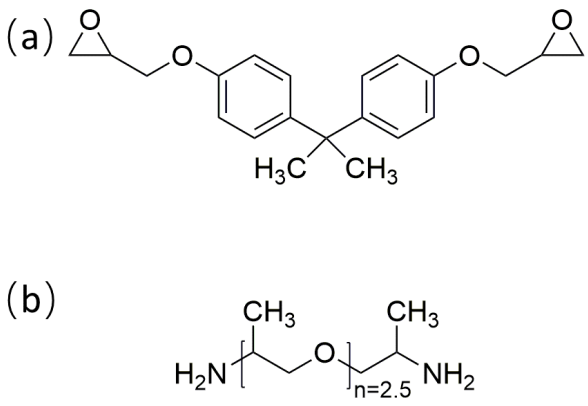

Figure 5.1: Molecular structure of (a) DGEBA and (b) Jeffamine D230.

AMBER is more focused on biomolecular applications for higher accuracy. In both cases, van der Waals interactions are modeled using a standard 12/6 Lennard–Jones pair potential with inner and outer cutoff radii of 8 Å and 12 Å. A shift function is used to ramp the energy and force smoothly to zero between the inner and outer cutoff radii. Periodic boundary conditions are prescribed in all three orthogonal directions. At different stages, the MD simulations are performed either under NPT conditions (constant pressure and temperature) or NVT conditions (constant volume and temperature) as explained below. In LAMMPS, temperature is maintained using a Nosé–Hoover thermostat [147] with a 100 fs coupling constant, and pressure is maintained with a Nosé–Hoover barostat [148] with a 1000 fs coupling constant.

5.2.3 Crosslinking methodology

In order to create a digital sample of DGEBA/Jeffamine D230 epoxy, we must simulate the curing process of the epoxy resin which involves the creation of crosslinks. Curing in a thermosetting polymer is a complex quantum-chemical process involving the breaking and formation of covalent bonds and hydrogen transfer. This is illustrated in Fig. 5.2 where epoxide groups react with primary amine hydrogens to form secondary amines

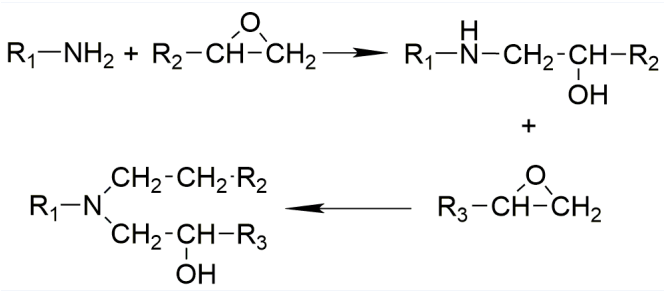

Figure 5.2: Reactions involved in the curing of an epoxy.

that can in turn react with epoxide groups. The curing time required to obtain a fully-crosslinking state is on the scale of tens of minutes to hours depending on the curing temperature and method. Direct simulation of such a process is computationally intractable. Accurate quantum mechanical computations are typically limited to systems of hundreds of atoms over nanosecond time scales. Instead various ad hoc methods have been developed to mimic the covalent bond formation process [149]. There are two main approaches: (1) a *single step* approach in which covalent bonds are assigned based on a Monte Carlo algorithm that attempts different combinations of bond pairs with the goal of minimizing the total length of all newly-formed bonds, and (2) a *multistep approach* in which an incrementally increasing threshold radius is used to form covalent bonds between atoms identified as "active" during an MD simulation at elevated temperature. It has been shown that the choice of crosslinking method has only a minimal impact on thermal and mechanical properties [149]. In our work, we use the multistep approach which is closer to the physical curing process.

For the epoxy system, the following crosslinking methodology is employed. Active atoms are identified in the epoxide groups in DGEBA and the amine groups in Jeffamine D230 in a preprocessing step. The C-O bond in the epoxide groups is broken forming an O-H bond and an active carbon atom. The nitrogen atom in amine groups is also made active by removing two hydrogens, as shown in Fig. 5.3. During the crosslinking simulation, a C-N bond is formed (and added to the FF's list of bonded interactions) whenever an active carbon in DGEBA comes within a threshold distance of an active nitrogen in Jeffamine D230. The curing process is carried out as follows:

1. The first step is to create an initial simulation box. DGEBA and Jeffamine D230

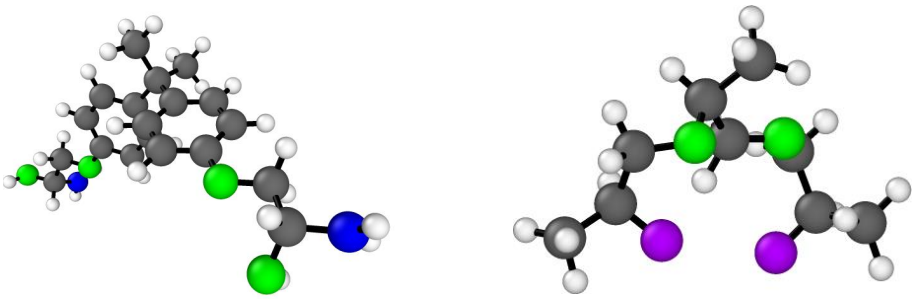

(a) (b)

Figure 5.3: Molecular structures of (a) active DGEBA and (b) active Jeffamine D230 with $n = 2$. The color coding in the figures is carbon (gray), active carbon (blue), oxygen (green), hydrogen (white) and active nitrogen (purple). Covalent bonds between atoms are shown as thick lines. Figures are generated using OVITO [6].

molecules are generated using Materials Studio [150], and randomly seeded into a LAMMPS simulation box to form a unit cell with DGEBA : Jeffamine D230 ($n = 2$) : Jeffamine D230 ($n = 3$) for a stoichiometric ratio of 4:1:1. The unit cell is duplicated to form a simulation box with 108 DGEBA monomers, 27 Jeffamine D230 monomers with $n = 2$, and 27 Jeffamine D230 monomers with $n = 3$. This system contains a total of 7452 atoms with a ratio of 2:1 between active carbon atoms and active nitrogen atoms. (We have also simulated a system eight times as large and obtained similar results.)

2. An MD simulation is performed for 100 ps under NPT conditions at a temperature of 450 K and atmospheric pressure. The purpose of this step is to form an equilibrium system with a target density of about 1.0 g/cm^3 before beginning the crosslinking simulation. At this density, the active atom sites are closer to each other making it easier to form bonds.

3. Identify all pairs of active carbon atoms and active nitrogen atoms separated by a distance smaller than the threshold distance for bond formation. (The choice of threshold has a strong effect on the degree of conversion that can be achieved

within the finite time of a simulation; see discussion below.) Each pair is marked as a possible bond pair if a bond does not already exist between them. If there are multiple possible bond pairs, bonds are formed between the closest pair of atoms. One active carbon can form one C-N bond, while one active nitrogen can form two C-N bonds.

4. An MD simulation is performed under NVT conditions for 4 ps (20,000 steps with a time step of 0.2 fs) at a temperature of 450 K. This step anneals the structure to relax internal stresses generated when new bonds are formed in step 3, and to bring other active sites close together for the next bonding step.

5. Repeat steps 3 and 4 until the target degree of conversion is reached. The degree of conversion is defined as the ratio between the number of bonds created and the maximum number of possible new bonds. In the current system, the maximum number of possible new C-N bonds is 216.

6. Once the target degree of conversion is reached, an MD simulation is performed for 100 ps under NPT conditions at a temperature of 450 K and atmospheric pressure. This final step equilibrates the crosslinked polymer.

As noted above, the choice of the threshold distance has a strong effect on the degree of conversion that can be achieved within a specified amount of time. According to density functional theory (DFT) calculations, the minimum distance at which hydrogen transfers between the epoxide and amine is about 2.2 Å [151]. However, in order to reach a desired conversion more quickly it is typical for the threshold distance to be taken larger than this value. Fig. 5.4 presents the final degree of conversion obtained in a 200 ps crosslinking simulation (performing step 3 and 4 in the above algorithm 50 times) for different threshold distances ranging from 3 Å to 5 Å at 350 K and 450 K. The results show that the degree of conversion increases with the threshold distance plateauing at a value of about 85%. As the curing process continues, the number of active sites decreases and the formation of a network system reduces the mobility of molecules. Thus it is more difficult to form new covalent bonds at a higher conversion. Changing the curing temperature does not have a large effect on the final conversion (at least for the temperatures studied). This indicates that sufficient sampling is taking

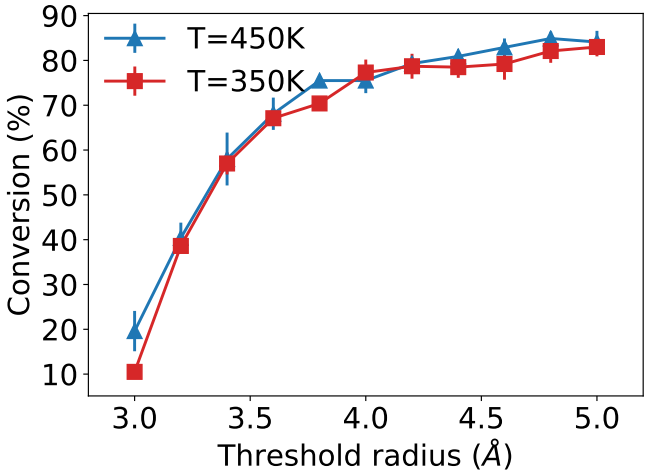

Figure 5.4: The final degrees of conversion of epoxy systems after a 200 ps crosslinking simulation as a function of the threshold distance. Results are for the DREIDING FF. Error bars represent the standard deviation of three independent simulations.

place at these temperatures.

Fig. 5.5 shows a crosslinked DGEBA/Jeffamine D230 system with an 87% degree of conversion generated using the DREIDING force field. (This is the highest conversion obtained by the multistep crosslinking approach described above.) Examples of bonding scenarios for an active nitrogen atom are shown in the insets. Note that since periodic boundary conditions are used in our simulations, new bonds are formed not only between the original set of active atoms, but also between active atoms and their periodic images. Three independent samples are generated using the multistep crosslinking method with different final conversions to obtain an average and standard deviation for property predictions. Depending on the target conversion and selected threshold radius, the total computation time for preparing a sample varies. For example to create a DGEBA/Jeffamine D230 epoxy sample with 80% conversion using a 4 Å threshold radius takes about 20 hours wall time using 24 processors on a parallel cluster.

The crosslinking methodology described above is validated by comparing with experiments the RDF and XRD pattern of a simulated epoxy structure with 87% conversion. The RDF $g(r)$ is the probability of finding an atom at a distance r from a reference

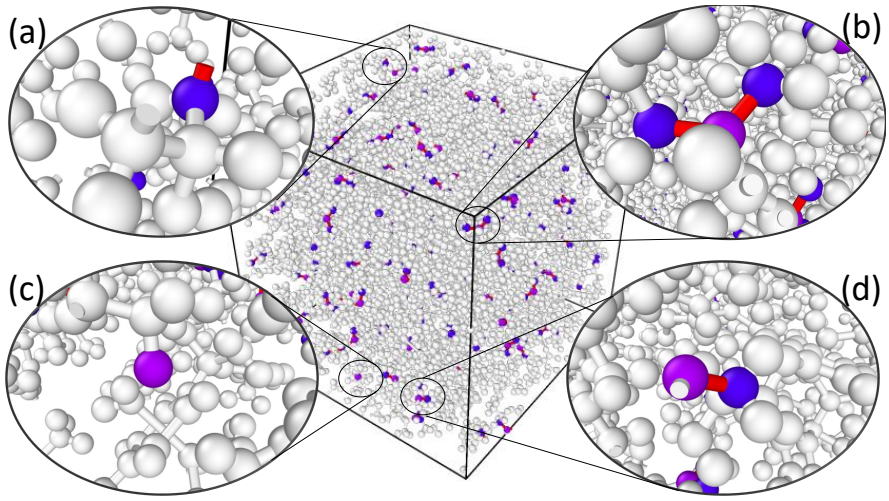

Figure 5.5: DGEBA/Jeffamine D230 system with an 87% degree of conversion. Active carbon atoms (blue), active nitrogen atoms (purple), and newly created C-N bonds (red) are emphasized. (a) An active nitrogen atom that forms one bond with a periodic image of an active carbon. (b) An active nitrogen atom that forms two bonds with active carbon atoms. (c) An active nitrogen atom that forms zero bonds with active carbon atoms. (d) An active nitrogen that forms one bond with an active carbon atoms. Figures are generated using OVITO [6].

atom relative to the random distribution of an ideal gas. The RDF is defined as

$$g(r) = \frac{n(r)/4\pi r^2 dr}{N/V} = \frac{n(r)V}{4\pi r^2 dr N}. \tag{5.1}$$

where $n(r)$ is the number of atoms within a spherical shell in the range $(r-dr/2, r+dr/2)$ with volume $4\pi r^2 dr$, dr is a small increment, and N/V is the average number density (N is the total number of atoms and V is the volume of the system). Fig. 5.6 shows the RDF calculated about the center of the simulation box for a system with 87% conversion using an increment of $dr = 0.1$ Å. Several well-defined peaks are observed in the range $r < 4$ Å that characterize the short-range ordered structure of the cured epoxy. The first peak at about 1.1 Å corresponds to the bond distance between carbon and hydrogen atoms. The second peak at about 1.43 Å is the distance between bonded carbon atoms and non-hydrogen atoms (e.g. C-O and C-C). The third and subsequent peaks are attributed to atoms that are more than two bonds apart, such as hydrogen

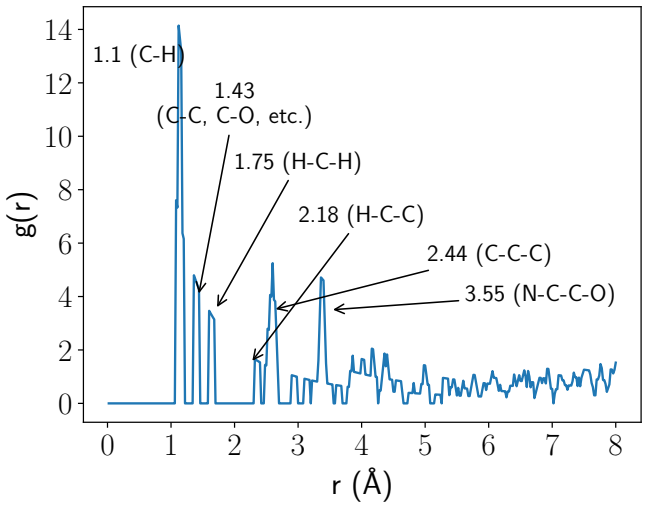

Figure 5.6: The RDF for epoxy with 87% conversion obtained from the crosslinking simulation.

Table 5.2: The a_i and b_i parameters in Eq. (5.3) for H, C, N, and O obtained from experiment [4].

Element	a_1	a_2	a_3	a_4	a_5	b_1	b_2	b_3	b_4	b_5
H	0.0088	0.0449	0.1481	0.2356	0.0914	0.1152	1.0867	4.9755	16.5591	43.2743
C	0.0489	0.2091	0.7537	1.1420	0.3555	0.1140	1.0825	5.4281	17.8811	51.1341
N	0.0267	0.1328	0.5301	1.1020	0.4215	0.0541	0.5165	2.8207	10.6297	34.3764
O	0.0365	0.1729	0.5805	0.8814	0.3121	0.0652	0.6184	2.9449	9.6298	28.2194

atoms in H-C-H sequences (∼1.75 Å), hydrogen and carbon atoms in H-C-C sequences (∼2.18 Å), outer carbon atoms in C-C-C sequences (∼2.44 Å), and oxygen and nitrogen in N-C-C-O sequences (∼3.55 Å). These bond lengths are in excellent agreement with experimental X-ray measurements [152,153]. Note that no sharp peaks are observed for distances > 4 Å and the RDF tends to 1, which is generally regarded as the proof of the amorphous nature of the epoxy resin system [154–156].

As a second validation, the XRD pattern for the simulated epoxy structure is compared with experiment. Various definitions for the XRD function and normalization have been proposed in the literature, although there have been significant attempts at clarifying these definitions [157, 158]. Here we use the Debye scattering equation [159]

with the structure factor,

$$S(q) = \frac{1}{\sum_{j=1}^{N} f_j(q)^2} \sum_{j=1}^{N} \sum_{k=1}^{N} f_j(q) f_k(q) \frac{\sin(q r_{jk})}{q r_{jk}}, \tag{5.2}$$

where $r_{jk} = |\mathbf{r}_j - \mathbf{r}_k|$ is the distance between atoms j and k, $q = |\mathbf{q}|$ is the norm of the scattering wave vector, and $f_j(q)$ is the atomic form factor for the element of atom j given by

$$f(q) = \sum_{i=1}^{m} a_i \exp(-b_i q^2), \tag{5.3}$$

where a_i and b_i are obtained from the work of Peng [4] with $m = 5$ and listed in Table 5.2. The angle between incident and diffracted radiation, 2θ, and the wavelength of the incident radiation, λ_{inc}, are related to q through:

$$q = \frac{4\pi}{\lambda_{\text{inc}}} \sin\theta, \tag{5.4}$$

where λ_{inc} is set to 1.542 Å which is the wavelength used in the experimental study [12]. Fig. 5.7 shows the structure factor $S(q)$ computed using Eq. (5.2) for a simulated DGEBA/Jeffamine D230 epoxy with 87% conversion compared with experimental XRD measurements for DGEBA/triethylamine (TEA) [12] and DGEBA/Diethylenetriamine (DETA) [11]. Our results are in excellent agreement with the experimental measurements showing a broad peak at an angle of about $2\theta = 18°$.

5.3 Results and discussion

Having generated the crosslinking system with target conversions, simulations are performed to determine the mass density, gel point, glass transition temperature, elastic moduli, and yield strengths.

5.3.1 Crosslinking and temperature induced volume change

The bonds that form during the crosslinking process pull end groups together and gradually convert the initial liquid phase into a crosslinked solid. This process leads to reduction in volume because molecules move from a van der Waals distance of separation to a covalent distance of separation. In our simulations, DGEBA/Jeffamine D230

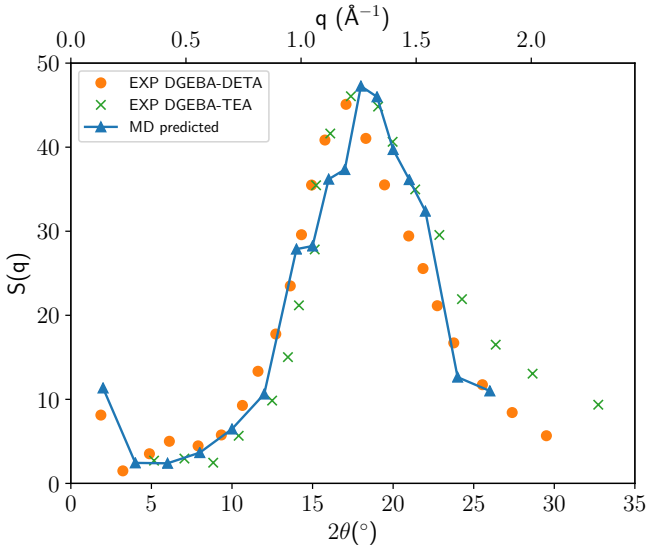

Figure 5.7: Structure factor for a simulated DGEBA/Jeffamine D230 epoxy with 87% conversion computed using Eq. (5.2) (blue line with triangles) compared with experimental measurements for DGEBA/DETA epoxy (orange dots) [11] and DGEBA/TEA epoxy (green crosses) [12]. The abscissas are converted from q to 2θ using Eq. (5.4) for λ_{inc} =1.542 Å.

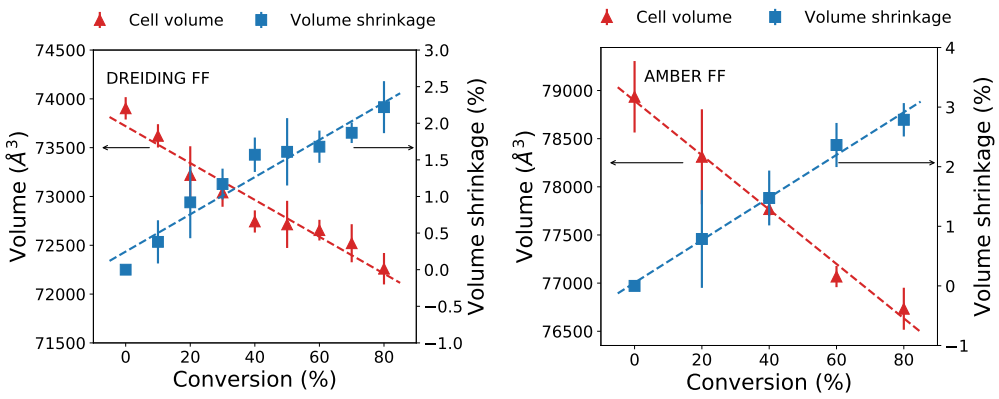

Figure 5.8: The volume (red triangles) and volume shrinkage (blue squares) of DGEBA/Jeffamine D230 system at 300 K as a function of conversion predicted by (a) DREIDING FF, and (b) AMBER FF. Error bars represent the standard deviation from three independent simulations.

systems with target conversions of 10%–80% are equilibrated at 300 K and atmospheric pressure. Fig. 5.8 presents the volume (and volume shrinkage) as a function of conversion obtained from simulations using the DREIDING and AMBER FFs. For the highest crosslinked system (80% conversion), a volume shrinkage of 2.22% is predicted by the DREIDING FF, and 2.79% by the AMBER FF, which are in agreement with experimental measurements of crosslinking-induced volume shrinkage of 2.0–5.3% [160]. Our results are in line with previous MD simulations for similar epoxy systems, e.g. Yang *et al.* [145] obtained a shrinkage of 4.24% for crosslinked EPN1180/Bisphenol-A with a conversion of 90%.

The mass density of the DGEBA/Jeffamine D230 system as a function of conversion at different temperatures obtained using the DREIDING FF is presented in Fig. 5.9. At lower temperatures, the crosslinking-induced volume shrinkage is smaller, e.g. the density increase from a conversion of 10% to 80% is 0.026 g/cm^3 at 300 K, which is smaller than the increase of 0.07 g/cm^3 at 425 K. The effect of temperature on density is stronger at lower conversion, e.g. at a conversion of 10% the density change from 425 K to 300 K is about 0.09 g/cm^3, whereas at a conversion of 80% the density changes

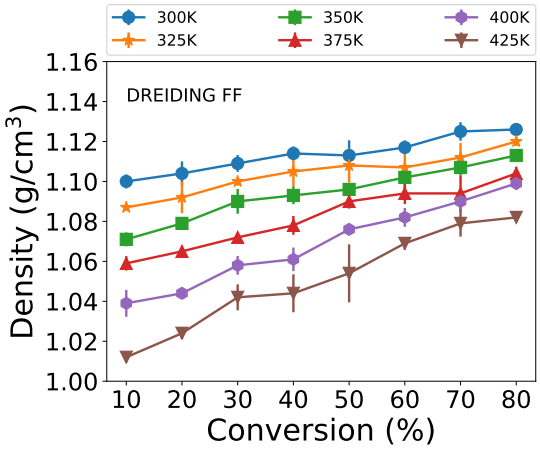

Figure 5.9: Mass density of DGEBA/Jeffamine D230 as a function of conversion at different temperatures. Results are obtained with the DREIDING FF. Error bars represent the standard deviation of three independent simulations.

Table 5.3: Mass density of DGEBA/Jeffamine D230 epoxy predicted by DREIDING and AMBER at different conversions at 300 K compared with an experimental result for high conversion epoxy. Units in g/cm^3

	0%	20%	40%	60%	80%	Experiment [5]
DREIDING	1.101±0.004	1.104±0.006	1.114±0.035	1.117±0.035	1.126±0.002	1.156±0.002
AMBER	1.043±0.005	1.049±0.007	1.061±0.001	1.072±0.002	1.073±0.003	

by half that amount at 0.05 g/cm^3. The full set of mass density results for both the DREIDING and AMBER FFs along with the experimental value for DGEBA/Jeffamine D230 at room temperature are presented in Table 6.1. Both FFs are in line with the experimental value, with DREIDING in slightly better agreement.

5.3.2 Gel point and glass transition temperature

Two important unrelated transitions in polymer networks that produce significant transformations in the physical properties of thermosetting polymers are *gelation* and *glass transition*.

Gelation. As the degree of conversion increases during the curing process, polymers

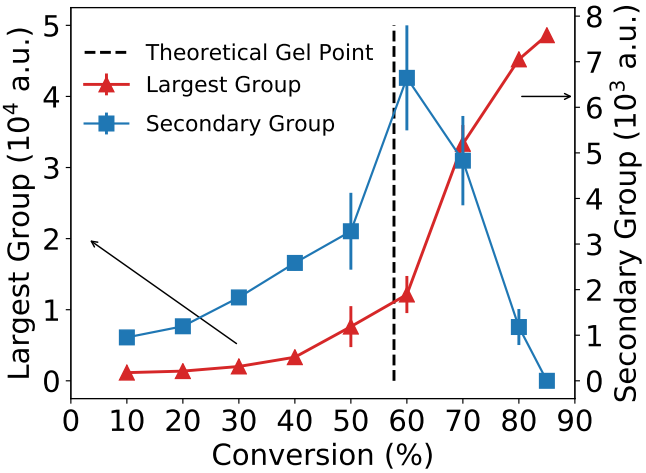

Figure 5.10: Molecular weight of the largest group (red triangles) and the second-largest group (blue squares) as a function of the degree of conversion. The dashed line is a theoretical prediction of the gel point at 57.5%. Results are obtained using the DREIDING FF. Error bars represent the standard deviation of three independent simulations.

of increasing size form until at a critical conversion called the *gel point* epoxies become insoluble macromolecules. In an MD simulation, the gel point can be approximated by monitoring the molecular weight of the largest and second largest group during the curing process [145]. As the gel point is approached, the molecular weight of the largest molecule increases significantly, while the molecular weight of the second largest molecule decreases accordingly. The results plotted in Fig. 5.10 for the DREIDING FF indicate a gel point at about 60% conversion. This value is in very good agreement with a theoretical prediction for the investigated system (bifunctionalized epoxy + four-functionalized curing agent) based on the derivation of Miller *et al.* [161], which gives a value of 57.7% (shown as a vertical dashed line in the figure).

Details on the growth of the network and the formation of macromolecules during crosslinking is shown in Fig. 5.11. One Jeffamine D230 molecule is able to connect with up to four epoxide groups. As curing proceeds, the percentage of Jeffamine D230 molecules that remain unlinked continuously decreases. At the same time the percentage of Jeffamine D230 linked with one, two, and three, epoxide groups increase until reaching

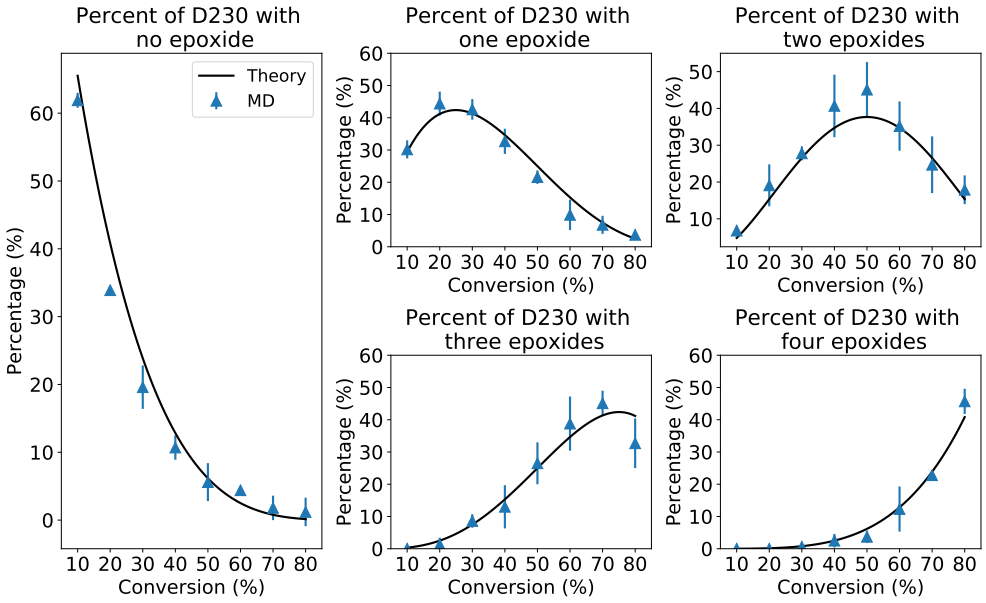

Figure 5.11: Percentage of Jeffamine D230 molecules linked to 0 to 4 epoxide groups at different conversions. The black lines are theoretical results. The blue triangles are MD simulation results using the DREIDING FF. Error bars represent the standard deviation of three independent simulations.

maxima at about 20%, 50%, and 70% conversion, respectively. At a high conversion of 80%, the percentage of Jeffamine D230 linked with zero and one epoxide groups are almost zero, whereas it is close to 50% for those linked with four epoxides. These results are in excellent agreement with our statistical theoretical analysis (balck line in Fig. 5.11). See the Appendix A for details.

Glass transition. Thermosetting polymers exhibit rubber-like behavior at higher temperatures, and glassy brittle behavior at lower temperatures. The transition occurs in a range centered on the *glass transition temperature* T_g. The transition is tied to a reduction of polymer mobility at lower temperature, which prevents the cooperative movements that are characteristic of rubbery and liquid states. The glass transition temperature is very important as it has a strong effect on the mechanical properties of the polymer. In addition, the chemorheology and internal stresses of a thermoset are influenced by T_g [162, 163].

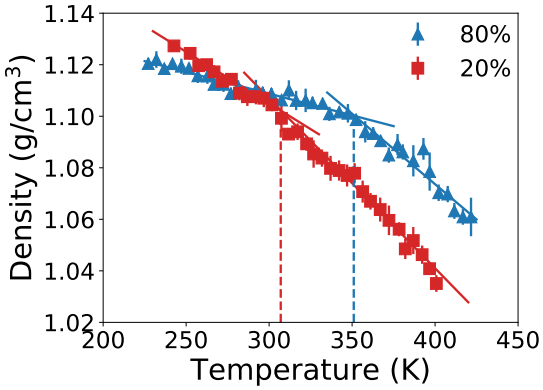

Figure 5.12: Mass density of DGEBA/Jeffamine D230 epoxy as a function of temperature at 20% (red squares) and 80% (blue triangles) conversions. Results obtained from MD simulations using the DREIDING FF. Data points and error bars represent the mean and standard deviation in 50 ps windows during the cooling process, which had a total duration of 2 ns.

The glass transition temperature can be obtained from MD by computing the mass density as a function of temperature. A bilinear response is expected with different slopes in the high temperature (rubbery regime) and low temperature (glassy regime). The temperature at which these two slopes intersect is T_{g}. To obtain the density versus temperature curves, an MD simulation is performed under NPT conditions at atmospheric pressure and with a temperature gradually varying from 450 K to 250 K. The duration of the simulation is 2 ns, which corresponds to a cooling rate[1] of 10^7 K/s. As the temperature is lowered, the mass density is computed in 10 ps intervals over a window of 10 ps. The results obtained with the DREIDING FF for 20% and 80% conversions are shown in Fig. 5.12. Both curves exhibit a bilinear response with a significant change in slope. T_{g} is determined by finding the intersection between linear regression fits to the data points above and below the slope change. The results are $T_{\mathrm{g}} = 349$ K at 80% conversion, and $T_{\mathrm{g}} = 307$ K at 20% conversion.

An interesting observation in Fig. 5.12 is that systems with a lower degree of conversion have a larger temperature induced volume change, which is consistent with the

[1]This high cooling rate is necessary due to the high computational cost of the simulations, but is accounted for theoretically as explained below.

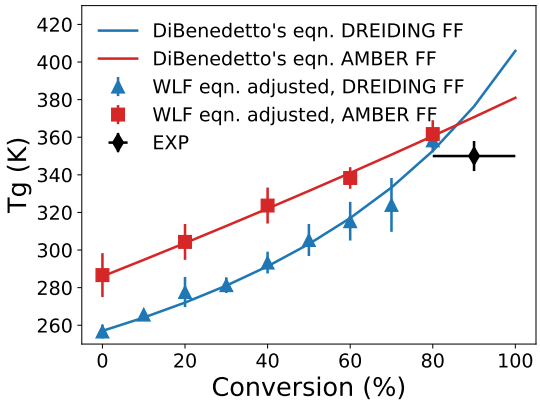

Figure 5.13: T_g as a function of conversion obtained by the AMBER FF (red squares) and the DREIDING FF (blue triangles). The simulation results are adjusted by the WLF equation and also fit to the DiBenedetto's equation (Eq. (5.5)) with least squares. The experimental T_g is shown as a range at high conversion (80%–100%) [13,14]. Error bars represent the standard deviation of three independent simulations.

results shown in Fig. 5.9. The reason for this behavior is related to the topology of polymer chains at different crosslinking conversions. A system with 20% conversion has more uncrosslinked free-moving short chains that can reorient into a condensed structure at lower temperatures. In contrast, at higher temperatures, the uncrosslinked short chains result in greater volume expansion. Thus the density of 20% conversion system is higher than that of the 80% system at lower temperature, but lower than the 80% system at higher temperature. Similar observations are obtained in experiments [164–166] and previous MD simulations [142] for related systems.

In order to compare the values of T_g obtained from the MD simulations with experimental data, it is necessary to account for the cooling rate. The effect of cooling rate on T_g can be quantified using the classical William–Landel–Ferry (WLF) equation [141,167–169], which is an empirical relation based on extensive experimental measurements on various systems ranging from polymers to organic liquids. The WLF equation predicts an increase of 3 K in T_g per order of magnitude increase in the cooling rate. Thus T_g predicted by our MD simulations with a cooling rate of 10^7 K/s should be 24 K higher than the experimental value (corresponding to an experimental cooling

rate of 20 K/min [14] or about 0.1 K/s). Fig. 5.13 presents the MD simulation results adjusted by the WLF equation compared with experimental data for fully crosslinked DGEBA/Jeffamine D230 epoxy due to Park and Qian *et al.* [13] 347–356 K, and Lee *et al.* [14] 344–352 K. The T_g values predicted by AMBER are higher than those predicted by DREIDING, but both FFs are in good agreement with each other and with experimental data at 80% conversion.

Theoretical studies of the dependence of T_g on crosslinking conversion have been carried out by Nielsen *et al.* [170], Dibenedetto [171], and Couchman [172]. Pascault *et al.* [173] showed that these approaches are equivalent if the thermosetting polymer is considered an equivalent random mixture of initial reactants and a fully-reacted network. Dibenedetto's analysis leads to the following relation,

$$\frac{T_g - T_g^0}{T_g^\infty - T_g^0} = \frac{\lambda\xi}{1-(1-\lambda)\xi}, \tag{5.5}$$

where λ is an adjustable parameter between zero and one that describes nonlinearity in the T_g–conversion curve, ξ is the degree of conversion, T_g is the glass transition temperature at conversion ξ, and T_g^0 and T_g^∞ are the glass transition temperatures at conversions of 0% and 100%, respectively. Eq. (5.5) is fit to the MD T_g results using least squares, and plotted in Fig. 5.13. The agreement is excellent. By using DiBenedetto's equation, T_g can be extrapolated to higher conversions, which is difficult to achieve with MD simulations.

5.3.3 Mechanical response to uniaxial tension and simple shear

The mechanical properties of DGEBA/Jeffamine D230 epoxy at 300 K are studied using non-equilibrium MD simulations of uniaxial tension and simple shear. These simulations are performed by continuously changing the shape of the simulation box at a constant strain rate in the direction of the deformation, while maintaining atmospheric pressure in other directions. The components of the stress (e.g. σ_{zz} for uniaxial tension in the z-direction, or σ_{xy} for the shear stress in the xy-plane) are recorded at every step. Fluctuations in the stress (which are relatively large due to the small system size) are smoothed out using a Savitzky–Golay filter [174], which is designed to increase the signal-to-noise ratio without significantly distorting the signal.

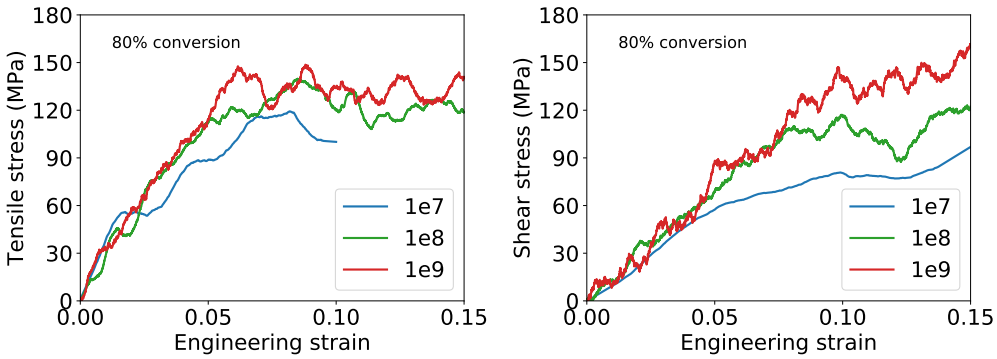

(a) (b)

Figure 5.14: Stress strain curves of for samples with 80% conversion under (a) uniaxial tension and (b) simple shear, obtained from MD simulations using the DREIDING FF at three strain rates (10^7, 10^8, and 10^9 s^{-1}). The results are smoothed by a Savitzky–Golay filter.

Role of strain rate

Epoxy samples at 80% conversion are deformed past their yield point in uniaxial tension and simple shear at three different strain rates (10^7, 10^8, and 10^9 s^{-1}). Although these rates are much higher than experiments, they are typical for MD simulations [141, 145, 175–177]. At 80% conversion, the polymer is highly networked and exhibit almost no strain-rate dependence during the initial elastic regime as shown in Figs. 5.14a and 5.14b. However, the yield and shear strengths show an increase with strain rate in agreement with experiments [178,179] and MD simulations [141,145] in similar systems. The reason is that at high strain rate certain relaxation mechanisms do not have sufficient time to activate during the loading process. Similar behavior occurs in crystalline systems as has been demonstrated for Ni nanopillar systems using an "equilibrium map" approach that exhaustively identifies and tracks the range of possible deformation mechanisms from which the rate-dependent response can be constructed [180].

Role of conversion

Uniaxial tension and simple shear simulations are performed at 300 K up to a strain of 20% with a constant strain rate of 10^8 s^{-1}. Separate simulations are performed along

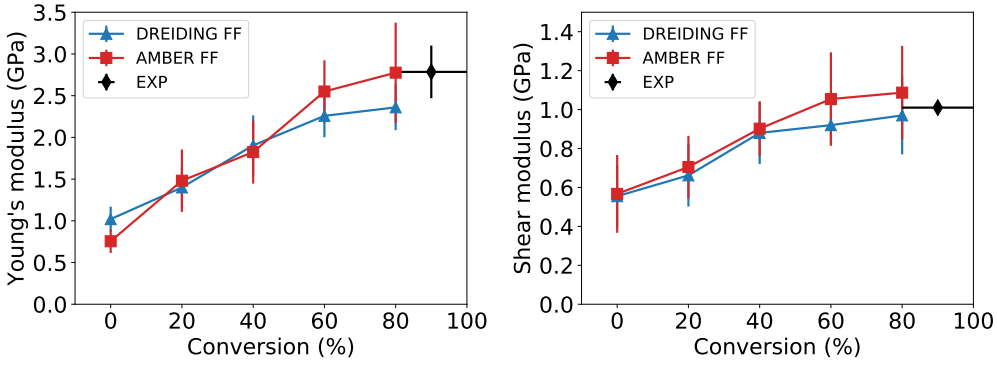

(a) (b)

Figure 5.15: (a) Young's modulus as a function of crosslinking conversion. The black diamond represents the experimental results [13, 15–17]. (b) Shear modulus as a function of crosslinking conversion. Error bars correspond to the standard deviation of simulations in three deformation directions of three independent configurations.

the x, y, and z-directions for uniaxial tension, and on the xy, xz, and yz planes for simple shear, for three independent samples at each conversion. Young's modulus and the shear modulus are calculated by linear regression from the normal/shear stress–strain curve from 1% to 4% strain. The results are presented in Fig. 5.15. Both Young's modulus and the shear modulus increase with conversion up to the gel point (about 60% conversion) and then saturate at high conversion. The saturation value for Young's modulus predicted by the AMBER FF is in good agreement with experimental values for fully-crosslinked DGEBA/Jeffamine 230 epoxy, which are in the range of 2.47–3.10 GPa [13, 15–17]. Experimental data for the shear modulus for the same epoxy system was not found. The saturation value for the shear modulus predicted by the AMBER FF is in good agreement with the measured value for a similar epoxy, which is 1.01±0.02 GPa [181]. The DREIDING FF values are lower than those of AMBER across the conversion range. The numerical values from MD and experiments are presented in Table 5.4.

The yield strength and shear strength as a function of conversion are shown in Fig. 5.16. Both increase with conversion and decreasing mobility of the polymer chains. The experimental yield strength of DGEBA/Jeffamine D230 epoxy is in range 57.1–91.8 MPa [15, 17] measured at strain rates in the range of 5.7×10^{-4} to 8.3×10^{-3} s^{-1}.

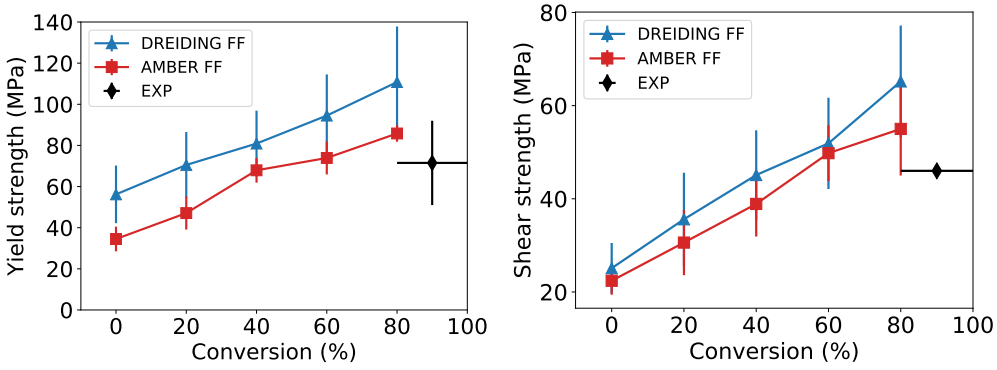

(a) (b)

Figure 5.16: (a) Yield strength as a function of crosslinking conversion. The black diamonds represents the experimental results [15,17]. (b) Shear strength as a function of crosslinking conversion. Error bars correspond to the standard deviation of simulations in three deformation directions of three independent configurations.

The experimental shear strength of a similar epoxy is 46 MPa [181]. The strain rate at which the experiment was performed is not reported. The MD values are computed at a much higher rate of 10^8 s^{-1} and are therefore expected to be larger than the experimental values. The AMBER value of the yield strength is at the top of the experimental range, and DREIDING is a bit larger. Numerical values at the maximum conversions studied are presented in Table 5.4.

5.4 Conclusion

MD simulations are performed to investigate the thermomechanical properties of the DGEBA/Jeffamine D230 epoxy system at different temperatures and crosslinking conversions using the DREIDING and AMBER FFs. Epoxy samples with different degrees of conversion are generated using a multistep crosslinking relaxation methodology. In this approach, new bonds are created whenever two predefined active sites move within a threshold distance of each other. The method yields crosslinked samples at a desired level of conversion without having to simulate the details of the chemical reactions during the curing process. Using the generated samples, MD simulations are performed to

Table 5.4: Mechanical properties of DGEBA/Jeffamine D230 epoxy predicted by the DREIDING and AMBER FFs for samples with 80% conversion at 300 K at a strain rate of 10^8 s^{-1}, compared with experimental results obtained at strain rates in the range 5.7×10^{-4} to 8.3×10^{-3} s^{-1}.

Source	Young's modulus (GPa)	Shear modulus (GPa)	Yield strength (MPa)	Shear strength (MPa)
DREIDING	2.360 ± 0.273	0.972 ± 0.098	110.8 ± 27.2	65.2 ± 12.7
AMBER	2.776 ± 0.604	1.087 ± 0.170	85.8 ± 4.3	63.9 ± 9.96
Experiment	2.47–3.10 [13, 15–17]	1.01±0.02 [181]	57.1–91.8 [15, 17]	46 [181]

compute crosslinking-induced volume shrinkage, mass density, gel point, glass transition temperature, elastic moduli and yield strengths. The dependence of these properties on conversion and temperature are investigated. The simulation results are compared to theoretical models and available experimental data, as well as MD simulations for similar epoxy systems. Key results for DGEBA/Jeffamine D230 epoxy include:

- The generated epoxy structure (for a high conversion of 87%) is validated by comparing calculated RDF and XRD structure factor curves with experimental measurements for similar systems. The agreement is excellent showing RDF peaks at experimental bond lengths, and a structure factor with a single broad peak centered on $2\theta = 18°$.

- The predicted volume shrinkage at 300 K for a 80% conversion relative to the uncured state are 2.22% (DREIDING) and 2.79% (AMBER), which lie in the experimentally measured range of 2.0–5.3%.

- The predicted mass density at 300 K is 1.126 ± 0.0015 g/cm^3 (DREIDING) and 1.073 ± 0.003 g/cm^3 (AMBER), in reasonable agreement with an experimental value of 1.156 ± 0.002 g/cm^3.

- The predicted gel point is around 60% conversion using both FFs, which is in a good agreement with a theoretical prediction for the gel point of 57.5%. A curing

agent occupation analysis shows that the MD simulations correctly capture the stochastic process of polymer curing.

- The glass transition temperature as a function of conversion is adjusted using the classic William–Landel–Ferry equation and fitted to the Dibenedetto's equation. The adjusted predicted glass transition temperature at high conversion are 358 K (DREIDING) and 362 K (AMBER) in good agreement with experimental values which fall in the range 344–356 K.

- Uniaxial tension and simple shear simulations using both DREIDING and AMBER show that the the elastic moduli are highly strain-rate dependent at low conversion, but are strain-rate independent above the gel point. The magnitudes of the elastic moduli increase with conversion and saturate after gelation. Young's modulus at 80% conversion at 300 K is 2.360 ± 0.273 GPa (DREIDING) and 2.776 ± 0.604 GPa (AMBER), which are close to the experimental range of 2.47–3.10 GPa. The shear modulus at 80% conversion at 300 K is 0.972 ± 0.098 GPa (DREIDING) and 1.087 ± 0.17 GPa (AMBER), which are close to the experimental value of 1.01 ± 0.02 GPa.

- The simulations show that the yield strength and shear strength are highly rate dependent and increase with conversion. The predicted yield strength at a strain rate of 10^8 s^{-1} is 110.8 ± 27.2 MPa (DREIDING) and 85.8 ± 4.3 MPa (AMBER). Experimental tensile strength for strain rates in the range of 5.7×10^{-4} to 8.3×10^{-3} s^{-1} are 57.1–91.8 MPa. The predicted shear strength is 65.2 ± 12.7 MPa (DREIDING) and 63.9 ± 9.96 MPa (AMBER). The experimental shear strength is 46 MPa. Given the very high strain rates in the MD simulations, higher strengths are expected.

We conclude that MD simulation are an effective tool for studying the thermomechanical properties of thermosetting epoxy systems. The simulations capture the stochastic process of crosslinking and predict properties in good agreement with experiment. Further, the MD simulation are able to track the evolution of properties throughout the curing process, which is difficult to obtain experimentally. Overall, we find the accuracy of the DREIDING and AMBER FFs to be comparable, with a slight advantage to AMBER in predicting mechanical properties.

It is also important to note two major limitations of using MD to study the thermomechanical behavior of polymeric materials. The first is related to the limited time and length scales accessible to MD simulations due to the computational cost. As a result, strain rate in MD is extremely high, many orders of magnitude larger than typical experiments, which can lead to significant differences in some properties (e.g. yield strengths) due to the viscoplastic nature of polymers. The small sample size used in MD simulation can lead to a large variability in results. It is therefore important to perform multiple simulations in order to obtain good statistics. The second limitation is related to the method used to create cross-linked samples. The proposed method is effective, but due to computational limitations cannot reach full crosslinking with 100% conversion leaving some active atoms with missing hydrogens in the system.

Chapter 6

Molecular Dynamics Based Cohesive Zone Law for Describing an Epoxy-Graphene Interface Mechanics

Molecular dynamics (MD) simulations are performed to obtain mode I and II fracture energies and cohesive laws for interfaces formed between DGEBA/Jeffamine D230 epoxy and single-layer graphene (SLG), multilayer graphene (MLG), and multilayer graphene oxide (MLGO). The elastic moduli and ultimate tensile and shear strengths of epoxy–graphene interfaces are calculated from uniaxial tension and simple shear loadings. The results show that Young's modulus and the ultimate tensile strength increase relative to bulk epoxy, whereas the shear modulus and ultimate shear strength are reduced. Failure of epoxy–graphene interfaces in tension occurs due to the formation of voids in the epoxy. Failure in shear is due to tangential slipping at the interface. Under mixed mode conditions, the shear modulus and shear strength decrease with increasing tensile load. The critical energy release rate G_c for the studied epoxy–SLG/MLG/MLGO systems are obtained using a continuum fracture mechanics approach and are found to be significantly lower than for bulk epoxy. All of the results are combined to define mode I and II cohesive laws for epoxy–SLG/MLG/MLGO interfaces that can be used in

theoretical models and numerical methods, such as finite elements, that employ cohesive zones.

6.1 Introduction

Fracture toughness is a vitally important property for thermosetting polymers such as epoxy. These materials are inherently brittle due to their highly crosslinked structure, which means that a small crack can lead to catastrophic failure. However, increasing fracture toughness by reducing crosslink density is impractical since that would also reduce the stiffness and heat distortion temperature of the material [182]. Instead toughening agents are often added to the thermosetting resin to improve fracture resistance. Despite the great success of polymeric tougheners such as reactive liquid rubbers, core-shell rubbers, and block copolymers, researchers have suggested that inorganic nanofillers (e.g. graphene-based materials, carbon nanotubes, nanoclays, and nanosilicas) could better serve as resin tougheners since they strengthen the matrix without reducing its elastic stiffness and glass transition temperature [183–185]. Among these nanofillers, graphene-based materials show great promise due to their high in-plane strength and Young's modulus, and excellent thermal and electrical properties [186–188]. Due to the high aspect ratio of graphene, substantial property enhancements can be achieved at small graphene loading (0.5 wt% or less) [13, 189–193]. At such small loadings, the base resin viscosity and glass transition temperature are largely unaffected [194]. These characteristics make graphene-based nanofillers an attractive option for resin toughening.

The toughening mechanisms associated with inorganic nanofillers are complex and not fully understood. For graphene-based thoughening they are thought to be related to crack pinning and debonding effects [13]. For wire-shaped nanofillers, such as carbon nanotubes, interfaces can be studied using a microdroplet test. In this experiment, a length of carbon nanotube is pinned by a drop of epoxy resin cured on it and is then pulled out [195]. The interfacial shear strength can be backed out from the pullout force. Such an approach is more difficult for graphene, due to its high-aspect ratio. Instead

high-fidelity molecular dynamics (MD) simulations can be performed to obtain interfacial properties and study failure mechanisms. Li et al. [196] characterized the interfacial properties of epoxy–multilayer graphene interfaces for two configurations (graphene aligned with or vertical to the interface) showing that in both cases the addition of graphene increased the tensile strength compared with bulk epoxy. Rahman et al. [197] computed Young's modulus and the pullout force in epoxy–graphene nanocomposites and found a 25–40% increase in modulus compared with bulk epoxy. The tribological properties [198] and thermal conductivity [199] of epoxy–graphene interfaces and the influence of graphene defects [200, 201] have also been studied with MD simulations.

In the current work, MD simulations are performed to measure interfacial properties of epoxy and single-layer graphene (SLG), multilayer graphene (MLG), and multilayer graphene functionalized by oxygen (MLGO) in tension and shear. The epoxy system studied corresponds to a diglycidyl ether of bisphenol A (DGEBA) resin with a Jeffamine D230 curing agent. MD simulations of uniaxial tension and simple shear loading are performed to obtain mechanical properties under mode I, mode II and mixed-mode conditions. Computed properties include Young's modulus, the shear modulus, ultimate tensile and shear strengths, and the nanofiller effect on epoxy mass density near the interface. A continuum fracture mechanics approach is used to infer the macroscopic critical energy release rate from the atomistic measurements. These results are combined to formulate interfacial cohesive laws for tension and shear that can be used in theoretical models and numerical methods, such as the finite element method (FEM), that employ cohesive zones.

This chapter is organized as follows. In Section 6.2 the structure of epoxy–SLG/MLG/MLGO interfaces and the algorithm used to generate the epoxy crosslinked network are introduced. Section 6.3 describes the MD simulations used to obtain mechanical properties. In Section 6.4, the continuum fracture mechanics model used to compute the critical energy release rate is introduced. Section 6.5 describes the derivation of the cohesive laws. This chapter concludes in Section 6.6 with a summary of the main results.

6.2 Structure and formation of epoxy-nanofiller interfaces

Transmission electron microscopy (TEM) measurements indicate that graphene-based nanofillers are of order 10 μm in size [13]. MD simulations of systems of this size are impractical and unnecessary to obtain mean interfacial properties. Instead simulations are performed on a representative periodic cell which contains a planar patch of the nanofiller (SLG/MLG/MLGO sheet) with cross-linked epoxy above and below. The cross-linked epoxy is generated from a DGEBA resin and Jeffamine D230 with structures shown in Fig. 5.1 following the procedure outlined in chapter 5. The SLG consists of a single layer of carbon atoms in the graphene structure with an in-plane size of 54.3 Å $\times$ 55.6 Å (Fig. 6.1(a)). MLG is comprised of four SLG layers in AB stacking of size 59.6 Å $\times$ 54.1 Å (Fig. 6.1(b)). The chemical structure of GO is still an open question due to its amorphous berthollide character and the lack of precise analytical techniques for characterizing different chemical groups. Depending on the processing conditions at least five different structures of GO have been proposed in which the oxygen atoms can be appear in epoxide groups (C-O-C) or hydroxide groups (C-OH) [202, 203]. It has been shown that GO is metastable and undergoes spontaneous chemical evolution to a quasiequilibrium state with a reduced O/C atomic ratio of 0.38. However, the relaxation is a long process (about 35 days at room temperature) [204]. In this work, we use the experimentally observed O/C atomic ratio of 0.5 [13] and assume a simplified structure in which oxygens are only present in epoxide groups with half the oxygen atoms on each side of the graphene layer (Fig. 6.1(c)). Four GO layers of size 63.3 Å $\times$ 63.9 Å are stacked together to form MLGO (Fig. 6.1(d)).

Numerical curing of the epoxy matrix in the presence of SLG/MLG/MLGO is performed using the procedure described in chapter 5; only key points are repeated here. During curing, epoxide groups in a DGEBA molecule react with amines in a Jeffamine D230 molecule to gradually form a network structure. Instead of simulating the actual chemical reactions that take place during this process, an ad hoc multistep method is used in which nitrogen and carbon atoms initially labeled as "active" form bonds when they move within a threshold radius in a preliminary MD simulation. The first step is to build an equilibrated mixture of the resin and curing agent. On each side of the SLG/MLG/MLGO nanofiller, 27 Jeffamine D230 monomers with $n = 2$, 27 Jeffamine

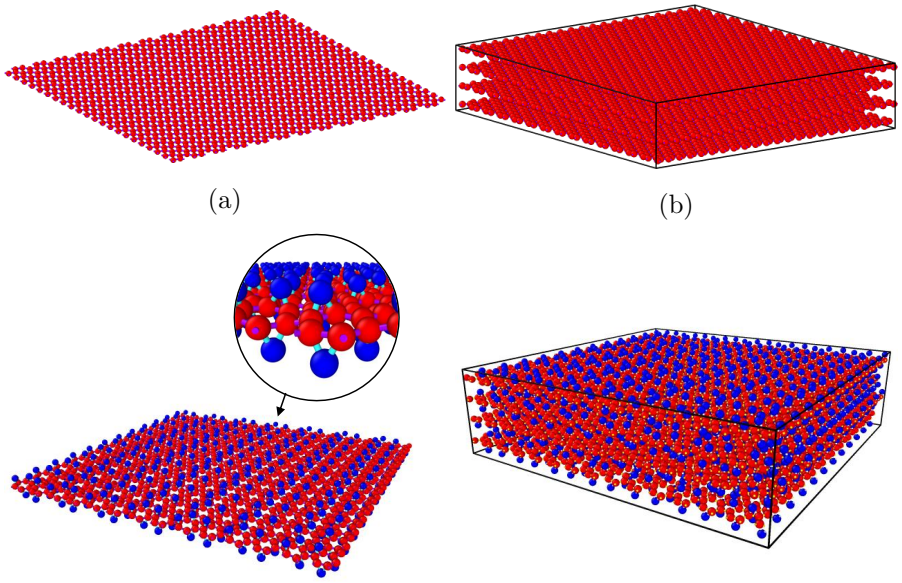

Figure 6.1: (a) Single-layer graphene (b) Multilayer graphene formed by stacking four layers of single-layer graphene in an AB pattern. (c) Single-layer graphene oxide with each carbon (red) bonded to oxygen (blue). (d) Multilayer graphene oxide comprised of four stacked layers of (c). Covalent bonds between atoms are shown as thick lines. Figures generated using OVITO [6].

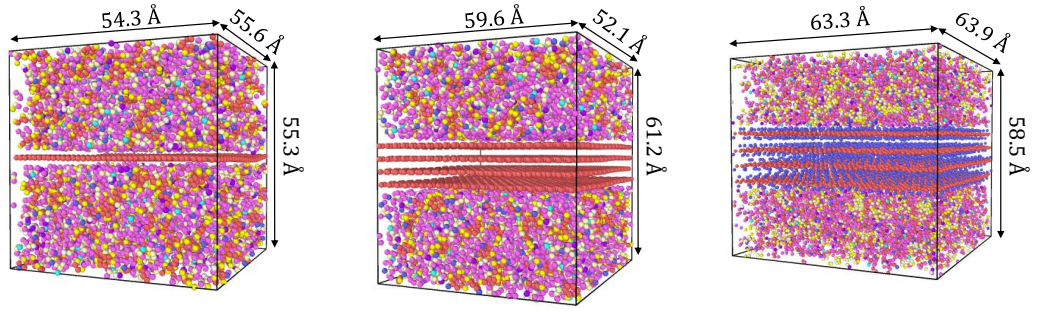

(a) (b) (c)

Figure 6.2: Interfacial DGEBA/Jeffamine D230 epoxy and (a) single-layer graphene, (b) multilayer graphene, and (c) multilayer graphene oxide. Figures generated using OVITO [6].

D230 monomers with $n = 3$, and 108 DGEBA monomers are added. An MD simulation is performed in the canonical ensemble (NPT) at a temperature of 450 K and atmospheric pressure for 100 ps to equilibrate the system. The crosslinking alogrithm is initiated and the simulation continues until the target conversion is reached (80% in this work). Following this the temperature is gradually reduced from 450 K to 300 K over a period of 100 ps. The process concludes with a final equilibration phase at 300 K for 100 ps. Epoxy–SLG/MLG/MLGO systems with 80% conversion are shown in Fig. 6.2. The crosslinked epoxy structure generated using this approach has been validated in chapter 5 by comparing the predicted radial distribution function and X-ray diffraction pattern with experimentally measured values.

All MD simulations are performed using LAMMPS [146] with the AMBER force field [39]. Van der Waals interactions are modeled using a 12/6 Lennard-Jones pair potential with inner and outer cutoff radii of 8 Å and 12 Å. Temperature is maintained using a Nosé–Hoover thermostat [148] with a 100 fs coupling constant, and pressure is maintained with a Nosé–Hoover barostat [147] with a 1000 fs coupling constant. Three independent samples are generated for each interface system to obtain a statistical average and standard deviation for predictions.

6.3 Properties of epoxy–SLG/MLG/MLGO interfaces

6.3.1 Mass density

The bonds that form during curing pull end groups together and gradually convert the initial liquid phase into a crosslinked solid. This process leads to reduction in volume because molecules move from a van der Waals distance of separation to a covalent distance of separation. Epoxy density profiles in epoxy–SLG/MLG/MLGO structures with conversions of 0% and 80% at 300 K are shown in Fig. 6.3. Van der Waals interactions between the epoxy and the close-packed graphene-based material create a density oscillation area (green) near the nanofillers (pink). Atoms from the epoxy structure pack near the graphene surface due to the attractive van der Waals interactions and form a local density maximum. The first layer of packed epoxy leads to an exclusion region (a local density minimum) due to short-range repulsion. The effect of the graphene surface diminishes with increasing distance and the oscillations decay rapidly. At higher conversion, the mobility of atoms decreases, and hence the oscillation region shrinks from 0.8–0.9 nm at 0% conversion to 0.65–0.7 nm at 80% conversion. Our results are in good agreement with previous MD simulations of epoxy–MLG interfaces [196]. The predicted average mass densities for epoxy at 300 K for epoxy–SLG/MLG/MLGO interfaces are listed in Table 6.1. The densities at 80% are in reasonable agreement with an experimental value of 1.153±0.002 g/cm^3 for DGEBA/Jeffamine D230 epoxy [5]. The volume shrinkage due to epoxy curing from 0% to 80% conversion is 2.14% for epoxy–SLG, 2.84% for epoxy–MLG, and 2.97% for epoxy–MLGO, which are in good agreement with an MD prediction of 2.79% for bulk epoxy and experimental values which are in the range of 2.0%–5.3% [205].

6.3.2 Mechanical response under uniaxial tension

To study the mechanical response of epoxy–SLG/MLG/MLGO interfaces under deformation, uniaxial tension and simple shear simulations are performed on systems with 80% conversion at 300 K. For uniaxial tension, the periodic box is stretched in the direction normal to the nanofiller at a constant strain rate of 10^8 s^{-1} while maintaining atmospheric pressure in the other two directions. Plots of the true stress (Cauchy stress) versus engineering strain are shown in Fig. 6.4 with results from our previous MD

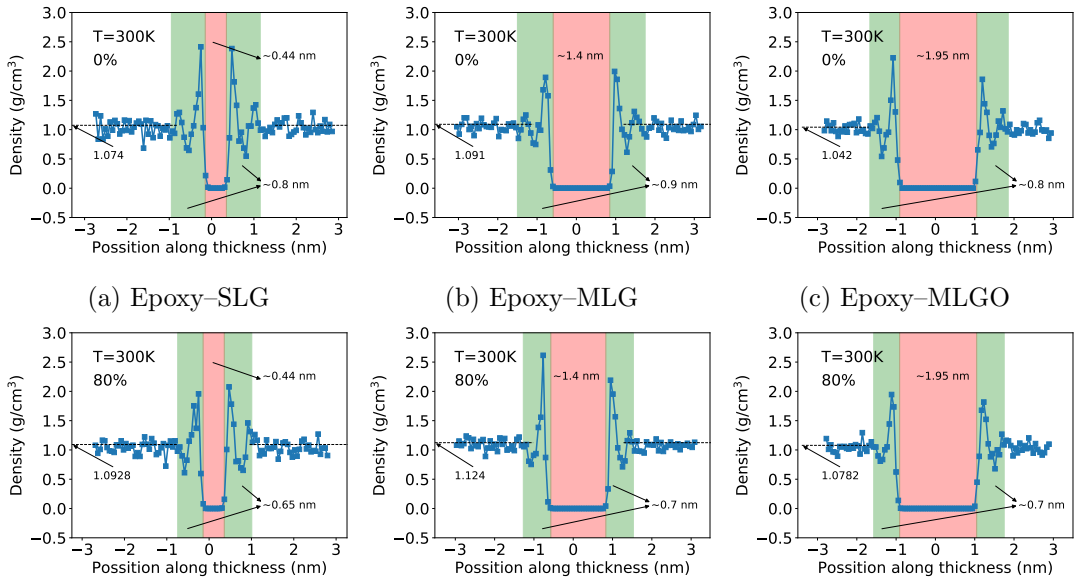

(a) Epoxy–SLG (b) Epoxy–MLG (c) Epoxy–MLGO

(d) Epoxy–SLG (e) Epoxy–MLG (f) Epoxy–MLGO

Figure 6.3: Epoxy density profiles in the direction normal to the interface in epoxy–SLG/MLG/MLGO with a conversion of (a)-(c) 0% and (d)-(f) 80% at 300 K and atmospheric pressure.

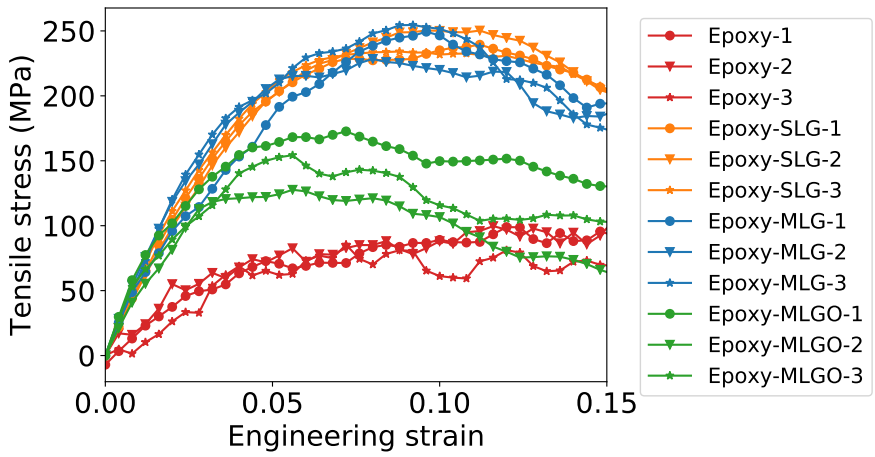

Figure 6.4: Tensile stress–strain curves obtained from MD simulations of uniaxial tension in the direction normal to the interface for epoxy–SLG/MLG/MLGO systems compared with bulk epoxy.

Table 6.1: The average mass density of epoxy in the epoxy–SLG/MLG/MLGO interfaces compared with the density of bulk epoxy obtained from MD simulations and experiments [5] at 300 K and atmospheric pressure. Unit in g/cm^3.

	Config. 1	Config. 2	Config. 3	Ave.	Exp.
Bulk epoxy (0%)	-	-	-	1.043±0.005	-
Epoxy–SLG (0%)	1.074	1.072	1.074	1.073±0.001	-
Epoxy–MLG (0%)	1.091	1.093	1.089	1.091±0.002	-
Epoxy–MLGO (0%)	1.048	1.042	1.046	1.045±0.003	-
Bulk epoxy (80%)	-	-	-	1.073±0.003	1.153±0.002
Epoxy–SLG (80%)	1.093	1.099	1.097	1.096±0.032	-
Epoxy–MLG (80%)	1.124	1.130	1.111	1.122±0.010	-
Epoxy–MLGO (80%)	1.074	1.078	1.077	1.076±0.002	-

simulation for bulk epoxy included for comparison. The systems containing the interface are stiffer than bulk epoxy. This is captured by Young's modulus for the different systems listed in Table 6.2 and shown graphically in Fig. 6.5(a), which is computed by fitting a straight line to the curves in Fig. 6.4 over a strain range of 0.005 to 0.025. All three interface systems have a similar Young's modulus, which is close to double that of bulk epoxy. The ultimate tensile strength of the interface systems is taken to be the maximum true stress prior to failure. These values are listed in Table 6.3 and shown graphically in Fig. 6.5(b) along with the yield strength[1] of bulk epoxy. The presence of the interface increases the tensile strength relative to bulk epoxy by 65–180% with values for epoxy–SLG/MLG larger than those for epoxy–MLGO. Our results are in good agreement with previous MD simulation results for a similar system [196].

Snapshots of the epoxy–MLG interface under uniaxial tension at strains of 0.04, 0.08, 0.12 and 0.16 are presented in Fig. 6.6 showing the formation of a void at the

[1]Bulk epoxy has a qualitatively different response than the interfacial systems studied here. Bulk epoxy exhibits an initial elastic–perfectly plastic response with a low yield strength associated with the formation and extension of a craze region. At the end of this process, at strains approaching 300%, the stress begins to rise again as covalent bonds are stretched reaching a very high ultimate tensile strength more than an order of magnitude larger than the interfacial systems. For comparison purposes, the initial yield strength of bulk epoxy is more relevant.

Table 6.2: Young's modulus for epoxy–SLG/MLG/MLGO interfaces at 300 K and atmospheric pressure compared with bulk epoxy. Units in GPa.

	Config. 1	Config. 2	Config. 3	Ave.	Change
Bulk epoxy	-	-	-	2.78±0.6	-
Epoxy–SLG	5.07	4.77	5.32	5.05±0.3	81.2%
Epoxy–MLG	6.02	4.69	5.85	5.52±0.7	98.6%
Epoxy–MLGO	6.13	4.01	6.24	5.46±1.2	96.4%

Table 6.3: Ultimate tensile strength of epoxy–SLG/MLG/MLGO interfaces at 300 K and atmospheric pressure compared with the yield strength of bulk epoxy. Units in MPa.

	Config. 1	Config. 2	Config. 3	Ave.	Change
Bulk epoxy	-	-	-	85.8±4.3	-
Epoxy–SLG	230	248	232	236.7±9.9	176.8%
Epoxy–MLG	245	253	226	241.3±13.9	181.2%
Epoxy–MLGO	117	156	151	141.3±21.2	65.3%

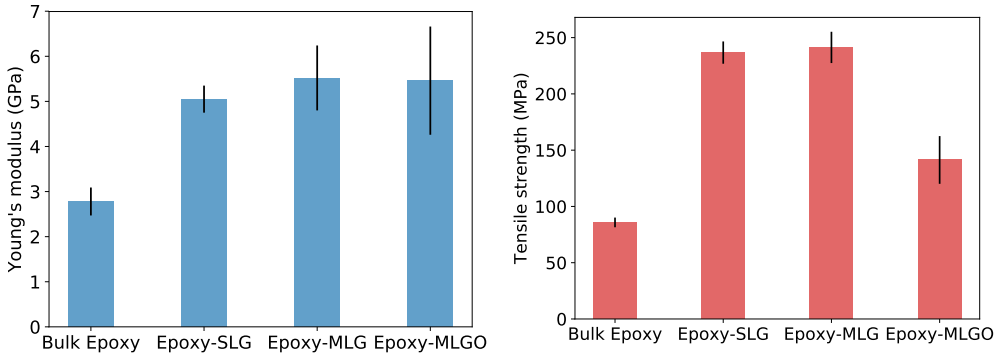

(a) (b)

Figure 6.5: Comparison of (a) Young's modulus and (b) ultimate tensile strength for epoxy–SLG/MLG/MLGO interfaces and yield strength for bulk epoxy. Error bars represent the standard deviation of three independent simulations.

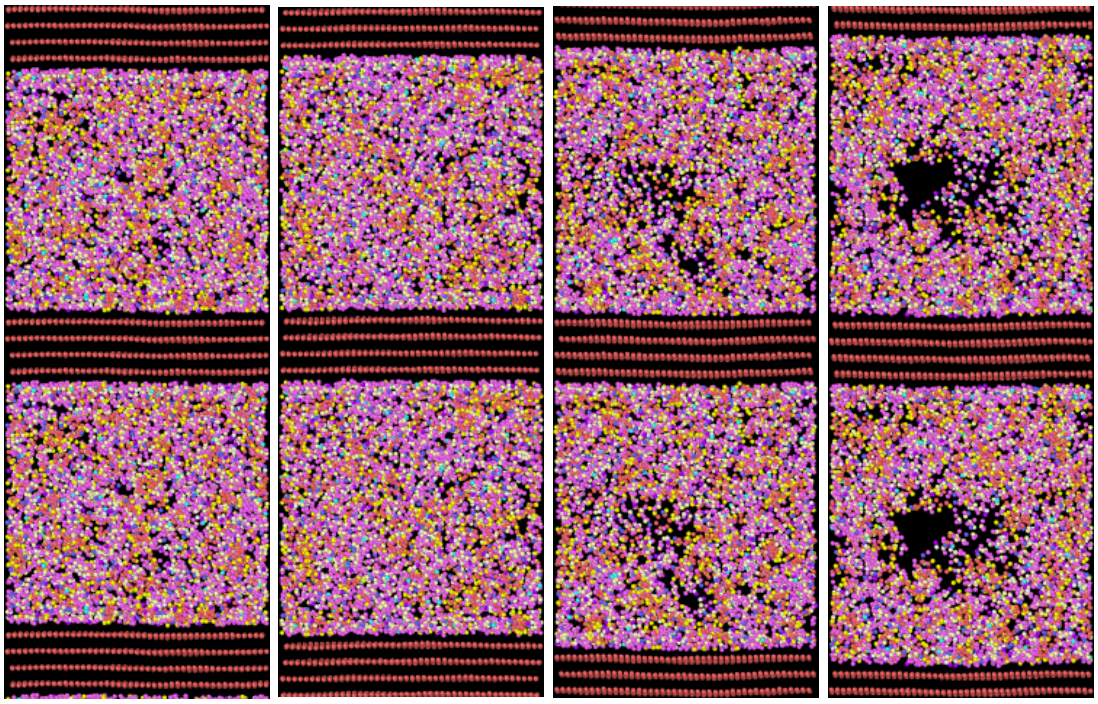

(a) strain of 0.04 (b) strain of 0.08 (c) strain of 0.12 (d) strain of 0.16

Figure 6.6: Snapshots of the epoxy–MLG interface under uniaxial tension at different strain levels. Two periodic images are displayed in the direction normal to the interface.

larger strains. Density profiles at different strains are shown in Fig. 6.7. Initially at smaller levels of strain the density decreases uniformly, however above a strain of 0.12 a local drop in density can be seen due to the formation of voids. Shrinkage of the cross-section area normal to the stretching direction is shown in Fig. 6.8. Initially, the cross-section areas decrease as the interfaces are stretched due to Poisson's effect. The shrinkage continues until the epoxy yields with the formation of voids. Further straining of the system causes the epoxy to debond from the nanofiller and leads to mechanical failure. This will be discussed in Section 6.4.

6.3.3 Mechanical response under simple shear

To explore the shear response of the interface, the periodic box is subjected to a simple shear deformation parallel to the interface in the graphene zigzag direction at a strain

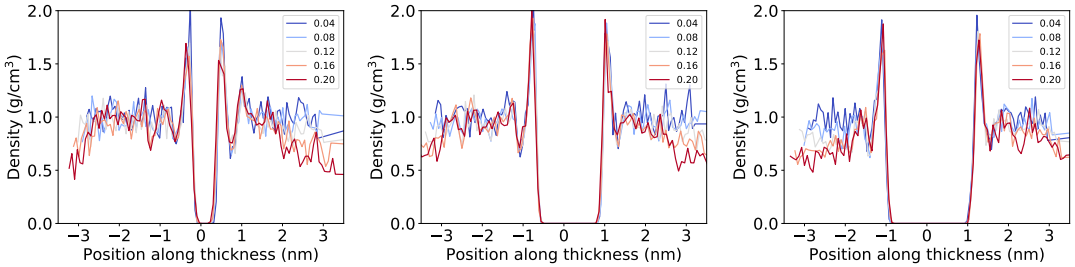

(a) (b) (c)

Figure 6.7: Mass density evolution during uniaxial tension at strains of 0.04, 0.08, 0.12, 0.16 and 0.2 for (a) epoxy–SLG, (b) epoxy–MLG, and (c) epoxy–MLGO interfaces.

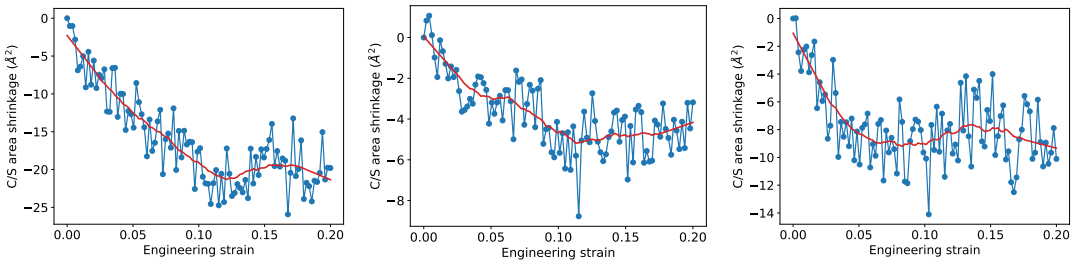

(a) (b) (c)

Figure 6.8: Cross-section area shrinkage during uniaxial tension for (a) epoxy–SLG, (b) epoxy–MLG, and (c) epoxy–MLGO interfaces.

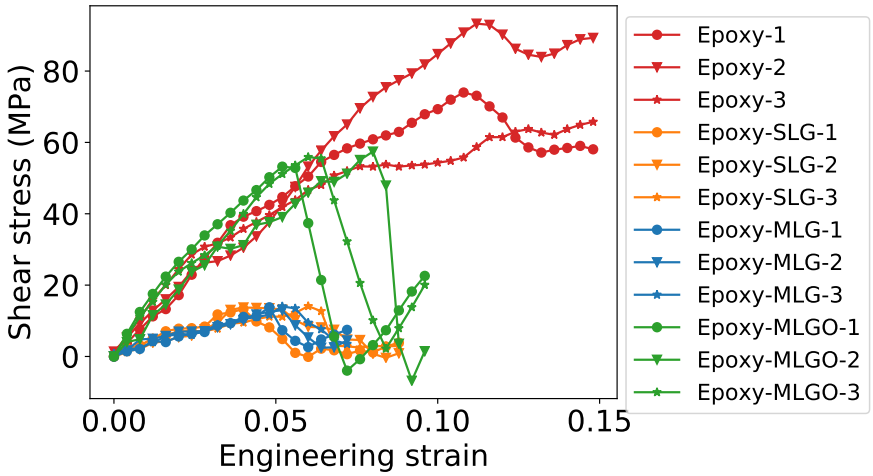

Figure 6.9: Shear stress–strain curves for MD simulations of simple shear parallel to epoxy–SLG/MLG/MLGO interfaces in the graphene zigzag direction compared with bulk epoxy.

rate of 10^8 s^{-1}. The shear stress–strain curves are shown in Fig. 6.9. The shear stress increases linearly with strain until slipping between the epoxy and nanofiller leads to a sudden drop. The epoxy–MLGO interface has a shear modulus and shear strength similar to bulk epoxy, whereas the epoxy–SLG/MLG interfaces have much lower values for both. The difference can be explained by the fact that the epoxy–MLGO interface is rough due to the presence of the oxygen atoms, whereas both the SLG and MLG interfaces are atomically flat.[2] The shear modulus is computed by fitting a straight line to the curves in Fig. 6.9 over a a strain range of 0.005 to 0.025. The results for the different systems are listed in Table 6.4 and shown graphically in Fig. 6.10(a). The shear modulus for epoxy–SLG/MLG is reduced by about 80% relative to bulk epoxy but is essentially unchanged for epoxy–MLGO. The ultimate shear strength (maximum shear stress prior to failure) measured from Fig. 6.9 is listed in Table 6.5 and displayed graphically in Fig. 6.10(b). The shear strength for epoxy–MLG is 14.6±1.3 MPa, which is in good agreement with experimental values for multi-wall carbon nanotubes and epoxy that range from 10.3 to 24.1 MPa [206].

[2]In real systems all three interfaces would exhibit additional roughness due to wrinkling, but this is not accounted for here.

Table 6.4: Shear modulus for the epoxy–SLG/MLG/MLGO interfaces at 300 K and atmospheric pressure compared with bulk epoxy. Units in GPa.

	Config. 1	Config. 2	Config. 3	Ave.	Change
Bulk epoxy	-	-	-	1.087±0.17	-
Epoxy–SLG	0.227	0.232	0.219	0.226±0.01	-79.2%
Epoxy–MLG	0.266	0.224	0.236	0.242±0.02	-77.7%
Epoxy–MLGO	1.133	1.105	0.969	1.069±0.08	-1.7%

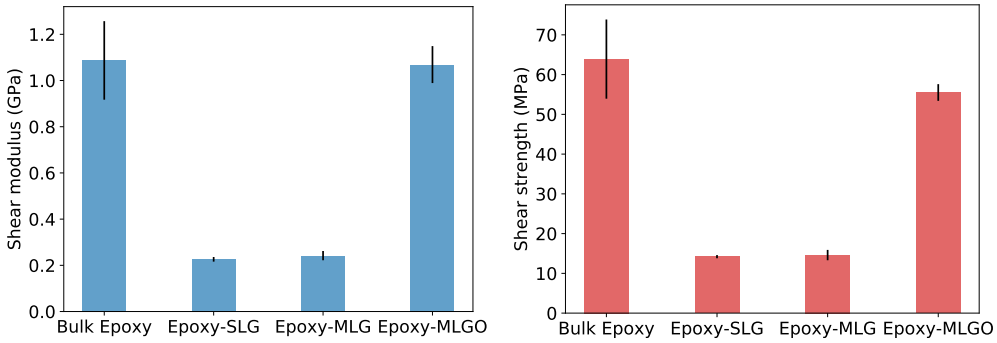

(a) (b)

Figure 6.10: Comparison of (a) the shear modulus and (b) the ultimate shear strength for epoxy–SLG/MLG/MLGO interfaces and bulk epoxy. Error bar represents the standard deviation of three independent simulations.

Shear resistance is strongly effected by the normal stress that is present under mixed-mode loading conditions. To study this effect, shear response is evaluated for different levels of applied normal strain[3] ranging from -0.03 to 0.03. The shear modulus, shear strength, and shear strain at failure γ_f under different normal strains are shown in Fig. 6.11 for epoxy–MLG/MLGO. — Since our findings indicate that SLG and MLG interfaces behave similarly, for the remainder of the chapter we only report results for MLG interfaces. — The shear modulus and the shear strength decrease linearly with normal strain, whereas the shear strain at failure is largely unaffected. Based on this, we provide the following relations for the shear modulus μ (in GPa), the shear strength

[3]In the simulations, the normal strain is applied first, followed by the shear loading.

Table 6.5: Ultimate shear strength of epoxy–SLG/MLG/MLGO interfaces at 300 K and atmospheric pressure compared with bulk epoxy. Units in MPa.

	Config. 1	Config. 2	Config. 3	Ave.	Change
Bulk epoxy	-	-	-	63.9±9.96	-
Epoxy–SLG	14.7	14.0	14.1	14.3±0.4	-77.7%
Epoxy–MLG	15.8	14.8	13.2	14.6±1.3	-77.1%
Epoxy–MLGO	53.2	55.9	57.4	55.5±2.1	-13.1%

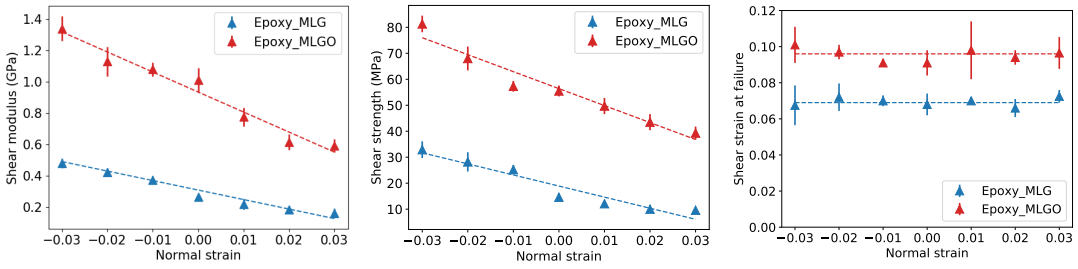

(a) (b) (c)

Figure 6.11: Shear response under mixed-mode conditions: (a) shear modulus, (b) shear strength, and (c) shear strain at failure for epoxy–MLG/MLGO interfaces under different normal strains. The error bars represent the standard deviations from three independent simulations. The results are fitted to the dashed lines with linear regressions.

τ_y (in MPa), and the failure shear strain γ_f for the MLG and MLGO systems:

$$\mu^{\mathrm{MLG}} = -6.11\epsilon + 0.31, \tag{6.1a}$$

$$\mu^{\mathrm{MLGO}} = -12.79\epsilon + 0.93, \tag{6.1b}$$

$$\tau_y^{\mathrm{MLG}} = -426.43\epsilon + 18.95, \tag{6.1c}$$

$$\tau_y^{\mathrm{MLGO}} = -651.9\epsilon + 56.39, \tag{6.1d}$$

$$\gamma_f^{\mathrm{MLG}} = 0.069, \tag{6.1e}$$

$$\gamma_f^{\mathrm{MLGO}} = 0.096, \tag{6.1f}$$

where $\epsilon \in [-0.03, 0.03]$ is the normal strain.

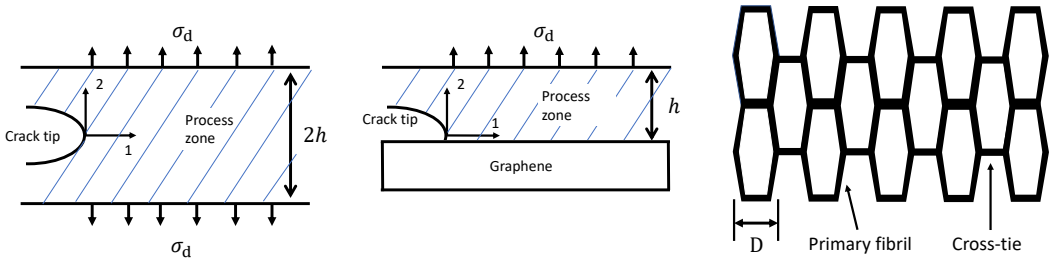

(a) (b) (c)

Figure 6.12: Schematic diagrams of (a) a semi-infinite strip model for bulk epoxy subjected to an uniform drawing stress σ_d, (b) similar to (a) for an epoxy–graphene interface, and (c) process zone fibril structure.

6.4 Fracture Energy

The fracture properties of most thermoplastic polymers are related to the stress-induced growth and breakdown of crazes. A *craze* is a load bearing region ahead of a crack where polymer chains group into fibrils normal to the crack plane. These primary fibrils are separated by gaps bridged by finer, less-stiff, transverse fibrils called *cross-ties* as shown in Fig. 6.12(c). Fracture in crazing materials involves the initial formation of a craze at a crack tip, followed by fibril breakdown and crack propagation. Although thermosetting polymers, such as epoxy, do not form large-scale crazes, the process zone at crack tips includes fibril formation and anisotropy similar to crazes in thermoplastic polymers [207]. This craze-like process zone constitutes a major source of fracture energy in epoxies. Typical values for the critical energy release rate G_c of epoxies are in the range 121–320 J/m^2 [13, 208], whereas the surface energy of epoxy is far smaller at about 0.1 J/m^2 [209, 210]. Thus fibril formation and breakdown in the process zone are critical for characterizing the fracture mechanics of epoxies.

A microstructural model for relating the average macroscopic G_c to the local breakdown of fibrils in the crack tip process zone was proposed by Brown [211] and later extended by Hui, Ruina, Kramer and coworkers [212, 213]. These approaches are equivalent for large craze thickness, which is applicable in the present case.[4] We therefore

[4]Our results yield a process zone thickness of about $2h = 200$ Å, and a fibril length of about $l \approx 10$ Å, giving a large ratio of $2h/l \approx 20$.

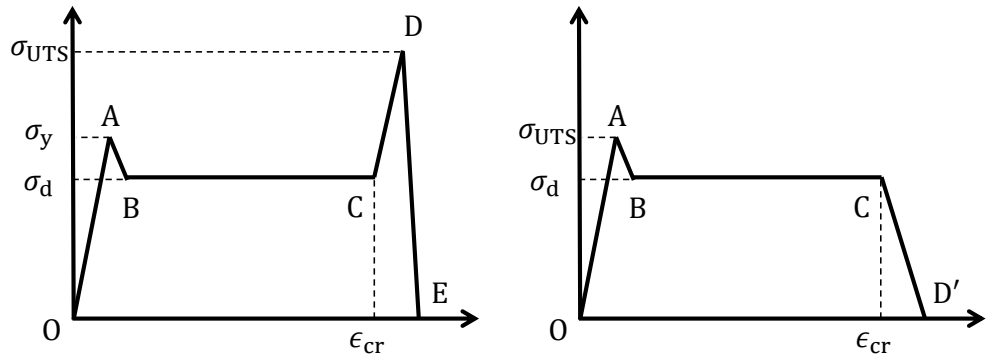

(a) (b)

Figure 6.13: Schematic stress–strain curve for (a) bulk epoxy and (b) epoxy–graphene interface.

follow Brown's approach, which is simpler, and has been used in the past to predict the macroscopic fracture energy for both thermosetting and thermoplastic polymers from MD simulations in good agreement with experiments [214, 215].

A typical schematic stress–strain curve for epoxy is shown in Fig. 6.13(a). The response consists of five regimes:

1. OA: An initial elastic response.

2. AB: Yielding and the formation of a process zone of thickness $2h_0$ consisting of voids separated by ligaments that bridge the crack.

3. BC: Stretching of the process zone at a constant "drawing stress" σ_d to create a fully-extended craze of thickness $2h = 2h_0\lambda_{cr}$, where $\lambda_{cr} = 1 + \epsilon_{cr}$ is the extension ratio at point C, and ϵ_{cr} is the normal strain in the stretching direction. The change in process zone thickness is then

$$2\Delta h = 2h - 2h_0 = 2h(1 - \lambda_{cr}^{-1}). \tag{6.2}$$

4. CD: Elastic stretching of individual craze fibrils.

5. DE: Fibril failure and resulting decohesion.

The critical energy release rate for crack extension is approximated as[5]

$$G_{\mathrm{c}} \approx (2\Delta h)\sigma_{\mathrm{d}} = 2h(1-\lambda_{\mathrm{cr}}^{-1})\sigma_{\mathrm{d}}. \tag{6.3}$$

In Eq. (6.3), σ_{d} and λ_{cr} can be measured from experiments or MD simulations, whereas $2h$ is determined through a fracture mechanics analysis.

Following Brown [211], fracture is modeled using a semi-infinite crack in an anisotropic linear elastic medium representing the fully-formed craze of height $2h$ subjected to a uniform opening stress σ_{d} as shown in Fig. 6.12(a). Assuming that the stress is fully relaxed in the fractured region far behind the crack and that the material is elastic and subjected to a uniform normal stress far ahead of the crack tip, the work for extending the crack by an infinitesimal area dA is[6]

$$g = \frac{W \times (2hdA) - 0}{dA} = 2hW, \tag{6.4}$$

where W is the strain energy density far ahead of the crack,

$$W = \frac{\sigma_{\mathrm{d}}^2}{2C_{22}}, \tag{6.5}$$

and C_{22} is the elastic constant of the craze in the fibril direction. Using Eqs. (6.4) and (6.5), the local energy release rate at the crack tip is

$$g = \frac{h\sigma_{\mathrm{d}}^2}{C_{22}}. \tag{6.6}$$

For an orthotropic material under plane strain conditions, the stress intensity factor k_{tip} is related to g by [216]

$$g = \frac{k_{\mathrm{tip}}^2}{2}\left[A_{22}(2A_{22}+2A_{12}+A_{66})\right]^{1/2}, \tag{6.7}$$

where A_{ij} are components of the compliance tensor $\boldsymbol{A} = \boldsymbol{C}^{-1}$. The process zone material is much stiffer in the fibril direction than the transverse direction ($A_{22} \ll A_{11}$) and

[5]The assumption here is that most of the fracture energy is expended in stretching the process zone to create the craze. The additional energy associated with the initial elastic response and the breaking of the fibrils is neglected.

[6]Note that in Brown's model, lower-case g (and later k_{tip}) correspond to fracture at the microscopic process zone level. This will later be related to the macroscopic energy release rate defined in Eq. (6.3).

Poisson's effect is assumed to be small ($A_{12} \ll A_{11}$). In addition it is assumed that the shear modulus is low so that A_{66} is of the same order as A_{11}. With these approximations Eq. (6.7) simplifies to

$$g = \frac{k_{\text{tip}}^2}{2}(C_{22}C_{66})^{-1/2}. \tag{6.8}$$

Equating Eqs. (6.6) and (6.8) and solving for k_{tip} gives

$$k_{\text{tip}} = \sigma_{\text{d}} \left(\frac{C_{66}}{C_{22}}\right)^{1/4} (2h)^{1/2}. \tag{6.9}$$

Consistent with the approximation in Eq. (6.3), failure is assumed to occur when the drawing stress σ_{d} causes a fibril to reach its maximum allowed stress of $\sigma_{\text{cr}}^{\text{fib}}$ (i.e. the assumption is that fracture occurs at point C in Fig. 6.13(a)). The opening stress ahead of the crack tip is given by

$$\sigma_{22} = k_{\text{tip}}(2\pi x)^{-1/2}, \tag{6.10}$$

where x is the distance from the crack tip along the 1-direction. Taking the distance to the first fibril as $x \approx D/2$, where D is the average spacing between adjacent fibrils (see Fig. 6.12(c)) gives

$$k_{\text{tip}} = \sigma_{\text{cr}}^{\text{fib}}(\pi D)^{1/2}. \tag{6.11}$$

Equating Eqs. (6.9) and (6.11), the craze thickness at fracture is

$$2h = \pi D \left(\frac{\sigma_{\text{cr}}^{\text{fib}}}{\sigma_{\text{d}}}\right)^2 \left(\frac{C_{22}}{C_{66}}\right)^{1/2}. \tag{6.12}$$

Finally, substituting Eq. (6.12) into Eq. (6.3), the macroscopic energy release rate for epoxy is

$$G_{\text{c}} = \pi D \frac{(\sigma_{\text{cr}}^{\text{fib}})^2}{\sigma_{\text{d}}} \left(1 - \frac{1}{\lambda}\right) \left(\frac{C_{22}}{C_{66}}\right)^{1/2}. \tag{6.13}$$

We extend the above analysis to epoxy–graphene systems. A typical schematic stress–strain curve for this case is shown in Fig. 6.13(b). The first three regimes are identical to those of bulk epoxy described above. The primary difference is that after the creation of the fully-extended craze at point C, failure occurs by decohesion at the van der Waals graphene–epoxy interface (CD′) instead of by breaking covalent bonds in the fibril that are much stronger.

The fracture mechanics model for the epoxy–graphene system is shown in Fig. 6.12(b). The network structure is interrupted by the presence of the graphene nanofiller. The

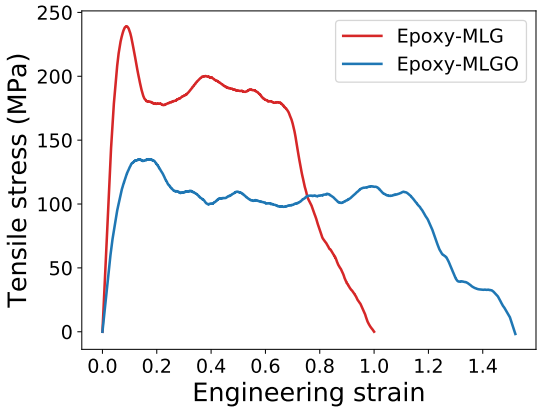

Figure 6.14: Stress–strain curves for uniaxial tension of epoxy–MLG/MLGO systems upto failure due to interfacial debonding.

regions above and below the nanofiller are independent and therefore the process zone height is taken to be h rather than $2h$. Then following a similar process to the derivation of Eq. (6.13), the critical energy release rate for epoxy–MLG/MLGO interfaces is

$$G_{\mathrm{c}}^{\mathrm{int}} = \frac{1}{2}\pi D \frac{(\sigma_{\mathrm{cr}}^{\mathrm{int}})^2}{\sigma_{\mathrm{d}}} \left(1 - \frac{1}{\lambda_{\mathrm{cr}}}\right) \left(\frac{C_{22}}{C_{66}}\right)^{1/2}, \tag{6.14}$$

where $\sigma_{\mathrm{cr}}^{\mathrm{int}}$ is the interfacial debonding stress between the epoxy and nanofiller.

The parameters in Eq. (6.14) are obtained from MD simulations in which epoxy–nanofiller interfaces are stretched until failure. The stress–strain curves are shown in Fig. 6.14. There are three regimes: (1) an initial linear elastic response (discussed in Section 6.3.2), (2) a plateau in which voids are formed in the epoxy creating a process zone, and (3) reduction of the stress to zero due to debonding between the epoxy and nanofiller. Results for the parameters are given in Table 6.7. The stretch ratio is $\lambda = 1 + \epsilon_{\mathrm{cr}}$ where ϵ_{cr} is the critical strain at which the process zone is fully developed and the stress begins to decrease. The elastic constants $C_{22} = 2.78 \pm 0.6$ GPa and $C_{66} = 1.087 \pm 0.17$ GPa are obtained from our previous MD simulation for bulk epoxy. The maximum stress $\sigma_{\mathrm{cr}}^{\mathrm{int}}$ and the average drawing stress σ_{d} are approximately the same and set equal to the average plateau stress in Fig. 6.14. The fibril spacing D is taken to be the mean spacing between voids that form during the plateau regime. In order to ensure that the measured values are converged, four epoxy–MLG/MLGO simulations

of increasing size are performed:

- System-I: 60×60 Å with 108 monomers DGEBA, 27 monomers of Jeffamine D230 with $n = 2$, 27 monomers Jeffamine D230 with $n = 3$ on each side. (This is the system used in section 6.3.2.)
- System-II: 80×80 Å with 260 monomers DGEBA, 65 monomers Jeffamine D230 with $n = 2$, 65 monomers Jeffamine D230 with $n = 3$ on each side.
- System-III: 100×100 Å with 500 monomers DGEBA, 125 monomers Jeffamine D230 with $n = 2$, 125 monomers Jeffamine D230 with $n = 3$ on each side.
- System-IV: 120×120 Å with 864 monomers DGEBA, 216 monomers Jeffamine D230 with $n = 2$, 216 monomers Jeffamine D230 with $n = 3$ on each side.

The fibril spacing D at different strains are measured using the open source code Zeo++ for analysis of porous materials [217] and are listed in Table 6.6. The average fibril spacing converges to about $D = 40$ Å, which is in good agreement with previous MD simulations for bulk epoxy which give 33.7 Å [214].

Using the parameters in Table 6.7, the critical energy release rate can be calculated from Eq. (6.14). The predicted fracture energy is $G_c^{\mathrm{MLG}} = 0.75 \pm 0.09$ J/m^2 for epoxy–MLG, and $G_c^{\mathrm{MLGO}} = 0.57 \pm 0.04$ J/m^2 for epoxy–MLGO. To our knowledge experimental values for these systems are unavailable, and therefore a direct comparison is not possible. However, our results are in line with experimental values obtained from pullout experiments of carbon nanotubes from epoxy (which include both mode I and II failure mechanisms) and are in the range of 0.44 to 0.86 J/m^2 [181].

6.5 The cohesive law

The properties computed in the previous two sections provide the ingredients for constructing cohesive laws under mode I (tension) and II (shear). This involves two steps: (1) approximation of the stress–strain curves in Fig. 6.14 by a suitable form, and (2) scaling the fracture energy to a macroscopic value through the introduction of a suitable length scale.

Table 6.6: The fibril spacing D (in Å) for different simulation cell sizes. The fibril spacing for System-I at a higher strain is not available because there is only one void in the simulation cell.

Strain	System-I	System-II	System-III	System-IV
		Epoxy–MLG		
0.2	37.0	36.9	40.0	43.2
0.3	-	34.9	43.6	40.6
0.4	-	36.6	40.1	37.2
0.5	-	37.8	38.2	36.0
Ave.	-	36.6±1.2	40.5±2.3	39.3±3.3
		Epoxy–MLGO		
0.2	34.6	36.9	39.0	39.5
0.3	-	38.7	42.7	39.4
0.4	-	38.2	42.0	41.3
0.5	-	37.3	40.5	42.1
Ave.	-	37.8±0.8	41.1±1.7	40.6±1.3

Table 6.7: Parameters obtained from MD simulations for the epoxy–MLG/MLGO critical energy release rate in Eq. (6.14).

	epoxy–MLG	epoxy–MLGO
$\sigma_{\rm cr}^{\rm int}$ (MPa)	186.6±6.9	104.1±3.5
$\sigma_{\rm d}$ (MPa)	186.6±6.9	104.1±3.5
$\epsilon_{\rm cr}$	0.69±0.02	1.13±0.04
λ	1.69±0.02	2.13±0.04
D (Å)	39.3±3.3	40.6±1.3
$(C_{22}/C_{66})^{1/2}$	1.6±0.06	1.6±0.06

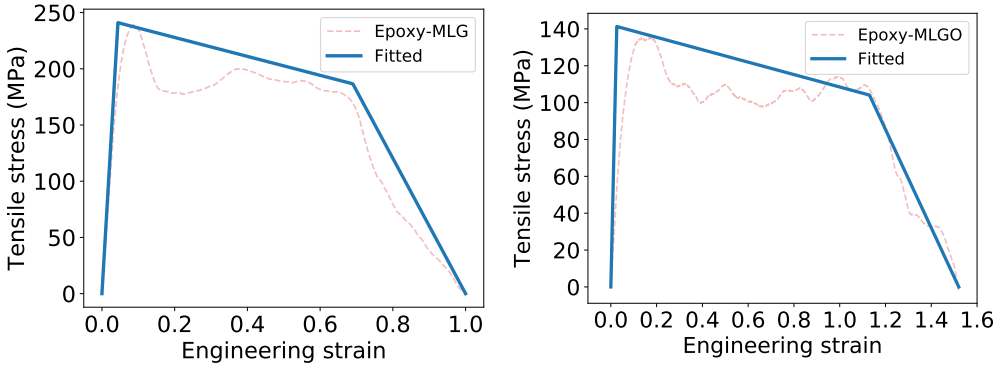

(a) (b)

Figure 6.15: Trilinear mode I cohesive law (blue lines) and the stress–strain curve obtained from MD simulations (red dashed lines) for (a) epoxy–MLG and (b) epoxy–MLGO interfaces.

For the tensile case, the stress–strain curve is approximated by a trilinear form as shown in Fig. 6.15. The first segment corresponds to the linear elastic regime which extends until the stress reaches the ultimate tensile strength ($\sigma_{\text{UTS}}^{\text{MLG}}$=241.3 MPa, $\sigma_{\text{UTS}}^{\text{MLGO}}$=141.3 MPa). The slope is Young's modulus for the interface (E^{MLG}=5.52 GPa, E^{MLGO}=5.46 GPa). The second segment corresponds to the post-yield process zone development regime. At the end of this segment the stress equals the debonding stress ($\sigma_{\text{cr}}^{\text{int}}$ listed in Table 6.7) and the strain equals the debonding strain (ϵ_{cr} listed in Table 6.7). The third segment corresponds to decohesion. The stress decreases to zero as the strain reaches the failure strain ($\epsilon_{\text{f}}^{\text{MLG}}$=1, $\epsilon_{\text{f}}^{\text{MLGO}}$=1.52). The trilinear cohesive law equations for MLG and MLGO are:[7]

$$\sigma^{\text{MLG}} = \begin{cases} 5520\epsilon & 0 \leq \epsilon \leq 0.044, \\ -81.7\epsilon + 246.7 & 0.044 \leq \epsilon \leq 0.69, \\ -602.0\epsilon + 602.0 & 0.69 \leq \epsilon \leq 1, \end{cases} \tag{6.15}$$

[7]Recall that the MLG response is also applicable to SLG as noted above.

$$\sigma^{\mathrm{MLGO}} = \begin{cases} 5460\epsilon & 0 \le \epsilon \le 0.026, \\ -34.3\epsilon + 142.9 & 0.026 \le \epsilon \le 1.13, \\ -266.9\epsilon + 405.7 & 1.13 \le \epsilon \le 1.52, \end{cases} \tag{6.16}$$

where $\sigma^{\mathrm{MLG/MLGO}}$ (in MPa) is the normal stress and ϵ is the normal strain.

In order to use Eqs. (8.5) and (6.16) in an FEM simulation it is necessary to rescale this microscopic cohesive law to a macroscopic energy scale. Different FEM codes do this in different ways. We focus on Abaqus [47] where the cohesive law is defined by specifying a traction–strain relation and a cohesive element thickness d which rescales the fracture energy [218]. We define d through the relation

$$G_{\mathrm{Ic}} = S_{\mathrm{I}} d, \tag{6.17}$$

where S_{I} is the area under the blue curve in Fig. 6.15. Using $G_{\mathrm{Ic}}^{\mathrm{MLG}} = 0.75$ J/m^2 and $G_{\mathrm{Ic}}^{\mathrm{MLGO}} = 0.57$ J/m^2, the cohesive element thickness for the epoxy–graphene interface is d^{MLG} =4.3 nm and d^{MLGO}=3.5 nm. The FEM traction–separation law then follows from Eqs. (8.5) or (6.16) by multiplying all strain values by d.

A similar procedure is used for the shear cohesive law except that a bilinear form is used to approximate the shear stress–strain response in Fig. 6.9. Another difference is that the dependence on the normal strain must be accounted for. The shear stress increases linearly with a slope equal to the shear modulus μ until reaching the shear strength τ_{y}, and then decreases linearly to zero at the failure shear strain γ_{f}. The bilinear mode II cohesive law is

$$\tau = \begin{cases} \mu\gamma & 0 \le \gamma \le \frac{\tau_{\mathrm{y}}}{\mu}, \\ \frac{\mu\tau_{\mathrm{y}}}{\tau_{\mathrm{y}} - \gamma_{\mathrm{f}}\mu}(\gamma - \gamma_{\mathrm{f}}) & \frac{\tau_{\mathrm{y}}}{\mu} \le \gamma \le \gamma_{\mathrm{f}}, \end{cases} \tag{6.18}$$

where γ is shear strain, τ is the shear stress, and μ, τ_{y}, and γ_{f} are the shear modulus, shear strength and shear strain at failure given in Eqs. (6.1a)–(6.1f) for the MLG and MLGO systems as a function of normal strain. The resulting mode II cohesive laws are shown in Fig. 6.16.

Using the values for d computed for the tensile case, the strain-dependent macroscopic mode II energy release rate is

$$G_{\mathrm{IIc}}(\epsilon) = S_{\mathrm{II}}(\epsilon) d, \tag{6.19}$$

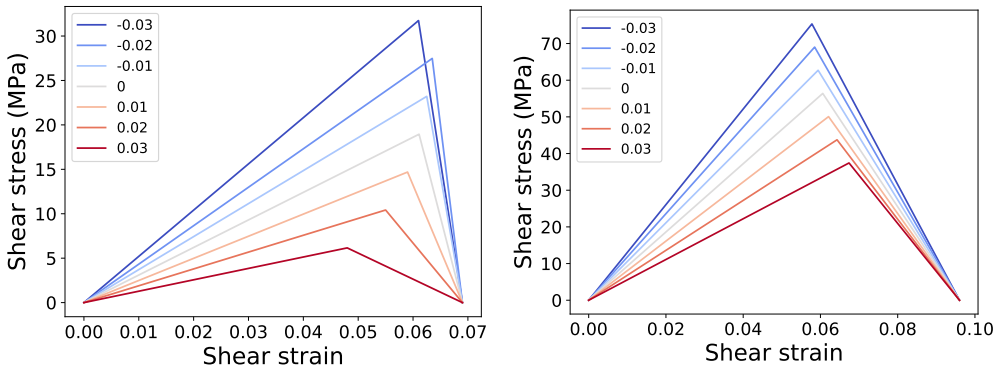

(a) (b)

Figure 6.16: Mode II cohesive law for (a) epoxy–MLG and (b) epoxy–MLGO interfaces at different normal strains ranging from -0.03 to 0.03.

where $S_{\mathrm{II}}(\epsilon)$ is the area under the shear stress–strain curve in Fig. 6.16 for a given normal strain ϵ.

For $\epsilon = 0$, $G_{\mathrm{IIc}}^{\mathrm{MLG}} = 2.26 \pm 0.06$ mJ/m^2, and $G_{\mathrm{IIc}}^{\mathrm{MLGO}} = 9.32 \pm 0.35$ mJ/m^2. The result for MLG is in line with an experimentally measured fracture energy of 2.8 mJ/m^2 for a graphene/PMMA system [219] and previous MD simulations which give 2.044 mJ/m^2 for a carbon nanotube/polyethylene system [220]. Experimental results for MLGO were not found in the literature.

6.6 Conclusion

MD simulations are performed to investigate interfacial mechanical properties for epoxy reinforced by graphene-based nanofillers: SLG, MLG and MLGO. The specific epoxy studied is formed through a multistep simulated curing process of a DGEBA resin with a Jeffamine D230 curing agent. Following annealing and equilibration, uniaxial tension and simple shear simulations are performed to obtain normal and tangential interfacial properties including interfacial elastic constants, interfacial strengths, and critical energy release rates. The results are combined to define mode I and II cohesive laws. Key findings include:

- Young's modulus is increased by 80–100% and the tensile strength is increased by

65–180% (relative to the initial yield of epoxy) due to the presence of graphene-based nanofillers. The composite fails in tension due to debonding between the epoxy and nanofiller.

- The shear modulus is reduced by about 80% for epoxy-SLG/MLG interfaces, but is unchanged for the epoxy–MLGO interface. The shear strength is reduced by 10–80%. The composite fails in shear due to localized slipping at the epoxy–nanofiller interface.

- The shear modulus and the shear strength decrease linearly with normal loading, whereas the critical shear strain at failure is largely unaffected.

- The critical energy release rate G_{Ic} for the epoxy–MLG interface is 0.75 ± 0.09 J/m^2, which is in good agreement with carbon nanotube pullout experiments. G_{Ic} for the epoxy–MLGO interface is 0.57 ± 0.04 J/m^2. Comparing these values with G_{Ic} for bulk epoxy, which lies in the range 121–320 J/m^2, the presence of nanofillers dramatically decreases the local fracture energy.

- The above results are combined to derive Mode I and II cohesive laws for epoxy–SLG/MLG and epoxy–MLGO interfaces (see Eqs. (8.5), (6.16) and (6.18)). A cohesive element thickness d is obtained that scales the fracture energy to macroscopic conditions: $d^{\mathrm{MLG}} = 4.3$ nm and $d^{\mathrm{MLGO}} = 3.5$ nm.

Future work includes employing the cohesive laws obtained in the current work in FEM simulations to study the fracture toughness of epoxy–graphene composites in a systematic manner. Interest lies in the influence of graphene-based nanofillers (as local weak points) on the overall increase of fracture toughness for epoxy–graphene composites.

Chapter 7

Rescaling Cohesive Element Properties for Mesh Independent Fracture Simulations

In finite element simulations of fracture, cohesive elements introduce artificial compliance into the model leading to changes in properties such as the effective stiffness, effective speed of sound, and crack propagation speed. In this chapter, the relation between effective material properties and cohesive element properties is determined analytically. Based on this, a simple method for rescaling the cohesive element thickness is proposed to reduce the effect of artificial compliance and to obtain mesh independent results. The effectiveness of this approach is demonstrated with four example problems: uniaxial stretching, beam bending, bar impact, and Kalthoff plate impact.

7.1 Introduction

Linear elastic fracture mechanics (LEFM) predicts a singular stress field at the tip of a crack. In reality material nonlinearity and large strains limit the magnitude of the stress. To model this behavior, Dugdale [221] and Barenblatt [222] independently introduced the notion of a *cohesive zone* (CZ) ahead of the crack tip where a different constitutive relation is introduced to eliminate the singularity. The response of the CZ is described

by a *cohesive law* that relates the stress acting on the zone to the separation and/or shear across it. A simple cohesive law that allows for fracture is a bilinear relation in which the stress grows linearly from zero to a maximum stress (tensile strength $\sigma_{\max}$ in mode-I fracture, shear strength $\tau_{\max}$ in mode-II and III fracture), and then decays linearly to zero at which point the material is fractured. Other cohesive laws with different functional forms have been proposed including an exponential law [223,224], a rigid–linear law [225], and mixed-mode laws in which the fracture modes are coupled. A detailed review of cohesive laws is given in [226].

CZs have been incorporated into the finite element method (FEM) to approximate the fracture process. Special *cohesive elements* are inserted between bulk elements in places where fracture is allowed. An early example was the work of Hillerborg et al. [227] who used this approach to simulate the fracture of quasi-brittle materials such as concrete. More recent examples include simulations of composite delamination [228, 229], and adhesive joint failure [223, 230]. In these applications fracture is confined to specific locations where the cohesive elements are placed (such as between a fiber and a matrix in a composite). To simulate arbitrary crack propagation in bulk systems, Xu and Needleman [224] extended the CZ-FEM approach by placing cohesive elements between all bulk elements. Thus any two elements can separate to form or extend a crack when the cohesive element between them fails. Alternatively, Camacho and Ortiz [225] proposed a method where new cohesive elements are introduced as needed by duplicating nodes along previously coherent element boundaries to simulate impact damage in brittle materials. In these methods, although crack propagation is limited to lie along element edges in two dimensions (or faces in three dimensions), arbitrary cracking can be simulated if the mesh is sufficiently refined.

In addition to the cohesive element approach, other methods have been proposed to simulate crack propagation in materials. In the extended finite element method (XFEM) of Belytschko and co-workers [231, 232] cracks are represented independently of the mesh, and the FEM formulation is enriched based on the LEFM crack-tip solution. In principle, XFEM allows for cracks of any shape and is efficient since mesh refinement is not required near the crack tip. The method is well-suited for fracture in pure materials, but becomes more complex for heterogeneous materials (such as interfacial fracture in bimaterials). Phase field methods for modeling fracture have been developed over the

past decade, see for example [233–235]. A scalar phase-field function is associated with the material, which is set to zero in broken areas and unity away from cracks, and is evolved based on a thermodynamically consistent variational framework.

Although both XFEM and phase field methods are excellent choices for simulating fracture, CZ-FEM continues to be attractive due to its simplicity, the clear physical meaning of the cohesive law, and its widespread availability in commercial FEM packages including ANSYS, LS-DYNA and Abaqus. However, a serious downside of CZ-FEM is that the addition of cohesive elements introduces an artificial compliance into the model that leads to mesh dependence in the results, especially when cohesive elements are inserted between all bulk elements. This changes both static and dynamic properties of the model with mesh resolution. The additional compliance decreases the effective Young's modulus E_{eff} of the model, and changes the effective speed of sound c_{eff} and the speed of crack propagation. The issue of mesh dependence in CZ-FEM was studied by Klein et al. [236] for a one-dimensional (1D) model where it was shown that artificial compliance was proportional to the element size h and inversely proportional to the cohesive element modulus K. This study implied that artificial compliance was inevitable and became bigger as the mesh was refined. Falk et al. [237] showed that cohesive element lengths can influence crack branching behavior. A recent study by Tabiei et al. [238] investigated a "CZ enlargement" approach for mesh independent simulations in which the CZ length is increased by scaling down the cohesive strength ($\sigma_{\max}$) in the vicinity of the crack tip.

In this chapter, we show that by appropriately scaling the cohesive element thickness with mesh size it is possible to maintain constant values of E_{eff} and c_{eff} with mesh refinement and obtain mesh independent results. This approach is consistent with the banded crack method of Bažant et al. [239] in which the dissipated energy due to crack formation is kept constant. The problem is first discussed theoretically in a 1D setting and then studied numerically for four problems: (1) uniaxial stretching of uniform and nonuniform meshes; (2) beam bending of uniform meshes; (3) uniaxial dynamic loading of uniform meshes; and (4) a Kalthoff plate impact problem. The simulations are performed using Abaqus [47].

7.2 1D analysis of cohesive element effects on FEM model properties

7.2.1 Cohesive Laws

Different FEM codes implement cohesive elements in different ways. We focus on Abaqus in which the mode-I fracture bilinear cohesive law (see Fig. 7.1(a)) is defined as

$$\sigma = \begin{cases} K\epsilon & \epsilon < \epsilon_{\text{peak}}, \\ \sigma_{\max} - K_{\text{e}}(\epsilon - \epsilon_{\text{peak}}) & \epsilon \geq \epsilon_{\text{peak}}, \end{cases} \tag{7.1}$$

where σ and ϵ are the stress and strain normal to the cohesive element, K and K_{e} are the cohesive moduli during damage initiation and damage evolution, $\sigma_{\max}$ and ϵ_{peak} are the stress and strain at the maximum loading the element can sustain. The area under the curve is the mode-I fracture energy G_{Ic} divided by the nominal cohesive element thickness d. The element properties are defined in Abaqus by specifying K, $\sigma_{\max}$, G_{Ic} or equivalently K, $\sigma_{\max}$, $u_{\max} = \epsilon_{\max} d$, where $\epsilon_{\max}$ is the strain at fracture and $u_{\max}$ is the maximum elongation of the cohesive element in the normal direction at fracture. A corresponding cohesive law for shearing is also defined with notation shown in Fig. 7.1(b).

It is important to note that in Abaqus the nominal thickness d associated with a cohesive element is not the geometric thickness of the element, but an artificial reference thickness relating elongation to strain. The geometric thickness is taken to be zero in the reference configuration.

7.2.2 Static properties in 1D: Effective stiffness

To explore the effect of adding cohesive elements to an FEM model, we consider a 1D periodic cell containing one square bulk element with initial length h and one cohesive element with artificial thickness d as depicted in Fig. 7.2(a). Since the cell is periodic, this represents an infinite repeating sequence of bulk elements separated by cohesive elements. The periodic cell is stretched uniformly by an amount Δ, which is accommodated by extensions in the bulk and cohesive elements:

$$\Delta = \Delta_{\text{b}} + \Delta_{\text{c}}. \tag{7.2}$$

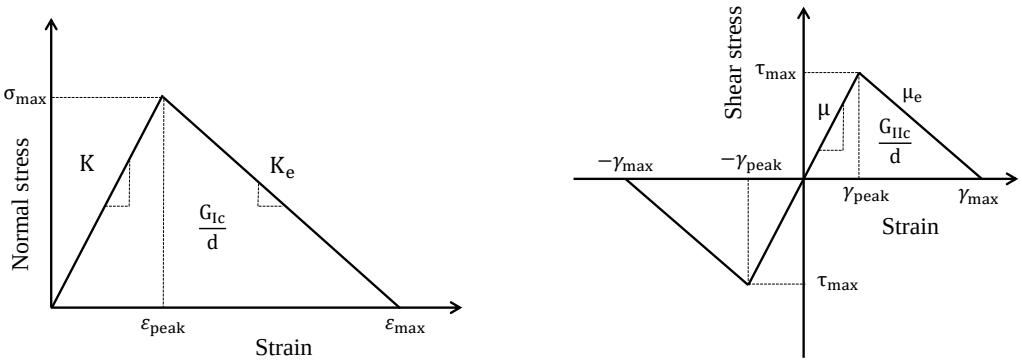

(a) (b)

Figure 7.1: Bilinear cohesive laws in (a) tension, and (b) shear.

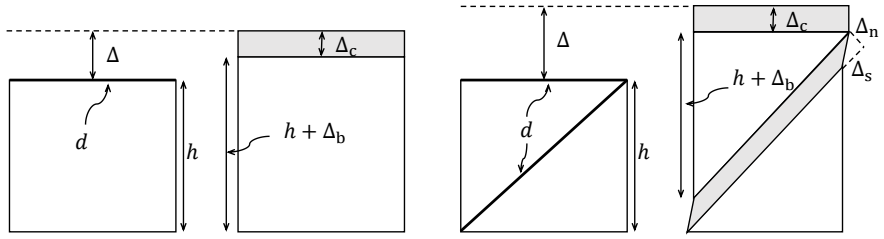

(a) (b)

Figure 7.2: Two types of 1D periodic cells. (a) One square bulk element and one cohesive element before (left) and after (right) uniaxial stretching. (b) Two triangular bulk elements separated by a cohesive elements at 45° and 0° before (left) and after (right) uniaxial stretching.

At equilibrium the stresses in the bulk element and cohesive element are equal. Taking this value to be σ, and assuming a linear elastic response for the bulk element, we have

$$\sigma = E\frac{\Delta_{\mathrm{b}}}{h} = K\frac{\Delta_{\mathrm{c}}}{d}, \tag{7.3}$$

where E is Young's modulus in the bulk material. Solving for Δ_{b} and Δ_{c} in Eq. (7.3) and substituting into Eq. (7.2) gives

$$\Delta = \sigma\left(\frac{h}{E} + \frac{d}{K}\right). \tag{7.4}$$

The strain relative to the reference configuration is $\epsilon = \Delta/h$. Therefore the effective Young's modulus E_{eff} of the periodic element is

$$E_{\mathrm{eff}} \equiv \frac{\sigma}{\epsilon} = \frac{\sigma h}{\Delta} = \frac{EKh}{Kh + Ed} = E\frac{1}{1 + \frac{E}{K}\frac{d}{h}}, \tag{7.5}$$

which gives

$$\frac{E_{\mathrm{eff}}}{E} = \frac{1}{1 + \frac{E}{K}\frac{d}{h}}. \tag{7.6}$$

This relation shows that the introduction of cohesive element necessarily reduces the stiffness of the model. The effect of cohesive element compliance is eliminated in the limit $d \to 0$ or $K \to \infty$.

A similar derivation can be performed for the element configuration shown in Fig. 7.2(b) where an inclined cohesive element at 45 degrees is also present (see Appendix B for details). In this case, the E_{eff}/E ratio is

$$\frac{E_{\mathrm{eff}}}{E} = \frac{1}{1 + \frac{(4+\sqrt{2})}{4}\frac{E}{K}\frac{d}{h} + \frac{\sqrt{2}}{4}\frac{E}{\mu}\frac{d}{h}}, \tag{7.7}$$

where μ is the shear modulus across the cohesive element. For the special case where $\mu = K/2$ (corresponding to a Poisson's ratio of zero) used in the numerical examples below, the result is

$$\frac{E_{\mathrm{eff}}}{E} = \frac{1}{1 + \frac{4+3\sqrt{2}}{4}\frac{E}{K}\frac{d}{h}}. \tag{7.8}$$

7.2.3 Dynamic properties in 1D: Effective speed of sound

Next we consider the effect of cohesive elements on the dynamics of a 1D periodic system. We take both bulk and cohesive elements to have the same mass density ρ.

The speed of sound in the bulk and cohesive elements is then given by

$$c_{\mathrm{b}} = \sqrt{\frac{E}{\rho}}, \quad c_{\mathrm{c}} = \sqrt{\frac{K}{\rho}}. \tag{7.9}$$

Assuming small deformation, the effective speed of sound for the periodic system c_{eff} is defined as the periodic cell length in the reference configuration h divided by the total time t that it takes a stress wave to pass through both the solid and cohesive element. The result for the square periodic cell in Fig. 7.2 is

$$c_{\mathrm{eff}} \equiv \frac{h}{t} = \frac{h}{\frac{h}{c_{\mathrm{b}}} + \frac{d}{c_{\mathrm{c}}}} = \frac{h}{\frac{h}{\sqrt{\frac{E}{\rho}}} + \frac{d}{\sqrt{\frac{K}{\rho}}}} = \frac{c_{\mathrm{b}}}{1 + \frac{d}{h}\sqrt{\frac{E}{K}}}. \tag{7.10}$$

Similar to the effective stiffness in Eq. (7.5), the effect of cohesive element compliance is eliminated for $d \to 0$ or $K \to \infty$.

For a model meshed with triangular elements (see Appendix B for details), the $c_{\mathrm{eff}}/c_{\mathrm{b}}$ ratio is

$$\frac{c_{\mathrm{eff}}}{c_{\mathrm{b}}} = \frac{1}{\frac{d}{h}\left[\frac{2\sqrt{B_{\mathrm{b}}+\frac{4}{3}\mu_{\mathrm{b}}}}{\sqrt{B_{\mathrm{c}}+\frac{4}{3}\mu_{\mathrm{c}}}+\sqrt{\mu_{\mathrm{c}}}} + \sqrt{\frac{B_{\mathrm{b}}+\frac{4}{3}\mu_{\mathrm{b}}}{B_{\mathrm{c}}+\frac{4}{3}\mu_{\mathrm{c}}}}\right] + 1}, \tag{7.11}$$

where B_{b}, B_{c}, μ_{b}, μ_{c} are the bulk modulus and shear modulus of bulk elements and cohesive elements, respectively. For the special case where $B_{\mathrm{b}} = E/3$, $B_{\mathrm{c}} = K/3$, $\mu_{\mathrm{b}} = E/2$, and $\mu_{\mathrm{c}} = K/2$ (corresponding to a Poisson's ratio of zero) used in the numerical examples below, the ratio is

$$\frac{c_{\mathrm{eff}}}{c_{\mathrm{b}}} = \frac{1}{1 + \frac{d}{h}\sqrt{\frac{E}{K}}\left(\frac{3\sqrt{2}+1}{\sqrt{2}+1}\right)}. \tag{7.12}$$

7.2.4 Rescaling cohesive element properties for mesh independence

It is clear from the derivation in the previous section that adding cohesive elements changes the effective stiffness and effective speed of sound in the medium. Fig. 7.3(a) shows the dependence of E_{eff}/E and $c_{\mathrm{eff}}/c_{\mathrm{b}}$ on K/E. Fig. 7.3(b) shows the dependence of E_{eff}/E and $c_{\mathrm{eff}}/c_{\mathrm{b}}$ on the normalized cohesive element thickness d/h (both curves overlap).

Our objective is to determine the cohesive element properties K and d in terms of the Young's modulus E and the element size h, so that as the mesh is refined E_{eff} and

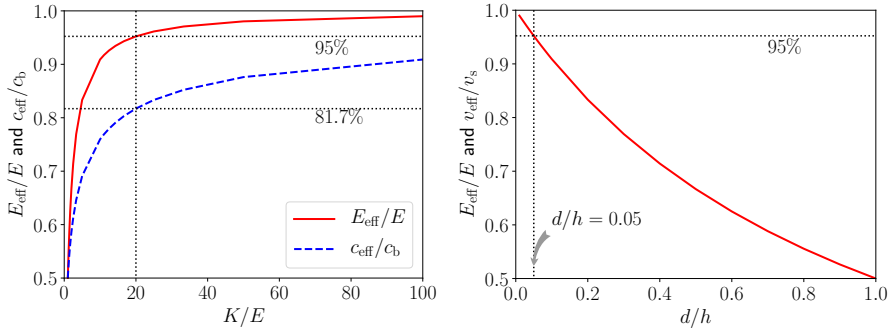

Figure 7.3: Dependence of effective properties on cohesive element properties. (a) The solid curve is the relation between E_{eff}/E and K/E, the dashed curve is the relation between $c_{\text{eff}}/c_{\text{b}}$ and K/E. (b) The relation between E_{eff}/E and $c_{\text{eff}}/c_{\text{b}}$ and the normalized cohesive element thickness d/h (both curves overlap).

c_{eff} remain constant and as close as possible to E and c_{b}. From Fig. 7.3(a) it is clear that changing K has different effects on E_{eff}/E and $c_{\text{eff}}/c_{\text{b}}$, whereas Fig. 7.3(b) shows that changing d has the same effect on both properties. Given this, in order to ensure mesh independence for a uniform mesh (i.e. no changes to the effective properties as the mesh size h is changed), it is recommended to rescale the cohesive element thickness so that d/h is kept constant. A value of $d/h = 0.05$ ensures that the effective properties are constant and within 95% of the bulk values for a quadrilateral mesh (91% for a triangular mesh as shown below).

7.3 Numerical results for the cohesive element rescaling method

To investigate the cohesive element rescaling method proposed in Section 7.2.4, we investigate the effects of mesh size and cohesive element parameters for four sample two-dimensional problems: (1) uniaxial stretching; (2) beam bending; (3) bar impact; and (4) crack propagation in Kalthoff plate impact. Simulations are performed using the Abaqus FEM code version 6.12 [47]. Cohesive elements are inserted between all bulk elements using the RiCoh perl script [240].

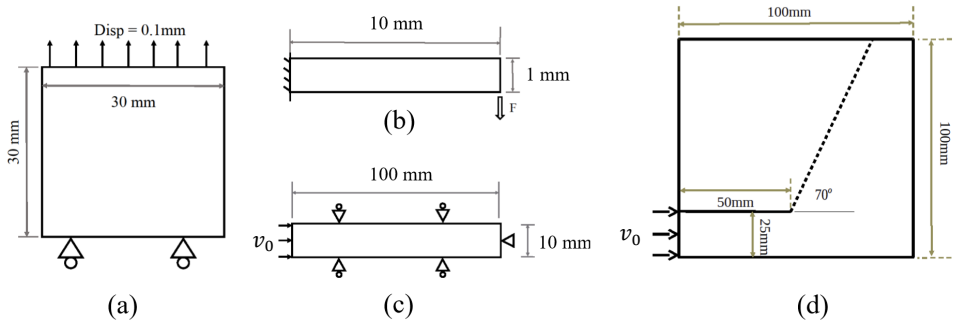

Figure 7.4: Geometries of the tested models. (a) Uniaxial stretching. (b) Beam bending. (c) Bar impact. (d) Kalthoff plate impact experiment (the model represents only half of the full structure due to symmetry). The expected crack direction is shown as a dashed line.

7.3.1 Uniaxial stretching problem

Our first example is uniaxial stretching of a block as shown in Fig. 7.4(a). A 30 mm by 30 mm square block is meshed by triangular plane strain elements with different uniform mesh sizes (3 mm, 2 mm, 1 mm, 0.5 mm) as well as a nonuniform mesh with element size linearly grading from 3 mm to 1 mm. The block is composed of a material with Young's modulus $E = 3$ GPa and a Poisson's ratio $\nu = 0$ to eliminate the Poisson effect for simplicity. The cohesive element relation is the bilinear stress–separation law in Eq. (8.3) with $K = 3$ GPa and a corresponding relation for shearing with $\mu = 1.5$ GPa. The maximum stress (normal and shear) and fracture energy are taken to be a very large value so that the cohesive elements never fail. The bottom edge is fixed by rollers. An upward displacement of 0.1 mm is applied to the top edge, corresponding to an applied strain of $\epsilon_{\text{apply}} = 0.033$. The effective Young's modulus E_{eff} of the block is calculated from the FEM solution by dividing the stress in an element (all elements have the same stress) by the applied strain ϵ_{apply}.

Fig. 7.5 shows the dependence of E_{eff}/E on the normalized cohesive element thickness d/h for a mesh size of $h = 3$ mm. The numerical results obtained from the FEM simulations (triangles) are nearly identical to the analytical results (solid line) from Eq. (7.8). The results show that the smaller d/h, the closer E_{eff} is to E. For static

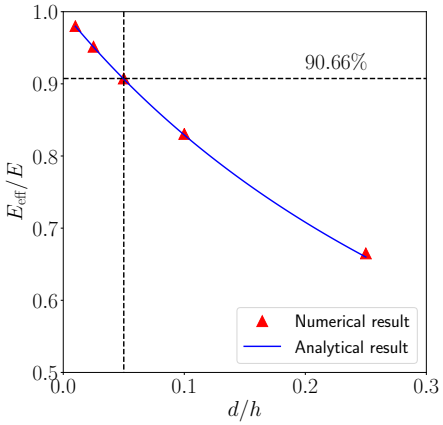

Figure 7.5: Uniaxial stretching results for a mesh size of $h = 3$ mm. The graph shows the numerical and analytical results for E_{eff}/E at different d/h ratios. The analytical results are obtained from Eq. (7.8).

calculations, in principal, d can be taken as small as desired. However, cohesive elements are typically used with explicit dynamics in which the time step is tied to smallest length scale which includes d. Therefore a compromise is required between accuracy in the effective properties and computational time. From Fig. 7.5 we see that taking $d/h = 0.05$ yields an effective stiffness within 10% of the bulk value, which is reasonably accurate and computationally tractable.

By rescaling the cohesive zone size d so that d/h is a constant for any mesh size, it is possible to obtain mesh independent results. Fig. 7.6(a) shows the effective stiffness as a function of mesh size for the four different mesh sizes shown in Fig. 7.6(b). The blue curve (stars) shows that a constant effective stiffness is maintained when d/h is kept constant (i.e. the thickness is set to $d = 0.05h$). In contrast, the red curve (triangles) shows that keeping d constant leads to significant mesh dependence in the effective stiffness.

For a nonuniform mesh (e.g. the model shown in Fig. 7.7(b)), the cohesive element thickness d could be set to a different value for each element in order to obtain the constant $d/h = 0.05$ ratio. This is ideal as it would give a uniform stiffness throughout the model. However, this is complicated to do in Abaqus because of the way cohesive elements are defined in this code. Instead we set the cohesive element thickness of all

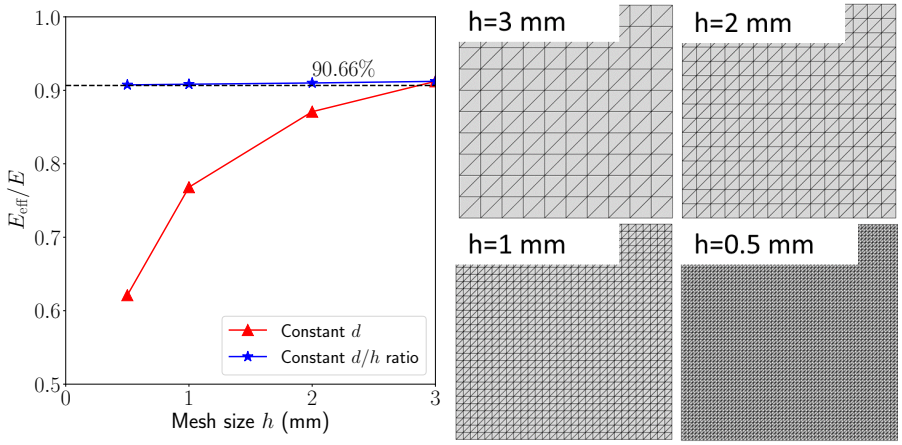

(a) (b)

Figure 7.6: Effective stiffness in uniaxial stretching for a uniform mesh. (a) The normalized effective stiffness as a function of mesh size. (b) The four meshes studied in (a).

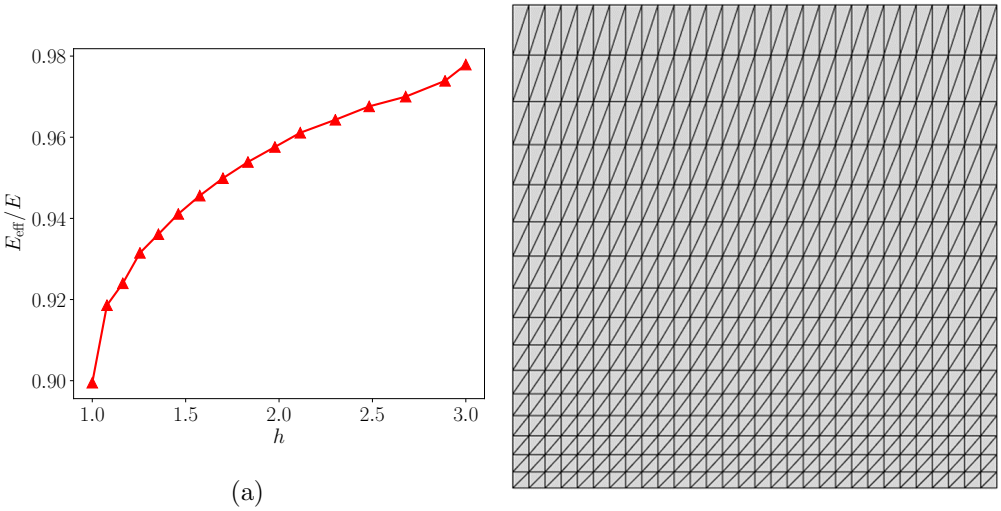

(a)

(b)

Figure 7.7: Uniaxial stretching results for a nonuniform mesh. (a) Normalized element stiffness measured in the simulation as a function of element size. Each point is an average over the stiffness of all elements of that size. (b) The nonuniform mesh with elements ranging from $h = 1$ mm on the bottom to $h = 3$ mm on the top studied in (a).

elements to the same value d defined by $d/h_{\min} = 0.05$, where $h_{\min}$ is the smallest element size. This ensures that all elements have a stiffness E_{elem} that is least 90% of E. Fig. 7.7(a) shows the element stiffness measured in the simulation (normalized by E) as a function of element size. The smallest element has $E_{\text{elem}} = 0.9E$ and the larger the element, the closer E_{eff} is to E. The effective stiffness of the entire structure is 95.5%.

7.3.2 Beam bending problem

Our second example is bending of a cantilever beam as shown in Fig. 7.4(b). We estimate the effective Young's modulus E_{eff} from the beam end deflection relation,

$$E_{\text{eff}} = -PL^3/(3\delta I), \tag{7.13}$$

where P is the applied force, L is the length of beam, δ is deflection at the end of the beam, and I is the moment of inertia of the beam cross section. The beam is of length $L = 10$ mm and height $H = 1$ mm and out-of-plane width $B = 1$ mm and is meshed with triangular plane strain elements with a mesh size of 0.1 mm. Cohesive elements with different thicknesses (1 mm, 0.1 mm, 0.01 mm, and 0.001 mm) are inserted between every bulk element. The material properties of the bulk and cohesive elements are the same as those of the uniaxial stretching model in Section 7.3.1. The beam is fully constrained at the left end and is subject to a vertical concentrated force of 0.01 N downward at the right end.

Fig. 7.8(a) shows the beam end deflections obtained from simulations for different normalized cohesive element thicknesses. The horizontal dashed line is the result for a model with only bulk elements (no cohesive elements). Fig. 7.8(b) shows the dependence of the normalized effective stiffness calculated using Eq. (7.13) on the normalized cohesive element thickness d/h for a mesh of size $h = 0.1$ mm. The numerical results obtained from FEM simulations (triangles) are nearly identical to the analytical results (solid line) calculated from Eq. (7.8). As before, Fig. 7.8(b) shows that taking $d/h = 0.05$ yields an effective stiffness within 10% of the bulk value.

Similar to the uniaxial stretching model, we rescale the cohesive element thickness d keeping d/h constant for any mesh size. Fig. 7.9 shows the effective stiffness as a function of mesh size for three meshes (0.02 mm, 0.05 mm and 0.1 mm). The blue curve

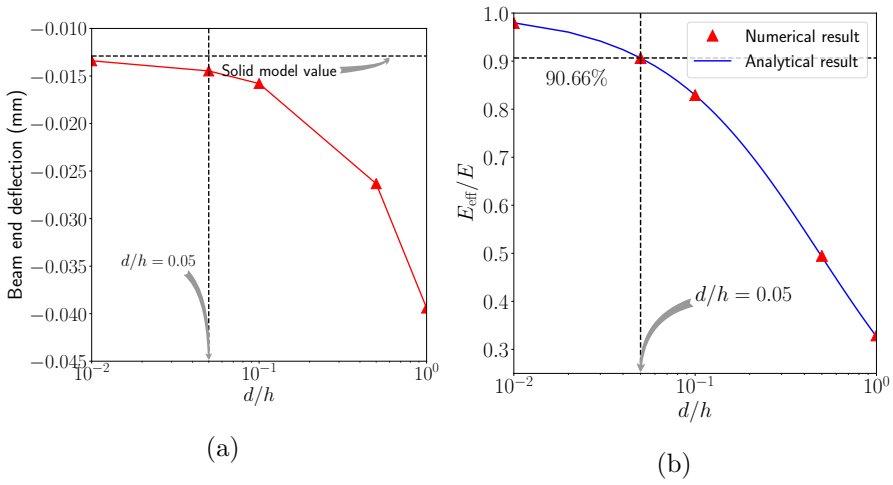

Figure 7.8: (a) The relation between the deflection at the end of the beam and the d/h ratio. The horizontal dashed line is deflection for a bulk model without cohesive elements. (b) The relation between E_{eff}/E and d/h. Numerical and analytic results overlap.

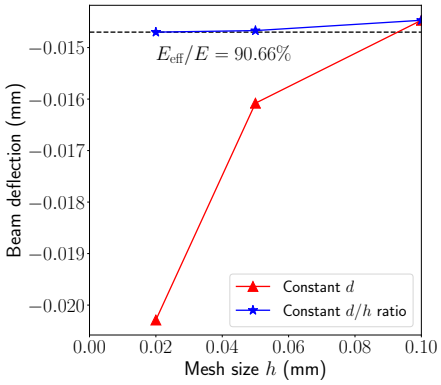

Figure 7.9: Numerical results of beam end deflection with/without mesh rescaling method. The horizontal dashed line is -0.0147 mm, which is the beam end deflection corresponding to $E_{\text{eff}}/E = 90.66\%$

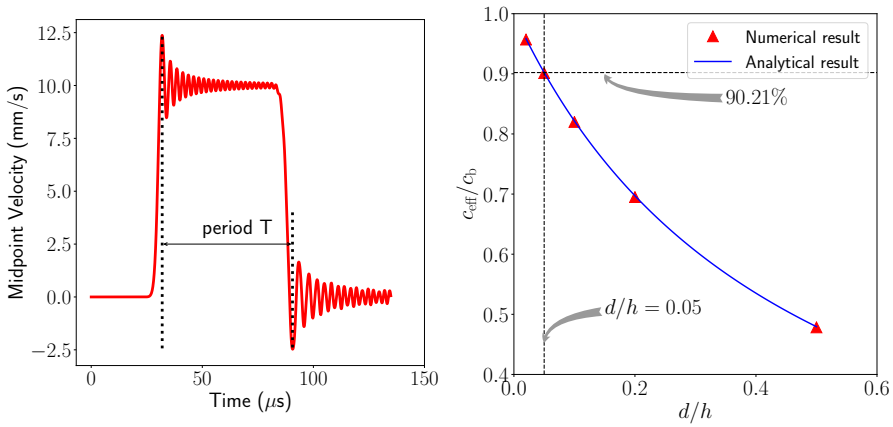

Figure 7.10: (a) Velocity as a function of time at the midpoint of a 1D bar model (without cohesive elements) used to compute the speed of sound (see text). (b) The effect of cohesive elements on the speed of sound. Numerical and analytical results for $c_{\text{eff}}/c_{\text{b}}$ as a function of the d/h ratio. Analytical results are obtained from Eq. (7.12).

(solid line) shows the results for the scaled case (d/h kept constant). For comparison, the red curve (triangles) shows the results when keep d constant (so that d/h changes). As expected the end deflection, and hence the effective stiffness, is independent of mesh size when the cohesive elements are appropriately rescaled. (The small variation for $h = 0.1$ mm is due to the periodicity of the analytical model which includes an extra cohesive element relative to the finite model used in the simulation.)

7.3.3 Impact bar problem

The next example explores the effect of cohesive elements on a dynamical property, namely the effective longitudinal speed of sound c_{eff} in a 1D bar impact problem as shown in Fig. 7.4(c). A 100 mm by 10 mm bar is meshed by triangular plane strain elements with different mesh sizes (5 mm, 2.5 mm, 2 mm, 1 mm). The right end of the bar is pinned. The top and bottom edges are constrained by rollers to prevent buckling in the vertical direction. An initial velocity $v_0 = 0.01$ m/s is applied to the left end of the bar. Both bulk and cohesive elements have a density $\rho = 10^3$ kg/m^3. Other material properties are the same as in the previous examples.

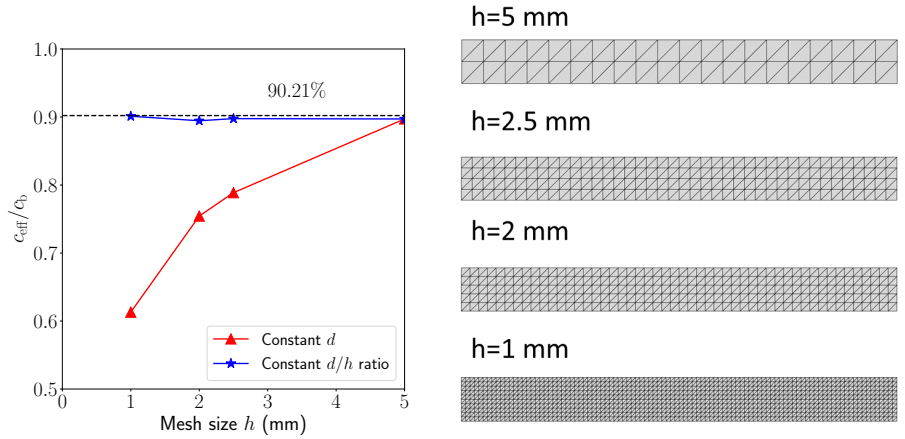

(a) (b)

Figure 7.11: (a) Effective longitudinal speed of sound as a function of mesh size in a 1D bar impact problem. (b) The four meshes studied in (a).

The objective is to study how the effective speed of sound changes with the introduction of cohesive elements. First, we assess the speed of sound for a pure bulk specimen (i.e. without cohesive elements). Fig. 7.10(a) shows the velocity as a function of time at the midpoint of the bar (halfway along its length). A compressive wave is initiated at the left end and reaches the midpoint after about 30 μs. The wave then continues to the right end and reflects, reaching the midpoint again as a tensile wave after about 90 μs. The period $T = 57.75$ μs between the first (positive) and second (negative) peaks reaching the midpoint is the time that it takes the stress wave to traverse the length of the bar ($L = 100$ mm). The speed of sound is thus $c_{\text{b}} = L/T = 1731.6$ m/s.

Next we introduce cohesive elements of thickness d between all elements and measure the effective speed of sound c_{eff} in this heterogeneous medium using the same approach described above for the pure bulk case. Fig. 7.10(b) shows the normalized effective speed of sound ($c_{\text{eff}}/c_{\text{b}}$) as a function of the normalized cohesive element thickness d/h for a mesh size of $h = 1$ mm. The numerical results (triangles) are in excellent agreement with the analytical curve obtained from Eq. (7.12). Fig. 7.10(b) shows that taking $d/h = 0.05$ yields an effective speed of sound within 10% of the bulk value.

Fig. 7.11(a) shows the normalized effective speed of sound $c_{\text{eff}}/c_{\text{b}}$ for the four mesh sizes shown in Fig. 7.11(b). The blue curve (stars) shows that a constant effective speed

of sound is maintained provided that the ratio d/h is kept constant (i.e. the thickness is set to $d = 0.05h$). In contrast, the red curve (triangles) shows that keeping d constant leads to significant mesh dependence in the effective speed of sound. Thus the rescaling method provides mesh independent results for effective (average) dynamical properties.

7.3.4 Kalthoff plate impact problem

As a final example, we simulate a Kalthoff plate-impact experiment in which a plate containing a pair of edge cracks symmetrically arranged about the centerline is impacted by a rigid flat-ended projectile with a constant velocity parallel to the centerline (Fig. 7.4(d) shows half the model). This method was introduced by Kalthoff [241] and Kalthoff and Winkler [242] who used it to study crack propagation in C-300 maraging steel. They found crack extension at an angle of 70° to the centerline. Similar results were obtained numerically by Batra et al. [243]. The Kalthoff plate impact problem is a popular benchmark problem for method development and has been used to evaluate cohesive element rescaling [238], XFEM [244] and phase field approaches [245].

In our problem, the plate is a rectangle of length 100 mm and height 200 mm, and the distance between the cracks is 50 mm. Due to symmetry, only half the problem is modeled as shown in Fig. 7.4(d). The projectile impact velocity is $v_0 = 20$ m/s, which is modeled by setting the initial velocity of the left edge of the model between the cracks to this value. The plate is made of steel with Young's modulus $E = 190$ GPa, Poisson's ratio $\nu = 0.3$ and mass density $\rho = 8$ g/cm^3. The cohesive zone moduli in the normal and tangential directions are $K_{\mathrm{n}} = 190$ GPa and $K_{\mathrm{s}} = 73$ GPa, respectively, the yield stress $\sigma_{\max}$ =400 MPa, and the critical energy release rates in mode I and II under plane strain conditions are $G_{\mathrm{Ic}} = G_{\mathrm{IIc}}$ =22.145 kJ/m^2. The simulations were performed using explicit dynamics with a fixed time step of 1 ns for a duration of 0.075 ms.

Fig. 7.12 shows the crack propagation results for different mesh sizes and cohesive element thicknesses (element edges are not shown to highlight the crack). The red dashed line is at 70° to the centerline. Fig. 7.12(a) shows the results for a mesh size of $h = 3$ mm and cohesive element thickness $d = 0.15$ mm ($d/h = 0.05$). The crack grows by separating the model along cohesive elements. The growth direction is therefore limited by the mesh resolution, but is roughly aligned the 70° direction observed in experiments. We note the presence of a horizontal crack in the lower right corner.

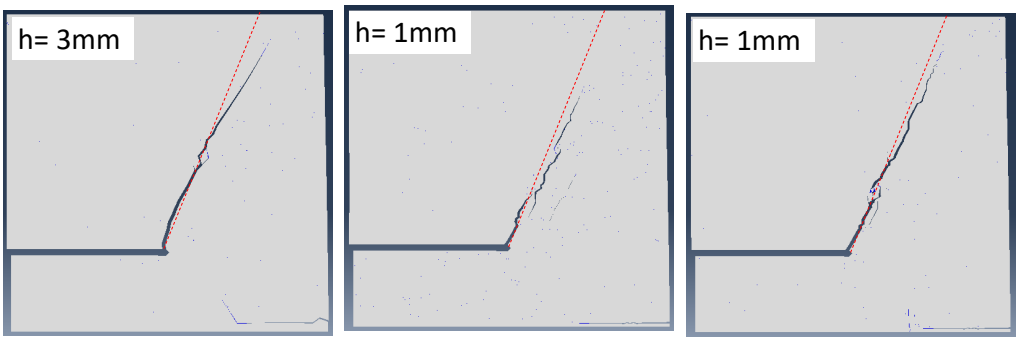

(a) (b) (c)

Figure 7.12: Crack propagation for a model with two mesh sizes. (a) Mesh size $h = 3$ mm, cohesive element thickness $d = 0.15$ mm, $d/h = 0.05$. (b) $h = 1$ mm, $d = 0.15$ mm, $d/h = 0.15$. (c) $h = 1$ mm, $d = 0.05$ mm, $d/h = 0.05$.

This is caused by a stress intensity at the artificial corner introduced by the symmetry conditions and can be ignored.

Fig. 7.12(b) shows the results for a mesh of size $h = 1$ mm and the same cohesive element thickness as in Fig. 7.12(a) ($d/h = 0.15$). The finer mesh allows the crack to follow the 70° direction more closely than in Fig. 7.12(a), however note that the length of the crack is shorter. This is because the higher d/h ratio makes the model more compliant and hence able to absorb more energy prior to fracture. This mesh dependence can be addressed by rescaling the cohesive element size. Fig. 7.12(c) shows the results for a mesh of size $h = 1$ mm with the cohesive element rescaled to $d = 0.05$ mm so that the d/h ratio is the same as in Fig. 7.12(a) ($d/h = 0.05$). The total crack length in Figs. 7.12(a) and 7.12(c) are about the same. This is shown in quantitatively in Fig. 7.13 where the crack length is plotted as a function of time for the three models in Fig. 7.12. We see that the coarse mesh and refined mesh with rescaled cohesive elements are in close agreement, whereas refining the mesh without rescaling leads to a significant difference in crack propagation.

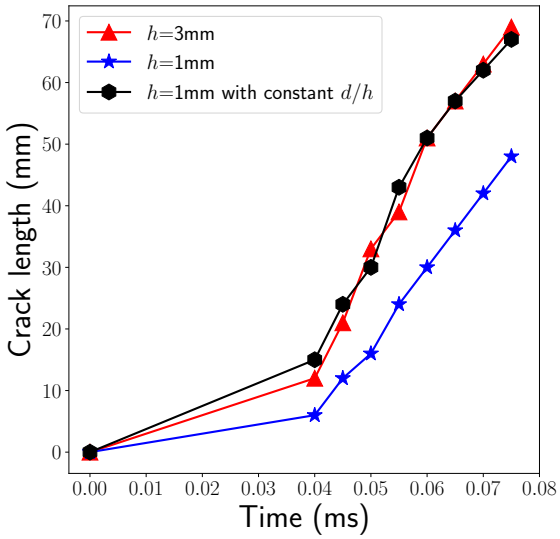

Figure 7.13: Crack length as a function of time in a Kalthoff plate impact simulation.

7.4 Conclusion

In order to simulate fracture within the FEM framework it is necessary for cracks to be able to form and grow. A popular approach is to introduce cohesive elements that fail under certain conditions between the other elements in the mesh allowing them to separate. This approach is physically reasonable and easy to implement, however, introduction of cohesive elements increases the compliance of the model leading to mesh dependence in the results. This is because cohesive elements are associated with an artificial thickness that effectively increases the size of the model. The change in compliance can be significant, especially when cohesive elements are inserted between all elements.

In this chapter, we show that mesh dependence can be minimized by suitably rescaling the cohesive element thickness d with mesh size, while keeping the cohesive element stiffness K constant. We derive analytical results for the effect of cohesive elements on the effective stiffness E_{eff} and effective speed of sound c_{eff} under 1D loading conditions. The results show that both E_{eff} and c_{eff} are decreased by the presence of cohesive elements. The larger K and the smaller d, the lesser the effect. Thus it is best to make the

cohesive elements as thin as possible and/or as stiff as possible — however this leads to numerical difficulties. Based on our simulations, good performance was obtained by setting K equal to the Young's modulus of the bulk material and $d/h = 0.05$ where h is the element size. This results in values for E_{eff} and c_{eff} within 10% of bulk values for a triangular mesh (5% for a square mesh). By maintaining d/h as a constant during mesh refinement (i.e. rescaling the cohesive element thickness with mesh size, $d = 0.05h$, mesh independent results are obtained for uniform meshes. For nonuniform meshes, rescaling by the minimum element size, $d = 0.05h_{\text{min}}$ minimizes mesh dependence effects.

The effect of cohesive elements and the proposed rescaling approach are tested in several example problems using the Abaqus finite element code: effective stiffness in uniaxial stretching and bending of a bar, effective speed of sound in a bar impact, and crack propagation speed and direction in Kalthoff plate impact. These problems are used to study the effect of cohesive element properties (K and d) and mesh refinement (h) on the results. For the 1D problems, the simulation results are in excellent agreement with the derived analytical expressions. In all cases, the proposed rescaling approach either eliminates (for uniform meshes) or significantly reduces mesh dependence for effective properties, such as average stiffness, speed of sound, and crack propagation speed and direction.

Chapter 8

An Atomistically-informed Multiscale Simulation for Epoxy–graphene Composites: Toughening Mechanism at Small Graphene Loading

An atomistically-informed cohesive element model is developed to study the fracture mechanism for graphene reinforced epoxy composites at different graphene loadings. In a compact tension specimen model, cohesive elements are inserted between each bulk element to allow the crack propagates along bulk element boundaries. The graphene inside epoxy matrix is modeled as an effective cohesive element which follows a cohesive law obtained from the molecular dynamics simulations. Different amounts of graphene effective cohesive elements are introduced into the model based on the graphene weight percentage (i.e. "graphene loading") in composites. Our results show that the micro-cracks nucleate at the epoxy–graphene interface at small graphene loading and weaken the stress concentration at the main crack, thus leading to increase in the overall fracture toughness. As graphene loading increases, micro-cracks connect with each other, which leads to a decrease of the overall fracture toughness due to an avalanche effect,

and the further increase of graphene loading causes percolation-like crack propagation. The simulation results are in good agreement with experimental data in the crack nucleation and avalanche region, but have deviations in the percolation region due to their limitations.

8.1 Introduction

As we have introduced in chapter 6, epoxies are widely used as adhesives, coating, and structures due to their excellent chemical resistance and mechanical properties. Graphene consists of a single layer of carbon atoms and has shown great promise as epoxy tougheners due to its excellent mechanical, thermal and electrical properties [186, 187]. Because of the high aspect ratio of graphene, substantial property enhancements can be achieved with graphene loading less than 0.5 wt% [190–192, 246]. More interestingly, many experiments have shown that the enhancement of fracture toughness is not proportional to the graphene loading, but has a peak at small loadings. Rafiee *et al.* [247] found that the improvement in K_{Ic} (65% increase) peaked at a graphene loading of 0.125 wt%. Wang *et al.* [248] showed that K_{Ic} of epoxy composites increased by 110% and 73% at 0.1 wt% and 0.05 wt% loading, respectively for two different graphene oxides. Recently, Park and Qian *et al.* [13] observed a maximum in K_{Ic} at loadings as small as 0.02-0.04 wt% for four types of graphene-based materials.

Although the improvements of mechanical properties at low graphene loading provide opportunities to produce cost-effective epoxy–graphene composites, the reinforcement mechanism is still under study. To-date, a range of possible toughening mechanisms have been proposed [249, 250] such as crack pinning, crack-tip blunting, particle-matrix debonding, micro-cracking, etc. and some of these mechanisms may occur cooperatively. Shekhawat *et al.* [251] used a fuse network model to study the brittle fracture in disordered media, which is akin to the epoxy–graphene composite system if we consider the increase of graphene loading increases the disorder of the system. Three failure mechanisms were found: Nucleation of micro-cracks for perfect material with a few isolated defects; percolation-like damage for a material with infinite order of defects; and the avalanche behavior between these two limits. In this chapter, we use a cohesive element model to simulate the crack initiation and propagation in an epoxy–multi-layer

(MLG) graphene composite, aiming to study the reinforcement mechanism at small graphene loading. Inspired by Shekhawat's work, we explain our results with *nucleation*, *avalanche*, and *percolation*, aiming to explain the nonlinear response of the K_{Ic} with graphene loading. In section 8.2, a method to set up a compact tension specimen (CTS) model for an epoxy–MLG composite is introduced. The constitutive laws and failure criterion for cohesive elements are also introduced. In section 8.3, we compared our simulation results with experimental results for the same epoxy–graphene composites, and explain the fracture mechanism at different loading. We conclude this chapter with a summary and an assessment of the limitations of this method in section 8.4.

8.2 Methods

8.2.1 Model setup

CTS is extensively used to establish the fracture toughness of a material. Park and Qian *et al.* [13] have used CTS to study the fracture toughness of epoxy–graphene composite at different graphene loading, and we use the same CTS geometry [18] in our simulation, shown in Fig. 8.1. In a CTS experiment, two holes in a specimen is fixed with two pins, and subjected to tension. The K_{Ic} is calculated through [252]

$$K_{\mathrm{Ic}} = \frac{P_{\mathrm{cr}}}{B}\sqrt{\frac{\pi}{W}}\left[16.7\left(\frac{a}{W}\right)^{1/2} - 104.7\left(\frac{a}{W}\right)^{3/2} + 369.9\left(\frac{a}{W}\right)^{5/2} - 573.8\left(\frac{a}{W}\right)^{7/2} + 360.5\left(\frac{a}{W}\right)^{9/2}\right], \tag{8.1}$$

where P_{cr} is the critical applied force that breaks the CTS, B is the thickness of the specimen, a and W are geometrical parameters shown in Fig. 8.1. In our work, two-dimensional plane strain simulations of a CTS are performed using Abaqus [47], with $W = 6$ mm, $a = 3$ mm, and B is the unit thickness.

Graphene is a two-dimensional material with lateral dimensions of micrometers and a thickness of nanometers [187]. Thus, instead of simulating graphene as a bulk material we use an effective cohesive element to represent the graphene inside an epoxy matrix. The constitutive law of the effective cohesive element is obtained from molecular dynamics (MD) simulations of the epoxy–MLG interface. The size for the effective cohesive elements needs to be as small as tens of micrometers [13]. However, considering

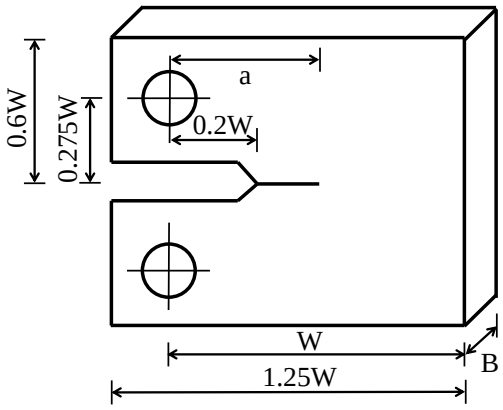

Figure 8.1: Geometry of a CTS [18].

computational efficiency, it is not necessary for the entire model to have element down to this size. Instead, only the region in front of the initial notch of a CTS needs to have a fine mesh, because it is more critical for fracture. Inserting cohesive elements between each bulk element can simulate the arbitrary crack propagation, however, it also introduces artificial compliance into the model. The artificial compliance increases as the mesh is refined, thus making the result mesh-dependent. It has been shown in chapter 7 that choosing the cohesive element thickness $d = 0.05h_{\min}$ ($h_{\min}$ is the smallest bulk element size) can produce mesh-independent result, and ensure that the effective Young's modulus and effective speed of sound of the cohesive model are at least 90% of the bulk material properties. Improved accuracy can be obtained by taking a smaller $d/h_{\min}$ ratio at an increased computational cost (especially for explicit dynamics simulation where the time step is tied to the smallest length scale which includes d). Thus, cohesive elements are introduced only in the region ahead of the initial notch, since the crack is tend to propagate directly ahead due to the symmetry of geometry and boundary conditions. The CTS model is separated into two regions: a refined mesh *region A* with the smallest element size $h_{\min}$ =20 μm, where cohesive elements are inserted between each bulk element, and a coarser mesh *region B* including only bulk elements, shown in Fig. 8.2.

To mimic the random distribution of the MLG inside an epoxy matrix, the MLG effective cohesive elements are randomly distributed in a *toughening area* inside *region*

A ahead of the initial notch with height of 200 μm and width of 6 mm. The graphene loading is defined as

$$\text{wt}\% = \frac{\#_{\text{G-E}} \times \text{L}_{\text{G-E}} \times \text{B} \times \rho_{\text{G}}}{\text{A}_{\text{t}} \times \text{B} \times \rho_{\text{E}}}, \tag{8.2}$$

where $\#_{\text{G-E}}$ is the number of epoxy–MLG interfaces, $\text{L}_{\text{G-E}}$ is the length of epoxy–MLG interfaces which is 20 μm, ρ_G is surface density of MLG which is 0.048×10^{-6} g/mm^2 [13], A_{t} is the area of the MLG region which is 1.2 mm^2, ρ_E = 1.15 g/cm^3 is the density of epoxy [5]. There are 9180 cohesive elements in the *toughening area*. Based on graphene loading, different amount of cohesive elements are defined as epoxy–MLG interfaces using the relation in Eq. (8.2), while the rest cohesive elements are defined as epoxy–epoxy interfaces. The CTS models with graphene loading of 0.016%, 0.032%, 0.05%, 0.067%, 0.1%, 0.134% are shown in Fig. 8.3. Three independent simulations with different graphene distribution are performed for each graphene loading to obtain a statistical average and standard deviation for predictions.

Instead of simulating the pin in real experiments, displacement control is applied to an arc on the hole to mimic the loading process, shown in Fig. 8.2. Since the real contact area between pin and CTS is unknown in experiments, the length of the arc is obtained by calibrating the pure epoxy simulation with experimental result [13]. In such a calibration, a CTS model with only epoxy–epoxy cohesive elements and epoxy bulk elements is pulled until breakdown. The arc length that makes the P_{cr} equal to the experimental value is used in the following simulations, which turns out to be 1 mm. All degrees of freedom in the lower arc are fixed, and an upward displacement of 0.24 mm is applied to the upper arc with a constant rate of 0.24 mm/s.

8.2.2 Material properties

We simulate the epoxy bulk material as a linear elastic isotropic material with Young's modulus E = 2.78 GPa, and the Possion's ratio ν =0.34 [253]. Epoxy–epoxy cohesive elements follows a bilinear cohesive zone law for mode I fracture, shown in Fig. 8.4. The cohesive zone law is

$$\sigma = \begin{cases} K\epsilon & \epsilon < \epsilon_{\text{peak}}, \\ \sigma_{\max} - K_{\text{e}}(\epsilon - \epsilon_{\text{peak}}) & \epsilon \geq \epsilon_{\text{peak}}, \end{cases} \tag{8.3}$$

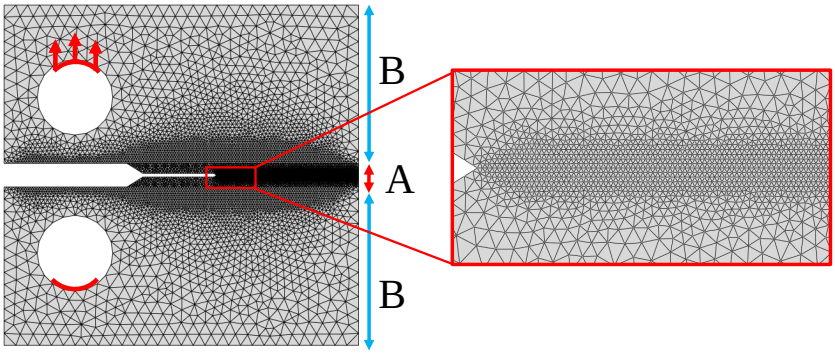

Figure 8.2: The mesh and boundary conditions for the CTS model, and a zoom-in figure for *region A*.

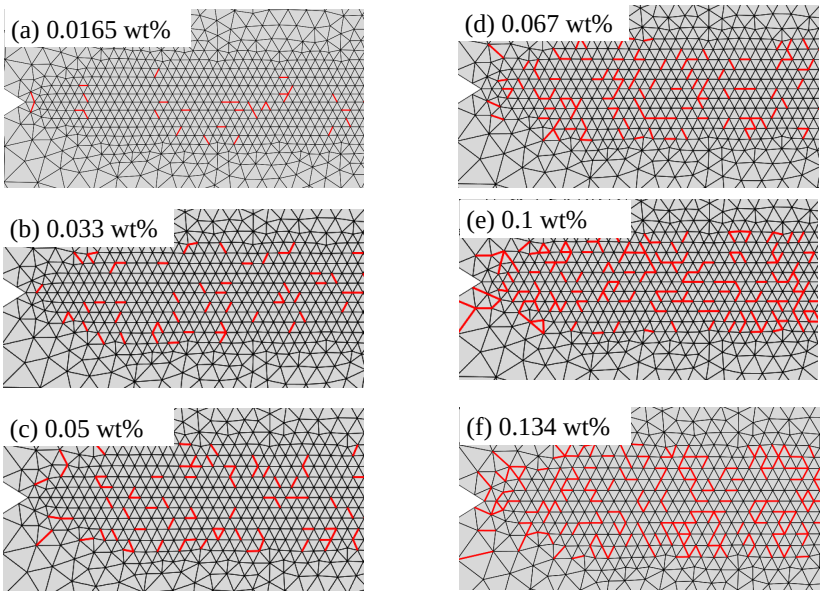

Figure 8.3: Zoom in of the crack tip in *region A* with toughener loading of (a) 0.0165%, epoxy–MLG cohesive elements (red line)/epoxy–epoxy cohesive elements (black line) ratio is 250/9180, (b) 0.033% (500/9180), (c) 0.05% (750/9180), (d) 0.064% (1000/9180), (e) 0.1% (1500/9180), and (f) 0.128% (2000/9180).

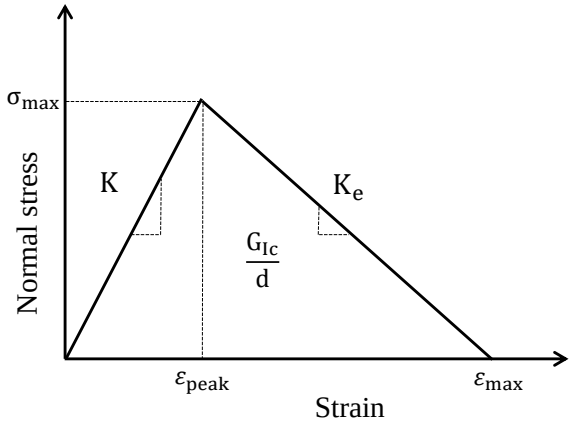

Figure 8.4: Schematic diagram of mode I bilinear fracture cohesive zone law.

where σ and ϵ are the stress and strain normal to the cohesive element, K and K_{e} are the cohesive moduli during damage initiation and damage evolution, $\sigma_{\max}$ and ϵ_{peak} are the stress and strain at the maximum loading the element can sustain. The area under the curve is the mode I fracture energy G_{Ic} divided by the nominal cohesive element thickness d. The element properties are defined in Abaqus by specifying K, $\sigma_{\max}$, G_{Ic} and d. In this work, the cohesive modulus for epoxy–epoxy interfaces is the same as the Young's modulus for bulk epoxy K =2.78 GPa, $\sigma_{\max} = 85.8$ MPa is the yield stress for bulk epoxy obtained from MD simulations. The fracture energy G_{Ic} for a plane strain problem is calculated based on the measured fracture toughness for bulk epoxy $K_{\mathrm{Ic}} = 0.97$ MPa·m$^{1/2}$ [13] through

$$G_{\mathrm{Ic}} = \frac{K_{\mathrm{Ic}}^2(1-\nu^2)}{E}, \tag{8.4}$$

where E and ν are the Young's modulus and the Possion's ratio for bulk epoxy. Using Eq. (8.4), the fracture energy release rate for epoxy–epoxy interfaces is G_{Ic}^{E-E} =299 J/m^2. The epoxy–epoxy cohesive element thickness is chosen to be $d^{\mathrm{E-E}} = 0.05h_{\min} = 1$ μm to obtain the mesh independent simulation.

The MLG effective cohesive elements follow a trilinear cohesive zone law for mode I fracture, which is obtained from the MD simulation for epoxy–MLG interfaces, shown in Fig. 8.5(a). The mode I cohesive zone law for epoxy–MLG interface (stress in MPa)

is

$$\sigma = \begin{cases} 5520\epsilon & 0 \leq \epsilon \leq 0.044, \\ -97.5\epsilon + 245.3 & 0.044 \leq \epsilon \leq 0.69, \\ -574.2\epsilon + 574.2 & 0.69 \leq \epsilon \leq 1. \end{cases} \tag{8.5}$$

The first linear curve in Eq. (8.5)(a) represents the initial linear elastic response of epoxy–MLG interfaces. The second linear curve represents the formation of craze-like processing zone in the epoxy near the graphene. The third linear curve represents the debonding between epoxy and graphene, which causes the final failure of epoxy–graphene interface. The critical fracture energy release rate for epoxy–MLG interface is G_{Ic}^{E-G} =0.75 J/m^2. The thickness of epoxy–MLG cohesive element $d^{\mathrm{E-G}} = 4.3$ nm $<< 0.05h_{\mathrm{min}}$, which can ensure the mesh-independent simulation.

The epoxy–MLG cohesive element follows a bilinear cohesive zone law for mode II fracture, shown in Fig. 8.6. Similar with the bilinear law for mode I fracture, μ is the shear modulus, τ_{y} is the shear strength of the epoxy–MLG interface, and γ_{f} is the shear strain at failure. Chapter 6 also showed that the shear properties of epoxy–MLG interface showed a strong mix-mode behavior, the shear modulus and shear strength decrease linearly as the normal strain goes from compression to tension, but the shear strain at failure is largely unaffected. The shear properties follows:

$$\begin{aligned} \mu^{\mathrm{E-G}} &= -6.11\epsilon + 0.31, \\ \tau_{\mathrm{y}}^{\mathrm{E-G}} &= -426.43\epsilon + 18.95 \\ \gamma_{\mathrm{f}}^{\mathrm{E-G}} &= 0.069, \end{aligned} \tag{8.6}$$

where $\epsilon \in [-0.03, 0.03]$ is the normal strain. The cohesive zone laws for epoxy–MLG cohesive element at normal strain of -0.03 to 0.03 are shown in Fig. 8.5(b).

A mode-independent failure criterion is used for simulations in this work, which means that either normal strain exceeds ϵ_{f} or shear strain exceeds γ_{f} can lead to failure of a cohesive element. The cohesive zone law for epoxy–MLG interface is implemented in Abaqus using VUMAT user material subroutine that is written in Fortran.

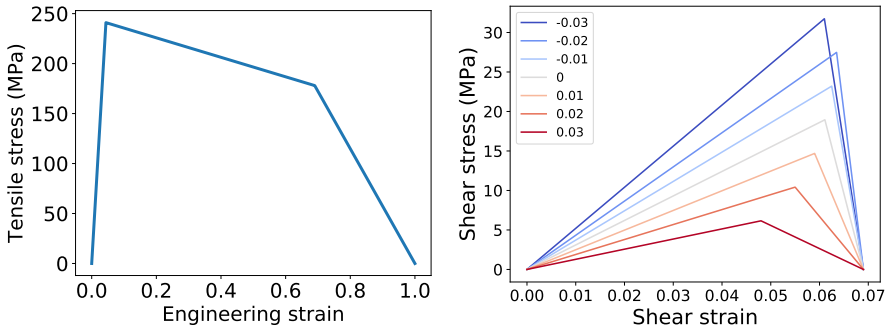

(a) (b)

Figure 8.5: The cohesive zone law for epoxy–MLG interface. (a) The trapezoidal-shape law for for mode I fracture, and (b) the bilinear law for mode II fracture at normal strain from -0.03 to 0.03.

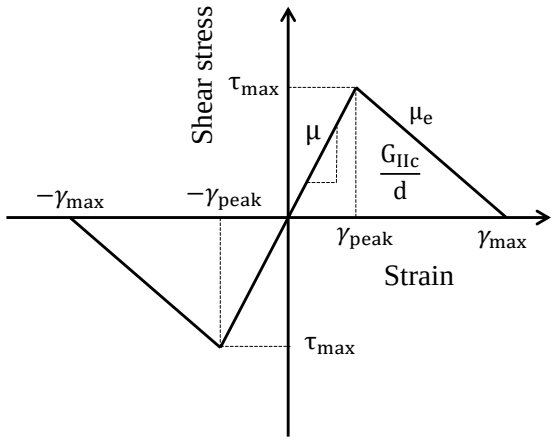

Figure 8.6: Schematic diagram of a mode II bilinear cohesive zone law.

Table 8.1: The critical force to break the CTS and the corresponding fracture toughness at different graphene loading.

Loading (wt%)	P_{cr} Ave. (N)	P_{cr} SD	K_{Ic} Ave. (MPa·m$^{1/2}$)	K_{Ic} SD
0	11.3	-	0.98	-
0.0165	12.8	0.44	1.11	0.038
0.033	14.2	0.97	1.23	0.085
0.05	14.8	0.88	1.29	0.077
0.067	12.5	0.59	1.09	0.051
0.1	9.07	0.43	0.79	0.038
0.134	8.5	0.68	0.74	0.059

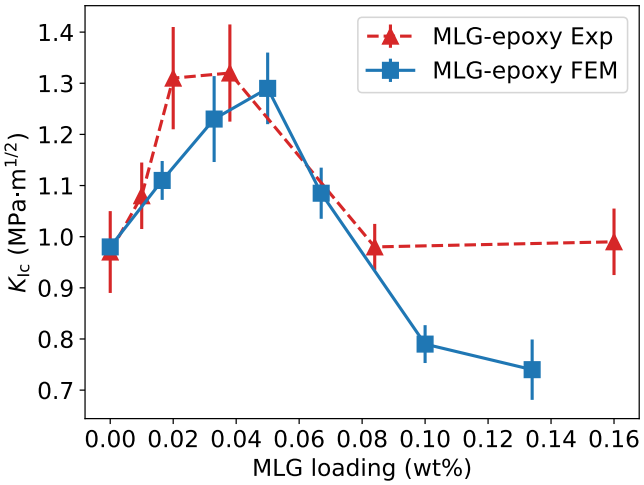

Figure 8.7: The simulations predicted K_{Ic} (blue) compared with the experimental results (red) [13].

8.3 Results and discussion

The maximum force to break the CTS, P_{cr}, and the corresponding K_{Ic} calculated using Eq. (8.1) at different graphene loading are listed in Table 8.1 and shown graphically in Fig. 8.7. The K_{Ic} at different graphene loading are compared with the experimental results. We can see that the K_{Ic} predicted by our simulation increases with graphene loading and reaches the maximum value of 1.3 MPa·m$^{1/2}$ at graphene loading of 0.05 wt%, which is in reasonable agreement with the experimental results. As graphene loading keeps increasing the K_{Ic} decreases, which is also in agreement with the experiment. However, after the graphene loading is larger than 0.08%, the experimental results show plateau, whereas the simulation results keep decreasing due to the limitation of this two-dimensional cohesive element model, because the current two-dimensional cohesive element model may not describe the composite system well at large graphene loading, which leads to the deviation between simulation results and experimental data. In the current model, the perfect connection between two cohesive elements may eliminate the mismatch between two close graphene sheet. In addition, cohesive elements can only be inserted along bulk element boundaries, which limits the orientation of graphene sheet inside an epoxy matrix. These limitations may cause the deviation at larger graphene loading.

The breakdown of CTS for pure epoxy happens when the applied displacement is 0.14 mm. The stress contours with graphene loading of 0 wt% (pure epoxy) 0.033 wt%, 0.067 wt%, and 0.1 wt% at an applied displacement of 0.14 mm are shown in Fig. 8.8. We can see that introducing graphene into epoxy matrix change the stress distribution at the crack tip. The fracture energy of the epoxy–graphene interface is much smaller than that of the pure epoxy. Thus, the epoxy–graphene interfaces break down firstly under applied load and form micro-cracks in the matrix. At small graphene loading of 0.033 wt%, the nucleation of micro-cracks decrease the stress concentration at the main crack tip, as shown in Fig. 8.8(b). Therefore, a higher P_{cr} is needed to break the specimen, which leads to a higher resulting fracture toughness. At graphene loading of 0.067 wt%, micro-cracks connects with each other and form avalanches effect, which decreases the overall fracture toughness. At graphene loading of 0.1 wt%, stress concentration at the main crack tip become less important and fracture processes via

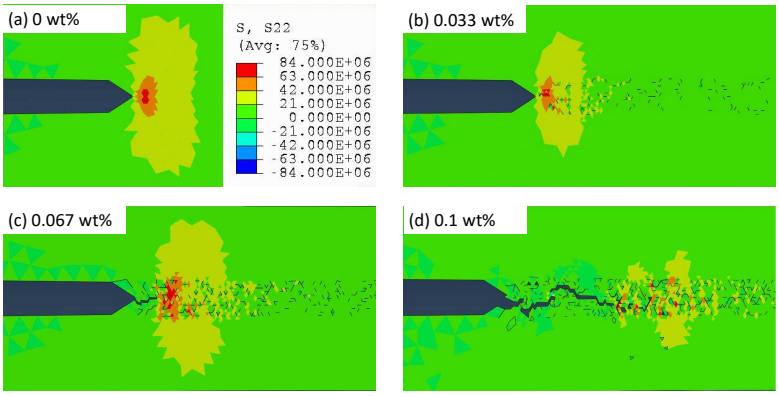

Figure 8.8: The normal stress contour at the crack tip at the applied displacement of 0.14 mm for (a) pure epoxy with graphene loading of 0 wt%, and composite with graphene loading of (b) 0.033 wt%, (c) 0.067 wt% and (d) 0.1 wt%. The unit of the scale legend is Pa. The black lines in the model represent the micro-cracks formed in the epoxy matrix.

percolation-like damage.

8.4 Conclusion

In this chapter, we perform CTS finite element simulations with cohesive zone to study the fracture mechanism for epoxy–graphene composites at different graphene loadings. Cohesive elements are inserted between each bulk element in a region ahead of the initial notch. The graphene is introduced into the model as effective cohesive elements which follow the cohesive zone law obtained from MD simulations for epoxy–graphene interface. Different amounts of cohesive elements are randomly chosen and defined as the graphene effective cohesive element to mimic the random distribution of graphene in an epoxy matrix. The graphene effective cohesive element has a lower fracture energy, thus breaks before the breakdown of epoxy–epoxy cohesive elements under applied load. At small graphene loading, the *nucleation* of micro-cracks at the epoxy–graphene interfaces weakens the stress concentration at the main crack and leads to the increase of fracture toughness. The density of micro-cracks increases with the graphene loading, and the *avalanche* effect decreases the overall fracture toughness of material. At a

larger graphene loading, the overall fracture toughness can hardly increase due to the *percolation*-like crack propagation.

Future directions include using a phase field model to study the fracture mechanism in the epoxy–graphene composites. Not as the cohesive element model, the crack propagation in a phase field model is not limited between the bulk elements boundaries. We may introduce a damage field with orientation as element internal variable to represent the orientation of graphene, which will help us to study the fracture mechanism at large graphene loading.

Chapter 9

Conclusions and Future Directions

The atomistically-informed finite element method is a useful computational tool to investigate materials, as it can simulate the material response in a continuum scale with large model size without losing the insights of the material from the atomistic scale. Thus, AFEM can be used to study a large number of problems that are difficult to study with phenomenological model, or involve different scales. For example, the phase transformations of silicon under pressure, and the fracture in an epoxy–graphene nanocomposite.

During my doctoral studies, I have implemented the Cauchy-Born rule into a commercial FEM code Abaqus (chapter 2) to explore the nonlinear mechanical response and PT prediction of it. I successfully predicted the diamond-cubic to bct5 and β-Sn PTs of silicon in a nanoindentation problem, which is in good agreement with experimental results and the previous numerical studies. I have proposed a modified Blatz-Ko hyperelastic model for material under ultra-high pressure (chapter 3), which is able to describe the pressure-dependence of elastic constants. I have implemented the two models introduced above in an *in situ* simulation of diamond anvil cell (chapter 4), and study PTs of silicon under pressure, and found that the nonhomogeneous environment surrounding silicon sample generated by the solidified helium is important for the PT of silicon.

I have also used the AFEM to study the fracture mechanism of epoxy–graphene composites under different graphene loading. A compact tension specimen cohesive element model is set up with cohesive elements inserted between each bulk epoxy element in a region ahead to the initial notch. Based on different graphene loadings, different amounts of cohesive elements are defined as effective epoxy–graphene elements, which follow a constitutive law based on the epoxy–graphene interfacial properties. It is different to measure the interfacial properties between epoxy and graphene via experiment due to the two-dimensional material nature of graphene. Alternatively, MD simulations are used to obtain the thermomechanical properties of bulk epoxy (chapter 5), and the interfacial properties of epoxy–graphene interface (chapter 6). The properties obtained from MD simulations are in good agreement with the experimental data. Inserting cohesive element between each bulk element can mimic the arbitrary crack propagation if the element size is small enough. However, the cohesive elements introduce artificial compliance into the model, which increases as the mesh is refined and makes the simulation results mesh-dependent. A method is proposed (chapter 7) to rescale the cohesive element properties in order to obtain the mesh-independent simulations. Finally, the cohesive law obtained from MD simulations are implemented into a cohesive element model of compact tension specimen to simulate the fracture propagation in epoxy–graphene composites (chapter 8). Three mechanisms are proposed to explain the fracture in epoxy–graphene composites: *Nucleation*, the micro-cracks formed at the epoxy–graphene interfaces decrease the stress concentration at the main crack, thus increase the critical force to break the specimen; *Avalanche*, as the graphene loading increase, the micro-cracks connect to form damage inside epoxy, thus decrease the overall fracture toughness of composite; *Percolation*, when the graphene loading is large in the epoxy, the stress concentration at the main crack tip becomes less important, and composite shows a percolation-like damage.

Some open directions for future research are listed:

- The current CB-KIM model is suitable for bulk material with a fixed size of unit cell. Thus, it can not predict the PTs that involve period extensions of reference unit cell, and the deformation of two-dimensional materials. Take use of the cascading Cauchy-Born rule and the exponential Cauchy-Born rule will expand the applicability of this model. The current CB-KIM model assumes the material

to be ideal crystal, thus may overestimate the PT pressure, because it is easier for material to have PT at the defect. The current CB-KIM model does not consider the dynamical action of atoms. However in a real material system, the atoms have thermal vibration near their mean positions. Other future directions may include introduce defects and finite temperature like the Hyper-QC method [29] into model.

- The MD simulation of epoxy–SLG/MLG/MLGO interfaces simulation in chapter 6 only consider the van der Waals interactions between epoxy and nanofillers. However, the nanofiller surfaces may be functionalized by building covalent bonds with epoxy, or connecting epoxy via short chain molecules [13]. Such functionalizations presumably increase the fracture energy of the interfaces because covalent bonds interactions are much stronger than the van der Waals interactions, thus need more energy for breakdown. It may be interesting to involve covalent bonds or short chain molecules between the epoxy and nanofillers, and study the mechanical properties and fracture energy of interface under these functionalizations.

- The shortcomings of the two-dimensional cohesive element model in predicting the crack propagation at large graphene loading have been discussed in chapter 8. Future work may include using the phase field model to study the fracture mechanism in the epoxy–graphene composites. Since the crack propagation and the orientation of graphene in a phase field model is not limited to the bulk element boundaries, phase field model may give us more insights of the fracture mechanism in an epoxy–graphene composite.

Appendix A

Theoretical Solution of Curing Agent Occupation Problem

The curing agent occupation problem is stated as follows:

> There are N curing agent molecules that can link to up to four epoxide groups through four independent active sites ($4N$ in total). If there are $4Np$ active sites that are already occupied, where $p \in [0, 1]$ is the occupation fraction, what is the expected number of curing agents with 0, 1, 2, 3 and 4 active sites occupied among the N curing agents?

In order to solve this problem, two assumptions are made:

1. The N curing agents are identical and independent.
2. The four active sites of a curing agent are identical and independent. Occupying any one of them does not affect the possibility of occupying other active sites.

Taking the expectation number of curing agents with four active sites occupied as

an example, we have:

$$\begin{aligned}
&\mathbb{E}[\text{Number of curing agents with 4 active sites occupied}] \\
&= \sum_{i=1}^{N} \mathbb{P}\left[\text{The } i\text{th curing agent has 4 active sites occupied}\right] \\
&= N \times \frac{C_4^4\ C_{4N-4}^{4Np-4}}{C_{4N}^{4Np}} \\
&= N \times \frac{\frac{(4N-4)!}{(4Np-4)!\,(4N-4Np)!}}{\frac{4N!}{4Np!\,(4N-4Np)!}} \\
&= Np\frac{(4Np-1)(4Np-2)(4Np-3)}{(4N-1)(4N-2)(4N-3)},
\end{aligned} \tag{A.1}$$

where $\mathbb{P}$ is the probability and $C_n^k = n!/[k!(n-k)!]$ is the combinations formula. Similarly, we have

$$\begin{aligned}
&\mathbb{E}[\text{Numbers of curing agents with 3 active sites occupied}] \\
&= N \times \frac{C_4^3\ C_{4N-4}^{4Np-3}}{C_{4N}^{4Np}} \\
&= N \times \frac{4 \times \frac{(4N-4)!}{(4Np-3)!\,(4N-4Np-1)!}}{\frac{4N!}{4Np!\,(4N-4Np)!}} \\
&= 16N^2p(1-p)\frac{(4Np-1)(4Np-2)}{(4N-1)(4N-2)(4N-3)}.
\end{aligned} \tag{A.2}$$

$$\begin{aligned}
&\mathbb{E}[\text{Numbers of curing agents with 2 active sites occupied}] \\
&= N \times \frac{C_4^2\ C_{4N-4}^{4Np-2}}{C_{4N}^{4Np}} \\
&= N \times \frac{6 \times \frac{(4N-4)!}{(4Np-2)!\,(4N-4Np-2)!}}{\frac{4N!}{4Np!\,(4N-4Np)!}} \\
&= 24N^2p(1-p)\frac{(4Np-1)(4N-4Np-1))}{(4N-1)(4N-2)(4N-3)}.
\end{aligned} \tag{A.3}$$

$$
\begin{aligned}
&\mathbb{E}[\text{Numbers of curing agents with 1 active sites occupied}] \\
&= N \times \frac{C_4^1 \; C_{4N-4}^{4Np-1}}{C_{4N}^{4Np}} \\
&= N \times \frac{4 \times \frac{(4N-4)!}{(4Np-1)!\,(4N-4Np-3)!}}{\frac{4N!}{4Np!\,(4N-4Np)!}} \\
&= 16N^2 p(1-p)\frac{(4N-4Np-1)(4N-4Np-2)}{(4N-1)(4N-2)(4N-3)}.
\end{aligned} \tag{A.4}
$$

$$
\begin{aligned}
&\mathbb{E}[\text{Numbers of curing agents with 0 active sites occupied}] \\
&= N \times \frac{C_4^0 C_{4N-4}^{4Np}}{C_{4N}^{4Np}} \\
&= N \times \frac{\frac{(4N-4)!}{4Np!\,(4N-4Np-4)!}}{\frac{4N!}{4Np!\,(4N-4Np)!}} \\
&= N(1-p)\frac{(4N-4Np-1)(4N-4Np-2)(4N-4Np-3)}{(4N-1)(4N-2)(4N-3)}.
\end{aligned} \tag{A.5}
$$

The predictions of this model are in excellent agreement with the results from a multistep MD crosslinking algorithm as shown in Fig. 5.11.

Appendix B

Analytical Solution of E_{eff}/E and $c_{\text{eff}}/c_{\text{b}}$ Ratio for a Model with Triangular Elements

B.1 Analytical solution of E_{eff}/E ratio for a model with triangular elements

The article provides an analytical solution for the effective Young's modulus E_{eff} of a 1D periodic cell consisting of one square bulk element and one cohesive element. Here we provide a similar solution for a 1D periodic cell containing two triangular bulk elements of size h and two cohesive elements with thickness d (one horizontal and one aligned at 45°) as shown in Fig. B.1. The periodic cell is stretched uniformly by an amount of Δ. The bulk elements and the horizontal cohesive element are stretched in the vertical direction by Δ_{b} and Δ_{c}, respectively. The inclined cohesive element experiences stretching in the normal direction Δ_{n} and shearing in the tangent direction Δ_{s}. We have

$$\Delta = \Delta_{\text{b}} + \Delta_{\text{c}} + \frac{\Delta_{\text{n}} + \Delta_{\text{s}}}{\sqrt{2}}. \tag{B.1}$$

At equilibrium, the stress in bulk elements and cohesive element is equal in the vertical direction. Denoting this value as σ, the stress state at an arbitrary point on

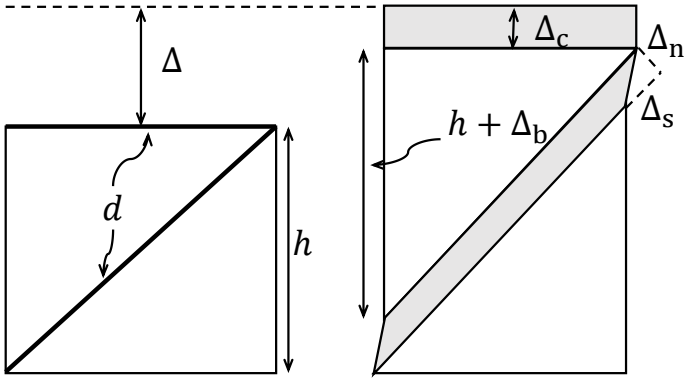

Figure B.1: 1D periodic unit cell containing two triangular elements separated by cohesive elements at 45° and 0° before (left) and after (right) uniaxial stretching.

the plane of the inclined cohesive element is

$$\sigma_{\mathrm{n}} = \sigma_{\mathrm{s}} = \sigma/2, \tag{B.2}$$

where σ_{n} and σ_{s} are normal stress and shear stress. Assuming a linear elastic response for the bulk element and small strain (i.e. neglecting changes to the orientation of the inclined cohesive element), we have

$$\begin{aligned} \sigma &= E\frac{\Delta_{\mathrm{b}}}{h} = K\frac{\Delta_{\mathrm{c}}}{d}, \\ \sigma_{\mathrm{n}} &= K\frac{\Delta_{\mathrm{n}}}{d}, \\ \sigma_{\mathrm{s}} &= \mu\frac{\Delta_{\mathrm{s}}}{d}, \end{aligned} \tag{B.3}$$

where E is Young's modulus of a bulk element, K and μ are Young's modulus and the shear modulus of a cohesive element, respectively. Solving for Δ_{b}, Δ_{c}, Δ_{n}, and Δ_{s} in Eq. (B.3) and substituting these together with Eq. (B.2) into Eq. (B.1) gives

$$\begin{aligned} \Delta &= \frac{\sigma h}{E} + \frac{\sigma d}{K} + \frac{\sqrt{2}}{2}\left(\frac{\sigma_{\mathrm{n}} d}{K} + \frac{\sigma_{\mathrm{s}} d}{\mu}\right) \\ &= \frac{\sigma h}{E}\left(1 + \frac{(4+\sqrt{2})Ed}{4Kh} + \frac{\sqrt{2}Ed}{4\mu h}\right). \end{aligned} \tag{B.4}$$

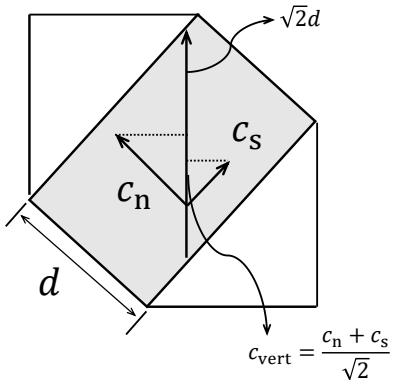

Figure B.2: Zoomed view of the inclined cohesive element (gray rectangle).

Therefore the ratio E_{eff}/E is

$$\frac{E_{\text{eff}}}{E} \equiv \frac{1}{E}\frac{\sigma}{(\Delta/h)} = \left[1 + \frac{(4+\sqrt{2})Ed}{4Kh} + \frac{\sqrt{2}Ed}{4\mu h}\right]^{-1}. \tag{B.5}$$

For the special case where $\mu = K/2$ (corresponding to a Poisson's ratio of zero) used in the numerical example in the article, the result is

$$\frac{E_{\text{eff}}}{E} = \left[1 + \frac{(3\sqrt{2}+4)Ed}{4Kh}\right]^{-1}. \tag{B.6}$$

B.2 Analytical solution of $c_{\text{eff}}/c_{\text{b}}$ ratio of a model with triangular elements

In this section we obtain an expression for the effective speed of sound c_{eff} for the same periodic 1D element described in Section B.1 consisting of two triangular elements and two cohesive elements.

As shown in Fig. B.2, the distance that the stress wave passes through in the inclined cohesive element is $\sqrt{2}d$. The component of the sound speed in the vertical direction is $c_{\text{vert}} = (c_{\text{n}} + c_{\text{s}})/\sqrt{2}$. Thus the total time that it takes the stress wave to pass through

the unit cell is

$$\begin{aligned} t &= \frac{\sqrt{2}d}{c_{\text{vert}}} + \frac{h}{c_{\text{b}}} + \frac{d}{c_{\text{n}}} \\ &= \frac{2d}{c_{\text{n}} + c_{\text{s}}} + \frac{h}{c_{\text{b}}} + \frac{d}{c_{\text{n}}}, \end{aligned} \tag{B.7}$$

where c_{b} is the speed of sound in bulk elements, c_{n} and c_{s} are the speed of sound in a cohesive element in the normal and tangential directions (corresponding to compressive and shear waves), respectively. These speeds are given by

$$\begin{aligned} c_{\text{b}} &= \sqrt{\frac{B_{\text{b}} + \frac{4}{3}\mu_{\text{b}}}{\rho}}, \\ c_{\text{n}} &= \sqrt{\frac{B_{\text{c}} + \frac{4}{3}\mu_{\text{c}}}{\rho}}, \\ c_{\text{s}} &= \sqrt{\frac{\mu_{\text{c}}}{\rho}}, \end{aligned} \tag{B.8}$$

where B_{b} and B_{c} are the bulk modulus of bulk and cohesive elements, μ_{b} and μ_{c} are the shear modulus of bulk and cohesive elements, and ρ is the mass density of material.

The $c_{\text{eff}}/c_{\text{b}}$ ratio follows as

$$\begin{aligned} \frac{c_{\text{eff}}}{c_{\text{b}}} \equiv \frac{1}{c_{\text{b}}}\frac{h}{t} &= \left[\frac{d}{h}\left(\frac{2c_{\text{b}}}{c_{\text{n}} + c_{\text{s}}} + \frac{c_{\text{b}}}{c_{\text{n}}}\right) + 1\right]^{-1} \\ &= \left[\frac{d}{h}\left(\frac{2\sqrt{B_{\text{b}} + \frac{4}{3}\mu_{\text{b}}}}{\sqrt{B_{\text{c}} + \frac{4}{3}\mu_{\text{c}}} + \sqrt{\mu_{\text{c}}}} + \sqrt{\frac{B_{\text{b}} + \frac{4}{3}\mu_{\text{b}}}{B_{\text{c}} + \frac{4}{3}\mu_{\text{c}}}}\right) + 1\right]^{-1}. \end{aligned} \tag{B.9}$$

For the special case where $\mu_{\text{c}} = K/2$, $\mu_{\text{b}} = E/2$, $B_{\text{c}} = K/3$, and $B_{\text{b}} = E/3$ (corresponding to a Poisson's ratio of zero) used in the numerical example in the article, the ratio is

$$\frac{c_{\text{eff}}}{c_b} = \left[1 + \frac{d}{h}\sqrt{\frac{E}{K}}\left(\frac{3\sqrt{2}+1}{\sqrt{2}+1}\right)\right]^{-1}. \tag{B.10}$$

References

[1] Chang-Sheng Zha, Ho-Kwang Mao, and Russell J Hemley. Elasticity of dense helium. *Physical Review B*, 70(17):174107, 2004.

[2] Chang-Sheng Zha, William A Bassett, and Sang-Heon Shim. Rhenium, an in situ pressure calibrant for internally heated diamond anvil cells. *Review of scientific instruments*, 75(7):2409–2418, 2004.

[3] Ming-Bang Lv, Yan Cheng, Yuan-Yuan Qi, Guang-Fu Ji, and Chang-Ge Piao. Elastic properties and phonon dispersions of rhenium in hexagonal-close-packed structure under pressure from first principles. *Physica B: Condensed Matter*, 407(4):778–783, 2012.

[4] L-M Peng, G Ren, SL Dudarev, and MJ Whelan. Robust parameterization of elastic and absorptive electron atomic scattering factors. *Acta Crystallographica Section A: Foundations of Crystallography*, 52(2):257–276, 1996.

[5] Daniel B Knorr, Kevin A Masser, Robert M Elder, Timothy W Sirk, Mark D Hindenlang, H Yu Jian, Adam D Richardson, Steven E Boyd, William A Spurgeon, and Joseph L Lenhart. Overcoming the structural versus energy dissipation trade-off in highly crosslinked polymer networks: Ultrahigh strain rate response in polydicyclopentadiene. *Composites Science and Technology*, 114:17–25, 2015.

[6] Alexander Stukowski. Visualization and analysis of atomistic simulation data with ovito–the open visualization tool. *Modelling and Simulation in Materials Science and Engineering*, 18(1):015012, 2009.

[7] P Loubeyre, R LeToullec, JP Pinceaux, HK Mao, J Hu, and RJ Hemley. Equation of state and phase diagram of solid ^{4}He from single-crystal X-ray diffraction over a large P-T domain. *Physical Review Letters*, 71(14):2272, 1993.

[8] Stanley P Marsh. *LASL shock Hugoniot data*, volume 5. Univ of California Press, 1980.

[9] Thomas S Duffy, Guoyin Shen, Dion L Heinz, Jinfu Shu, Yanzhang Ma, Ho-Kwang Mao, Russell J Hemley, and Anil K Si ngh. Lattice strains in gold and rhenium under nonhydrostatic compression to 37 GPa. *Physical Review B*, 60(22):15063, 1999.

[10] Simone Anzellini, Agnès Dewaele, Florent Occelli, Paul Loubeyre, and Mohamed Mezouar. Equation of state of rhenium and application for ultra high pressure calibration. *Journal of Applied Physics*, 115(4):043511, 2014.

[11] Yu Rok Lee, Soon Cheol Kim, Hyung-il Lee, Han Mo Jeong, Anjanapura V Raghu, Kakarla Raghava Reddy, and Byung Kyu Kim. Graphite oxides as effective fire retardants of epoxy resin. *Macromolecular Research*, 19(1):66–71, 2011.

[12] Bin Yu, Yongqian Shi, Bihe Yuan, Shuilai Qiu, Weiyi Xing, Weizhao Hu, Lei Song, Siuming Lo, and Yuan Hu. Enhanced thermal and flame retardant properties of flame-retardant-wrapped graphene/epoxy resin nanocomposites. *Journal of Materials Chemistry A*, 3(15):8034–8044, 2015.

[13] Yong Tae Park, Yuqiang Qian, Clement Chan, Taewon Suh, Mehrdad Ghasemi Nejhad, Christopher W Macosko, and Andreas Stein. Epoxy toughening with low graphene loading. *Advanced Functional Materials*, 25(4):575–585, 2015.

[14] Andre Lee and Joseph D Lichtenhan. Thermal and viscoelastic property of epoxy–clay and hybrid inorganic–organic epoxy nanocomposites. *Journal of Applied Polymer Science*, 73(10):1993–2001, 1999.

[15] Jun Ma, Mao-Song Mo, Xu-Sheng Du, Patrick Rosso, Klaus Friedrich, and Hsu-Chiang Kuan. Effect of inorganic nanoparticles on mechanical property, fracture toughness and toughening mechanism of two epoxy systems. *Polymer*, 49(16):3510–3523, 2008.

[16] Lu Shan, KNE Verghese, CG Robertson, and KL Reifsnider. Effect of network structure of epoxy dgeba-poly (oxypropylene) diamines on tensile behavior. *Journal of Polymer Science Part B: Polymer Physics*, 37(19):2815–2819, 1999.

[17] CR Amaral, RJ Sanchez Rodriguez, F Gonzalez Garcia, LPB Junior, and EA Carvalho. Impact of aliphatic amine comonomers on dgeba epoxy network properties. *Polymer Engineering & Science*, 54(9):2132–2138, 2014.

[18] ASTM Standard. E647. *Standard test method for measurement of fatigue crack growth rates. Annual book of ASTM Standards*, 3, 2000.

[19] Ellad B Tadmor and Ronald E Miller. *Modeling materials: continuum, atomistic and multiscale techniques*. Cambridge University Press, 2011.

[20] Ellad B Tadmor, Michael Ortiz, and Rob Phillips. Quasicontinuum analysis of defects in solids. *Philosophical Magazine A*, 73(6):1529–1563, 1996.

[21] Ellad B Tadmor, Rob Phillips, and Michael Ortiz. Mixed atomistic and continuum models of deformation in solids. *langmuir*, 12(19):4529–4534, 1996.

[22] Ellad B Tadmor. *The quasicontinuum method. Modeling microstructure on multiple length scales: A mixed continuum and atomistics approach.* PhD dissertation, Brown University, 1997.

[23] VB Shenoy, R Miller, EB Tadmor, R Phillips, and M Ortiz. Quasicontinuum models of interfacial structure and deformation. *Physical Review Letters*, 80(4):742, 1998.

[24] R Miller, M Ortiz, R Phillips, V Shenoy, and Ellad B Tadmor. Quasicontinuum models of fracture and plasticity. *Engineering Fracture Mechanics*, 61(3-4):427–444, 1998.

[25] Ronald E Miller and Ellad B Tadmor. The quasicontinuum method: Overview, applications and current directions. *Journal of Computer-Aided Materials Design*, 9(3):203–239, 2002.

[26] Laurent M Dupuy, Ellad B Tadmor, Ronald E Miller, and Rob Phillips. Finite-temperature quasicontinuum: Molecular dynamics without all the atoms. *Physical Review Letters*, 95(6):060202, 2005.

[27] WK Kim and EB Tadmor. Accelerated quasicontinuum: a practical perspective on hyper-qc with application to nanoindentation. *Philosophical Magazine*, 97(26):2284–2316, 2017.

[28] Viacheslav Sorkin, Ryan S Elliott, and Ellad B Tadmor. A local quasicontinuum method for 3d multilattice crystalline materials: Application to shape-memory alloys. *Modelling and Simulation in Materials Science and Engineering*, 22(5):055001, 2014.

[29] Woo Kyun Kim, Mitchell Luskin, Danny Perez, AF Voter, and Ellad B Tadmor. Hyper-qc: An accelerated finite-temperature quasicontinuum method using hyperdynamics. *Journal of the Mechanics and Physics of Solids*, 63:94–112, 2014.

[30] John Edward Jones. On the determination of molecular fields. i. from the variation of the viscosity of a gas with temperature. In *Proceedings of the Royal Society of London A: Mathematical, Physical and Engineering Sciences*, volume 106, pages 441–462. The Royal Society, 1924.

[31] John Edward Jones. On the determination of molecular fields. ii. from the equation of state of a gas. In *Proceedings of the Royal Society of London A: Mathematical, Physical and Engineering Sciences*, volume 106, pages 463–477. The Royal Society, 1924.

[32] JE Lennard-Jones. On the forces between atoms and ions. *Proceedings of the Royal Society of London. Series A, Containing Papers of a Mathematical and Physical Character*, 109(752):584–597, 1925.

[33] Murray S Daw and Michael I Baskes. Embedded-atom method: Derivation and application to impurities, surfaces, and other defects in metals. *Physical Review B*, 29(12):6443, 1984.

[34] Murray S Daw, Stephen M Foiles, and Michael I Baskes. The embedded-atom method: a review of theory and applications. *Materials Science Reports*, 9(7):251–310, 1993.

[35] Murray S Daw. Model of metallic cohesion: The embedded-atom method. *Physical Review B*, 39(11):7441, 1989.

[36] Frank H Stillinger and Thomas A Weber. Computer simulation of local order in condensed phases of silicon. *Physical review B*, 31(8):5262, 1985.

[37] Stephen L Mayo, Barry D Olafson, and William A Goddard. Dreiding: A generic force field for molecular simulations. *Journal of Physical chemistry*, 94(26):8897–8909, 1990.

[38] Scott J Weiner, Peter A Kollman, David A Case, U Chandra Singh, Caterina Ghio, Guliano Alagona, Salvatore Profeta, and Paul Weiner. A new force field for molecular mechanical simulation of nucleic acids and proteins. *Journal of the American Chemical Society*, 106(3):765–784, 1984.

[39] Junmei Wang, Romain M Wolf, James W Caldwell, Peter A Kollman, and David A Case. Development and testing of a general amber force field. *Journal of computational chemistry*, 25(9):1157–1174, 2004.

[40] William L Jorgensen and Julian Tirado-Rives. The OPLS [optimized potentials for liquid simulations] potential functions for proteins, energy minimizations for crystals of cyclic peptides and crambin. *Journal of the American Chemical Society*, 110(6):1657–1666, 1988.

[41] William L Jorgensen, David S Maxwell, and Julian Tirado-Rives. Development and testing of the OPLS all-atom force field on conformational energetics and properties of organic liquids. *Journal of the American Chemical Society*, 118(45):11225–11236, 1996.

[42] MJ Hwang, TP Stockfisch, and AT Hagler. Derivation of class II force fields. 2. derivation and characterization of a class II force field, CFF93, for the alkyl functional group and alkane molecules. *Journal of the American Chemical Society*, 116(6):2515–2525, 1994.

[43] Huai Sun. Force field for computation of conformational energies, structures, and vibrational frequencies of aromatic polyesters. *Journal of Computational Chemistry*, 15(7):752–768, 1994.

[44] Huai Sun. Compass: an ab initio force-field optimized for condensed-phase applications overview with details on alkane and benzene compounds. *The Journal of Physical Chemistry B*, 102(38):7338–7364, 1998.

[45] H Sun, P Ren, and JR Fried. The compass force field: parameterization and validation for phosphazenes. *Computational and Theoretical Polymer Science*, 8(1-2):229–246, 1998.

[46] Dassault Systemes Biovia. Discovery studio modeling environment. *San Diego: Dassault Systèmes*, 2017.

[47] ABAQUS Version. 6.13 documentation, 2013. *Dassault Systemes Simulia Corp., Providence, RI, USA*.

[48] A Mujica, Angel Rubio, A Munoz, and RJ Needs. High-pressure phases of group-IV, III–V, and II–VI compounds. *Reviews of Modern Physics*, 75(3):863, 2003.

[49] A Kailer, Yu G Gogotsi, and KG Nickel. Phase transformations of silicon caused by contact loading. *Journal of Applied Physics*, 81(7):3057–3063, 1997.

[50] Vladislav Domnich, Yury Gogotsi, and Sergey Dub. Effect of phase transformations on the shape of the unloading curve in the nanoindentation of silicon. *Applied Physics Letters*, 76(16):2214–2216, 2000.

[51] Jing Zhu Hu, Larry D Merkle, Carmen S Menoni, and Ian L Spain. Crystal data for high-pressure phases of silicon. *Physical Review B*, 34(7):4679, 1986.

[52] Radek Erban, Ioannis G Kevrekidis, David Adalsteinsson, and Timothy C Elston. Gene regulatory networks: A coarse-grained, equation-free approach to multiscale computation. *The Journal of chemical physics*, 124(8):084106, 2006.

[53] Radek Erban, Ioannis G Kevrekidis, and Hans G Othmer. An equation-free computational approach for extracting population-level behavior from individual-based models of biological dispersal. *Physica D: Nonlinear Phenomena*, 215(1):1–24, 2006.

[54] L Chen, PG Debenedetti, CW Gear, and IG Kevrekidis. From molecular dynamics to coarse self-similar solutions: A simple example using equation-free computation. *Journal of non-newtonian fluid mechanics*, 120(1):215–223, 2004.

[55] Ioannis G Kevrekidis, C William Gear, and Gerhard Hummer. Equation-free: The computer-aided analysis of complex multiscale systems. *AIChE Journal*, 50(7):1346–1355, 2004.

[56] E Weinan, Bjorn Engquist, Xiantao Li, Weiqing Ren, and Eric Vanden-Eijnden. Heterogeneous multiscale methods: a review. *Commun. Comput. Phys*, 2(3):367–450, 2007.

[57] Augustin Louis Baron Cauchy. *Exercises de mathématiques*, volume 1. Bure frères, 1826.

[58] Max Born and Kun Huang. *Dynamical theory of crystal lattices*. Clarendon Press, 1954.

[59] Max Born. *Atomtheorie des Festen Zustandes (Dynamik der Kristallgitter)*. Springer-Verlag, 2013.

[60] GS Smith, EB Tadmor, N Bernstein, and E Kaxiras. Multiscale simulations of silicon nanoindentation. *Acta Materialia*, 49(19):4089–4101, 2001.

[61] Ryan S Elliott, Nicolas Triantafyllidis, and John A Shaw. Stability of crystalline solidsi: Continuum and atomic lattice considerations. *Journal of the Mechanics and Physics of Solids*, 54(1):161–192, 2006.

[62] Ryan S Elliott, John A Shaw, and Nicolas Triantafyllidis. Stability of crystalline solidsii: Application to temperature-induced martensitic phase transformations in a bi-atomic crystal. *Journal of the Mechanics and Physics of Solids*, 54(1):193–232, 2006.

[63] Marino Arroyo and Ted Belytschko. Finite crystal elasticity of carbon nanotubes based on the exponential Cauchy-Born rule. *Physical Review B*, 69(11):115415, 2004.

[64] Kuan Zhang and Marino Arroyo. Understanding and strain-engineering wrinkle networks in supported graphene through simulations. *Journal of the Mechanics and Physics of Solids*, 72:61–74, 2014.

[65] EB Tadmor, RS Elliott, James P Sethna, RE Miller, and Chandler A Becker. The potential of atomistic simulations and the knowledgebase of interatomic models. *Jom*, 63(7):17, 2011.

[66] Yuri Mishin. EAM potential (LAMMPS cubic hermite tabulation) for Cu developed by Mishin, Mehl and Papaconstantopoulos (2001) v005. OpenKIM, https://doi.org/10.25950/bbcadadf, 2018.

[67] Ryan S. Elliott. EAM Model Driver for tabulated potentials with cubic Hermite spline interpolation as used in LAMMPS v005. OpenKIM, https://doi.org/10.25950/68defa36, 2018.

[68] Amit K Singh. Stillinger-Weber potential for Si due to Stillinger and Weber (1985) v005. OpenKIM, https://doi.org/10.25950/c74b293f, 2018.

[69] Gustav Kirsch. *Die theorie der elastizität und die bedürfnisse der festigkeitslehre*. Springer, 1898.

[70] Junhao Li and Ellad Tadmor. Elastic constants for cubic crystals at zero temperature and pressure v006. OpenKIM, https://doi.org/10.25950/5853fb8f, 2019.

[71] GS Smith, EB Tadmor, and Efthimios Kaxiras. Multiscale simulation of loading and electrical resistance in silicon nanoindentation. *Physical Review Letters*, 84(6):1260, 2000.

[72] ER Weppelmann, JS Field, and MV Swain. Observation, analysis, and simulation of the hysteresis of silicon using ultra-micro-indentation with spherical indenters. *Journal of Materials Research*, 8(4):830–840, 1993.

[73] ER Weppelmann, JS Field, and MV Swain. Influence of spherical indentor radius on the indentation-induced transformation behaviour of silicon. *Journal of materials science*, 30(9):2455–2462, 1995.

[74] William A Bassett. Diamond anvil cell, 50th birthday. *High Pressure Research*, 29(2):163–186, 2009.

[75] J Thomasson, Y Dumont, J-C Griveau, and C Ayache. Transport measurements at low temperatures in a diamond anvil cell with helium as pressure medium. *Review of Scientific Instruments*, 68(3):1514–1517, 1997.

[76] Takemura Kenichi, P Ch Sahu, Kunii Yoshiyasu, and Toma Yasuo. Versatile gas-loading system for diamond-anvil cells. *Review of Scientific Instruments*, 72(10):3873–3876, 2001.

[77] Reinhard Boehler. New diamond cell for single-crystal X-ray diffraction. *Review of Scientific Instruments*, 77(11):115103, 2006.

[78] RL Mills, DH Liebenberg, JC Bronson, and LC Schmidt. Procedure for loading diamond cells with high-pressure gas. *Review of Scientific Instruments*, 51(7):891–895, 1980.

[79] P Loubeyre, JM Besson, JP Pinceaux, and JP Hansen. High-pressure melting curve of ^{4}He. *Physical Review Letters*, 49(16):1172, 1982.

[80] HK Mao, RJ Hemley, Y Wu, AP Jephcoat, LW Finger, CS Zha, and WA Bassett. High-pressure phase diagram and equation of state of solid helium from single-crystal X-ray diffraction to 23.3 GPa. *Physical Review Letters*, 60(25):2649, 1988.

[81] Guangtian Zou, Yanzhang Ma, Ho-Kwang Mao, Russell J Hemley, and Stephen A Gramsch. A diamond gasket for the laser-heated diamond anvil cell. *Review of Scientific Instruments*, 72(2):1298–1301, 2001.

[82] Jagannadham Akella, Samuel T Weir, Yogesh K Vohra, Heather Prokop, Shane A Catledge, and Gary N Chesnut. High pressure phase transformations in neodymium studied in a diamond anvil cell using diamond-coated rhenium gaskets. *Journal of Physics: Condensed Matter*, 11(34):6515, 1999.

[83] Jung-Fu Lin, Jinfu Shu, Ho-Kwang Mao, Russell J Hemley, and Guoyin Shen. Amorphous boron gasket in diamond anvil cell research. *Review of Scientific Instruments*, 74(11):4732–4736, 2003.

[84] Andreas Audétat and Hans Keppler. Solubility of rutile in subduction zone fluids, as determined by experiments in the hydrothermal diamond anvil cell. *Earth and Planetary Science Letters*, 232(3-4):393–402, 2005.

[85] Murli H Manghnani, Keith Katahara, and Edward S Fisher. Ultrasonic equation of state of rhenium. *Physical Review B*, 9(4):1421, 1974.

[86] Paul J Blatz and William L Ko. Application of finite elastic theory to the deformation of rubbery materials. *Transactions of the Society of Rheology*, 6(1):223–251, 1962.

[87] Gerd Steinle-Neumann, Lars Stixrude, and Ronald E Cohen. First-principles elastic constants for the hcp transition metals fe, co, and re at high pressure. *Physical Review B*, 60(2):791, 1999.

[88] Ellad B. Tadmor, Ronald E. Miller, and Ryan S. Elliott. *Continuum Mechanics and Thermodynamics: From Fundamental Principles to Governing Equations*. Cambridge University Press, Cambridge, 2012.

[89] Gerhard A Holzapfel. *Nonlinear Solid Mechanics*, volume 24. Wiley Chichester, 2000.

[90] M Itskov. The derivative with respect to a tensor: some theoretical aspects and applications. *ZAMM-Journal of Applied Mathematics and Mechanics/Zeitschrift für Angewandte Mathematik und Mechanik: Applied Mathematics and Mechanics*, 82(8):535–544, 2002.

[91] John R Ray. Effective elastic constants of solids under stress: Theory and calculations for helium from 11.0 to 23.6 GPa. *Physical Review B*, 40(1):423, 1989.

[92] Woldemar Voigt. *Lehrbuch der kristallphysik (mit ausschluss der kristalloptik)*. Springer-Verlag, 2014.

[93] A Reuss. Berechnung der fließgrenze von mischkristallen auf grund der plastizitätsbedingung für einkristalle. *ZAMM-Journal of Applied Mathematics and Mechanics/Zeitschrift für Angewandte Mathematik und Mechanik*, 9(1):49–58, 1929.

[94] Richard Hill. The elastic behaviour of a crystalline aggregate. *Proceedings of the Physical Society. Section A*, 65(5):349, 1952.

[95] JMJ Den Toonder, JAW Van Dommelen, and FPT Baaijens. The relation between single crystal elasticity and the effective elastic behaviour of polycrystalline materials: theory, measurement and computation. *Modelling and Simulation in Materials Science and Engineering*, 7(6):909, 1999.

[96] David A Young, AK McMahan, and Marvin Ross. Equation of state and melting curve of helium to very high pressure. *Physical Review B*, 24(9):5119, 1981.

[97] Marvin Ross and David A Young. Helium at high density. *Physics Letters A*, 118(9):463–466, 1986.

[98] Pascal Vinet, John R Smith, John Ferrante, and James H Rose. Temperature effects on the universal equation of state of solids. *Physical Review B*, 35(4):1945, 1987.

[99] UC Shrivastava. Theory of the anomalous temperature dependence of C_{12} in NaCl-like structure solids direct observation of phononlattice interactions. *Physica Status Solidi (B)*, 100(2):641–649, 1980.

[100] Orson L Anderson. *Equations of State of Solids for Geophysics and Ceramic Science*, volume 31 of *Oxford Monographs on Geology and Geophysics*. Oxford University Press, 1995.

[101] Madan Singh, Prem P Singh, Braj RK Gupta, and Munish Kumar. Temperature and pressure dependence of elastic constants. *High Temperatures High Pressures*, 33(2):199–206, 2001.

[102] Orson L Anderson. The volume dependence of thermal pressure in solids. *Journal of Physics and Chemistry of Solids*, 58(2):335–343, 1997.

[103] Orson L Anderson, Hitoshi Oda, Anastasia Chopelas, and Donald G Isaak. A thermodynamic theory of the grüneisen ratio at extreme conditions: MgO as an example. *Physics and Chemistry of Minerals*, 19(6):369–380, 1993.

[104] Mark Rivers, Vitali B Prakapenka, Atsushi Kubo, Clayton Pullins, Christopher M Holl, and Steven D Jacobsen. The COMPRES/GSECARS gas-loading system for diamond anvil cells at the advanced photon source. *High Pressure Research*, 28(3):273–292, 2008.

[105] SP Timoshenko and JN Goodier. *Theory of elasticity, 3rd edn.* McGraw-Hill, New York, 1982.

[106] NR Serebryanaya, VD Blank, and VA Ivdenko. Gete-phases under shear deformation and high pressure up to 56 GPa. *Physics Letters A*, 197(1):63–66, 1995.

[107] Dassault Systemes Simulia. *ABAQUS/Standard User's Manual, Version 6.13*. Simulia, 2013. Section 37.1.2.

[108] E. B. Tadmor, G. S. Smith, N. Bernstein, and E. Kaxiras. Mixed finite element and atomistic formulation for complex crystals. *Physical Review B*, 59(1):235–245, 1999.

[109] G. S. Smith, E. B. Tadmor, and E. Kaxiras. Multiscale simulation of loading and electrical resistance in silicon nanoindentation. *Physical Review Letters*, 84(6):1260–1263, 2000.

[110] G. S. Smith, E. B. Tadmor, N. Bernstein, and E. Kaxiras. Multiscale simulations of silicon nanoindentation. *Acta Materialia*, 49(19):4089–4101, 2001.

[111] L Dubrovinsky, N Dubrovinskaia, E Bykova, M Bykov, V Prakapenka, C Prescher, K Glazyrin, H-P Liermann, M Hanfland, Marcus Ekholm, et al. The most incompressible metal osmium at static pressures above 750 gigapascals. *Nature*, 525(7568):226–229, 2015.

[112] Leonid Dubrovinsky, Natalia Dubrovinskaia, Vitali B Prakapenka, and Artem M Abakumov. Implementation of micro-ball nanodiamond anvils for high-pressure studies above 6 mbar. *Nature communications*, 3:1163, 2012.

[113] Russell J Hemley, Ho-kwang Mao, Guoyin Shen, James Badro, Philippe Gillet, Michael Hanfland, and Daniel Häusermann. X-ray imaging of stress and strain of diamond, iron, and tungsten at megabar pressures. *Science*, 276(5316):1242–1245, 1997.

[114] A Werner, JA Sanjurjo, and M Cardona. X-rays investigation of the α β phase transition in the gexsi1- x solid solutions at high pressure. *Solid State Communications*, 44(2):155–158, 1982.

[115] H Olijnyk, SK Sikka, and WB Holzapfel. Structural phase transitions in Si and Ge under pressures up to 50 gpa. *Physics Letters A*, 103(3):137–140, 1984.

[116] E Soignard and PF McMillan. An introduction to diamond anvil cells and loading techniques. In *High-Pressure Crystallography*, pages 81–100. Springer, 2004.

[117] David M Adams, Andrew G Christy, and Andrew J Norman. Optimization of diamond anvil cell performance by finite element analysis. *Measurement Science and Technology*, 4(3):422, 1993.

[118] Andreiy I Kondratyev and Yogesh K Vohra. Finite-element modeling of stresses and strains in a diamond anvil cell device: case of a diamond-coated rhenium gasket. *High Pressure Research*, 27(3):321–331, 2007.

[119] William C Moss, John O Hallquist, Robin Reichlin, Kenneth A Goettel, and Sue Martin. Finite element analysis of the diamond anvil cell: Achieving 4.6 mbar. *Applied physics letters*, 48(19):1258–1260, 1986.

[120] Biao Feng and Valery I Levitas. Finite-element simulations of elastoplastic flow during compression of a sample in a diamond anvil cell under extremely high pressure: Effects of geometry and material properties. *Physical Review Applied*, 10(6):064060, 2018.

[121] Valery I Levitas and Oleg M Zarechnyy. Modeling and simulation of strain-induced phase transformations under compression in a diamond anvil cell. *Physical Review B*, 82(17):174123, 2010.

[122] Biao Feng, Valery I Levitas, and Yanzhang Ma. Strain-induced phase transformation under compression in a diamond anvil cell: Simulations of a sample and gasket. *Journal of Applied Physics*, 115(16):163509, 2014.

[123] Biao Feng, Valery I Levitas, and Oleg M Zarechnyy. Plastic flows and phase transformations in materials under compression in diamond anvil cell: Effect of contact sliding. *Journal of Applied Physics*, 114(4):043506, 2013.

[124] Biao Feng and Valery I Levitas. Effects of gasket on coupled plastic flow and strain-induced phase transformations under high pressure and large torsion in a rotational diamond anvil cell. *Journal of Applied Physics*, 119(1):015902, 2016.

[125] Biao Feng and Valery I Levitas. Coupled phase transformations and plastic flows under torsion at high pressure in rotational diamond anvil cell: Effect of contact sliding. *Journal of Applied Physics*, 114(21):213514, 2013.

[126] Biao Feng and Valery I Levitas. Large elastoplastic deformation of a sample under compression and torsion in a rotational diamond anvil cell under megabar pressures. *International Journal of Plasticity*, 92:79–95, 2017.

[127] Diamond anvil cell manual: Cell preparation, ac susceptibility and electrical resistivity measurements. Technical report, Washington University Physics Schilling High Pressure Lab, 2014.

[128] Aiyasami Jayaraman. Diamond anvil cell and high-pressure physical investigations. *Reviews of Modern Physics*, 55(1):65, 1983.

[129] Yogesh K Vohra and Thomas S McCauley. Metastable phases of carbon during fracture of diamond under ultrahigh compressive stresses. *Diamond and Related Materials*, 3(8):1087–1090, 1994.

[130] Karl E Spear and John P Dismukes. *Synthetic diamond: emerging CVD science and technology*, volume 25. John Wiley & Sons, 1994.

[131] LL Boyer, Efthimios Kaxiras, JL Feldman, JQ Broughton, and MJ Mehl. New low-energy crystal structure for silicon. *Physical review letters*, 67(6):715, 1991.

[132] Jing Han, Song Xu, Jiapeng Sun, Liang Fang, and Hua Zhu. Pressure-induced amorphization in the nanoindentation of single crystalline silicon. *RSC advances*, 7(3):1357–1362, 2017.

[133] Kausala Mylvaganam and Liangchi Zhang. Effect of crystal orientation on the formation of bct-5 silicon. *Applied Physics A*, 120(4):1391–1398, 2015.

[134] Fan Long Jin, Xiang Li, and Soo Jin Park. Synthesis and application of epoxy resins: A review. *Journal of Industrial and Engineering Chemistry*, 29:1–11, 2015.

[135] DC Doherty, BN Holmes, P Leung, and RB Ross. Polymerization molecular dynamics simulations. i. cross-linked atomistic models for poly (methacrylate) networks. *Computational and Theoretical Polymer Science*, 8(1-2):169–178, 1998.

[136] Chunyu Li and Alejandro Strachan. Molecular scale simulations on thermoset polymers: A review. *Journal of Polymer Science Part B: Polymer Physics*, 53(2):103–122, 2015.

[137] Irene Yarovsky and Evan Evans. Computer simulation of structure and properties of crosslinked polymers: application to epoxy resins. *Polymer*, 43(3):963–969, 2002.

[138] David R Heine, Gary S Grest, Christian D Lorenz, Mesfin Tsige, and Mark J Stevens. Atomistic simulations of end-linked poly (dimethylsiloxane) networks: structure and relaxation. *Macromolecules*, 37(10):3857–3864, 2004.

[139] Chaofu Wu and Weijian Xu. Atomistic molecular modelling of crosslinked epoxy resin. *Polymer*, 47(16):6004–6009, 2006.

[140] Hai Bo Fan and Matthew MF Yuen. Material properties of the cross-linked epoxy resin compound predicted by molecular dynamics simulation. *Polymer*, 48(7):2174–2178, 2007.

[141] Chunyu Li and Alejandro Strachan. Molecular dynamics predictions of thermal and mechanical properties of thermoset polymer epon862/detda. *Polymer*, 52(13):2920–2928, 2011.

[142] Ananyo Bandyopadhyay, Pavan K Valavala, Thomas C Clancy, Kristopher E Wise, and Gregory M Odegard. Molecular modeling of crosslinked epoxy polymers: The effect of crosslink density on thermomechanical properties. *Polymer*, 52(11):2445–2452, 2011.

[143] Vikas Varshney, Soumya S Patnaik, Ajit K Roy, and Barry L Farmer. A molecular dynamics study of epoxy-based networks: cross-linking procedure and prediction of molecular and material properties. *Macromolecules*, 41(18):6837–6842, 2008.

[144] Po Han Lin and Rajesh Khare. Molecular simulation of cross-linked epoxy and epoxy-poss nanocomposite. *Macromolecules*, 42(12):4319–4327, 2009.

[145] Shaorui Yang and Jianmin Qu. Computing thermomechanical properties of crosslinked epoxy by molecular dynamic simulations. *Polymer*, 53(21):4806–4817, 2012.

[146] Steve Plimpton, Paul Crozier, and Aidan Thompson. Lammps-large-scale atomic/molecular massively parallel simulator. *Sandia National Laboratories*, 18:43, 2007.

[147] William G Hoover. Canonical dynamics: Equilibrium phase-space distributions. *Physical review A*, 31(3):1695, 1985.

[148] William G Hoover. Constant-pressure equations of motion. *Physical Review A*, 34(3):2499, 1986.

[149] Changwoon Jang, Timothy W Sirk, Jan W Andzelm, and Cameron F Abrams. Comparison of crosslinking algorithms in molecular dynamics simulation of thermosetting polymers. *Macromolecular Theory and Simulations*, 24(3):260–270, 2015.

[150] Materials studio. *BIOVIA, Dassault Systèmes, San Diego California, USA*, 2014.

[151] Jan-Eric Ehlers, Nelson G Rondan, Lam K Huynh, Ha Pham, Maurice Marks, and Thanh N Truong. Theoretical study on mechanisms of the epoxy- amine curing reaction. *Macromolecules*, 40(12):4370–4377, 2007.

[152] Frank H Allen, Olga Kennard, David G Watson, Lee Brammer, A Guy Orpen, and Robin Taylor. Tables of bond lengths determined by X-ray and neutron diffraction. part 1. bond lengths in organic compounds. *Journal of the Chemical Society, Perkin Transactions 2*, (12):S1–S19, 1987.

[153] Richard A Engh and Robert Huber. Accurate bond and angle parameters for X-ray protein structure refinement. *Acta Crystallographica Section A: Foundations of Crystallography*, 47(4):392–400, 1991.

[154] Jin Woo Kang, Kyoungsei Choi, Won Ho Jo, and Shaw Ling Hsu. Structure–property relationships of polyimides: A molecular simulation approach. *Polymer*, 39(26):7079–7087, 1998.

[155] Wenqing Zhang, Yang Qing, Weihong Zhong, Gang Sui, and Xiaoping Yang. Mechanism of modulus improvement for epoxy resin matrices: A molecular dynamics simulation. *Reactive and Functional Polymers*, 111:60–67, 2017.

[156] Chaofu Wu and Weijian Xu. Atomistic molecular simulations of structure and dynamics of crosslinked epoxy resin. *Polymer*, 48(19):5802–5812, 2007.

[157] David A Keen. A comparison of various commonly used correlation functions for describing total scattering. *Journal of Applied Crystallography*, 34(2):172–177, 2001.

[158] Spyros V Kallivokas, Aristotelis P Sgouros, and Doros N Theodorou. Molecular dynamics simulations of EPON-862/DETDA epoxy networks: structure, topology, elastic constants, and local dynamics. *Soft matter*, 15(4):721–733, 2019.

[159] Bertram Eugene Warren. *X-ray Diffraction*. Courier Corporation, 1990.

[160] B Yates, BA McCalla, LN Phillips, DM Kingston-Lee, and KF Rogers. The thermal expansion of carbon fibre-reinforced plastics. *Journal of Materials Science*, 14(5):1207–1217, 1979.

[161] Douglas R Miller and Christopher W Macosko. A new derivation of postgel properties of network polymers. *Rubber chemistry and technology*, 49(5):1219–1231, 1976.

[162] Arturo Hale, Christopher W Macosko, and Harvey E Bair. Glass transition temperature as a function of conversion in thermosetting polymers. *Macromolecules*, 24(9):2610–2621, 1991.

[163] Sue Ann Bidstrup and Christopher W Macosko. Chemorheology relations for epoxy-amine crosslinking. *Journal of Polymer Science Part B: Polymer Physics*, 28(5):691–709, 1990.

[164] Hatsuo Ishida and Douglas J Allen. Physical and mechanical characterization of near-zero shrinkage polybenzoxazines. *Journal of polymer science Part B: Polymer physics*, 34(6):1019–1030, 1996.

[165] Hatsuo Ishida and Hong Yee Low. A study on the volumetric expansion of benzoxazine-based phenolic resin. *Macromolecules*, 30(4):1099–1106, 1997.

[166] Xiaorong Wang and Victor J Foltz. Crosslinking induced volume expansion in the glass state. *Polymer*, 47(14):5090–5096, 2006.

[167] Malcolm L Williams, Robert F Landel, and John D Ferry. The temperature dependence of relaxation mechanisms in amorphous polymers and other glass-forming liquids. *Journal of the American Chemical society*, 77(14):3701–3707, 1955.

[168] John D Ferry and John Douglass Ferry. *Viscoelastic properties of polymers*. John Wiley & Sons, 1980.

[169] Armand Soldera and Noureddine Metatla. Glass transition of polymers: Atomistic simulation versus experiments. *Physical Review E*, 74(6):061803, 2006.

[170] Lawrence E Nielsen. Cross-linking–effect on physical properties of polymers. *Journal of Macromolecular Science, Part C*, 3(1):69–103, 1969.

[171] AT DiBenedetto. Prediction of the glass transition temperature of polymers: a model based on the principle of corresponding states. *Journal of Polymer Science Part B: Polymer Physics*, 25(9):1949–1969, 1987.

[172] PR Couchman. Thermodynamics and the compositional variation of glass transition temperatures. *Macromolecules*, 20(7):1712–1717, 1987.

[173] JP Pascault and RJJ Williams. Glass transition temperature versus conversion relationships for thermosetting polymers. *Journal of Polymer Science Part B: Polymer Physics*, 28(1):85–95, 1990.

[174] Abraham Savitzky and Marcel JE Golay. Smoothing and differentiation of data by simplified least squares procedures. *Analytical chemistry*, 36(8):1627–1639, 1964.

[175] Jörg Rottler and Mark O Robbins. Yield conditions for deformation of amorphous polymer glasses. *Physical Review E*, 64(5):051801, 2001.

[176] AV Lyulin, B Vorselaars, MA Mazo, NK Balabaev, and MAJ Michels. Strain softening and hardening of amorphous polymers: Atomistic simulation of bulk mechanics and local dynamics. *EPL (Europhysics Letters)*, 71(4):618, 2005.

[177] David MacNeill and Jörg Rottler. From macroscopic yield criteria to atomic stresses in polymer glasses. *Physical Review E*, 81(1):011804, 2010.

[178] Amos Gilat, Robert K Goldberg, and Gary D Roberts. Strain rate sensitivity of epoxy resin in tensile and shear loading. *Journal of Aerospace Engineering*, 20(2):75–89, 2007.

[179] Justin D Littell, Charles R Ruggeri, Robert K Goldberg, Gary D Roberts, William A Arnold, and Wieslaw K Binienda. Measurement of epoxy resin tension, compression, and shear stress–strain curves over a wide range of strain rates using small test specimens. *Journal of Aerospace Engineering*, 21(3):162–173, 2008.

[180] Subrahmanyam Pattamatta, Ryan S Elliott, and Ellad B Tadmor. Mapping the stochastic response of nanostructures. *Proceedings of the National Academy of Sciences*, page 201402029, 2014.

[181] T Ozkan, Q Chen, and Ioannis Chasiotis. Interfacial strength and fracture energy of individual carbon nanofibers in epoxy matrix as a function of surface conditions. *Composites Science and Technology*, 72(9):965–975, 2012.

[182] G Levita, S De Petris, A Marchetti, and Andrea Lazzeri. Crosslink density and fracture toughness of epoxy resins. *Journal of materials science*, 26(9):2348–2352, 1991.

[183] RP Singh, M Zhang, and D Chan. Toughening of a brittle thermosetting polymer: Effects of reinforcement particle size and volume fraction. *Journal of materials science*, 37(4):781–788, 2002.

[184] Victor MF Evora and Arun Shukla. Fabrication, characterization, and dynamic behavior of polyester/TiO_2 nanocomposites. *Materials Science and Engineering: A*, 361(1-2):358–366, 2003.

[185] Stephan Sprenger. Epoxy resin composites with surface-modified silicon dioxide nanoparticles: A review. *Journal of Applied Polymer Science*, 130(3):1421–1428, 2013.

[186] Jeffrey R Potts, Daniel R Dreyer, Christopher W Bielawski, and Rodney S Ruoff. Graphene-based polymer nanocomposites. *Polymer*, 52(1):5–25, 2011.

[187] Andre K Geim and Konstantin S Novoselov. The rise of graphene. *Nature materials*, 6(3):183–191, 2007.

[188] Nadiim Domun, H Hadavinia, T Zhang, T Sainsbury, GH Liaghat, and S Vahid. Improving the fracture toughness and the strength of epoxy using nanomaterials–a review of the current status. *Nanoscale*, 7(23):10294–10329, 2015.

[189] Minoo Naebe, Jing Wang, Abbas Amini, Hamid Khayyam, Nishar Hameed, Lu Hua Li, Ying Chen, and Bronwyn Fox. Mechanical property and structure of covalent functionalised graphene/epoxy nanocomposites. *Scientific reports*, 4:4375, 2014.

[190] Sasha Stankovich, Dmitriy A Dikin, Geoffrey HB Dommett, Kevin M Kohlhaas, Eric J Zimney, Eric A Stach, Richard D Piner, SonBinh T Nguyen, and Rodney S Ruoff. Graphene-based composite materials. *nature*, 442(7100):282–286, 2006.

[191] KP Pramoda, H Hussain, HM Koh, HR Tan, and CB He. Covalent bonded polymer–graphene nanocomposites. *Journal of Polymer Science Part A: Polymer Chemistry*, 48(19):4262–4267, 2010.

[192] Swetha Chandrasekaran, Narumichi Sato, Folke Tölle, Rolf Mülhaupt, Bodo Fiedler, and Karl Schulte. Fracture toughness and failure mechanism of graphene based epoxy composites. *Composites Science and Technology*, 97:90–99, 2014.

[193] Siyao He, Yuqiang Qian, Kunwei Liu, Christopher W Macosko, and Andreas Stein. Effects of inorganic fillers on toughening of vinyl ester resins by modified graphene oxide. *Industrial & Engineering Chemistry Research*, 57(13):4592–4599, 2018.

[194] Siyao He, Nicholas D Petkovich, Kunwei Liu, Yuqiang Qian, Christopher W Macosko, and Andreas Stein. Unsaturated polyester resin toughening with very low loadings of GO derivatives. *Polymer*, 110:149–157, 2017.

[195] Mei Zu, Qingwen Li, Yuntian Zhu, Moutushi Dey, Guojian Wang, Weibang Lu, Joseph M Deitzel, John W Gillespie Jr, Joon-Hyung Byun, and Tsu-Wei Chou. The effective interfacial shear strength of carbon nanotube fibers in an epoxy matrix characterized by a microdroplet test. *Carbon*, 50(3):1271–1279, 2012.

[196] Chunyu Li, Andrea R Browning, Stephen Christensen, and Alejandro Strachan. Atomistic simulations on multilayer graphene reinforced epoxy composites. *Composites Part A: Applied Science and Manufacturing*, 43(8):1293–1300, 2012.

[197] R Rahman and A Haque. Molecular modeling of crosslinked graphene–epoxy nanocomposites for characterization of elastic constants and interfacial properties. *Composites Part B: Engineering*, 54:353–364, 2013.

[198] Yunlong Li, Shijie Wang, and Quan Wang. A molecular dynamics simulation study on enhancement of mechanical and tribological properties of polymer composites by introduction of graphene. *Carbon*, 111:538–545, 2017.

[199] Bohayra Mortazavi, Olivier Benzerara, Hendrik Meyer, Julien Bardon, and Said Ahzi. Combined molecular dynamics-finite element multiscale modeling of thermal conduction in graphene epoxy nanocomposites. *Carbon*, 60:356–365, 2013.

[200] Janghyuk Moon, Seunghwa Yang, and Maenghyo Cho. Interfacial strengthening between graphene and polymer through stone-thrower-wales defects: Ab initio and molecular dynamics simulations. *Carbon*, 118:66–77, 2017.

[201] Rui Sun, Lili Li, Chuang Feng, Sritawat Kitipornchai, and Jie Yang. Tensile behavior of polymer nanocomposite reinforced with graphene containing defects. *European Polymer Journal*, 98:475–482, 2018.

[202] Daniel R Dreyer, Sungjin Park, Christopher W Bielawski, and Rodney S Ruoff. The chemistry of graphene oxide. *Chemical society reviews*, 39(1):228–240, 2010.

[203] T Nakajima, A Mabuchi, and R Hagiwara. A new structure model of graphite oxide. *Carbon*, 26(3):357–361, 1988.

[204] Suenne Kim, Si Zhou, Yike Hu, Muge Acik, Yves J Chabal, Claire Berger, Walt De Heer, Angelo Bongiorno, and Elisa Riedo. Room-temperature metastability of multilayer graphene oxide films. *Nature materials*, 11(6):544, 2012.

[205] B Yates, MJ Overy, JP Sargent, BA McCalla, DM Kingston-Lee, LN Phillips, and KF Rogers. The thermal expansion of carbon fiber-reinforced plastics. *Journal of Materials Science*, 13(2):433–440, 1978.

[206] Shigeki Yashiro, Yoshihisa Sakaida, Yoshinobu Shimamura, and Yoku Inoue. Evaluation of interfacial shear stress between multi-walled carbon nanotubes and epoxy based on strain distribution measurement using raman spectroscopy. *Composites Part A: Applied Science and Manufacturing*, 85:192–198, 2016.

[207] Albert F Yee and Raymond A Pearson. Toughening mechanisms in elastomer-modified epoxies. *Journal of materials science*, 21(7):2462–2474, 1986.

[208] WD Bascom, RL Cottington, RL Jones, and P Peyser. The fracture of epoxy-and elastomer-modified epoxy polymers in bulk and as adhesives. *Journal of Applied Polymer Science*, 19(9):2545–2562, 1975.

[209] Sarah-Jane V Frankland, Thomas C Clancy, Jeffrey A Hinkley, and Gates TS. Molecular dynamics simulations of adhesion at epoxy interfaces. (NASA/20080040188), 2008.

[210] Anthony J Kinloch. *Adhesion and adhesives: science and technology*. Springer Science & Business Media, 2012.

[211] HR Brown. A molecular interpretation of the toughness of glassy polymers. *Macromolecules*, 24(10):2752–2756, 1991.

[212] CY Hui, A Ruina, C Creton, and EJ Kramer. Micromechanics of crack growth into a craze in a polymer glass. *Macromolecules*, 25(15):3948–3955, 1992.

[213] Y Sha, CY Hui, A Ruina, and EJ Kramer. Continuum and discrete modeling of craze failure at a crack tip in a glassy polymer. *Macromolecules*, 28(7):2450–2459, 1995.

[214] Zhaoxu Meng, Miguel A Bessa, Wenjie Xia, Wing Kam Liu, and Sinan Keten. Predicting the macroscopic fracture energy of epoxy resins from atomistic molecular simulations. *Macromolecules*, 49(24):9474–9483, 2016.

[215] Ting Ge, Gary S Grest, and Mark O Robbins. Tensile fracture of welded polymer interfaces: Miscibility, entanglements, and crazing. *Macromolecules*, 47(19):6982–6989, 2014.

[216] Paul C Paris and George C Sih. Fracture toughness testing and its applications. *ASTM STP*, 381:52–60, 1965.

[217] Thomas F Willems, Chris H Rycroft, Michaeel Kazi, Juan C Meza, and Maciej Haranczyk. Algorithms and tools for high-throughput geometry-based analysis of crystalline porous materials. *Microporous and Mesoporous Materials*, 149(1):134–141, 2012.

[218] Jiadi Fan and Ellad B Tadmor. Rescaling cohesive element properties for mesh independent fracture simulations. *Engineering Fracture Mechanics*, 213:89–99, 2019.

[219] Zhaohe Dai, Guorui Wang, Luqi Liu, Yuan Hou, Yueguang Wei, and Zhong Zhang. Mechanical behavior and properties of hydrogen bonded graphene/polymer nanointerfaces. *Composites Science and Technology*, 136:1–9, 2016.

[220] Amnaya P Awasthi, Dimitris C Lagoudas, and Daniel C Hammerand. Modeling of graphene–polymer interfacial mechanical behavior using molecular dynamics.

Modelling and Simulation in Materials Science and Engineering, 17(1):015002, 2008.

[221] Donald S Dugdale. Yielding of steel sheets containing slits. *Journal of the Mechanics and Physics of Solids*, 8(2):100–104, 1960.

[222] Grigory Isaakovich Barenblatt. The mathematical theory of equilibrium cracks in brittle fracture. *Advances in applied mechanics*, 7:55–129, 1962.

[223] X-P Xu and A Needleman. Void nucleation by inclusion debonding in a crystal matrix. *Modelling and Simulation in Materials Science and Engineering*, 1(2):111, 1993.

[224] X-P Xu and Alan Needleman. Numerical simulations of fast crack growth in brittle solids. *Journal of the Mechanics and Physics of Solids*, 42(9):1397–1434, 1994.

[225] Godofredo T Camacho and M Ortiz. Computational modelling of impact damage in brittle materials. *International Journal of solids and structures*, 33(20-22):2899–2938, 1996.

[226] Kyoungsoo Park and Glaucio H Paulino. Cohesive zone models: a critical review of traction-separation relationships across fracture surfaces. *Applied Mechanics Reviews*, 64(6):060802, 2011.

[227] Arne Hillerborg, Mats Modéer, and P-E Petersson. Analysis of crack formation and crack growth in concrete by means of fracture mechanics and finite elements. *Cement and concrete research*, 6(6):773–781, 1976.

[228] Pedro P Camanho and Carlos G Dávila. Mixed-mode decohesion finite elements for the simulation of delamination in composite materials. Technical Report NASA/TM-2002-211737, 2002.

[229] Albert Turon, Carlos G Davila, Pedro Ponces Camanho, and J Costa. An engineering solution for mesh size effects in the simulation of delamination using cohesive zone models. *Engineering fracture mechanics*, 74(10):1665–1682, 2007.

[230] BRK Blackman, H Hadavinia, AJ Kinloch, and JG Williams. The use of a cohesive zone model to study the fracture of fibre composites and adhesively-bonded joints. *International journal of fracture*, 119(1):25–46, 2003.

[231] Nicolas Moës and Ted Belytschko. Extended finite element method for cohesive crack growth. *Engineering fracture mechanics*, 69(7):813–833, 2002.

[232] Natarajan Sukumar, David L Chopp, Nicolas Moës, and Ted Belytschko. Modeling holes and inclusions by level sets in the extended finite-element method. *Computer methods in applied mechanics and engineering*, 190(46):6183–6200, 2001.

[233] Christian Miehe, Martina Hofacker, and Fabian Welschinger. A phase field model for rate-independent crack propagation: Robust algorithmic implementation based on operator splits. *Computer Methods in Applied Mechanics and Engineering*, 199(45):2765–2778, 2010.

[234] C Miehe, F Welschinger, and M Hofacker. Thermodynamically consistent phase-field models of fracture: Variational principles and multi-field fe implementations. *International Journal for Numerical Methods in Engineering*, 83(10):1273–1311, 2010.

[235] M. J. Borden, C. V. Verhoosel, M. A. Scott, T. J. R. Hughes, and C. M. Landis. A phase-field description of dynamic brittle fracture. *Computer Methods in Applied Mechanics and Engineering*, 217:77–95, 2012.

[236] PA Klein, JW Foulk, EP Chen, SA Wimmer, and HJ Gao. Physics-based modeling of brittle fracture: cohesive formulations and the application of meshfree methods. *Theoretical and Applied Fracture Mechanics*, 37(1):99–166, 2001.

[237] Michael L Falk, Alan Needleman, and James R Rice. A critical evaluation of cohesive zone models of dynamic fracture. In *Proceedings of the 5th European mechanics of materials conference on scale transitions from atomistics to continuum plasticity*, pages 43–50, 2001.

[238] Ala Tabiei and Wenlong Zhang. Cohesive element approach for dynamic crack propagation: Artificial compliance and mesh dependency. *Engineering Fracture Mechanics*, 180:23–42, 2017.

[239] Zdeněk P Bažant and Byung H Oh. Crack band theory for fracture of concrete. *Materials and Structures*, 16(3):155–177, 1983.

[240] RiCoh Manual. http://galileo.pmi.lv/~tarasov/ricoh/index.html.

[241] Jorg F Kalthoff. Shadow optical analysis of dynamic shear fracture. *Optical Engineering*, 27(10):271035–271035, 1988.

[242] JF Kalthoff and S Winkler. Failure mode transition at high rates of shear loading. *DGM Informationsgesellschaft mbH, Impact Loading and Dynamic Behavior of Materials*, 1:185–195, 1988.

[243] RC Batra and MVS Ravinsankar. Three-dimensional numerical simulation of the kalthoff experiment. *International Journal of fracture*, 105(2):161–186, 2000.

[244] Thomas Menouillard, Julien Rethore, Alain Combescure, and Harridh Bung. Efficient explicit time stepping for the extended finite element method (X-FEM). *International Journal for Numerical Methods in Engineering*, 68(9):911–939, 2006.

[245] Timon Rabczuk, Goangseup Zi, Stephane Bordas, and Hung Nguyen-Xuan. A simple and robust three-dimensional cracking-particle method without enrichment. *Computer Methods in Applied Mechanics and Engineering*, 199(37):2437–2455, 2010.

[246] Daniel R Bortz, Erika Garcia Heras, and Ignacio Martin-Gullon. Impressive fatigue life and fracture toughness improvements in graphene oxide/epoxy composites. *Macromolecules*, 45(1):238–245, 2011.

[247] Mohammad A Rafiee, Javad Rafiee, Zhou Wang, Huaihe Song, Zhong-Zhen Yu, and Nikhil Koratkar. Enhanced mechanical properties of nanocomposites at low graphene content. *ACS nano*, 3(12):3884–3890, 2009.

[248] Xiao Wang, Jie Jin, and Mo Song. An investigation of the mechanism of graphene toughening epoxy. *Carbon*, 65:324–333, 2013.

[249] Amar C Garg and Yiu-Wing Mai. Failure mechanisms in toughened epoxy resinsa review. *Composites Science and Technology*, 31(3):179–223, 1988.

[250] Shao-Yun Fu, Xi-Qiao Feng, Bernd Lauke, and Yiu-Wing Mai. Effects of particle size, particle/matrix interface adhesion and particle loading on mechanical properties of particulate–polymer composites. *Composites Part B: Engineering*, 39(6):933–961, 2008.

[251] Ashivni Shekhawat, Stefano Zapperi, and James P Sethna. From damage percolation to crack nucleation through finite size criticality. *Physical review letters*, 110(18):185505, 2013.

[252] Allan F Bower. *Applied mechanics of solids*. CRC press, 2009.

[253] AN Netravali, RB Henstenburg, SL Phoenix, and P Schwartz. Interfacial shear strength studies using the single-filament-composite test I: Experiments on graphite fibers in epoxy. *Polymer Composites*, 10(4):226–241, 1989.